

---

Theses and Dissertations

---

Summer 2012

# Performance evaluation of a network of polarimetric X-Band radars used for rainfall estimation

Piotr Domaszczyński  
*University of Iowa*

Copyright 2012 Piotr Domaszczyński

This dissertation is available at Iowa Research Online: <https://ir.uiowa.edu/etd/3286>

---

## Recommended Citation

Domaszczyński, Piotr. "Performance evaluation of a network of polarimetric X-Band radars used for rainfall estimation." PhD (Doctor of Philosophy) thesis, University of Iowa, 2012.  
<https://doi.org/10.17077/etd.59zxkec2>.

---

Follow this and additional works at: <https://ir.uiowa.edu/etd>



Part of the [Civil and Environmental Engineering Commons](#)

PERFORMANCE EVALUATION OF A NETWORK OF POLARIMETRIC X-BAND  
RADARS USED FOR RAINFALL ESTIMATION

by

Piotr Domaszczyński

An Abstract

Of a thesis submitted in partial fulfillment  
of the requirements for the Doctor of  
Philosophy degree in Civil and Environmental Engineering  
in the Graduate College of  
The University of Iowa

July 2012

Thesis Supervisor: Professor Witold F. Krajewski

## ABSTRACT

Networks of small, often mobile, polarimetric radars are gaining popularity in the hydrometeorology community due to their rainfall observing capabilities and relative low purchase cost. In recent years, a number of installations have become operational around the globe. The problem of signal attenuation by intervening rainfall has been recognized as the major source of error in rainfall estimation by short-wavelength (C-, X, K-band) radars. The simultaneous observation of precipitation by multiple radars creates new prospects for better and more robust attenuation correction algorithms and, consequently, yields more accurate rainfall estimation.

The University of Iowa hydrometeorology group's acquisition of a network of four mobile, polarimetric, X-band radars has resulted in the need for a thoughtful evaluation of the instrument. In this work, we use computer simulations and the data collected by The University of Iowa Polarimetric Radar Network to study the performance of attenuation correction methods in single-radar and network-based arrangements.

To support the computer simulations, we developed a comprehensive polarimetric radar network simulator, which replicates the essential aspects of the radar network rainfall observing process. The simulations are based on a series of physics- and stochastic-based simulated rainfall events occurring over the area of interest. The characteristics of the simulated radars are those of The University of Iowa Polarimetric Radar Network. We assess the correction methods by analyzing the errors in reflectivity and rainfall rate over the area of interest covered by the network's radars.

To enable the implementation of the attenuation correction methods to the data collected by The University of Iowa Polarimetric Radar Network, we first developed a set of utilities to assist with efficient data collection and analysis. Next, we conducted a series of calibration tests to evaluate the relative calibration and channel balance of the

network's radars. Finally, in an attempt to verify the results obtained via computer simulations, we applied the set of attenuation correction algorithms to the data collected by The University of Iowa Polarimetric Radar Network.

Abstract Approved: \_\_\_\_\_  
Thesis Supervisor  
\_\_\_\_\_  
Title and Department  
\_\_\_\_\_  
Date

PERFORMANCE EVALUATION OF A NETWORK OF POLARIMETRIC X-BAND  
RADARS USED FOR RAINFALL ESTIMATION

by

Piotr Domaszczyński

A thesis submitted in partial fulfillment  
of the requirements for the Doctor of  
Philosophy degree in Civil and Environmental Engineering  
in the Graduate College of  
The University of Iowa

July 2012

Thesis Supervisor: Professor Witold F. Krajewski

Copyright by  
PIOTR DOMASZCZYNSKI  
2012  
All Rights Reserved

Graduate College  
The University of Iowa  
Iowa City, Iowa

CERTIFICATE OF APPROVAL

---

PH.D. THESIS

---

This is to certify that the Ph.D. thesis of

Piotr Domaszczyński

has been approved by the Examining Committee  
for the thesis requirement for the Doctor of Philosophy  
degree in Civil and Environmental Engineering at the July 2012 graduation.

Thesis Committee: \_\_\_\_\_  
Witold F. Krajewski, Thesis Supervisor

\_\_\_\_\_  
A. Allen Bradley

\_\_\_\_\_  
Anton Kruger

\_\_\_\_\_  
James A. Smith

\_\_\_\_\_  
Larry J. Weber

To those who always believed in me

It was a great step in science when men became convinced that, in order to understand the nature of things, they must begin by asking, not whether a thing is good or bad, noxious or beneficial, but of what kind it is? And how much is there of it? Quality and Quantity were then first recognised as the primary features to be observed in scientific inquiry.

James Clerk Maxwell  
*A Treatise on Electricity and Magnetism* (1873)

## ABSTRACT

Networks of small, often mobile, polarimetric radars are gaining popularity in the hydrometeorology community due to their rainfall observing capabilities and relative low purchase cost. In recent years, a number of installations have become operational around the globe. The problem of signal attenuation by intervening rainfall has been recognized as the major source of error in rainfall estimation by short-wavelength (C-, X, K-band) radars. The simultaneous observation of precipitation by multiple radars creates new prospects for better and more robust attenuation correction algorithms and, consequently, yields more accurate rainfall estimation.

The University of Iowa hydrometeorology group's acquisition of a network of four mobile, polarimetric, X-band radars has resulted in the need for a thoughtful evaluation of the instrument. In this work, we use computer simulations and the data collected by The University of Iowa Polarimetric Radar Network to study the performance of attenuation correction methods in single-radar and network-based arrangements.

To support the computer simulations, we developed a comprehensive polarimetric radar network simulator, which replicates the essential aspects of the radar network rainfall observing process. The simulations are based on a series of physics- and stochastic-based simulated rainfall events occurring over the area of interest. The characteristics of the simulated radars are those of The University of Iowa Polarimetric Radar Network. We assess the correction methods by analyzing the errors in reflectivity and rainfall rate over the area of interest covered by the network's radars.

To enable the implementation of the attenuation correction methods to the data collected by The University of Iowa Polarimetric Radar Network, we first developed a set of utilities to assist with efficient data collection and analysis. Next, we conducted a series of calibration tests to evaluate the relative calibration and channel balance of the

network's radars. Finally, in an attempt to verify the results obtained via computer simulations, we applied the set of attenuation correction algorithms to the data collected by The University of Iowa Polarimetric Radar Network.

## TABLE OF CONTENTS

LIST OF TABLES .....	ix
LIST OF FIGURES .....	xii
CHAPTER 1 INTRODUCTION.....	1
1.1 Motivation.....	1
1.2 Problem statement .....	3
1.3 Literature review .....	5
1.3.1 Weather radar attenuation correction studies .....	5
1.3.2 Simulation-based studies in weather radar .....	8
1.4 Objectives and methodology .....	9
CHAPTER 2 THE POLARIMETRIC RADAR NETWORK SIMULATOR.....	15
2.1 Introduction.....	15
2.2 Description of the simulator .....	15
2.2.1 Run-time configuration of the simulator .....	16
2.2.2 Spatial domain and area of interest .....	16
2.2.3 Raindrop Model Description.....	17
2.2.4 Radar’s spatial sampling model .....	18
2.2.5 DSD input fields.....	18
2.2.6 T-Matrix scattering method .....	19
2.3 Simulated radar variables .....	21
2.3.1 Polarimetric Observables.....	21
2.3.2 Measurement noise.....	22
2.3.3 Differential propagation phase smoothing.....	23
2.4 Network data merging .....	24
2.5 Evaluation of simulation results.....	25
2.6 Validation of the simulator .....	26
2.7 Sample simulation results .....	28
2.7.1 Field values versus radar observables .....	28
2.7.2 Effect of beam geometry.....	29
2.7.3 Introducing noise to observations.....	30
2.7.4 Radar location effect.....	31
2.7.5 Network data merging .....	31
2.8 Summary of Chapter 2.....	33
CHAPTER 3 ANALYSIS OF ATTENUATION CORRECTION METHODS IN A NETWORKED ENVIRONMENT BY MEANS OF COMPUTER SIMULATIONS .....	52
3.1 Introduction.....	52
3.2 Simulation design.....	53
3.3 Single-radar attenuation correction methods .....	54
3.3.1 The “forward” algorithm [Method 1] .....	55
3.3.2 The $\Phi$ DP constrained method [Method 2].....	55
3.3.3 The constrained method with optimal parameter $\alpha$ [Method3] .....	56
3.3.4 The KDP method [Method 4] .....	57
3.4 Simulation results for single-radar methods .....	57

3.4.1 Spatial scaling of the single-radar attenuation correction results .....	59
3.4.2 Range dependent accuracy of the single-radar correction methods.....	60
3.4.3 Performance analysis of the single radar attenuation correction methods .....	60
3.5 Data merging methods for single-radar products.....	63
3.5.1 Inverse-distance weighting [Method 1].....	64
3.5.2 Minimum distance [Method 2].....	65
3.5.3 Minimum PIA [Method 3].....	65
3.5.4 PIA-based weighting [Method 4].....	66
3.5.5 Maximum value [Method 5] .....	66
3.6 Results for network merging methods.....	66
3.6.1 Performance analysis of the data merging methods.....	67
3.7 Network based attenuation correction method .....	69
3.7.1 Simulation results for the network based attenuation correction method .....	70
3.7.2 Performance analysis of the network based attenuation correction method .....	71
3.8 Summary of Chapter 3.....	73
CHAPTER 4 DEVELOPMENT OF UTILITIES IN SUPPORT OF DATA PROCESSING, ANALYSIS, AND DISPLAY.....	119
4.1 Introduction.....	119
4.2 The network's technical specifications .....	120
4.3 Data acquisition system.....	121
4.3.1 Radar Control Board (RCB) parameters.....	121
4.3.2 Digital receiver control parameters .....	122
4.3.3 Data Processing Algorithm .....	123
4.3.3.1 Pulse-Pair Mode (PP).....	124
4.3.3.2 DPP Mode .....	126
4.3.3.3 The FFT Mode.....	127
4.3.3.4. FFT2 Mode.....	127
4.3.3.5 FFT2I Mode .....	128
4.4 Custom Data Processing Utilities.....	129
4.4.1 Radar data format .....	129
4.4.2 Estimation of the radar calibration constant .....	130
4.4.3 Calculation of polarimetric variables .....	133
4.4.3.1 Radar reflectivity factor: .....	134
4.4.3.2 Differential phase shift.....	134
4.4.3.3 Radial velocity.....	135
4.4.3.4 Spectral analysis .....	135
4.4.3.5 Raw I/Q Pairs .....	136
4.4.4 Custom data visualization tools.....	136
4.4.5 Metadata computation .....	137
4.5 Summary of Chapter 4.....	139
CHAPTER 5 CALIBRATION OF THE UNIVERSITY OF IOWA POLARIMETRIC RADAR NETWORK .....	149
5.1 Introduction.....	149
5.2 Experiment design.....	150
5.3 H/V channel imbalance analysis (inter-calibration).....	151

5.3.1 Analysis of the XPOL-2 node .....	152
5.3.2 Analysis of the XPOL-3 node .....	155
5.3.3 Analysis for the XPOL-5 node.....	157
5.3.4 H/V channel imbalance analysis summary .....	158
5.4 Network cross-calibration experiment .....	160
5.4.1 The XPOL-2 and XPOL-3 pair .....	161
5.4.2 The XPOL-3 and XPOL-5 pair .....	162
5.5 Summary of Chapter 5.....	163
CHAPTER 6 THE IMPLEMENTATION OF ATTENUATION CORRECTION ALGORITHMS TO DATA COLLECTED BY THE UNIVERSITY OF IOWA POLARIMETRIC RADAR NETWORK .....	191
6.1 Introduction.....	191
6.2 Network configuration.....	192
6.3 Collected data sample.....	192
6.4 Radar-rain gauge comparison .....	193
6.5. Basin-centric rainfall accumulation estimation.....	195
6.6 Implementation of single-radar attenuation correction methods .....	196
6.7 Network data merging .....	199
6.8 Summary of Chapter 6.....	201
CHAPTER 7 SUMMARY AND CONCLUSIONS.....	222
7.1 Introduction.....	222
7.2 Revisiting the original objective .....	222
7.3 Summary of the obtained results.....	223
7.4 Note on the technical aspects of network data collection.....	227
7.5 Conclusions and future directions .....	227
REFERENCES.....	229

## LIST OF TABLES

Table 3.1: Results summary based on single-radar correction methods for the area of interest ( <b>HUC<sub>123</sub></b> ).....	87
Table 3.2: Results summary based on single-radar correction methods for the area of interest ( <b>HUC<sub>123</sub></b> ).....	88
Table 3.3: Results summary based on single-radar correction methods for the area of interest ( <b>HUC<sub>1</sub></b> ).....	89
Table 3.4: Results summary based on single-radar correction methods for the area of interest ( <b>HUC<sub>2</sub></b> ).....	90
Table 3.5: Results summary based on single-radar correction methods for the area of interest ( <b>HUC<sub>3</sub></b> ).....	91
Table 3.6: Results summary based on single-radar correction methods for the area of interest ( <b>HUC<sub>1</sub></b> ).....	92
Table 3.7: Results summary based on single-radar correction methods for the area of interest ( <b>HUC<sub>2</sub></b> ).....	93
Table 3.8: Results summary based on single-radar correction methods for the area of interest ( <b>HUC<sub>3</sub></b> ).....	94
Table 3.9: Results summary based on single-radar correction methods for single point location ( <b>P<sub>1</sub></b> ).....	95
Table 3.10: Results summary based on single-radar correction methods for single point location ( <b>P<sub>2</sub></b> ).....	96
Table 3.11: Results summary based on single-radar correction methods for single point location ( <b>P<sub>3</sub></b> ).....	97
Table 3.12: Results summary based on single-radar correction methods for single point location ( <b>P<sub>1</sub></b> ).....	98
Table 3.13: Results summary based on single-radar correction methods for single point location ( <b>P<sub>2</sub></b> ).....	99
Table 3.14: Results summary based on single-radar correction methods for single point location ( <b>P<sub>3</sub></b> ).....	100
Table 3.15: Results for merging methods computed for the area of interest ( <b>HUC<sub>123</sub></b> ).....	101
Table 3.16: Results for merging methods computed for the area of interest ( <b>HUC<sub>123</sub></b> ).....	102
Table 3.17: Results for merging methods computed for the area of interest ( <b>HUC<sub>1</sub></b> ).....	103

Table 3.18: Results for merging methods computed for the area of interest ( <b>HUC<sub>2</sub></b> ).....	104
Table 3.19: Results for merging methods computed for the area of interest ( <b>HUC<sub>3</sub></b> ).....	105
Table 3.20: Results for merging methods computed for the area of interest ( <b>HUC<sub>1</sub></b> ).....	106
Table 3.21: Results for merging methods computed for the area of interest ( <b>HUC<sub>2</sub></b> ).....	107
Table 3.22: Results for merging methods computed for the area of interest ( <b>HUC<sub>3</sub></b> ).....	108
Table 3.23: Results for merging methods computed for single point location ( <b>P<sub>1</sub></b> ).....	109
Table 3.24: Results for merging methods computed for single point location ( <b>P<sub>2</sub></b> ).....	110
Table 3.25: Results for merging methods computed for single point location ( <b>P<sub>3</sub></b> ).....	111
Table 3.26: Results for merging methods computed for single point location ( <b>P<sub>1</sub></b> ).....	112
Table 3.27: Results for merging methods computed for single point location ( <b>P<sub>2</sub></b> ).....	113
Table 3.28: Results for merging methods computed for single point location ( <b>P<sub>3</sub></b> ).....	114
Table 3.29: Results summary based on single-radar correction methods for the area of interest ( <b>HUC<sub>123</sub></b> ) - network-based approach. ....	115
Table 3.30: Results summary based on single-radar correction methods for the area of interest ( <b>HUC<sub>123</sub></b> ) - network-based approach. ....	116
Table 3.31: Results for merging methods computed for the area of interest ( <b>HUC<sub>123</sub></b> ) - network-based approach. ....	117
Table 3.32: Results for merging methods computed for the area of interest ( <b>HUC<sub>123</sub></b> ) - network-based approach. ....	118
Table 4.1: Values of radar constant <i>C</i> for individual radars. ....	146
Table 4.2: Members of descriptive metadata table.....	147
Table 4.3: Members of hydrologic metadata. Rays are subdivided into 5 sectors; only first sector (bin1) is presented in the table. Every member with name ending with “avg” is based on 10-minute average. Members are calculated for PP and DPP modes. ....	148
Table 6.1: Rain gauge network configuration. The table lists latitude and longitude location of each rain gauge used in the study together with their distance and azimuth orientation from the XPOL-3 and XPOL-5 radars/.....	214
Table 6.2: Rainfall accumulations [mm] for two events as estimated by XPOL-2 and XPOL-5 radars, for locations corresponding to rain gauges, together with rain gauge-based rainfall accumulations. ....	215
Table 6.3 Single-radar attenuation correction methods. Rainfall accumulations [mm] for the 12/03/2012 event as estimated by XPOL-2 and XPOL-5 radars, for locations corresponding to rain gauges and the overlap area. ....	216

Table 6.4 Network data merging. Rainfall accumulation [mm] results for the 12/03/2012 event and the rain gauge <b>ICY01</b> location. Rain gauge recorded accumulation was 16.82 mm. ....	217
Table 6.5 Network data merging. Rainfall accumulation [mm] results for the 12/03/2012 event and the rain gauge <b>ICY02</b> location. Rain gauge recorded accumulation was 17.2 mm. ....	218
Table 6.6 Network data merging. Rainfall accumulation [mm] results for the 12/03/2012 event and the rain gauge <b>OXF</b> location. Rain gauge recorded accumulation was 17.18 mm. ....	219
Table 6.7 Network data merging. Rainfall accumulation [mm] results for the 12/03/2012 event and the rain gauge <b>KNT</b> location. Rain gauge recorded accumulation was 16.95 mm. ....	220
Table 6.8 Network data merging. Rainfall accumulation [mm] results for the 12/03/2012 event and the radar <b>overlap area</b> . ....	221

## LIST OF FIGURES

Figure 1.1: Equilibrium drop shapes for drop diameters of 1-6mm.....	12
Figure 1.2: Example of severe signal attenuation experienced by X-band radar (left) as compared to S-band radar (right). Data collected during the IHOP experiment [Martin and Xue, 2006]. .....	13
Figure 1.3: Conceptual image illustrating a network of polarimetric radars operated as a single instrument.....	14
Figure 2.1: Simulator’s block diagram demonstrating its modular design. ....	35
Figure 2.2: An example of a 40 km x 40 km spatial domain with an outline of a hypothetical area of interest. The shape of the area of interest is that of the Cleer Creek watershed (HUC 07080209). Superimposed is a single field of horizontal reflectivity values. ....	36
Figure 2.3: Comparison of different models representing water droplets vertical to horizontal axis ratio as a function of equivolumetric drop diameter $D$ . ....	37
Figure 2.4: Four consecutive time steps ( $T_1$ , $T_2$ , $T_3$ and $T_4$ ) of DSD parameters showing time evolution of a simulated rainfall event.....	38
Figure 2.5 Analysis of backscatter differential phase. A) Sample profile of “true” differential phase in a stratiform rainfall – red line, filtered using FIR filter – green line; differential phase as recorded by radar – blue line; backscatter differential phase – black line; B) same as in A, but for a single rainfall core case; A’) profiles of $K_{DP}$ : “true” - black line; estimated from FIR filtered differential phase – green line, as estimated from differential phase when no backscatter differential phase $\delta$ is present – red line; B’) same as A’ but for the single core rainfall case. ....	39
Figure 2.6: High-resolution “true” variables used in the simulator as a reference. A) horizontal reflectivity $Z_H$ (dBZ); B) differential reflectivity $Z_{DR}$ (dB); C) specific differential phase $K_{DP}$ ( $^{\circ}/\text{km}$ ); D) rainfall rate $RR$ , (mm/h). ....	40
Figure 2.7: Simulation results showing Z-R relationship for a stratiform rainfall event and a corresponding least-square fit. ....	41
Figure 2.8: Simulation results showing Z-R relationship for a convective rainfall event and a corresponding least-square fit. ....	42
Figure 2.9: Scatterplot showing $A_H$ - $K_{DP}$ relationship for the simulated scenario. Black line is a least-square fit to the data and the red line is the relationship suggested by Jameson [1992]. ....	43
Figure 2.10: Scatterplot showing $Z_{DR}$ - $Z_H$ relationship. Superimposed is the function (expression is presented in the Figure) corresponding to the “Florida case” as reported by Zhang, [2006]. ....	44

Figure 2.11: Scatterplot showing relationship between backscatter differential phase $\delta$ and the differential reflectivity $Z_{DR}$ . Black line has form $\delta = Z_{DR}^2$ .....	45
Figure 2.12: Polarimetric variables as recorded by a simulated radar: A) horizontal reflectivity $Z_H$ (dBZ); B) differential reflectivity $Z_{DR}$ (dB); C) specific differential phase $K_{DP}$ ( $^{\circ}/\text{km}$ ); D) differential phase $\Psi_{DP}$ ( $^{\circ}$ ). Reported values and histograms are based on comparison with the “true” field values. ....	46
Figure 2.13: Analysis of the beam width effect on radar observations of reflectivity values. A) $1^{\circ}$ beam width; B) $3^{\circ}$ beam width.....	47
Figure 2.14: Analysis of measurement noise. A) Horizontal reflectivity recorded in the absence of measurement noise, B) horizontal reflectivity corrupted by random noise. ....	48
Figure 2.15: Comparison of the reflectivity simulations for radars positioned in different locations within the spatial domain. ....	49
Figure 2.16: Merging horizontal reflectivity data. A,C,E) Individual radars and corresponding reflectivity data; B) merging using the “maximum value” method; D) merging by taking simple average of all available input data; F) merged reflectivity values using inverse weighting method.....	50
Figure 2.17: Merging specific differential phase data. A,C,E) Three individual radars and corresponding $K_{DP}$ data; B) merging using the “maximum value” method; D) merging by taking simple average of all available input data; F) merged reflectivity values using inverse weighting method.....	51
Figure 3.1: Network setup with indicated radars' locations, sample scan coverage and an outline of the watersheds of interest and the point locations of interest.....	76
Figure 3.2: A set of polarimetric variables as simulated for a single radar. ....	77
Figure 3.3: Range profiles of mean difference in reflectivity values for single-radar attenuation correction methods.....	78
Figure 3.4: Standard deviation of the difference in reflectivity values for single-radar attenuation correction methods.....	79
Figure 3.5: Reflectivity field corrected using the “forward” method. Instability of the method can be seen after radar beam passes high intensity region.....	80
Figure 3.6: The process of estimating the "optimal" $\alpha$ parameter. The "true" profile of differential phase shift (green line) is presented together with the profile obtained in simulations (black line) and the profile estimated using a given $\alpha$ parameter (purple). A) $\alpha=0.03$ , B) $\alpha=0.2$ , C) “optimal” $\alpha=0.27$ , D) $\alpha=0.34$ , E) $\alpha=0.39$ , F) $\alpha=0.5$ .....	81
Figure 3.7: Error value calculated based on Equation 3.7 as a function of parameter $\alpha$ . ....	82
Figure 3.8: Comparison of network node contributions between the Minimum Distance method and the Minimum PIA method. A) Reflectivity field [dBZ],	

B) Minimum Distance method contributions, C) minimum PIA Method contributions .....	83
Figure 3.9: Range profiles of mean difference in reflectivity values for merged products.....	84
Figure 3.10: Standard deviation of the difference in reflectivity values for merged products.....	85
Figure 3.11: Schematic illustration of the "Backward" method, for network-based attenuation correction. R1, R2, R3, R4 are locations for network nodes. For each of the marked radar rays, the PIA value is estimated. ....	86
Figure 4.1: X-band polarimetric radar network node at Iowa City landfill. ....	140
Figure 4.2: Data acquisition algorithm flow chart. ....	141
Figure 4.3: Pulse-Pair and Double Pulse-Pair Mode pulsing sequences. ....	142
Figure 4.4: FFT Mode pulsing sequences.....	143
Figure 4.5: Sample data visualization product. Horizontal reflectivity, $Z_H$ polar plot....	144
Figure 4.6: Sample data visualization product. Differential phase shift $\Phi_{DP}$ . ....	145
Figure 5.1: Radars of the University of Iowa Polarimetric Radar Network at the Iowa City landfill during the calibration experiment (April 2011). ....	165
Figure 5.2: Example of a time series of reflectivity profiles collected during the calibration experiment. ....	166
Figure 5.3: Time series of reflectivity profiles recorded by the XPOL-3 node on 05/20/2011 at the Iowa City landfill. ....	167
Figure 5.4: Mean reflectivity profiles for horizontal $Z_H$ and vertical $Z_V$ reflectivity recorded on 05/20/2011 by the XPOL-2 radar.....	168
Figure 5.5: Mean differential reflectivity $Z_{DR}$ profiles recorded on 05/20/2011 by the XPOL-2 radar. ....	169
Figure 5.6: Mean reflectivity profiles for horizontal $Z_H$ and vertical $Z_V$ reflectivity recorded on 04/21/2011 by the XPOL-2 radar.....	170
Figure 5.7: Mean reflectivity profiles for horizontal $Z_H$ and vertical $Z_V$ reflectivity recorded on 04/22/2011 by the XPOL-2 radar.....	171
Figure 5.8: Mean differential reflectivity profiles for the three analyzed cases recorded by the XPOL-2 radar. ....	172
Figure 5.9: Time series of reflectivity profiles recorded by the XPOL-3 node on 04/18/2011 at the Iowa City landfill. ....	173
Figure 5.10: Mean reflectivity profiles for horizontal $Z_H$ and vertical $Z_V$ reflectivity recorded on 04/18/2011 by the XPOL-3 radar.....	174

Figure 5.11: Mean differential reflectivity $Z_{DR}$ profiles recorded on 04/18/2011 by the XPOL-3 radar. ....	175
Figure 5.12: Mean reflectivity profiles for horizontal $Z_H$ and vertical $Z_V$ reflectivity recorded on 04/15/2011 by the XPOL-3 radar. ....	176
Figure 5.13: Mean reflectivity profiles for horizontal $Z_H$ and vertical $Z_V$ reflectivity recorded on 04/21/2011 by the XPOL-3 radar. ....	177
Figure 5.14: Mean reflectivity profiles for horizontal $Z_H$ and vertical $Z_V$ reflectivity recorded on 04/22/2011 by the XPOL-3 radar. ....	178
Figure 5.15 Mean differential reflectivity profiles for the four analyzed cases recorded by the XPOL-3 radar. ....	179
Figure 5.16: Time series of reflectivity profiles recorded by the XPOL-5 node on 04/02/2011 at the Iowa City landfill. ....	180
Figure 5.17: Mean reflectivity profiles for horizontal $Z_H$ and vertical $Z_V$ reflectivity recorded on 04/02/2011 by the XPOL-5 radar. ....	181
Figure 5.18: Mean differential reflectivity $Z_{DR}$ profiles recorded on 04/02/2011 by the XPOL-5 radar. ....	182
Figure 5.19: Mean reflectivity profiles for horizontal $Z_H$ and vertical $Z_V$ reflectivity recorded on 03/24/2011 by the XPOL-5 radar. ....	183
Figure 5.20: Mean reflectivity profiles for horizontal $Z_H$ and vertical $Z_V$ reflectivity recorded on 04/05/2011 by the XPOL-5 radar. ....	184
Figure 5.21: Mean differential reflectivity profiles for the three analyzed cases recorded by the XPOL-5 radar. ....	185
Figure 5.22: Mean reflectivity profiles as simultaneously recorded by the XPOL-2 and XPOL-3 network nodes on 04/21/2011. ....	186
Figure 5.23: Mean reflectivity profiles as simultaneously recorded by the XPOL-2 and XPOL-3 network nodes on 04/22/2011. ....	187
Figure 5.24: Mean difference between reflectivity profiles estimated by XPOL-2 and XPOL-3 radar for two separate rainfall events. ....	188
Figure 5.25: Mean reflectivity profiles as simultaneously recorded by the XPOL-3 and XPOL-4 network nodes on 12-13/11/2010. ....	189
Figure 5.26: Mean difference between reflectivity profiles estimated by XPOL-3 and XPOL-5 radars on 12-13/11/2010. ....	190
Figure 6.1: Configuration of The University of Iowa Polarimetric Radar Network. The green dots reflect the location of deployed units and the orange dots are the anticipated locations for additional nodes. Red dots show locations of a rain gauge and disdrometer network. ....	203

Figure 6.2: Geographic distribution of the network's elements. The red (yellow) ring shows the coverage of the XPOL-5 (XPOL-3) radar. Rain gauges are showed with green markers. ....	204
Figure 6.3: Beam blockage by ground clutter as experienced by XPOL-3 and XPOL-5 radars at 0° elevation. Only narrow bands of reflectivity are visible due to the blockage. ....	205
Figure 6.4: Beam blockage by ground clutter as experienced by XPOL-3 and XPOL-5 radars at 3° elevation. ....	206
Figure 6.5: Rainfall rate time series. A) Rainfall rate recorded by the ICY01 rain gauge. B) Rainfall rates derived based on radar observations. ....	207
Figure 6.6: Comparison of radar derived rainfall rates for XPOL-3 and XPOL-5 nodes. Selected data points correspond to the location of the KNT rain gauge. ....	208
Figure 6.7: Comparison of radar derived rainfall rates for XPOL-3 and XPOL-5 nodes. Selected data points correspond to the location of the OXF rain gauge. ....	209
Figure 6.8: Overlap area for the XPOL-2 and XPOL-5 radars used as the area of interest for calculation of the total rainfall accumulation. ....	210
Figure 6.9: Total rainfall accumulation maps for the 12/03/2012-12/04/2012 event. Data based on 3° elevation scans. ....	211
Figure 6.10: Bright band contamination. Total rainfall accumulation maps for the 12/03/2012-12/04/2012 event. Data based on 6° elevation scans. ....	212
Figure 6.11: A) Example of a $\Phi_{DP}$ profile (black line) and its smoothed version (red line), B) Corresponding reflectivity profile. ....	213

## CHAPTER 1

### INTRODUCTION

#### 1.1 Motivation

The importance of rain and accurate rainfall estimation can be demonstrated through countless examples. Rain is the primary source of fresh water for most areas of the world and therefore plays a fundamental role in social, environmental, and economic development around the globe [e.g., *Postel et al.*, 1996; *Postel*, 2000; *Arjen et al.*, 2012]. In the hydrologic cycle, water evaporates into the air, condenses, and falls to the Earth's surface in the form of precipitation, thereby providing an indispensable resource for life on our planet. Observations of global and regional precipitation patterns, the estimation of rainfall variability, and documentation of rainfall changes over time can help us better understand and predict such extreme hydrologic events as erosion, floods, tornadoes, hurricanes, and droughts. Reliability of hydrologic modeling and forecasting is directly linked to the quality of available rainfall information [e.g., *Habib et al.*, 2008; *Collier*, 2009; *Germann et al.*, 2009; *Villarini et al.*, 2009, 2010]. Social venues such as agriculture, communication, water management, public safety, and many others depend on quality short- and long-term forecasts of hydrologic events.

Unavoidably high spatial and temporal variability of rainfall creates fundamental difficulties in accurate precipitation estimation. Rainfall amounts are measured with a variety of instruments that represent different measurement techniques as well as different spatial and temporal scales, and they are therefore characterized by different measurement errors. Rain gauges are commonly used to provide direct rainfall amounts on the ground, but their limited coverage area (typically a 30 cm diameter orifice; [e.g., *Brock et al.*, 1995; *Ciach*, 2003]) cannot represent the spatial extent of the phenomenon.

Conventional, non-polarimetric weather radars, operating at S- or C-band frequencies, can effectively capture rainfall's spatio-temporal variability, but their

quantitative estimates that are based on power-law type relationships (*Marshall and Palmer, 1948*) are highly uncertain [e.g., *Zawadzki, 1984; Austin, 1987; Joss and Waldvogel, 1990; Anagnostou et al., 1999*]. Some of the well-recognized error sources in radar rainfall measurements include: ground clutter contamination, anomalous propagation, non-uniform beam filling, partial beam blockage, signal attenuation due to intervening rainfall, bright band contamination, changes in the vertical structure of rainfall, and mixed-type precipitation. Obtaining a high quality rainfall product often requires a multi-sensor approach with in-situ instruments (e.g., rain gauges and disdrometers) and remote sensing instruments (e.g., satellites, radars) that can make simultaneous observations [e.g., *Krajewski and Smith, 1995, 2002*].

Recent advancements in radar polarimetry have resulted in a significant increase in the accuracy of radar rainfall estimates [e.g., *Bringi et al., 1982; Keenan et al., 1998; Zrníc and Ryzhkov, 1999; Krajewski and Smith, 2002*]. Attenuation correction methods utilizing polarimetric information show much better stability when compared to non-polarimetric methods and can be credited for the recent increased interest and more widespread use of small, often mobile, X-band radar applications [*Matrosov et al., 2002*].

The acquisition of a network of four mobile, polarimetric, X-band radars by The University of Iowa hydrometeorology group resulted in the need for a thoughtful evaluation of the instrument. This work is motivated by the need to assess the performance of a network of polarimetric, X-band radars for rainfall estimation. Among other aspects of our analysis, we put special emphasis on the problem of attenuation correction and the error structure of rainfall products. Presented work will be used to enhance the operations of The University of Iowa Polarimetric Radar Network. Specifically, our work will foster a better understanding of the limitations and capabilities of the instrument and offer guidance in optimal operation and data collection strategies.

## 1.2 Problem statement

The typical operating frequency of weather radars can span over many bands. For example, NEXRAD, the national weather radar network in the United States, uses S-band radars that operate at 3GHz [Crum *et al.*, 1993]. The Canadian national weather network utilizes radars operating at the C-band (5.5 GHz) [Paul and Lapczak, 2002]. Operating at such frequencies, in addition to relatively long pulse widths, allows radars to provide valuable information for ranges over 200 km [Sauvageot, 1992]. From the hydrologic perspective, where the domain of interest is often limited in size to a watershed, a city, a county, or a research validation site, higher frequency radars (X-, Ka-, Ku-band) can provide rainfall products with higher spatial and temporal resolution but at a significantly lower cost. This lower cost is due to the fact that higher frequency radars can provide high spatial and temporal resolution products with much smaller antennae. The smaller size and lighter structure often allow the radars to be installed on mobile platforms (trucks, trailers), which yields flexibility in network configuration, remote deployment, and a lower maintenance cost. Recently, there has been an increasing interest in utilizing X-band, polarimetric radars in locations where conventional radars provide limited information (mountain and coastal regions, gaps in the NEXRAD system, close-to-the-ground sampling, etc.) [e.g., Testud *et al.*, 2000; Junyent *et al.*, 2010; Maki *et al.*, 2010].

The advantages of X-band polarimetric radars are contrasted by the fact that utilizing higher carrier frequency results in a higher atmospheric attenuation that can lead to severe signal degradation in the case of heavy rainfall [Doviak and Zrnica, 1993]. Different attenuation correction methods proposed in recent years can be classified into non-polarimetric (based on estimates of reflectivity values only) and polarimetric methods. The polarimetric-based methods have been shown to yield better rainfall estimation [e.g., Sauvageot *et al.*, 1996, 1998; Testud *et al.*, 2000; Matrosov *et al.*, 2002]. In addition to the improved rainfall estimation, attenuation correction methods based on polarimetric variables (reflectivity  $Z_{H,V}$ , differential reflectivity  $Z_{DR}$ , and specific

differential phase shift  $K_{DP}$ ) have proven more stable and more accurate when compared to the non-polarimetric methods [e.g., *Blackman and Illingworth, 1997; Bringi et al., 2002; Anagnostou et al., 2004, 2006*], which has contributed to the recent increase in popularity of polarimetric, X-band radars.

Polarimetric methods for rainfall estimation and attenuation correction are based on the fact that falling raindrops are not spherical but resemble oblate spheroids, as shown in Figure 1.1 [e.g., *Pruppacher and Beard, 1970; Green, 1975; Beard and Chuang, 1987*].

The amount of raindrop flattening is a function of drop diameter, i.e., larger drops are distorted more than the small ones. Therefore, horizontal and vertical polarizations of the radar waves differ more as the contributions of large drops increase. Since rainfall intensity is a high ( $\sim 3.4$ ) order moment of drop size distribution, it is influenced by the large drops and, therefore, renders polarimetric information relevant for rainfall estimation.

When moderate to heavy rainfall interferes with a radar pulse, significant signal loss can occur. In Figure 1.2, we present data from the 2002 IHOP experiment that took place in Oklahoma [e.g., *Martin and Xue, 2006; Xiao and Sun, 2007*]. During the experiment, collocated S-band and X-band radars operated simultaneously, which allowed for the direct comparison of radar returns and associated attenuation.

Figure 1.2 illustrates that the X-band radar suffered total signal attenuation after passing over a region of extreme rainfall. In an event of a total signal loss, successful correction for attenuation is not possible with a single-radar approach due to the lack of a valuable reference signal. This problem can only be addressed by providing additional radar information from a separate source that has not experienced total signal loss. This is where the concept of polarimetric radar networks becomes useful.

The University of Iowa Polarimetric Radar Network was designed to provide the hydrologic research community with a resource capable of providing high quality, re-

deployable, and reliable rainfall information over a domain of interest. Figure 1.3 presents a conceptual image of a network operated as a single instrument. The problem of attenuation and how it should be addressed in a networked environment is the leading focus of this work. To address the problem of attenuation correction in a network of radars, we use computer simulations and data collected by The University of Iowa Polarimetric Radar Network.

Over the past 60 years, the problem of attenuation in radar systems has been extensively studied. Below, we provide a brief review of the literature that is relevant to this work.

### 1.3 Literature review

The importance and widespread demand for high quality rainfall information at local and global scales drives many research activities focusing on different aspects of precipitation observation and motivates a continuous search for better and more reliable precipitation estimation techniques. In the following subsections, we give a brief description of the literature related to the focus of this work. We start with a review of previous studies that have focused on the problem of attenuation correction, especially with respect to radars operating at X-band frequencies. We follow with examples of studies that have implemented computer simulations into weather radar research.

#### 1.3.1 Weather radar attenuation correction studies

The problem of signal attenuation in weather radars has been observed and recognized since the beginning of radar technology. *Ryde* [1946] and *Atlas and Banks* [1951] were among the first to point out the problem of signal attenuation. The work of *Atlas and Banks* [1951] provided an expected echo pattern for hypothetical rainfall events for a range of radar wavelengths from 3.2 cm to 10 cm, demonstrating that attenuation is almost negligible at 10 cm (S-band) but becomes considerable as the radar wavelength becomes shorter. This early discovery negated many of the advantages of short

wavelength radars such as smaller antenna size, lower cost, mobility, higher spatial resolution, and sensitivity.

*Hitschfeld* and *Bordan* [1954] suggested the first method for attenuation correction in radar profiles based on observed reflectivity. The parametric relationship between radar reflectivity factor  $Z$  and specific attenuation  $k$ , also referred to as the “forward” algorithm, is known to be unstable and very sensitive to radar calibration, as later suggested by *Hildebrand* [1978]. This instability makes reflectivity data almost useless for quantitative rainfall estimation [*Johnson and Brandes*, 1987]. To mitigate the instability in the *Hitschfeld-Bordan* method, auxiliary measurements of rainfall or attenuation is necessary. With the development of airborne and spaceborne platforms, downward looking radars were able to obtain such auxiliary measurement from ocean surface reflections in order to estimate the path integrated attenuation (PIA). A number of algorithms based on PIA information have been suggested [e.g., *Meneghini et al.*, 1983; *Marzoug and Amayenc*, 1994; *Iguchi and Meneghini*, 1994; *Kozu and Iguchi*, 1996] and are all based on the same principle. The feasibility of the so-called PIA-constrained method to correct ground-based radar estimates has been investigated by *Delrieu et al.* [1997], in which the PIA information was based on mountain returns. The obvious limiting factor for the method is the availability of targets capable of providing stable returns (mountains, buildings, towers, etc.). Alternative techniques for attenuation correction based on a similar principle include the dual-frequency radar method [e.g., *Fujita*, 1983; *Kozu and Nakamura*, 1991; *Marzoug and Amayenc*, 1994] and the “stereoradar” technique in which two radars observe a storm cell from different angles [e.g., *Kozu and Nakamura*, 1991; *Kabeche and Testud*, 1995; *Berne et al.*, 2005].

The development of polarization-diverse radars [*Bringi and Hendry*, 1990] resulted in improved attenuation correction methods, as compared to the methods based on reflectivity measurements alone. *Bringi et al.* [1990] showed, based on scattering simulations, that the relationship between the specific differential shift  $K_{DP}$  and horizontal

$A_H$  and the differential attenuation  $A_{DP}$  is almost linear. This simple linear relationship has been adapted as an attenuation correction method to C- and S-band radar data by many researchers [e.g., *Ryzhkov and Zrnica*, 1995; *Smyth and Illingworth*, 1998; *Carey et al.*, 2000; *Testud et al.*, 2000; *Bringi et al.*, 2001]. The scattering simulations used by *Jameson* [1992] and *Carey* [2000] suggest that the coefficient of the linear relationship proposed by *Bringi* [1990] is highly sensitive to the variability of DSD, temperature, and the drop shape model. *Ryzhkov and Zrnica* [1995] proposed an empirical method for coefficient estimation, based on radar observations, but its application yields good results only in an average sense and should only be applied to regions with homogenous rainfall.

The method proposed by *Testud et al.* [2000], referred to as the “ZHPI algorithm,” uses a fixed coefficient for the  $A_H$ - $K_{DP}$  relationship, but with a constrained PIA value derived from the total increase in differential propagation phase  $\Phi_{DP}$ . The method proved to be stable, as evaluated by *Le Bouar et al.* [2001] for a C-band radar data. *Smyth and Illingworth* [1998], working with S-band radar data, suggested a constrained method where the coefficient of the  $A_H$ - $K_{DP}$  relationship is not fixed, but the method assumes that stratiform precipitation regions behind the strong convective systems are within the radar’s range. This condition is hard to achieve, especially for X-band radars, because of its much shorter observable range when compared to typical C- and S-band applications.

Based on the method of *Testud et al.* [2000], *Bringi* [2001] proposed and evaluated a “self-consistent method with constraints” that was based on C-band radar data, where the “optimal” value of the coefficient for the  $A_H$ - $K_{DP}$  relationship is calculated based on the radar data itself.

The majority of the work described above has been evaluated and adopted to C- and S-band radars. In the past several years, there has been an increased number of studies focusing on X-band radar data. This includes the iterative method proposed by *Matrosov* [2002] and focuses on stabilizing the slope factor  $\beta$  in a relationship between

the drop axis ratio and drop diameter  $a/b=1-\beta D$  [Gorgucci *et al.*, 2002] along a radar profile. Anagnostou *et al.* [2004] adopted the “ZHPI” method of Testud *et al.* [2000] to X-band and applied a method to correct horizontal reflectivity  $Z_H$  and differential reflectivity  $Z_{DR}$  using the DSD-based approach suggested by Testud *et al.* [2000] and Le Bouar *et al.* [2001]. Park *et al.* [2005] adapted the self-consistent method with constraints [Bringi, 2001] to X-band radar data collected by the MP-X in Japan. An alternative self-consistent method utilizing both  $Z_H$  and  $Z_{DR}$  has been proposed and evaluated at the X-band by Gorgucci [2006]. Based on data collected during the 2002 IHOP experiment that took place in Oklahoma [e.g., Martin and Xue, 2006; Xiao and Sun, 2007], Anagnostou *et al.* [2006] evaluated the accuracy of differential phase shift-based attenuation correction methods at the X-band.

The increased popularity of polarimetric, X-band radars has resulted in a number of recent studies evaluating new and existing attenuation correction methods. Although the correction algorithms based on polarimetric variables show promising results, their operational deployment has been limited due to a number of factors that will be discussed in this work.

### 1.3.2 Simulation-based studies in weather radar

Numerical simulations of weather radar observations have been successfully used in the past to analyze various aspects of rainfall estimation. Zawadzki [1984] used the simulation approach to evaluate some of the radar rainfall estimation errors and their hydrologic consequences. Krajewski and Georgakakos [1985] proposed a method for generating synthetic radar data for a range of hydrologic applications. A simulation scheme based on a 2D stochastic space-time model for generating radar-estimated rainfall fields has been described by Krajewski *et al.* [1993]. Anagnostou and Krajewski [1997] further extended the method to include simulated polarimetric variables based on a two-dimensional rainfall intensity field complemented with a vertical structure of

hydrometeors. *Caumont et al.* [2006] used numerical simulations to evaluate a method for assimilation of radar data into a numerical forecast model. *Cheong et al.* [2008] designed a three-dimensional radar simulator capable of generating simulated time series of radar data where the characteristics of the simulated fields are derived from a high-resolution weather model or actual measured data. A full X-band radar simulator, which works with the 3D output fields from a numerical mesoscale model, has been developed by *Zahiri et al.* [2008]. *Gosset and Zawadzki* [2001], *Berne and Uijlenhoet* [2005], and *Uijlenhoet and Berne* [2008] studied the effects of spatial rain drop size distribution variations on radar attenuation correction, and *Gosset* [2004] used simulation to investigate non-uniform beam filling. Computer simulations of the scattering properties of hydrometeors supported a number of studies in the field of weather radar [e.g., *Oguci*, 1983; *Vivekanandan*, 1999; *Marzano et al.*, 2006].

To the best of our knowledge, numerical simulators have not been used to assess the performance of networks of X-band radars, their rainfall estimation ability, and attenuation correction methods.

#### 1.4 Objectives and methodology

The broad objective of this study is to contribute to better rainfall estimation through the use of polarimetric weather radar networks. The specific goals are formulated to support the development, operations, and evaluation of The University of Iowa Polarimetric Radar Network and include:

- Use of computer simulations to assess the network's ability to correct the signal attenuation caused by intervening rainfall.
- Development of utilities supporting the collection and analysis of data collected by The University of Iowa Polarimetric Radar Network.
- Inter-calibration of the network's radars.

- Application of attenuation correction methods to the data collected by the network.

To address the first issue, we developed a comprehensive radar network simulator capable of mimicking, to a certain extent, the workings of a network of polarimetric radars. In Chapter 2, we give a detailed description of the simulator and provide results from a set of simulation scenarios designed to test the simulator's functionality, capabilities, strengths, and limitations. To validate the simulator, we examine obtained simulation results and compare them to the well-known polarimetric relationships previously published in the literature.

Chapter 3 details an effort where the simulator is employed to evaluate a number of attenuation correction methods. We examine existing, single-radar methods previously published in the literature and propose alternative attenuation correction methods that take advantage of the data redundancy that exists in a networked environment and that, to best of our knowledge, have not been previously evaluated. We used The University of Iowa Polarimetric Radar Network as an underlying model for the simulator design.

Over the spring and summer of 2011, The University of Iowa Polarimetric Radar Network became operational. Its first objective was to collect a set of rainfall data and use it to ensure the correctness and good working condition of the network. A suite of utilities has been developed to support data collection and analysis. The utilities perform a range of tasks such as the computation of polarimetric variables from "raw" radar data, computation of hydrologic metadata based on the collected variables, and data visualization. A description of individual modules, their functionality, and their application to the data collected by the network is presented in Chapter 4.

An evaluation of the actual network starts in Chapter 5 with the inter-calibration and cross-calibration experiments. The purpose of this subsection is to verify whether individual radars and individual polarimetric channels of each of the four radars

constituting the network are well balanced. Inter-calibration results are later used to account for additional losses in the radar's channels and to secure optimal operation of the network after deployment.

In Chapter 6, we consider the network's data collected during operational deployment, with radars located on the outskirts of the Clear Creek watershed in the vicinity of Iowa City, IA. Clear Creek is a heavily instrumented experimental watershed with a number of existing hydrologic instruments. We compared data collected in a network configuration with observations made by in-situ instruments in order to evaluate a number of attenuation correction schemes. We conclude with the summary and discussion section in Chapter 7.

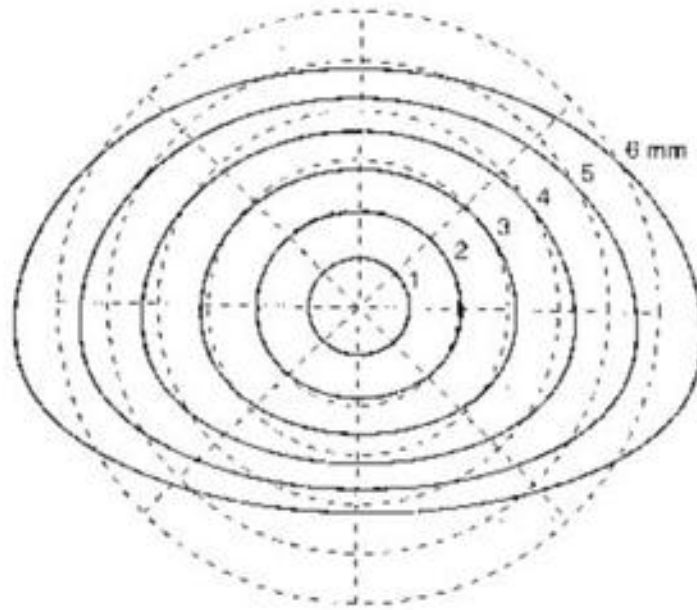


Figure 1.1: Equilibrium drop shapes for drop diameters of 1-6mm.

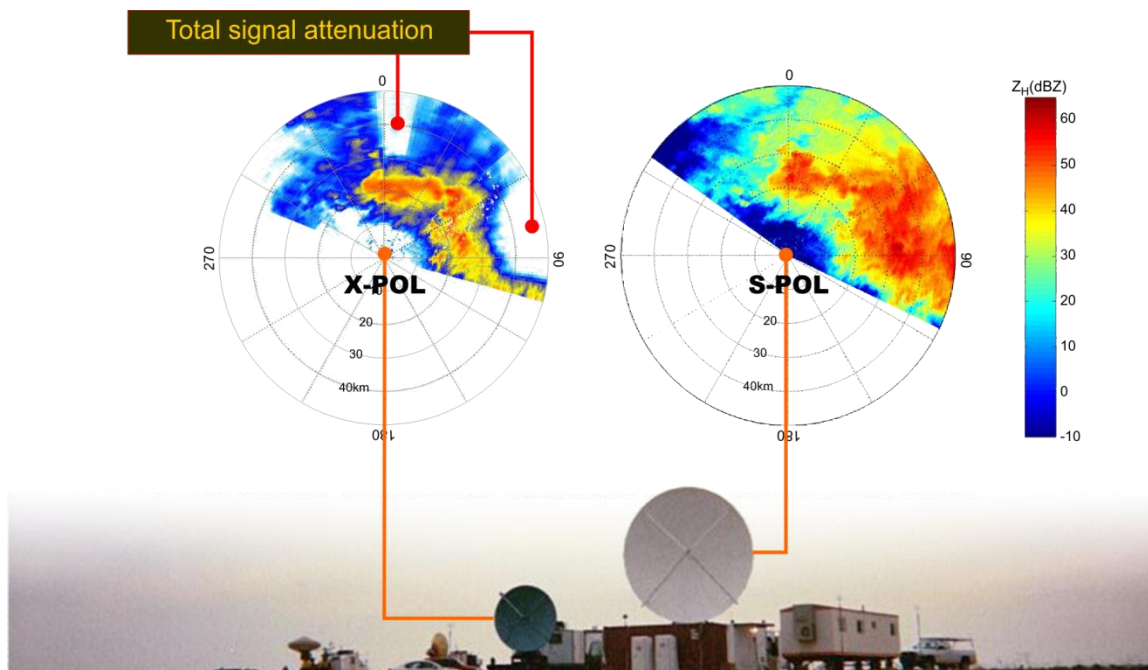


Figure 1.2: Example of severe signal attenuation experienced by X-band radar (left) as compared to S-band radar (right). Data collected during the IHOP experiment [Martin and Xue, 2006].

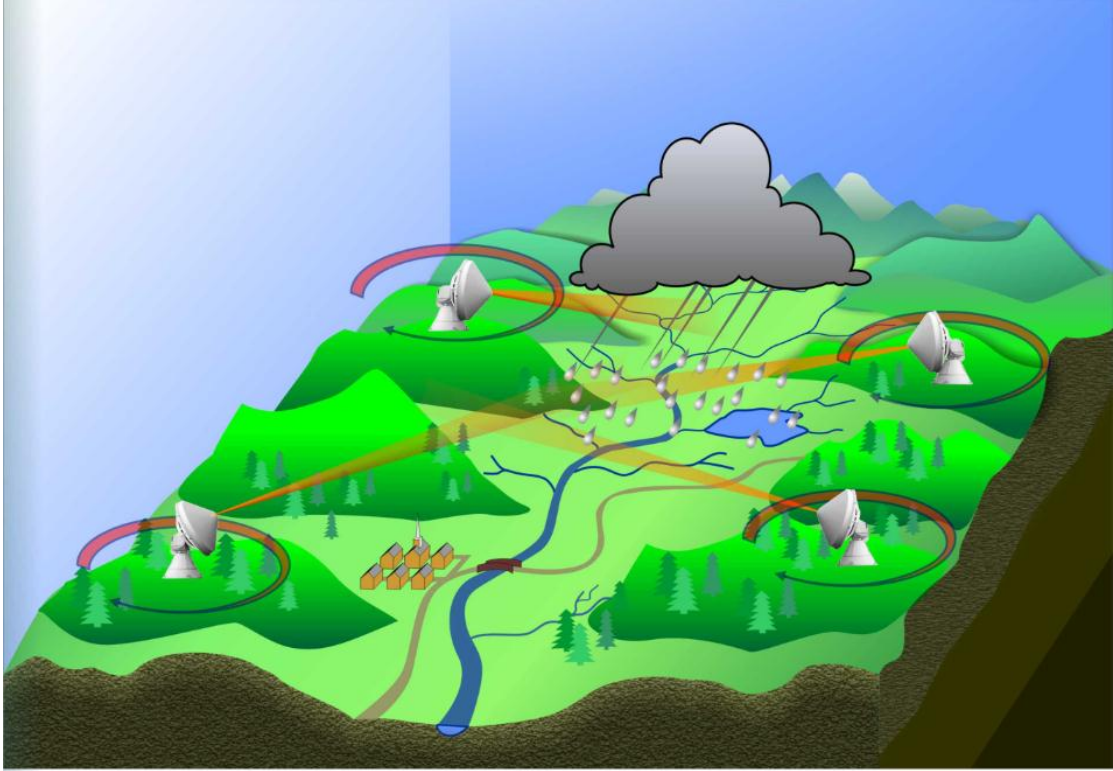


Figure 1.3: Conceptual image illustrating a network of polarimetric radars operated as a single instrument.

## CHAPTER 2

### THE POLARIMETRIC RADAR NETWORK SIMULATOR

#### 2.1 Introduction

Because computer simulations are efficient and cost-effective means of simulating many scientific processes, we started the analysis of attenuation correction methods in a networked environment by developing a comprehensive radar network simulator capable of mimicking, to a certain extent, the workings of a polarimetric radar network. To secure the validity of the simulation results, we compared our extensive tests of the simulator's outputs to well-known polarimetric relationships that are published in the literature. After validating the simulator, we provide a set of sample simulation scenarios, each of which is designed to test a separate aspect of the simulator's functionality.

#### 2.2 Description of the simulator

In practice, operating a network of several radars (nodes) as a single instrument means that information from individual radars is shared in data post-processing. In this case, the quality of the final rainfall products varies depending on how many nodes are used, how radar data are merged, and what quality control steps are implemented. When building the simulator, we mimicked the physical processes of radar wave interactions with (simulated) raindrops to "obtain" radar observables. This allowed us to investigate several different ways of combining the "obtained" data to generate the final rainfall products in an approach known in the satellite remote sensing community as an Observing System Simulation Experiment (OSSE) [Arnold and Dey, 1986; Masutani *et al.*, 2006]. When building the simulator, we investigated different attenuation correction methods because signal attenuation by rain is the "Achilles heel" of X-band radars for rainfall estimation. The simulator was later used to compare methods that use single radar information with those that use observations from multiple radars. Since different

radars that are observing the same storm suffer different degrees of signal attenuation, combining and sharing radar data can be beneficial.

In the following section, we describe the simulator by identifying its most significant modules. Figure 2.1 shows a general schematic of the simulator. The rainfall input is in the form of a high-resolution map of simulated raindrop size distributions (DSD), and drop shape is described based on the current state-of-the-art modeling of drop distortion from spheroids, as documented in the literature. The propagation and interaction of radar waves with the rain drops account for the dominant scattering processes. We have simplified the radar system effects from processes occurring on the antenna, in the waveguides, and in the signal generator and receiver by corrupting the observables of the physical variables with random noise [Atlas, 2002].

### 2.2.1 Run-time configuration of the simulator

To allow for different simulation scenarios, we created an “input-parameter” module. In the module, users can specify radar-specific parameters such as carrier frequency or antenna elevation as well as different the shape and size of the domain of interest or the type of drop flattening model. Flexibility in specifying input parameters allows for the realization of many different simulation scenarios. Radar-specific simulation parameters include the number of networked radars, their locations within the spatial domain, the radar’s carrier frequency, beam width, range gate size, maximum range, and antenna elevation. Dielectric properties of water droplets, ambient temperature, and physical constants are also specified here along with post-processing steps like the data merging method, attenuation correction algorithm, and final product format.

### 2.2.2 Spatial domain and area of interest

In most cases, X-band polarimetric radars can provide useful returns up to 60 km in range from the radar location, but the quality of the signal degrades with distance due

to beam broadening and possible bright band contamination [Matrosov *et al.*, 2005]. Moderate to heavy rainfall conditions can also drastically limit the maximum usable range to as little as 10 km from the radar. The simulator has been designed to operate in a spatial domain in which size can be specified by the user. We typically refer to a spatial domain as a rectangular area enclosing all the network's radars together with the domain of interest. The size of the spatial domain should be based on the number and locations of networked radars with respect to the area of interest. The DSD input file corresponds in size to the spatial domain.

Within the spatial domain, users can select a specific area of interest that can be of arbitrary shape and that is defined as a mask superimposed over the spatial domain. Typically, the area of interest can correspond to a watershed or city limits, for example. A sample spatial domain that is 40 km x 40 km in size with an outline of an area of interest is presented in Figure 2.2. In the data processing and analysis steps, only information from within the area of interest will be included.

### 2.2.3 Raindrop Model Description

Raindrops in an equilibrium state are nearly oblate, and their shape is governed by the balance between surface tension and gravity [Green, 1975]. Drops with diameters  $D \leq 1$  mm are approximately spherical with axis ratios  $a/b = 1$ , where  $a$  and  $b$  are the minor and major axes of rotation, respectively; however, for larger drops, this ratio changes almost linearly with the equivalent spherical diameter,  $D$ . Since polarimetric variables ( $Z_{DR}$ ,  $K_{DP}$ ) are highly sensitive to the drop axis ratio, even a small change in the equilibrium state can lead to measurable differences in radar estimates. There is no consensus on the best model to represent drop axis ratio, and many research groups have presented similar, yet distinguishable, methods of describing this relationship [e.g., Pruppacher and Beard, 1970; Green, 1975; Beard and Chuang, 1987; Andsager *et al.* 1999]. Rather than following a particular drop model in our simulations, we make it

possible to use any existing drop axis ratio model so that the influence of the model on the rainfall product can be assessed. In Figure 2.3, we present sample relationships between axis ratio and drop diameter that are available in the simulator.

#### 2.2.4 Radar's spatial sampling model

The radar beam width, defined as twice the angle from the beam center to where the power drops by half (i.e., 3 dB), side lobes, antenna rotation speed, and radar's parameter configuration contribute to recorded values of reflectivity, phase shift, and other measured variables. For simulation purposes, we use a weighting approach in which field values are weighted both in azimuth and range. We ignore the side lobes, approximate the main lobe with a Gaussian function, and calculate individual weights based on the beam width and sampling interval, which corresponds to the antenna rotation speed. A Gaussian-shape function is also used for range weighting [Doviak and Zrníc, 1993], where individual weights are calculated based on range resolution and sampling distance corresponding to the radar's sampling strategy.

#### 2.2.5 DSD input fields

The physical basis for the radar simulation is provided in the form of simulated DSD fields at high spatial and temporal resolutions (100 m x 100 m spatial resolution field with 6 min temporal spacing) that are generated according to the method proposed by Schleiss *et al.* [2009; 2011]. The DSD itself is modeled using a normalized gamma distribution [e.g., Testud *et al.*, 2001, Bringi and Chandrasekar, 2001] given by:

$$N(D) = N_w f(\mu) \left( \frac{D}{D_0} \right)^\mu \exp(-\Lambda D) \quad (2.1)$$

$$f(\mu) = \frac{6}{3.67^4} \frac{(3.67 + \mu)^{\mu+4}}{\Gamma(\mu + 4)} \quad (2.2)$$

where  $N(D)$  [ $\text{m}^{-3}$ ] is the number of raindrops per unit volume with equivolumetric diameters between  $D$  and  $dD$  [ $\text{mm}$ ],  $N_w$  [ $\text{m}^{-3} \text{mm}^{-1}$ ] is the intercept parameter,  $D_0$  [ $\text{mm}$ ] is the equivalent median volume drop diameter; and  $\mu$  [-] is the shape parameter. The slope parameter  $\Lambda$  [ $\text{mm}^{-1}$ ] is defined as:

$$\Lambda D_0 = 3.67 + \mu \quad (2.3)$$

The novelty of the method used by *Schleiss et al.* [2009; 2011] is that the values of  $(N_w, D_0, \mu)$  describing the DSD at each pixel in the simulation domain are simulated so that they exhibit realistic spatial and temporal structures and cross-correlations. The method can produce both intermittent and non-intermittent rainfall fields. By varying the parameterization of the simulator, it is possible to generate large numbers of different types of rainfall fields (stratiform vs. convective) and space-time structures. To give insight into the character of the simulated input fields, we present a sequence of four DSD input fields in Figure 2.4. The selected event highlights the method's ability to generate DSD fields for a variety of rainfall conditions.

### 2.2.6 T-Matrix scattering method

At the very center of the simulator, we model interactions between the radar's electromagnetic energy and individual raindrops. Depending on the radar's frequency and transmitted power, ambient temperature, drop size, drop axis ratio, and radar antenna elevation angle, the amount of energy scattered back to the radar and the energy propagating forward can vary. This process can be conveniently described using the T-matrix method [*Waterman*, 1971], which is based on the linearity of Maxwell's equations and enables us to relate the scattered  $E^{sct}$  and incident  $E^{inc}$  electric fields by means of a transmission matrix  $\mathbf{T}$  and scattering matrix  $\mathbf{S}$ :

$$\mathbf{E}^{sct} = \mathbf{T}^t \mathbf{S} \mathbf{T} \mathbf{E}^{inc} \quad (2.4)$$

The transmission matrix  $\mathbf{T}$  describes the changes in electromagnetic waves due to propagation effects, whereas the scattering matrix  $\mathbf{S}$  corresponds to the interactions of

electromagnetic energy with individual water droplets within the radar's resolution volume.

In the simulator, we followed the T-matrix numerical solution by implementing codes that were initially developed by *Mishchenko et al.* [1996]. After modest modifications, the codes accept variable input parameters and allow for different simulation scenarios. For a given radar frequency, drop axis ratio model, ambient temperature, polarization (vertical or horizontal), and antenna elevation angle, the amplitude scattering matrix elements are computed. We denote backscattering amplitude matrix elements as  $f_{hh}, f_{hv}, f_{vh}, f_{vv}$  and forward scattering amplitude matrix elements as  $\hat{f}_{hh}, \hat{f}_{hh}, \hat{f}_{hh}, \hat{f}_{hh}$ .

For each drop with a diameter  $D$  from range  $D_{min}$  to  $D_{max}$  with interval  $dD$ , a 16-element ensemble-averaged Mueller matrix  $\langle n\mathbf{M} \rangle$  [Collett, 2005] is constructed. We define the matrix elements following *Vivekanandan et al.* [1991]. Below, we present the Mueller matrix elements that are used to define polarimetric variables:

$$\begin{aligned}
M_{11} &= \frac{1}{2} \left( |f_{hh}|^2 + |f_{hv}|^2 + |f_{vh}|^2 + |f_{vv}|^2 \right) \\
M_{12} &= \frac{1}{2} \left( |f_{hh}|^2 - |f_{hv}|^2 + |f_{vh}|^2 - |f_{vv}|^2 \right) \\
M_{21} &= \frac{1}{2} \left( |f_{hh}|^2 + |f_{hv}|^2 - |f_{vh}|^2 - |f_{vv}|^2 \right) \\
M_{22} &= \frac{1}{2} \left( |f_{hh}|^2 - |f_{hv}|^2 - |f_{vh}|^2 + |f_{vv}|^2 \right) \\
M_{33} &= \text{Re}(f_{hh}f_{vv}^* + f_{hv}f_{vh}^*) \\
M_{34} &= \text{Im}(f_{hh}f_{vv}^* - f_{hv}f_{vh}^*) \\
M_{43} &= -\text{Im}(f_{hh}f_{vv}^* + f_{hv}f_{vh}^*) \\
M_{44} &= \text{Re}(f_{hh}f_{vv}^* - f_{hv}f_{vh}^*)
\end{aligned} \tag{2.5}$$

The matrix elements have units of back scattering cross section per unit volume [ $\text{m}^2 \text{m}^{-3}$ ], and we assume a zero canting angle for raindrops. The integration range of diameters  $D_{min} - D_{max}$  and the increment  $dD$  can be modified when we investigate the

effect of large drops on radar observables. Elements of the Mueller matrix  $\mathbf{M}$ , as well as elements of the backscattering matrix  $f_{hh}, f_{hv}, f_{vh}, f_{vv}$  and forward scattering matrix  $\hat{f}_{hh}, \hat{f}_{hv}, \hat{f}_{vh}, \hat{f}_{vv}$ , are used to define radar observables for each radar bin.

### 2.3 Simulated radar variables

Polarimetric weather radars generally transmit short pulses of electromagnetic energy in two orthogonal channels. After the transmission period, the radar receives energy returns from precipitation (and other targets in radar's path) by both channels and records them. The received energy is amplified and converted to radar observables in the post-processing stage. In this paragraph, we define conventional radar parameters by means of the Mueller matrix and the amplitude scattering matrix elements.

#### 2.3.1 Polarimetric Observables

The radar reflectivity factor is determined by the number and size distribution of the meteorological targets filling the radar's sample volume. Reflectivity for both channels and the differential reflectivity are computed as follows:

$$\begin{aligned} Z_H &= \frac{4\pi\lambda^4}{|K|^2 \pi^5} \frac{(M_{11} + M_{12} + M_{21} + M_{22})}{2} \\ Z_V &= \frac{4\pi\lambda^4}{|K|^2 \pi^5} \frac{(M_{11} - M_{12} - M_{21} + M_{22})}{2} \\ Z_{DR} &= 10 \log_{10} \left( \frac{M_{11} + M_{12} + M_{21} + M_{22}}{M_{11} - M_{12} - M_{21} + M_{22}} \right) \end{aligned} \quad (2.6)$$

where,  $Z_H$  [ $\text{mm}^6 \text{m}^{-3}$ ],  $Z_V$  [ $\text{mm}^6 \text{m}^{-3}$ ], and  $Z_{DR}$  [dB] are the horizontal, vertical, and differential reflectivity, respectively,  $\lambda$  [mm] is the radar's wavelength, and  $K = (\epsilon_r - 1)/(\epsilon_r + 1)$ , where  $\epsilon_r$  is the relative dielectric constant of water.

The co-polar cross correlation coefficient,  $\rho_{HV}$ , [Jameson, 1989] and the backscatter differential phase,  $\delta$ , between the  $H$ - and  $V$ -polarized waves [Mueller, 1984] are given by:

$$\rho_{HV} = \frac{2}{|K|^2} \left( \frac{\lambda}{\pi} \right)^4 \sqrt{\frac{(M_{33} + M_{44})^2 + (M_{43} - M_{34})^2}{Z_H Z_V}}$$

$$\delta = \frac{180}{\pi} \tan^{-1} \left[ \frac{M_{43} - M_{34}}{M_{33} + M_{44}} \right] \quad (2.7)$$

The specific differential phase,  $K_{DP}$  ( $^{\circ}/km$ ), [Sachidananda and Zrnić, 1986] and specific attenuation,  $A_{h,v}$  (dBZ/km), are defined as:

$$K_{DP} = \frac{\lambda \cdot 180}{\pi} \left[ \operatorname{Re} \left( \hat{f}_{hh} \right) - \operatorname{Re} \left( \hat{f}_{vv} \right) \right] N(D) dD$$

$$A_{h,v} = 8.686 \cdot \lambda \cdot \operatorname{Im} \left( \hat{f}_{hh,vv} \right) N(D) dD \quad (2.8)$$

where,  $Re$  and  $Im$  indicate the real and imaginary part of a complex number, respectively. The defined formulas are implemented in the simulator as the basis for estimating radar polarimetric variables.

### 2.3.2 Measurement noise

We account for the uncertainties present in measurements of reflectivity,  $Z_{H,V,DR}$ , and the specific differential phase shift,  $K_{DP}$ , by introducing normally distributed noise with zero mean [dBZ for reflectivity and  $^{\circ}/km$  for  $K_{DP}$ ] and standard deviation  $\sigma_Z = 1dBZ$  and  $\sigma_{Kdp} = 0.2^{\circ}/km$  [Ryzhkov et al., 2005] for reflectivity and specific differential phase shift measurements, respectively. Noise is introduced on a gate-by-gate basis and is uncorrelated from one gate to the next. It should be noted that even when noise levels in both  $H$ - and  $V$ - channels are equal, the corresponding Signal-to-Noise Ratios ( $SNR_{H,V}$ ) can be different for radar resolution volumes where  $Z_{DR} \neq 0$ . This leads to the amplification of the noise statistics for  $Z_{DR}$ . To account for this amplification, the noise standard deviation for  $Z_{DR}$  is modeled as follows:

$$SD(Z_{DR}) = 10 \log \left\{ 1 + \left[ \frac{2(1 - \rho_{H,V}^2)}{M} \right]^{1/2} \right\} \quad (2.9)$$

where  $M$  is the number of received samples [Melnikov and Zrnić, 2004]. For the purpose of this paper, we assume  $M = 64$ . The described model can be modified to simulate user-defined error characteristics.

### 2.3.3 Differential propagation phase smoothing

The most promising single-radar attenuation correction methods are based on specific differential phase ( $K_{DP}$ ) estimates [Bringi et al., 2001; Park et al. 2005a and 2005b; Smyth and Illingworth, 1998; Testud et al. 2000]. Unlike reflectivity, phase shift measurements are not affected by receiver calibration errors, errors in measurements of transmitted power, attenuation, or partial beam blockage. At X-band frequencies, signal attenuation by intervening rain is almost linearly proportional to  $K_{DP}$  measurements. In practice, the specific differential phase  $K_{DP}$  is derived from the differential phase,  $\Psi_{DP}$ , which is defined as:

$$\Psi_{DP}(r) = 2 \int_0^r K_{dp} dr + \delta + \varepsilon \quad (2.10)$$

where  $\delta$  is the backscatter differential phase defined in Equation 2.7 and  $\varepsilon$  corresponds to random fluctuations in  $K_{DP}$ .

Before radar observations of differential phase  $\Psi_{DP}$  can be used to estimate  $K_{DP}$ , we must eliminate random fluctuations and the effect of the backscatter differential phase  $\delta$ . This operation is dictated by the requirement for the  $\Psi_{DP}$  signal to be a smooth monotonic function of distance. Smoothing is commonly done by applying a FIR (Finite Impulse Response) filter according to *Hubbert and Bringi's* method [1995]. An iterative implementation of the filter is often necessary in order for  $\Psi_{DP}$  to become a smooth function. In Figure 2.5, we closely examine the effects of smoothing and how it affects the quality of  $K_{DP}$  estimates. For the present purpose, we selected two radar radials, each representing a different rainfall regime. In Figure 2.5, panels A and A' show a single

radar radial crossing a light rainfall zone, whereas panels B and B' correspond to an isolated and moderate rainfall core.

We employed the simulator to obtain “measured” (as observed by the radar) as well as the “true” values of differential phase  $\Psi_{DP}$  (Figure 2.5, panels A and B). Next, we superimposed profiles of differential phase  $\Phi_{DP}$  after the smoothing procedure [Hubbert and Bringi, 1995] had been applied to the measured  $\Psi_{DP}$ . As can be seen, the filtering approach effectively removed random fluctuations but not the backscatter differential phase effect. This is significant since the remaining backscatter differential phase  $\delta$  affects the quality of  $K_{DP}$  estimates derived from  $\Psi_{DP}$ . Once again, the simulator has been applied to compare the “true”  $K_{DP}$  profiles against profiles estimated from the smoothed  $\Psi_{DP}$ . Obtained results are presented in Figure 2.5 panels A' and B', where we also provide profiles of  $K_{DP}$  estimated from the filtered differential phase, but this time the backscatter phase shift  $\delta$  was set to zero along the whole radial before the smoothing procedure was applied. Although we believe that there is room for further improvement of the smoothing algorithm to better account for the backscatter differential phase effect, it is outside of the scope of this work to discuss alternative approaches to the removal of the backscatter phase shift from propagation phase profiles. The above analysis exemplifies how the simulator can be used to study different aspects of the radar rainfall estimation process.

#### 2.4 Network data merging

The main advantage of using the network approach for generating rainfall products is that information from all network nodes can be merged to create a common product. This is especially important for severe weather events in which total signal loss can be experienced by any of the nodes. The network approach can help eliminate the signal loss problem, improve attenuation correction, and increase the products' spatial and temporal resolutions. For each point within the network's domain, we are provided

with multiple observations coming from the network's radars. How to combine this information to maximize the quality of the final product warrants further investigation. The simulator can be used to evaluate different merging strategies in a synthetic environment. Possible merging methods include: selecting a maximum observed value, taking a linear combination of inputs, using inverse distance weighting, weighting conditioned on distance, using total path attenuation, and more. The proper order of data processing should also be investigated, since it is not clear whether merging should occur before or after attenuation correction of individual radars. Chapter 3 focuses on the implementation of numerous merging methods in the simulator.

### 2.5 Evaluation of simulation results

Comparing how different aspects of the simulated process affect the final rainfall products should help us select the network's optimal configuration. We focus the process of evaluating simulation results on estimating the products' overall bias and standard deviation when compared to the input field values for the domain of interest. Figure 2.6 presents an example set of high-resolution "true" variables used for comparison. The presented field has dimensions of  $40 \text{ km} \times 40 \text{ km}$  with each cell being  $0.1 \text{ km} \times 0.1 \text{ km}$ . While not significant from the simulator's perspective, the domain of interest outlined in Figure 2.6 covers the Clear Creek Experimental Watershed (HUC 07080209; also [Muste *et al.*, 2009]) located west of Iowa City, IA. The watershed is the "home base" for The University of Iowa Polarimetric Radar Network. Arbitrarily, the simulation results are based on the comparison of the "true" and network-estimated variables based only on points within the domain of interest; hence the requirement for all of the network's nodes to fully cover the domain of interest unless otherwise specified by the user.

To compare different attenuation methods, rainfall retrieval algorithms, or data merging strategies, the results of the simulation can be presented in a number of ways. In this work, we report the difference (expressed in units of a given variable) and the

relative difference (expressed in %) between the network-observed values and the “true” values. The distribution of residuals providing both the mean and standard deviation values can be accompanied by a graphical representation for a complete evaluation. While the single number indicators are a quick way to assess different methods, they often oversimplify the results. A graphical representation can help us notice any spatial patterns or instabilities and can suggest ways to improve the network’s configuration.

In this chapter, we use the simulator only to get a first look at its performance rather than to quantitatively compare different algorithms. Results obtained from individual cases are most strongly affected by initial rainfall conditions and can change from case to case. The simulator can provide general guidance as to how algorithms compare with respect to each other only when the number of realizations in an ensemble is large enough to minimize the effect of individual rainfall field characteristics.

## 2.6 Validation of the simulator

In addition to the rigorous testing of individual simulator modules during the developmental stage, we completed a validation exercise where we looked at relationships between polarimetric variables obtained from random simulation runs and compared them to corresponding relationships previously published in the literature. Our goal was to examine whether statistical relationships observed in data from operational polarimetric radars can be replicated using the simulator. We start the validation by analyzing the power-law relationship between the radar reflectivity factor ( $Z$ ) and the rainfall rate ( $R$ ), commonly known as the  $Z$ - $R$  relationship [*Marshall and Palmer, 1948*]. We analyzed two cases of DSD fields and recorded the polarimetric variables corresponding to the area of interest. The first case can be described as a light stratiform event with a few moderate cells, whereas the second event was selected to be convective with moderate rainfall rates.

Figure 2.7 plots data from the stratiform event, and a power-law type curve is fitted using the least-squares approach. Although, in practice, coefficients for the  $Z$ - $R$  relationship can vary depending on many conditions, we find the obtained results well within the acceptable range and very close to the relationship presented by *Marshall and Palmer* [1948].

Similarly, in Figure 2.8, we present results for the convective case. As denoted in the Figure, estimated coefficients are within expected ranges as they are close to those used by the NEXRAD system [*Seo et al.*, 2011] for rainfall estimation.

Next, we focused on the relationship between the specific attenuation ( $A_H$ ) and specific differential phase ( $K_{DP}$ ). Using the convective case, we compare the relationship and corresponding power-law coefficients to the results presented by *Jameson* [1992]. Data from the simulation are presented in Figure 2.9.

Another commonly studied relationship is the relationship between differential reflectivity ( $Z_{DR}$ ) and horizontal reflectivity ( $Z_H$ ). In Figure 2.10, we show simulated data based on the convective rainfall case. As discussed by *Zhang et al.* [2006], the  $Z_{DR}$ - $Z_H$  relationship can take on many forms depending on the type of rainfall and geographic location. For comparison, we plot the uncorrected (for attenuation)  $Z_H$  and  $Z_{DR}$  relationship together with the curve obtained by *Zhang et al.* [2006] and referred to as the “Florida case.” We conclude the validation by examining the relationship between the backscatter differential phase ( $\delta$ ) and differential reflectivity ( $Z_{DR}$ ). Based on the simulated data presented in Figure 2.11, we find this relationship to be almost quadratic. Limited previous studies, mostly based on similar simulations, also point to this form of relationship [*Otto and Russchenberg*, 2010].

The set of statistical relationships for polarimetric variables presented above was obtained assuming an X-band radar with zero degrees antenna elevation, no present mixed-precipitation, and an ambient temperature of 10 °C. Although limited in its nature, the presented set shows that the simulator is capable of mimicking, to a certain

extent, characteristics of polarimetric radars. Having validated the simulator, we now move to the subsection where a number of simulation scenarios is presented, each designed to analyze a different aspect of rainfall measurement by polarimetric radars.

## 2.7 Sample simulation results

To demonstrate the simulator's capabilities and how it can be used to address research questions, we designed several simulation scenarios and discuss obtained results hereafter. Since most hydrologic studies have a spatial extent limited to a watershed, a city, or a research network, we will only consider values from within the watershed area, as outlined in Figure 2.2, to evaluate the simulation results.

The strongest advantage of the simulator is its modular design. It allows for almost full flexibility in specifying many aspects of the simulation. Users can choose to investigate how different parts of the radar rainfall measurement process contribute to the final rainfall products. It is also important to note that the simulator as a research project undergoes constant development to adopt new knowledge and algorithms as they become available.

Below, we present four simulation scenarios that focus on different aspects of radar rainfall observations and present selected capabilities of the simulator. Each simulation scenario is based on a single input DSD field. We are aware that analysis results are affected by a specific rainfall distribution within the simulation domain, but this chapter presents the functionality and capabilities of the simulator rather than focusing on a systematic analysis of the network's optimal configuration.

### 2.7.1 Field values versus radar observables

Weather radars generate data on a radar-centric, polar grid. We start the demonstration of the simulator by providing a short review of polarimetric variables as recorded by a radar randomly located within the study domain, as depicted in Figure 2.12.

Presented variables can be immediately compared to the “true” field values, as previously demonstrated in Figure 2.6, and the results of the comparison can be reported. The differences between the “true” polarimetric variables and what is observed by a radar can have a very complex character that is often referred to as the “radar error structure.” Many factors contribute to those differences, including limited spatial resolution of radar data, radar calibration, polarimetric channel balance, beam broadening, signal attenuation, ground clutter, or retrieval algorithms. Although not all of these factors can be adequately represented in the proposed simulator, we believe that we can improve our understanding of the underlying processes by analyzing results from different simulation scenarios.

### 2.7.2 Effect of beam geometry

Radar beam geometry, and specifically beam width, is related to the shape and size of the radar’s antenna dish and the radar’s carrier frequency. In the current subsection, we will investigate how the radar’s beam width affects the accuracy of the observed reflectivity values over the domain of interest. To focus solely on beam geometry effects, we modified the simulator and removed the effects of signal attenuation and random signal fluctuations in reflectivity measurements. The simulator’s modular design allows for such selective exclusion of individual processes. We compare observations made when the radar beam width is set to  $1^\circ$  and  $3^\circ$  consecutively while other parameters remain equal. The selection of beam widths is arbitrary, serves as an example, and corresponds to the range of most common weather radar applications. Figure 2.13 summarizes the simulation results. As expected, the  $1^\circ$  beam provides a more detailed image and better matches the high variability of the input field. In the case of the  $3^\circ$  beam width, the large variability of the input field is not represented as well, leading to a greater overall standard deviation of simulated reflectivity values.

This rather simple simulation run allowed us to isolate a radar-specific characteristic (beam width) and analyze its effect on the final radar product. It also illustrates in simple terms the general idea of how the simulator can help us better understand the error sources in the radar rainfall estimation process.

### 2.7.3 Introducing noise to observations

Polarimetric variables estimated by weather radars are inherently corrupted by noise. The ratio of the level of meteoroidal signal power to the level of noise power donated, often referred to as SNR (signal-to-noise ratio), propagates to estimated radar variables and affects the overall quality of measurements. The main sources of noise are the thermal noise associated with background radiation and the electronic noise associated with a radar's active elements. To simplify the effect of noise resulting from a wide variety of sources in a complicated electric/electronic system such as a weather radar, we corrupt reflectivity observations on a gate-by-gate basis, with a normally distributed noise signal with mean  $\mu=0$  dBZ and a standard deviation  $\sigma=1$  dBZ. The levels of noise represent an optimistic scenario as it is a consensus opinion of the weather radar community [Atlas, 2002] that absolute radar calibration below  $\mu = 1$  dBZ level is difficult to achieve and that the standard deviation on the order of 1 dBZ for noise levels corresponds to a "well-functioning" radar. In reality, these values might be larger.

We conducted two simulation runs to assess the effects of the added signal noise on reflectivity estimates. For otherwise identical scenarios, simulated reflectivity values were affected by noise, while for the second run they were not. Radar beam width was set to  $1.4^\circ$  as this corresponds to the characteristics of The University of Iowa Polarimetric Radar Network radars. Comparison of the simulated observations with and without the noise is presented in Figure 2.14. As expected, the addition of random noise to observations increased the overall noise level of the simulated results. It is also important to note that simulated reflectivity values not contaminated by random noise

show a considerable amount of error when compared to the “true” values. The source of observed differences is mostly explained by the beam broadening process and higher spatial resolution of the input DSD fields compared to the radar beam dimensions at far ranges.

#### 2.7.4 Radar location effect

Depending on the shape, size, and location of the domain of interest, the positioning of a radar with respect to the domain of interest can affect the quality of the radar’s rainfall estimates. In the current simulation scenario, we investigate how the location of a radar within the spatial domain affects the quality of observed reflectivity values. We arbitrarily selected four radar locations within the domain and conducted simulation runs for otherwise identically configured conditions and the same rainfall case. For each location, radars provided full coverage of the domain of interest. The simulated reflectivity values for all locations were subsequently corrected for attenuation using the  $\Phi_{DP}$  constrained method [Testud, 2000] (for a brief definition see section 3.3.2). In Figure 2.15, we present the results obtained for each simulation scenario. It is important to note that the ground clutter contamination model is not implemented into the simulator at this stage. Application of a realistic ground clutter model would require detailed geographic information about the domain of interest and could greatly improve the accuracy of the presented simulator. In the presented analysis, the case where the radar is positioned within the domain of interest is considerably affected by the lack of a ground clutter model and, hence, the results should be interpreted with caution.

#### 2.7.5 Network data merging

Until now, the presented sample simulation scenarios only included analysis based on individual radars. We now move our focus to networks of radars. Simultaneous observation of the domain of interest by a network of radars creates redundant information which can be merged in order to obtain a common network

product. In practice, we may not have the full flexibility in selecting the physical locations for the network's nodes and, thus, depending on network's configuration, we can optimize the network's performance by selecting an optimal merging technique. The simulator offers a suitable environment in which to test different merging techniques. In this section, we examine only three merging techniques and apply them to horizontal reflectivity values  $Z_H$  as well as to a specific differential phase  $K_{DP}$ . Merging techniques include: the maximum value method, a simple averaging of data, and the inverse distance weighted interpolation method [*Shepard, 1968*], where a value at a given point is calculated as:

$$f(x, y) = \sum_{i=1}^n w_i f_i \quad (2.11)$$

where  $n$  is the number of networked radars,  $f_i$  is the value observed by the  $i^{th}$  radar, and  $w_i$  is the assigned weight:

$$w_i = \frac{h_i^{-p}}{\sum_{i=1}^n h_i^{-p}} \quad (2.12)$$

where  $h_i$  is the distance from the radar and  $p$  characterizes the weighting function. For this simulation, we use  $p=2$ . The three presented methods represent a small subset of possible merging techniques and serve only to demonstrate how the simulator can be used to compare different techniques of data merging.

We positioned three radar nodes within the study domain, each providing full coverage of the domain of interest. The simulator provided reflectivity and differential phase shift estimates for the selected locations. Obtained reflectivity values were corrected for attenuation before merging using the  $\Phi_{DP}$  constrained method [*Testud, 2000*]. To better illustrate the merging process, we included reflectivity and specific differential phase estimates for individual radars in Figure 2.16 and Figure 2.17 (panels A, C and E). The merging results for horizontal reflectivity are presented in panels B, D,

and F for both of the Figures, where panel B shows the result of the merging with the “maximum value” method; panel D corresponds to the “average merging” technique, and panel F shows the results where data was merged using the inverse weighting method.

Based on the results presented in Figure 2.16 and Figure 2.17, we can conclude that selecting the optimal merging method for a network of radars is not a trivial process. An optimal merging method can significantly improve the network’s performance but, at the same time, selecting an incorrect merging technique can lead to an escalation of errors and a dramatic decrease in the quality of the network’s rainfall products. It is also worth noting that when merging specific differential phase ( $K_{DP}$ ) values the simple averaging yielded the best results, whereas for reflectivity it was the inverse weighting method that showed the best performance. Another important observation can be made when analyzing Figure 2.17: we observed that, depending on the location within the domain, radars have a tendency to misrepresent the true location of the specific differential phase. This is especially visible when comparing individual observations with the outcome of the “maximum value” merging method (Figure 2.17, panel B). Visible shifting in  $K_{DP}$  can be attributed to the previously mentioned problem of residual backscatter phase shift  $\delta$  (section 2.3.3). The exercise also revealed an important advantage when using a network of radars rather than a single radar approach. As seen in Figure 2.17, panel D, merging of three network nodes with the “averaging method” can mitigate the “ $\delta$ -shifting” problem to a certain degree.

We must emphasize that all the results presented in this section are based on a single input field and, as such, can only serve as a demonstration of the simulator’s capabilities.

## 2.8 Summary of Chapter 2

In Chapter 2, we presented a detailed description of a polarimetric radar network simulator. The simulator has been developed to imitate, to a certain degree, the data

collection mechanisms of a network of polarimetric, X-band radars and provide a cost-effective way to evaluate a number of rainfall retrieval, attenuation correction, and data merging methods. We also describe the architecture of the simulator and the design of its main modules. We simulated radar observables based on high-resolution, synthetic DSD fields and simulated backscattering and propagation effects using the T-matrix approach. Description of the main modules is followed by the simulator's validation, where we examine a number of relationships between simulated polarimetric variables and compare them to the relationships previously published in the literature. To demonstrate the basic functionality of the simulator, we conducted a number of simulation scenarios, each of which was designed to test one aspect of the weather radar measurement process. We look at the effect of beam width, measurement noise, radar, and location for single-radar scenarios. In a network approach, we examine how different data merging methods can be implemented.

Although we are aware of the limitations of the simulator with respect to the accuracy of the simulated data, we believe that in its present form, it can help us address many questions related to radar rainfall measurement. Successful implementation of the simulator has the potential to enhance operations of The University of Iowa Polarimetric Radar Network.

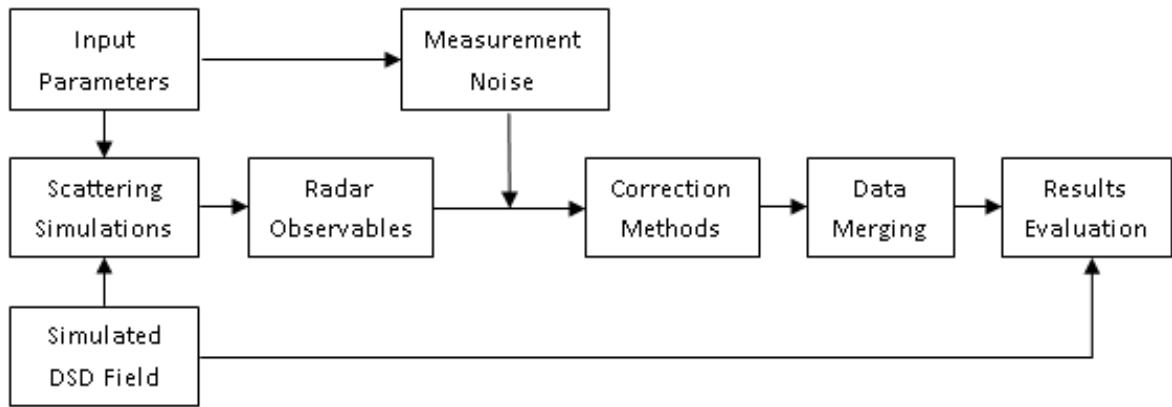


Figure 2.1: Simulator's block diagram demonstrating its modular design.

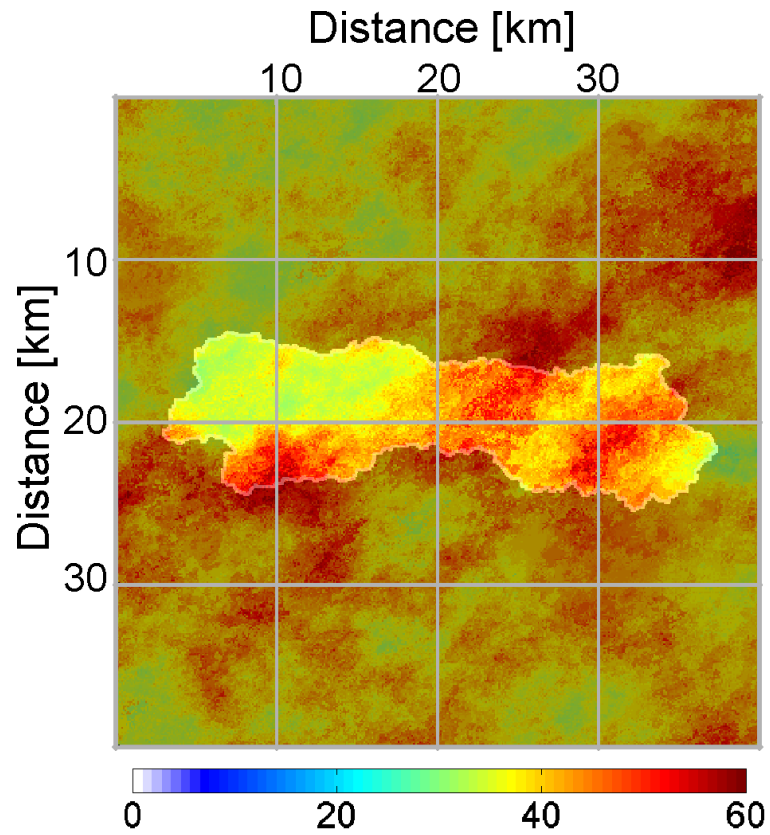


Figure 2.2: An example of a 40 km x 40 km spatial domain with an outline of a hypothetical area of interest. The shape of the area of interest is that of the Clear Creek watershed (HUC 07080209). Superimposed is a single field of horizontal reflectivity values.

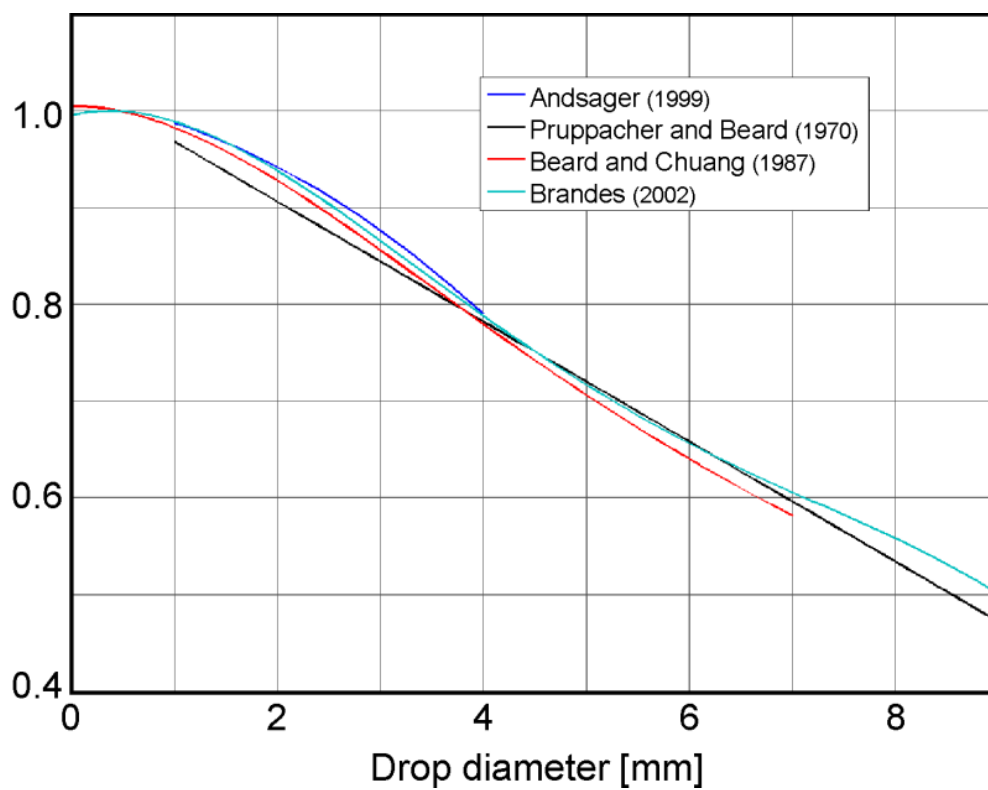


Figure 2.3: Comparison of different models representing water droplets vertical to horizontal axis ratio as a function of equivolumetric drop diameter  $D$ .

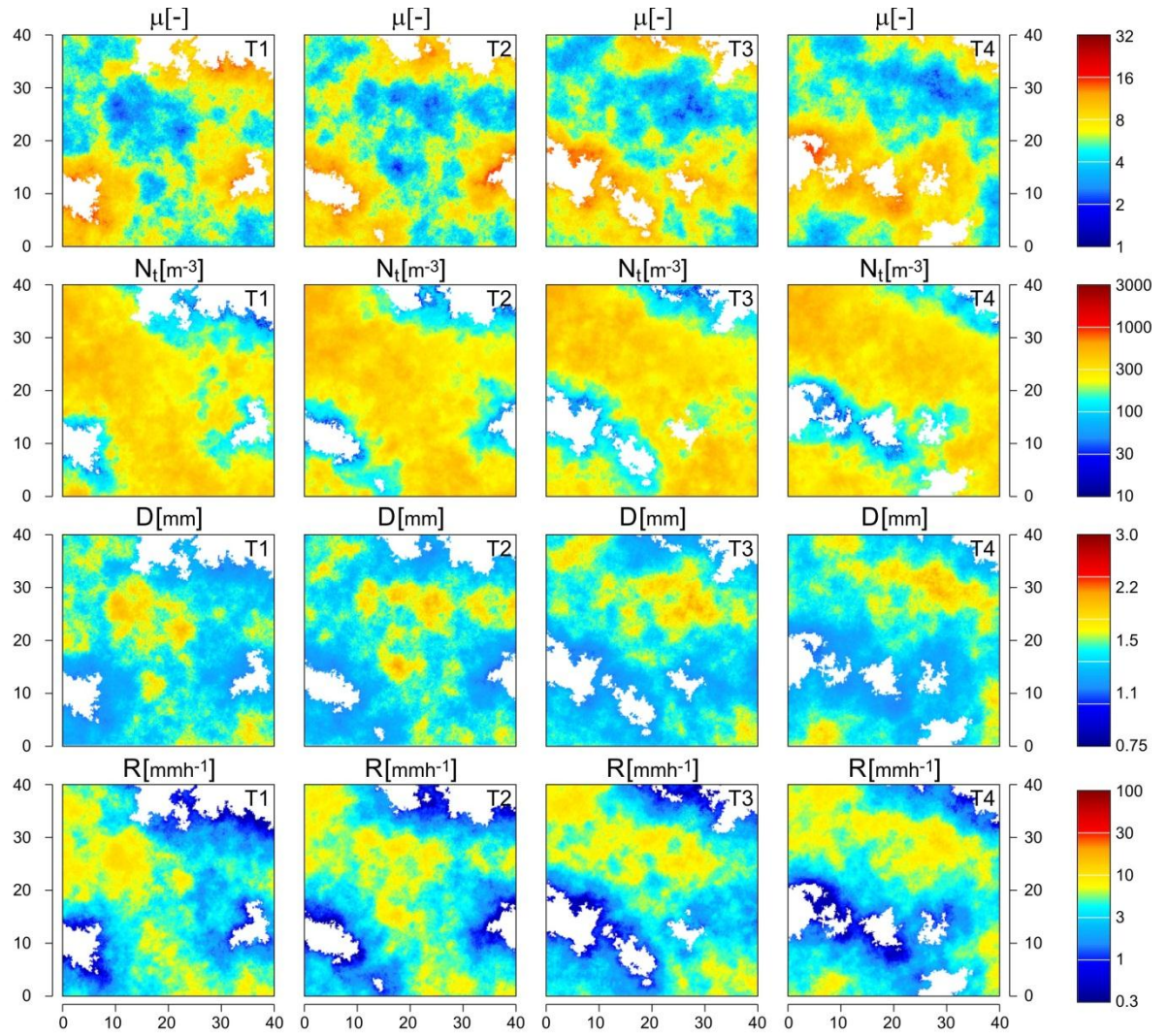


Figure 2.4: Four consecutive time steps (T1, T2, T3 and T4) of DSD parameters showing time evolution of a simulated rainfall event.

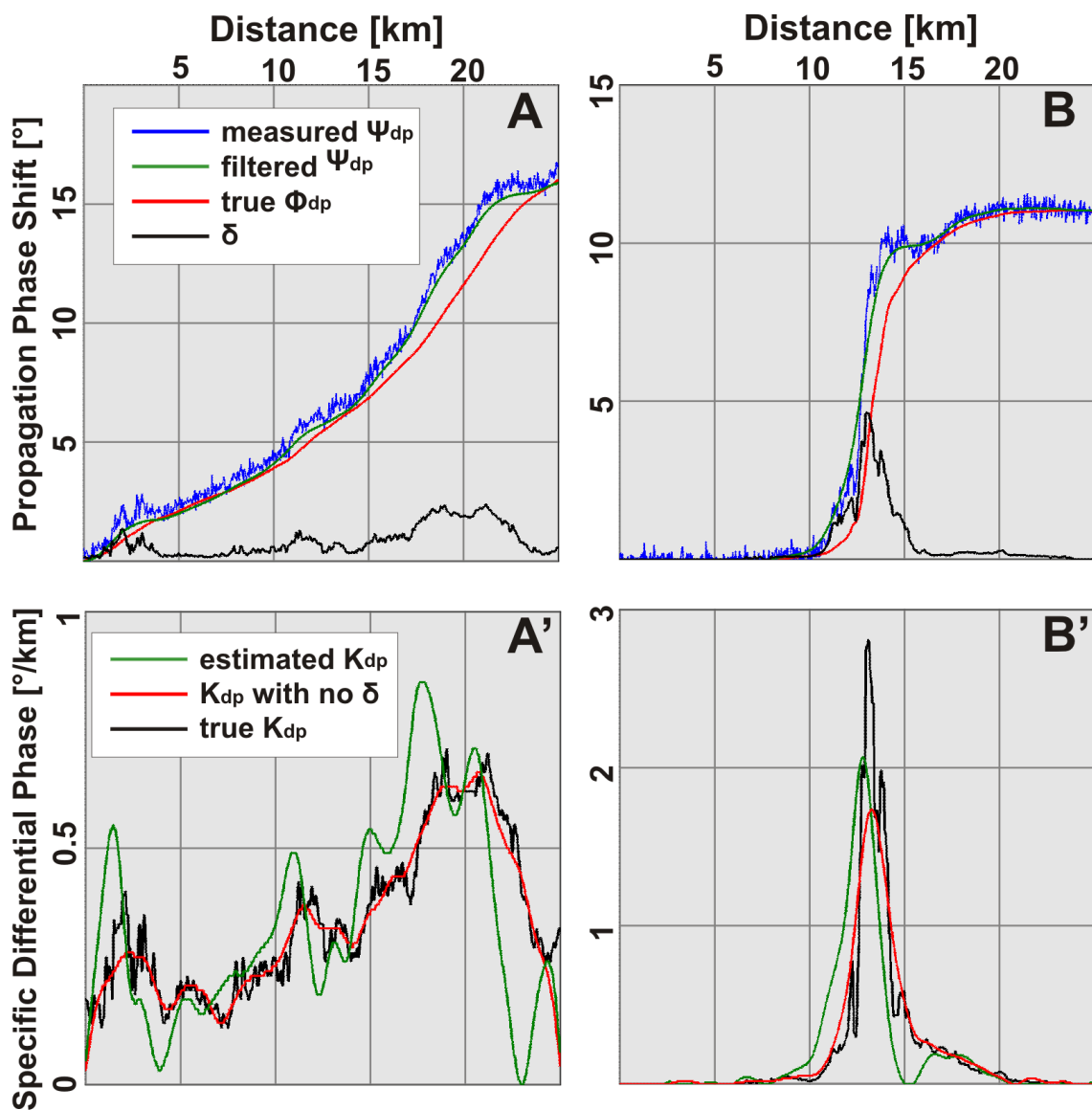


Figure 2.5 Analysis of backscatter differential phase. A) Sample profile of “true” differential phase in a stratiform rainfall – red line, filtered using FIR filter – green line; differential phase as recorded by radar – blue line; backscatter differential phase – black line; B) same as in A, but for a single rainfall core case; A’) profiles of  $K_{DP}$ : “true” - black line; estimated from FIR filtered differential phase – green line, as estimated from differential phase when no backscatter differential phase  $\delta$  is present – red line; B’) same as A’ but for the single core rainfall case.

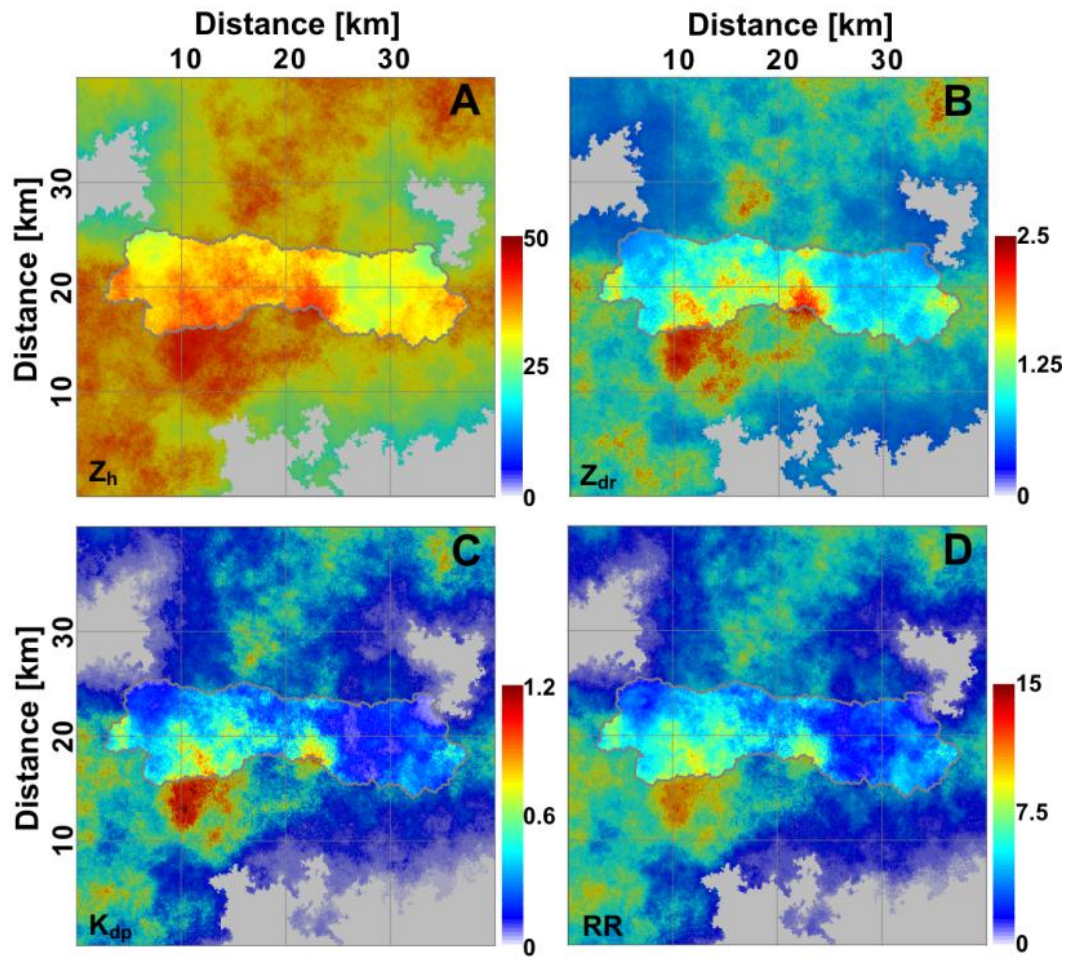


Figure 2.6: High-resolution “true” variables used in the simulator as a reference. A) horizontal reflectivity  $Z_H$  (dBZ); B) differential reflectivity  $Z_{DR}$  (dB); C) specific differential phase  $K_{DP}$  ( $^{\circ}/\text{km}$ ); D) rainfall rate  $RR$ , (mm/h).

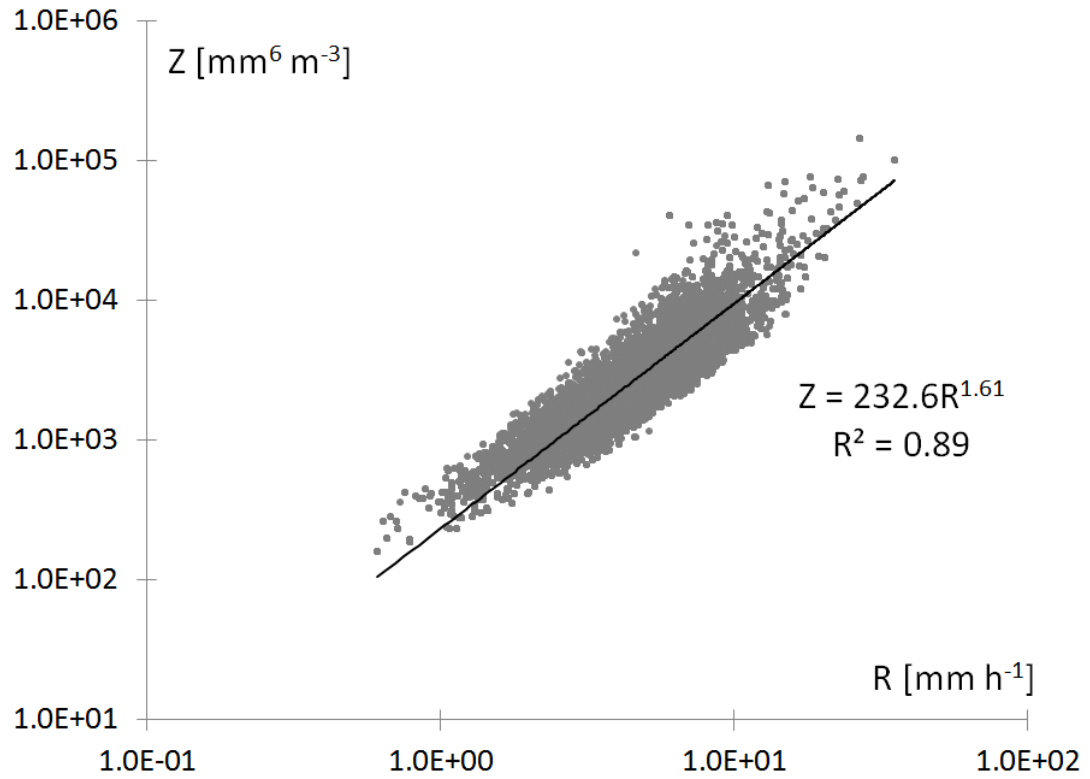


Figure 2.7: Simulation results showing Z-R relationship for a stratiform rainfall event and a corresponding least-square fit.

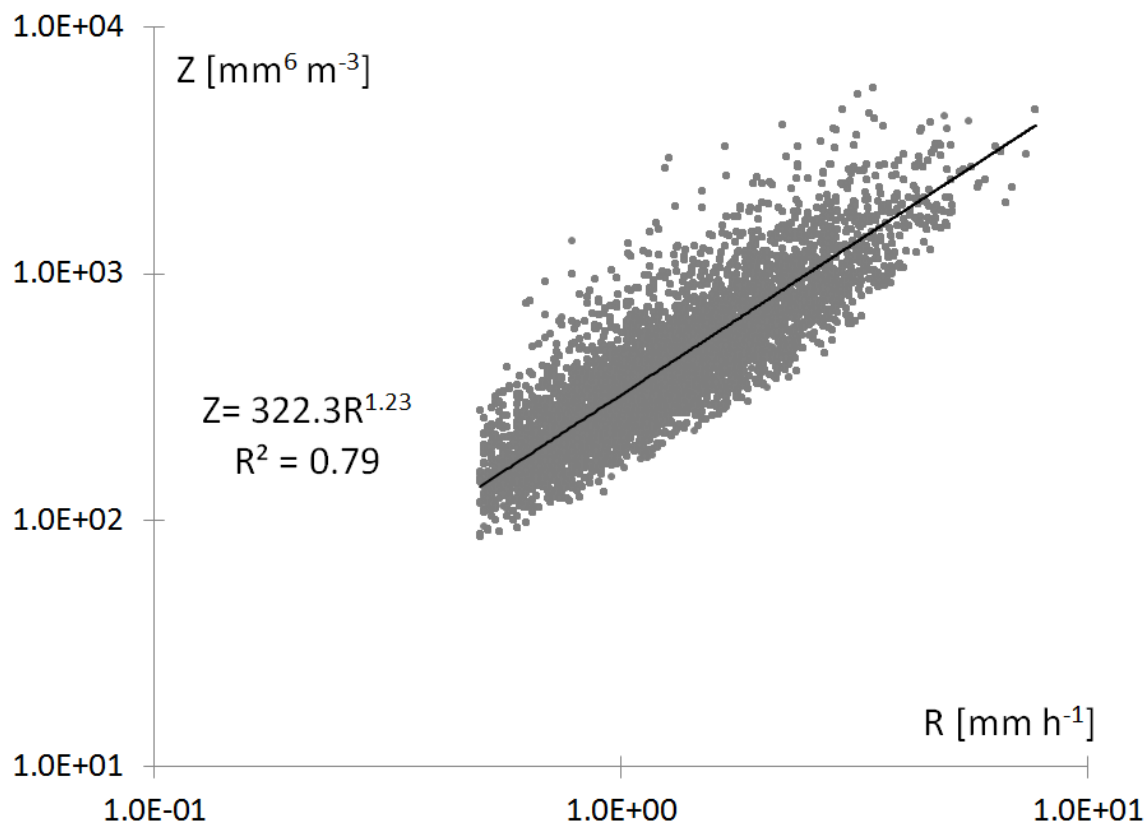


Figure 2.8: Simulation results showing Z-R relationship for a convective rainfall event and a corresponding least-square fit.

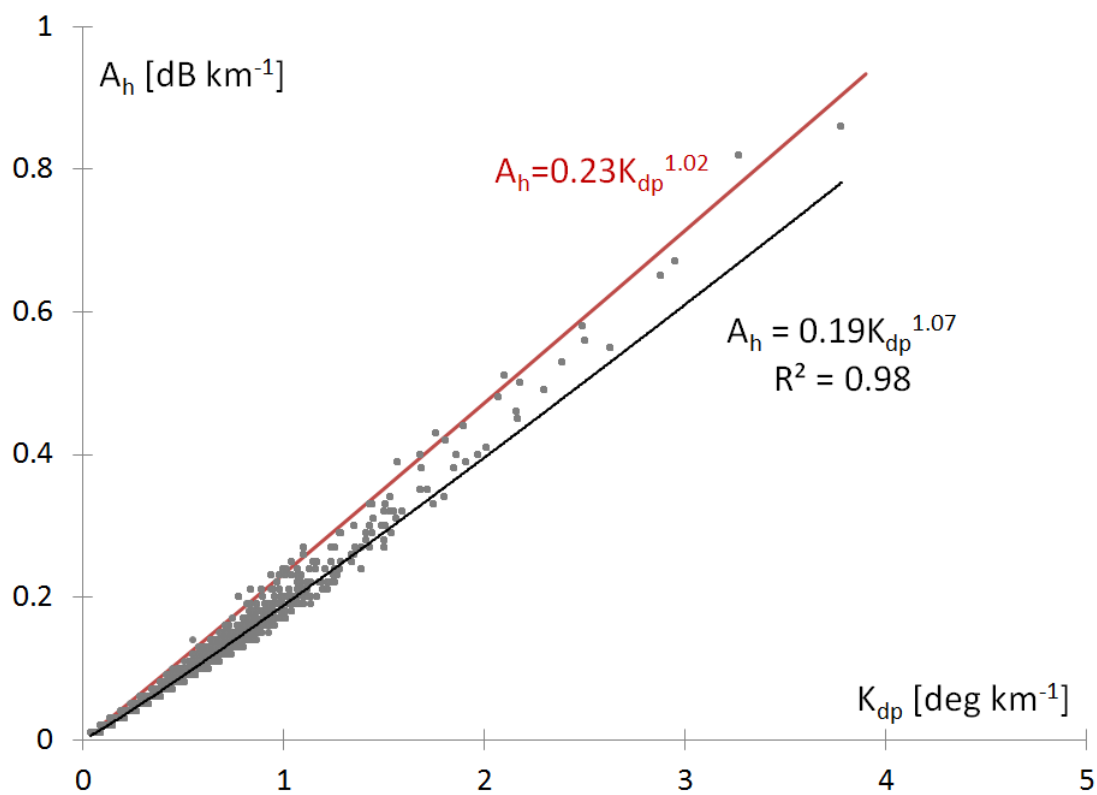


Figure 2.9: Scatterplot showing  $A_H$ - $K_{DP}$  relationship for the simulated scenario. Black line is a least-square fit to the data and the red line is the relationship suggested by Jameson [1992].

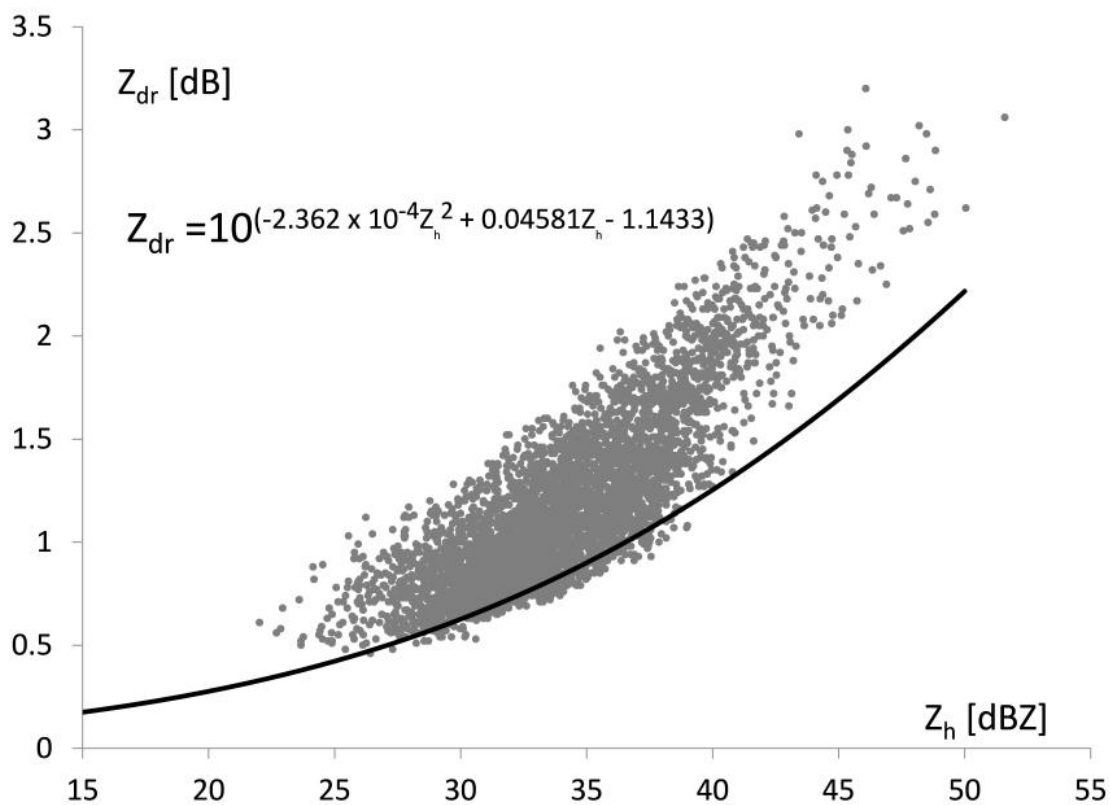


Figure 2.10: Scatterplot showing  $Z_{DR}$ - $Z_H$  relationship. Superimposed is the function (expression is presented in the Figure) corresponding to the “Florida case” as reported by *Zhang*, [2006].

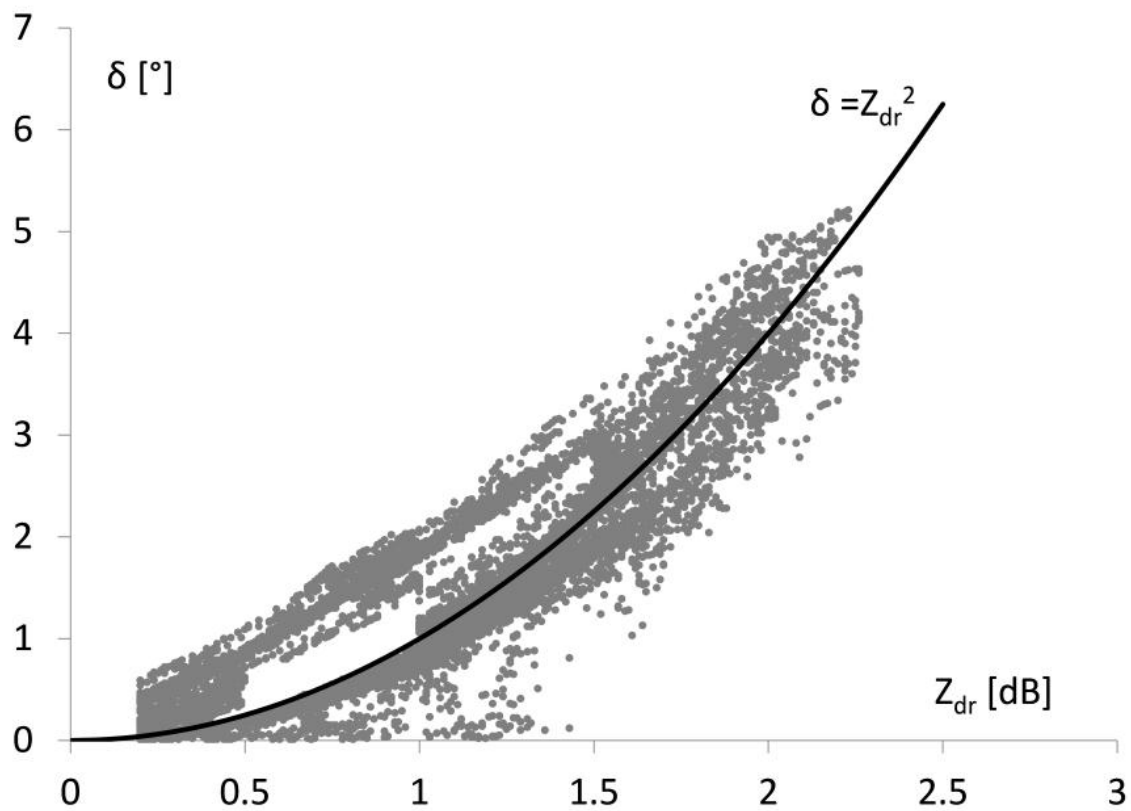


Figure 2.11: Scatterplot showing relationship between backscatter differential phase  $\delta$  and the differential reflectivity  $Z_{DR}$ . Black line has form  $\delta = Z_{DR}^2$ .

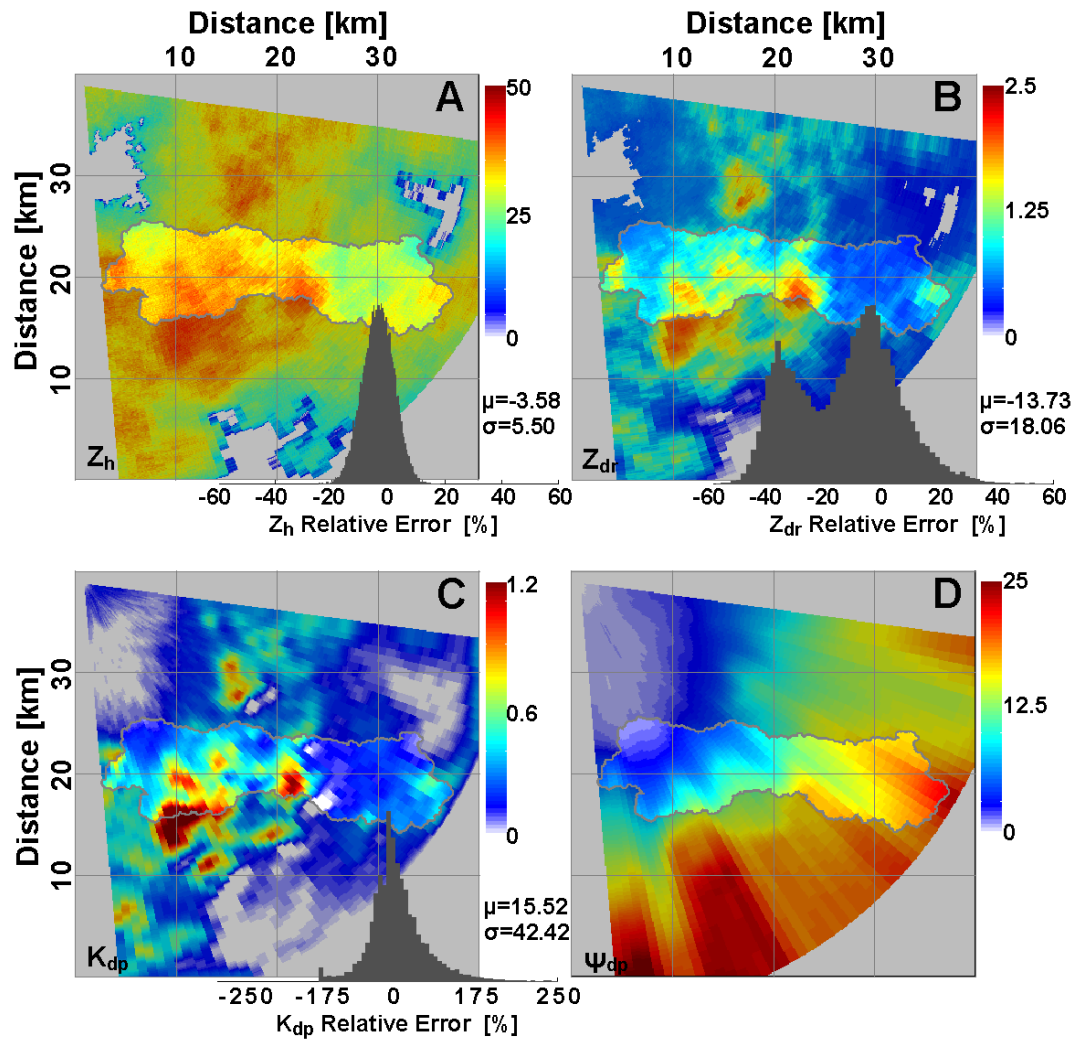


Figure 2.12: Polarimetric variables as recorded by a simulated radar: A) horizontal reflectivity  $Z_H$  (dBZ); B) differential reflectivity  $Z_{DR}$  (dB); C) specific differential phase  $K_{DP}$  ( $^{\circ}/\text{km}$ ); D) differential phase  $\Psi_{DP}$  ( $^{\circ}$ ). Reported values and histograms are based on comparison with the “true” field values.

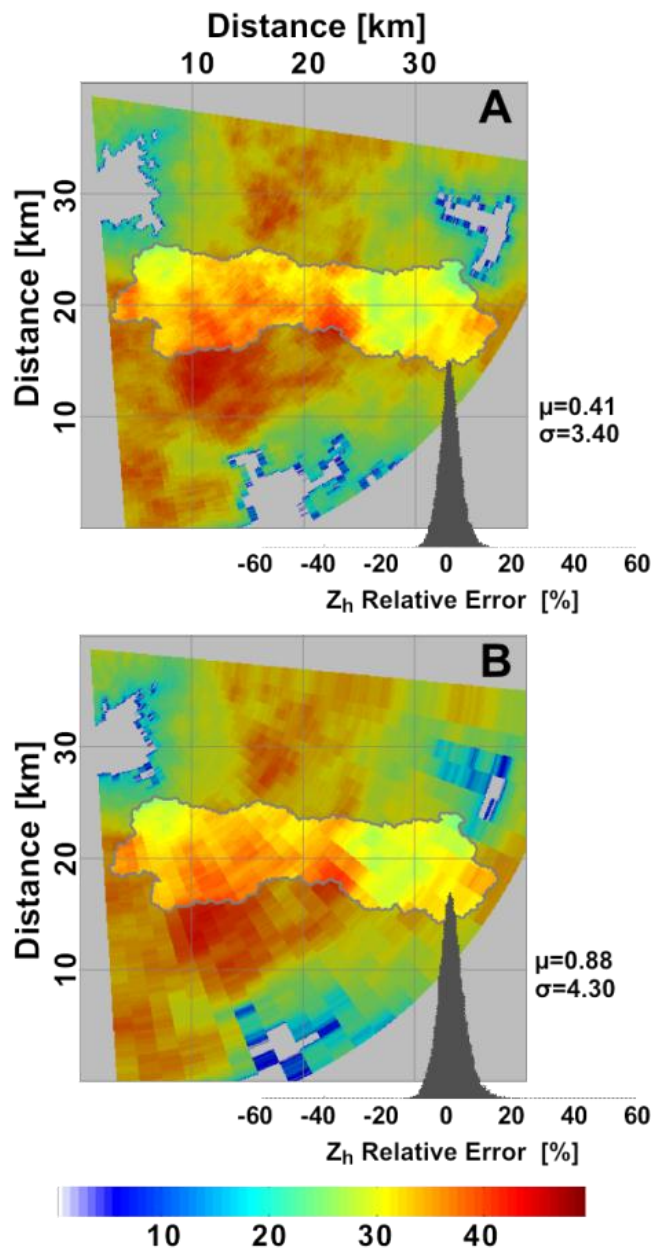


Figure 2.13: Analysis of the beam width effect on radar observations of reflectivity values. A) 1° beam width; B) 3° beam width.

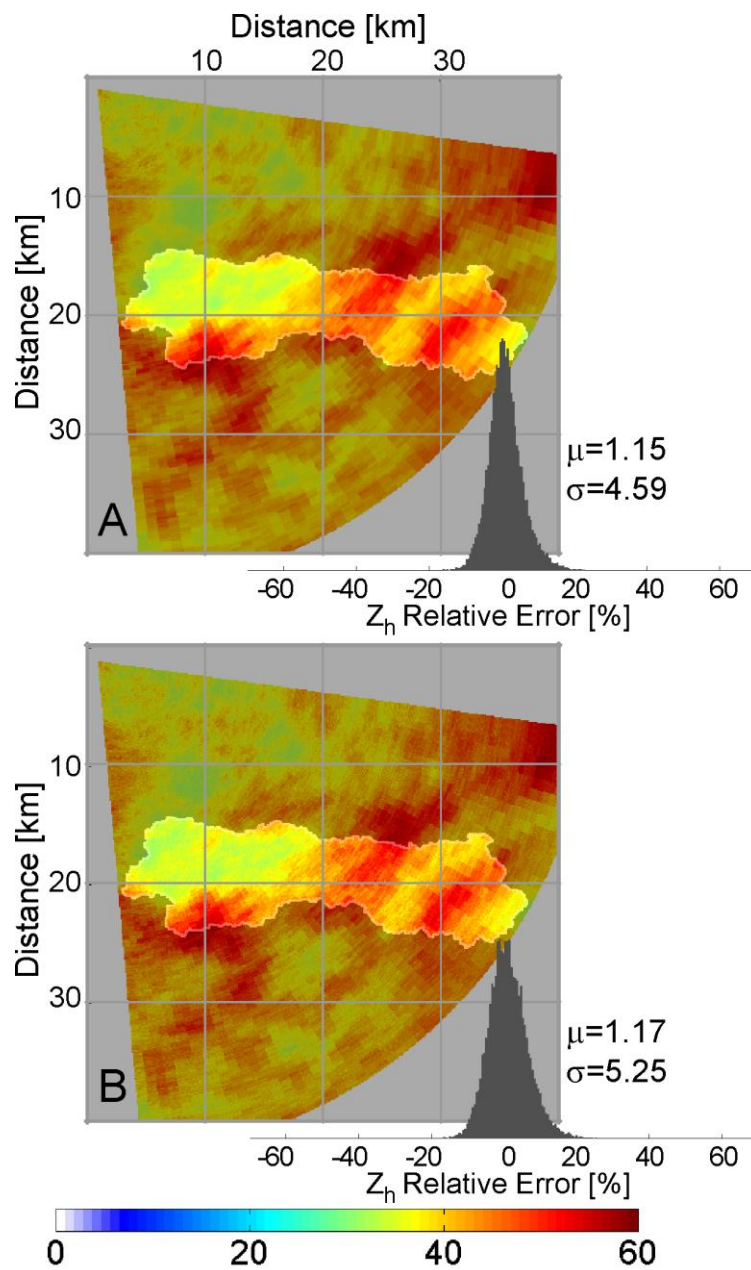


Figure 2.14: Analysis of measurement noise. A) horizontal reflectivity recorded in the absence of measurement noise, B) horizontal reflectivity corrupted by random noise.

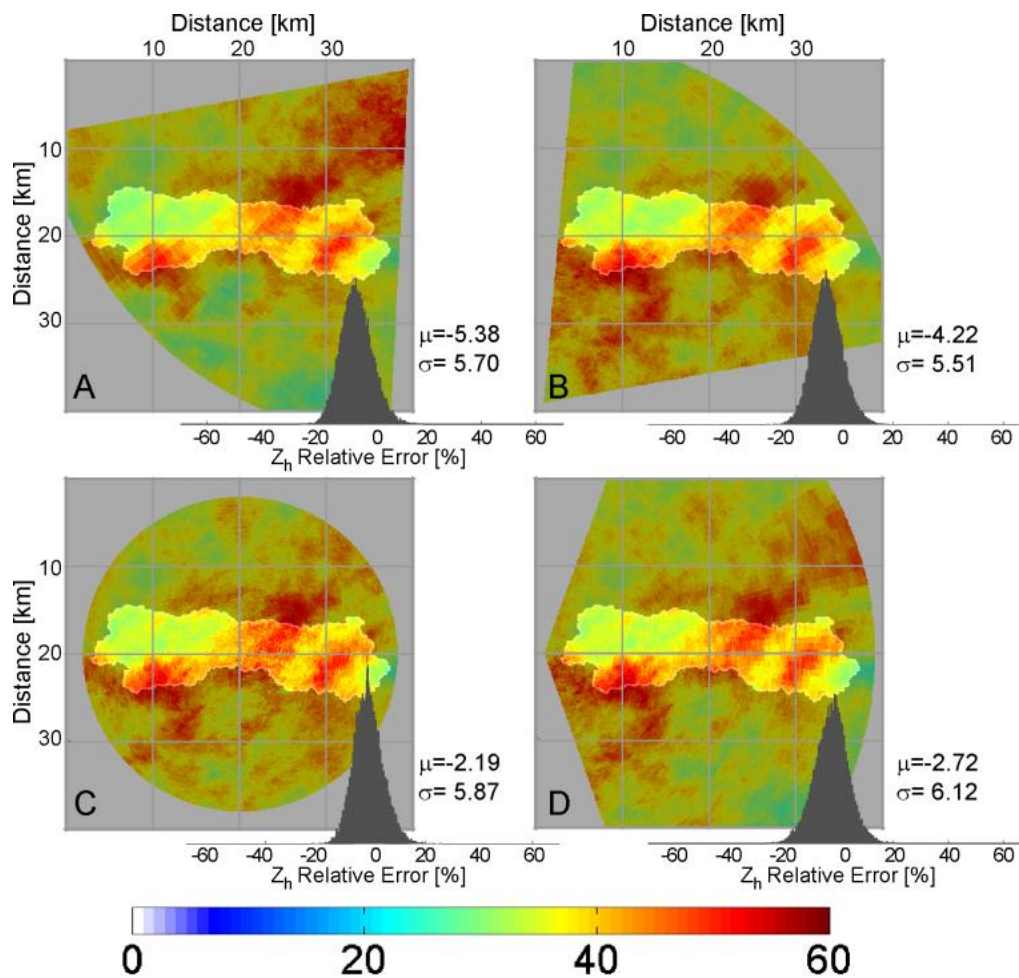


Figure 2.15: Comparison of the reflectivity simulations for radars positioned in different locations within the spatial domain.

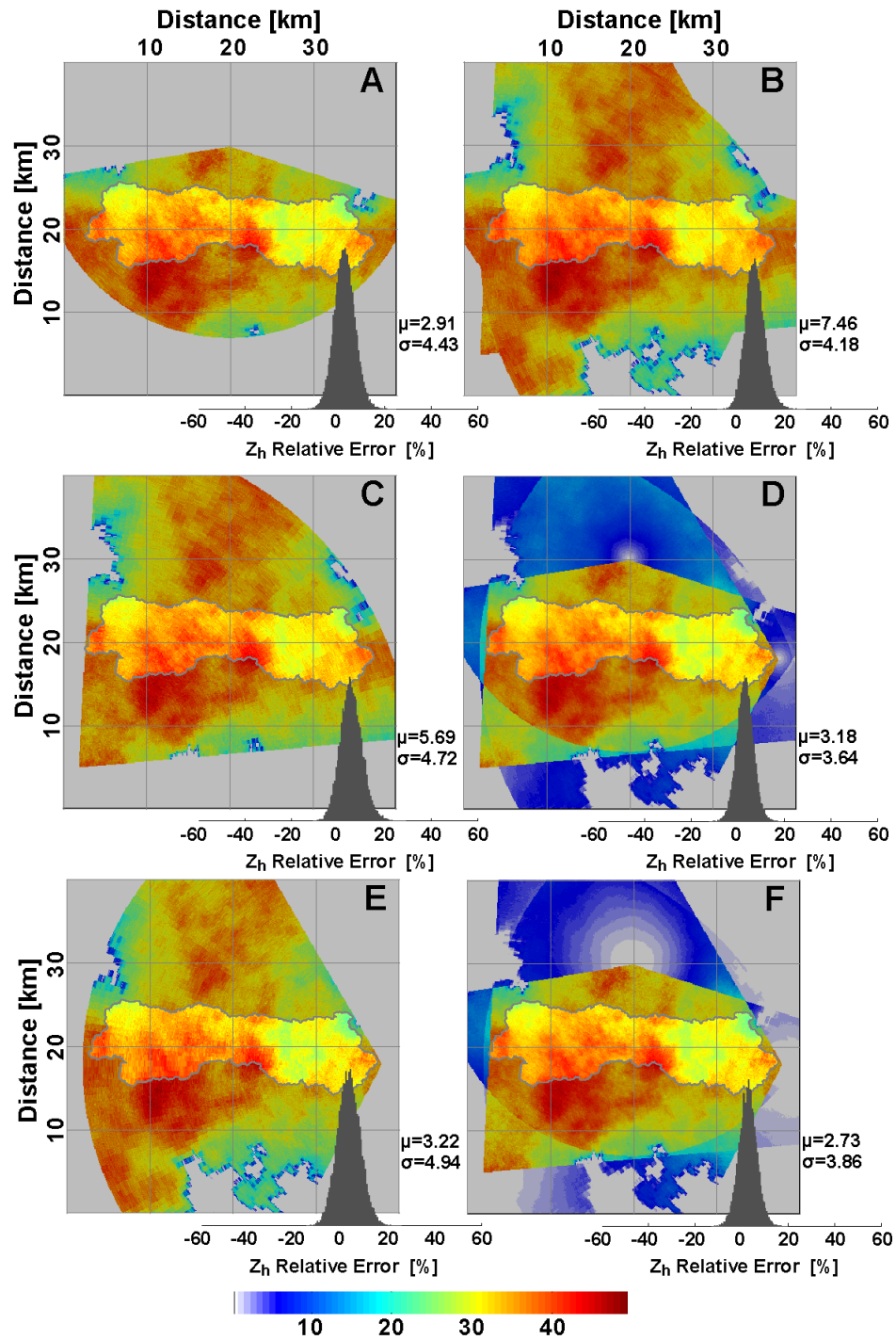


Figure 2.16: Merging horizontal reflectivity data. A,C,E) Individual radars and corresponding reflectivity data; B) merging using the “maximum value” method; D) merging by taking simple average of all available input data; F) merged reflectivity values using inverse weighting method.

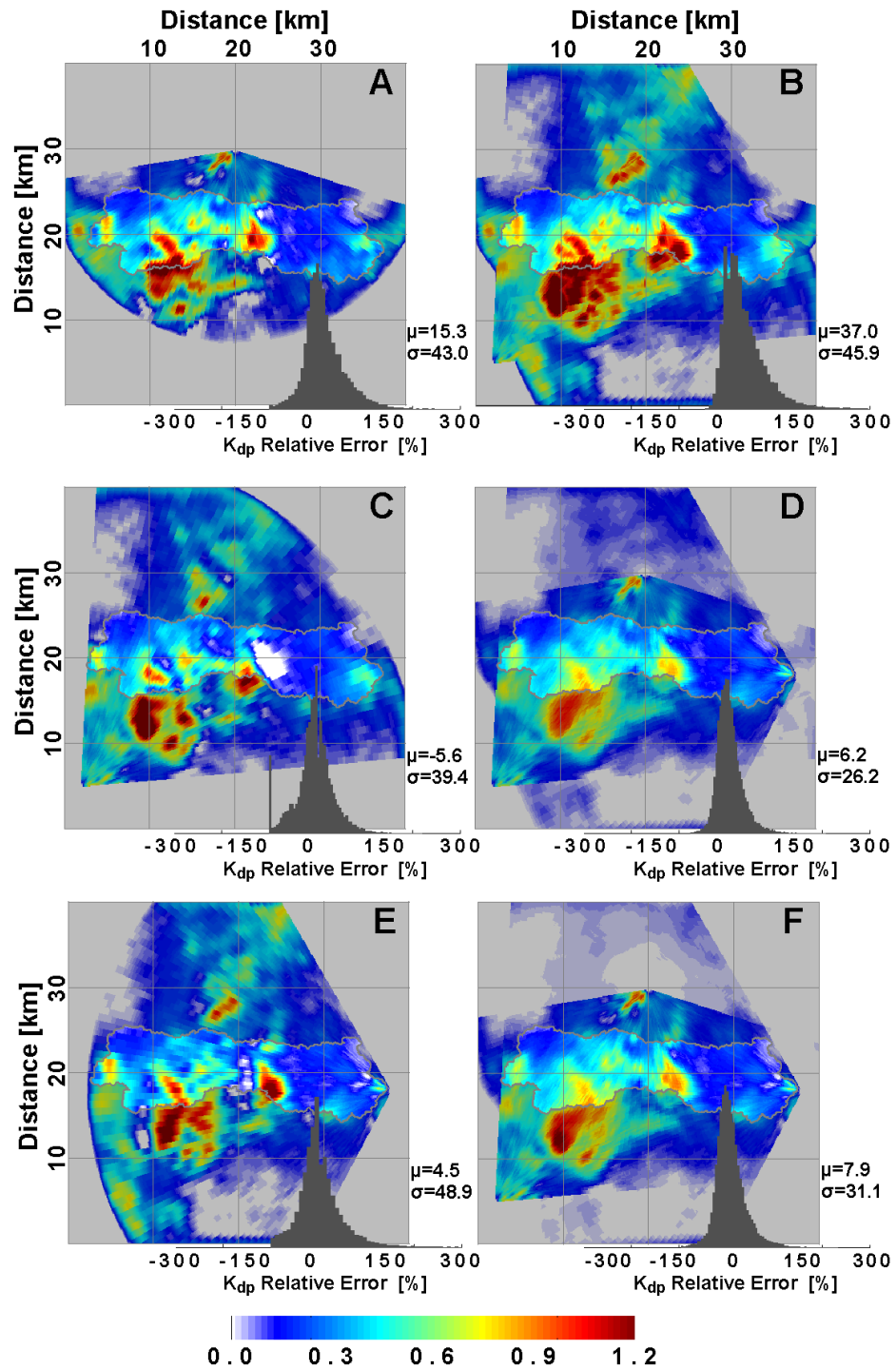


Figure 2.17: Merging specific differential phase data. A,C,E) Three individual radars and corresponding  $K_{DP}$  data; B) merging using the “maximum value” method; D) merging by taking simple average of all available input data; F) merged reflectivity values using inverse weighting method.

## CHAPTER 3

### ANALYSIS OF ATTENUATION CORRECTION METHODS IN A NETWORKED ENVIRONMENT BY MEANS OF COMPUTER SIMULATIONS

#### 3.1 Introduction

Networks of small, often mobile, polarimetric radars are gaining popularity due to their rainfall observing capabilities and relatively low purchase cost [e.g., *Matrosov et al.*, 2005; *Krajewski and Smith*, 2002]. In recent years, a number of installations have become globally operational [e.g., *Junyent et al.*, 2010; *Maki et al.*, 2010]. Networks of polarimetric radars often operate at X-band frequencies, where signal attenuation by intervening rainfall can lead to severe signal degradation and/or total signal loss. Operating a network of radars with an overlapping view of the domain of interest (a watershed, a city, etc.) creates an opportunity for better, more reliable attenuation correction methods. Applying single-radar attenuation correction algorithms to a network of radars is common, but it does not take full advantage of available redundant data. In this chapter, we employ the polarimetric radar network simulator described in Chapter 2 to evaluate a number of available single-radar attenuation correction algorithms in a networked environment and propose a set of network-based correction methods. Our analysis is based on a series of physics- and stochastic-based simulated rainfall events occurring over the area of interest. The characteristics of the simulated radars are those of The University of Iowa Polarimetric Radar Network, which is being prepared for use by US hydrologic research community. The evaluation of each attenuation correction method is based on its accuracy in estimating reflectivity, rainfall rates, and mean aerial precipitation over a single point as well as for watersheds of different sizes within the area of interest. The previously developed simulator and

obtained simulation results are being used as a first approximation in evaluation of the capabilities of polarimetric radar networks prior to their acquisition and field deployment.

### 3.2 Simulation design

The physical basis for the simulation is provided as a high-resolution ( $0.1 \text{ km} \times 0.1 \text{ km}$ ) DSD field covering the area of interest. The method used to simulate the parameters of the drop size distribution has been proposed by *Schleiss et al.* [2009, 2011] and has been briefly described in section 2.2.5. To test attenuation correction methods using the simulator, we have simulated 24 rainfall events ranging in intensity from light through moderate to strong. Each event consists of ten consecutive data fields with a six-minute time interval between consecutive DSD fields, giving us a total of a 24 hour equivalent test case. Including a large input data sample decreases the effect of individual DSD fields on the overall simulation results. A sample input DSD field is shown in Figure 2.4, where the system's advection and evolution in time of individual DSD parameters can be observed.

We placed four radars within the area of interest. Each radar operates at a frequency of 9.43 GHz, which matches the carrier frequency of The University of Iowa Polarimetric Radar Network. The radars' locations have been arbitrarily selected, but the goal is to provide a realistic network configuration and full coverage of the domain of interest. Radars are constrained to scan only a sector rather than a full 360 degree evolution for faster data processing. Each sector is selected to fully cover the area of interest, which in this case has been selected as three adjacent watersheds positioned centrally within the spatial domain. We used a zero degree antenna elevation, an ambient temperature of  $10^\circ \text{ C}$ , a radar beam width of  $1.4^\circ$ , and a 30 m range resolution for all radars constituting the network.

Figure 3.1 features the positioning of the radars, scan coverage, and the watersheds of interest. In addition, the figure shows three individual point locations that were selected as test locations for future reference.

Values of horizontal reflectivity  $Z_H$  (dBZ), vertical reflectivity  $Z_V$  (dBZ), and differential reflectivity  $Z_{DR}$  (dB), together with propagation phase  $\Psi_{DP}$  ( $^\circ$ ) and cross correlation coefficient  $\rho$ , have been recorded on a radar-centric polar grid for each of the radars. To convert propagation phase shift values to the specific differential shift  $K_{DP}$  ( $^\circ/\text{km}$ ), we first applied the smoothing procedure described in 2.3.3 and later differentiated the smoothed  $\Phi_{DP}$  profiles following the equation:

$$K_{DP}(r_1) = \frac{\Phi_{DPf}(r_2) - \Phi_{DPf}(r_1)}{2(r_2 - r_1)} \quad (3.1)$$

where  $r_1$  and  $r_2$  are range gates and  $\Phi_{DPf}$  stands for a filtered, or “smoothed,” differential shift.

Figure 3.2 shows a sample set of simulated radar observables as simulated for individual radars in a sample test case.

The input dataset consisting of 24 rainfall cases and that is equivalent to 24 hours of continuous rainfall has been processed in the simulator. Obtained radar-centric polarimetric variables for all four network nodes are the basis for testing and evaluation of both single-radar and network-based attenuation correction algorithms.

### 3.3 Single-radar attenuation correction methods

We begin our analysis by investigating a group of attenuation correction methods developed for single-radar operations. The methods have been previously published in the literature and are often used in operational radars. Below, we provide a brief description of each method.

### 3.3.1 The “forward” algorithm [Method 1]

First we introduce the *Hitschfeld and Bordan* method [1954], which is known as the forward algorithm because attenuation is estimated cumulatively in the direction away from the radar. In this method, the corrected reflectivity  $Z(r)$  is expressed as:

$$Z(r) = \frac{Z_a(r)}{\left[ 1 - \frac{0.2 \ln(10)}{\beta} \int_0^r \left( \frac{Z_a(s)}{\alpha} \right)^{1/\beta} ds \right]^\beta} \quad (3.2)$$

where  $Z_a(r)$  is the measured reflectivity value, and coefficients  $\alpha$  and  $\beta$  relate reflectivity to one-way specific attenuation by  $Z = \alpha A^\beta$ . The default values for the parameters were selected as  $\alpha = 1.12 \cdot 10^5$  and  $\beta = 1.32$  [Berne and Uijlenhoet, 2005]. The Hitschfeld and Bordan algorithm is known to be highly unstable and often leads to the overestimation of attenuation. To detect the algorithm’s instability, a limit on the path-integrated attenuation (PIA) along a ray is often required to constrain the algorithm. In the current implementation, we use a 60 dBZ limit on PIA and when the limit is reached for any given radar profile, correction of reflectivity values is aborted.

### 3.3.2 The $\Phi_{DP}$ constrained method [Method 2]

At X-band frequencies, the specific attenuation and the specific differential phase show a linear relation [Jameson, 1992] of the form:

$$A_H(r) = \alpha K_{DP}(r) \quad (3.3)$$

The existence of this linear relationship led to the development of attenuation correction algorithms based on measurements of the specific differential phase. The algorithm originally proposed by *Testud* [2000], called “ZPHI,” was developed for spaceborne radar with frequencies greater than 10 GHz. Following the derivations of *Bringi and Chandrasekar* [2001], we implemented the algorithm, in which specific attenuation is estimated as follows:

$$A_H(r) = \frac{[Z_a(r)]^b (10^{0.1(b\alpha)\Delta\Phi_{DP}(r_0:r_m)} - 1)}{I(r_0:r_m) + (10^{0.1(b\alpha)\Delta\Phi_{DP}(r_0:r_m)} - 1)I(r:r_m)} \quad (3.4)$$

where  $b = 0.76$  [Delrieu et al. 1997],  $\alpha = 0.233 \text{ dB}^\circ$  [Jameson, 1992], and:

$$I(r_n:r_m) = 0.46b \int_{r_n}^{r_m} [Z_a(r)]^b dr \quad (3.5)$$

Once the specific attenuation  $A_H(r)$  is calculated for each range gate, the reflectivity can be corrected using the following equation:

$$10\log_{10}[Z_H(r)] = 10\log_{10}[Z_a(r)] + 2 \int_{r_0}^r A_H(s) ds \quad (3.6)$$

The main limitation of this algorithm is the sensitivity of the parameter  $\alpha$  to the temperature and mean axis ratio of the raindrops. The assumption of a constant value of  $\alpha$  can lead to biased estimates of specific attenuation in the presence of hail and mixed phase hydrometeors.

### 3.3.3 The constrained method with optimal parameter $\alpha$

#### [Method 3]

An iterative approach can be used to overcome the limitations of a constant  $\alpha$  value in the  $\Phi_{DP}$  constrained method [Method 2], where a range of  $\alpha$  values is applied to Equation 3.4 in order to find the optimal solution. The criterion is based on minimizing an error function:

$$E = \sum_{j=1}^N |\Phi_{DP}^{flt}(r_j) - \Phi_{DP}^c(r_j, \alpha)| \quad (3.7)$$

where  $\Phi_{DP}^c(r, \alpha)$  is a differential propagation phase profile constructed for a given  $\alpha$  value as:

$$\Phi_{DP}^c(r, \alpha) = 2 \int_{r_0}^r \frac{A_H(s, \alpha)}{\alpha} ds \quad (3.8)$$

and  $\Phi_{DP}^{filt}$  is the filtered (smoothed) differential propagation phase. In practice, we use simulated values of propagation phase  $\Psi_{dp}$  since the effects of backscatter differential phase  $\delta$  cannot be completely removed, as previously described in 2.3.3.

### 3.3.4 The $K_{DP}$ method [Method 4]

The  $K_{DP}$  method is considered a “simple” attenuation correction approach because of the straightforward relationship it relies on. As shown by *Jameson* [1992], the relationship between horizontal attenuation and the specific differential phase for the X-band radars can be represented as a linear function, as shown in Equation 3.3.

In the simulator, the specific differential phase  $K_{DP}$  is obtained by differentiating profiles of the “smoothed” differential phase shift. The smoothing procedure is presented in section 2.3.3, and the differentiation is based on Equation 3.1.

The limitation of this method is the same as in the  $\Phi_{DP}$  constrained method because the parameter  $\alpha$  is highly sensitive to temperature and the selection of a fixed  $\alpha$  value can significantly influence the method’s accuracy [*Carey*, 2000]. It is also important to note that the smoothing of the propagation shift over many range gates decreases the spatial resolution of the reflectivity estimates for attenuation correction methods based on a specific differential phase.

The presented set of attenuation correction methods has been implemented into the simulator. In the following, we present the results of simulations designed to evaluate each of the described methods in a single-radar environment.

## 3.4 Simulation results for single-radar methods

As previously described, the input dataset corresponding to 24 one-hour long rainfall events has been used to generate radar-centric values of reflectivity and specific differential phase profiles. Four single-radar attenuation correction methods presented in the previous section have been applied to correct horizontal reflectivity values for all four radars. To assess these methods, we focused on estimating the difference  $\varepsilon_Z$  [dBZ]

between the “true” reflectivity  $Z_H$  and the corrected reflectivity  $Z_{He}$ , both expressed in units of dBZ:

$$\varepsilon_Z(i, j) = Z_H(i, j) - Z_{He}(i, j) \quad (3.9)$$

where,  $i, j$  are indices corresponding to a location within the area of interest.

In the analysis, we consider only values from within the area of interest, which for this study is the watershed outlined in Figure 3.1. Table 3.1 summarizes the results obtained for the area of interest (HUC<sub>123</sub>). To allow for easier analysis of the presented results, we color-coded each table with methods results ranging from the best to the worst by using the following color scheme:

-  - best result,
-  - second best,
-  - 3<sup>rd</sup> result,
-  - worst result.

In Table 3.1, symbols R<sub>1</sub>, R<sub>2</sub>, R<sub>3</sub>, and R<sub>4</sub> indicate results obtained for corresponding radars, as depicted in Figure 3.1. Individual columns correspond to specific attenuation correction methods starting from the uncorrected values ( $Z_{Hm}$ ), followed by the forward algorithm ( $Z_H 1$ ) results,  $\Phi_{DP}$  constrained method ( $Z_H 2$ ) results, the constrained method with optimal parameter  $\alpha$  ( $Z_H 3$ ) results, and the  $K_{DP}$  method ( $Z_H 4$ ) results.

Reflectivity values are a common way to present weather radar measurements, but the non-linear and very dynamic scale of the reflectivity-to-rainfall ( $Z$ - $R$ ) relationship can make it difficult for a reader to get a sense of the extent to which the presented methods differ from each other. To address this discrepancy, we supplemented the presented results with additional rainfall rate-based analysis. First, rainfall rates from horizontal reflectivity are calculated by implementing the  $Z$ - $R$  relationship [Marshall and Palmer, 1948] with coefficients  $\alpha=300$  and  $\beta=1.4$ . Next, based on rainfall rate values, a mean

aerial precipitation  $MAP$  [mm/h] for all 24h rainfall cases with 6-minute intervals is calculated as:

$$MAP_i = \frac{1}{N} \sum_{n=1}^N RR_n \quad (3.10)$$

where,  $i$  is an index of a given time stamp and  $N$  is the number of 100 m x 100 m resolution cells constituting the domain of interest.

Table 3.2 shows relative errors in the mean aerial precipitation [%] over the area of interest, denoted in Figure 3.1 as HUC<sub>123</sub>.

Similarly to the results reported for reflectivity, we color-coded the results to allow for faster analysis of the presented results.

#### 3.4.1 Spatial scaling of the single-radar attenuation correction results

In many hydrologic studies involving radar rainfall data, depending on the focus of a research investigation and available radar coverage, the targeted area of interest can vary from a single point (e.g., radar vs. rain gauge comparison) to large watersheds or even continents. As depicted in Figure 3.1, we compared the corrected reflectivity values for a range of domains from a set of point locations, through three watersheds within the area of interest, to the full area of interest in order to analyze how the results of individual attenuation correction methods are affected by the size of the area of interest.

We reported both the mean and standard deviations of the difference between horizontal reflectivity estimates and the “true” reflectivity. Results for the three selected watersheds (HUC<sub>1</sub>, HUC<sub>2</sub>, and HUC<sub>3</sub>) are presented in Tables 3.3-3.5. Tables 3.6-3.8 summarize the results for the three individual, single-point locations (P<sub>1</sub>, P<sub>2</sub>, and P<sub>3</sub>).

As previously stated, the results based on reflectivity estimates are supplemented with mean aerial precipitation results. The results for watersheds HUC<sub>1</sub>, HUC<sub>2</sub>, and

HUC<sub>2</sub> are summarized in Tables 3.9-3.11, and results for single-point locations P<sub>1</sub>, P<sub>2</sub>, and P<sub>3</sub> are summarized in Tables 3.12-3.14.

### 3.4.2 Range dependent accuracy of the single-radar correction methods

Pulses of electromagnetic energy emitted from a radar's antenna are concentrated into a narrow beam. As the energy travels away from the radar, its density decreases due to beam broadening. The further away from the radar, the larger the physical dimensions of a radar range gate. This increasing volume and decreasing energy density causes the quality of radar rainfall estimates to be strongly range-dependent [Krajewski *et al.*, 2011]. Attenuation correction methods applied to a single radar reflectivity field may exert additional range-dependent inaccuracy. In this subsection, we examine how the accuracy of reflectivity estimates is affected by individual attenuation correction methods or, in other words, what constitutes the range dependent characteristic of the correction methods.

For the text, we selected a single, simulated rainfall event equivalent to ~4 hours of moderate rainfall. The simulation included four network radars collecting horizontal reflectivity data on a polar grid. We compared the collected reflectivity values to the "true" reflectivity, and the results are presented below. In Figure 3.3 and Figure 3.4, we present the results for each of the four single-radar attenuation correction methods as compared to the "true" reflectivity values. The reported values are those of mean and standard deviation of the  $\epsilon_z$  value, as defined in Equation 3.9.

### 3.4.3 Performance analysis of the single radar attenuation correction methods

We used the simulator to analyze the attenuation correction methods based on polarimetric and non-polarimetric variables. In the analysis, we examined how the corrected reflectivity values compare to the "true" reflectivity and how differences in

reflectivity estimates translate to differences in mean aerial precipitation over a selected domain of interest.

To evaluate the effect of the size of the domain of interest, each attenuation correction method was employed to provide corrected reflectivity and corresponding rainfall rates for single point locations and watersheds of varying sizes.

Additionally, we looked at how the accuracy of simulated radar-centric estimates changes with the distance from the radar.

Based on the presented results, we found that for the given data set and the described simulation conditions, the polarimetric methods with constraints on the propagation phase shift outperformed the non-polarimetric method and the method based on the  $A_H-K_{DP}$  relationship only. As the focus moved from a single point to watersheds increasing in size, the methods stabilized their performance. Single point estimates were often affected by their distance to a given radar. Reporting the results based on reflectivity and rainfall rate showed how reflectivity estimates and corresponding errors translate to errors in mean aerial precipitation. Our analysis of range-dependence revealed that as we move further and further away from the radar, the performance of all methods drops significantly. The dominant factor behind the performance decrease is the beam's broadening.

Using the obtained results, we will now briefly discuss important pros and cons of the tested methods to summarize their performance in our analysis.

The first method, referred to as the “forward” algorithm, is a non-polarimetric method based on a parametric  $A_H-Z_H$  relationship. The greatest disadvantage of the method is its instability. In cases of heavy rainfall, the method significantly overestimated attenuation values. To control the instability, a maximum PIA value was introduced. For any given ray, when the integrated path attenuation reached 60 dBZ, the method was no longer applied. An example of instability in the “forward” method is

presented in Figure 3.5. In light rain conditions, no significant overestimation occurred, and the method showed good performance.

The second method, based on a constrained differential propagation phase  $\Phi_{DP}$  shift, consistently showed good performance in the test regardless of radar location within the spatial domain and simulated rainfall conditions. This method combines small mean difference between the “true” and corrected reflectivity values, with standard deviation being among the smallest observed. This solid performance has been noted for single-point locations as well as for larger areas of interest. Using a single value for the parameter  $\alpha$  in the correction method based on Equation 3.4 proved to be a better strategy than allowing for the parameter to obtain an “optimal” value, as was the case for method 3.

As previously mentioned, the difference between the second and the third method is that in the third method, parameter  $\alpha$  takes on an optimal value based on the procedure described in 3.3.3. During the course of this study, we found that estimating the optimal value for the parameter  $\alpha$  has its limitations and can occasionally lead to erroneous results. Based on the simulations, the method consistently underestimated the results. In the post-processing of the simulated data, it has been established that the reason for underestimation is the residual backscatter differential shift  $\delta$  of the differential propagation phase profiles, as described in section 2.2.3. In the following section, we illustrate the process of optimal estimation of the parameter  $\alpha$  and how the simulated results are affected by differential backscatter differential shift  $\delta$ . Figure 3.6 depicts a series of differential phase shift profiles. The “true” differential phase shift and the simulated and consequently smoothed profiles are accompanied by the “constructed” profiles for a range of  $\alpha$  parameters. As the value of the parameter  $\alpha$  changes, the “constructed” profiles of the differential phase shift change their shape and the corresponding error (Equation 3.7) takes on a different value. Figure 3.7 illustrates a history of error values for a range of parameter  $\alpha$  values. It can be observed that there is

a local minimum that corresponds to the optimal “constructed” differential phase shift profile. Since the residual backscatter differential shift has a tendency to “shift” differential phase shift profiles, the resulting optimal parameter is often smaller than the “true” optimal parameter value. Smaller values of parameter  $\alpha$  will lead to underestimation of the corrected reflectivity values. It is outside of the scope of this work to explore how to prevent the non-optimal estimation of the parameter  $\alpha$ .

The last method is based on the  $A_H - K_{DP}$  relationship. The profiles of  $K_{DP}$  are calculated from the smoothed propagation phase shift, as described in 2.3.3. The smoothing of  $K_{DP}$  aims to remove the naturally high variability of the specific differential phase as well as to minimize the effect of the backscatter differential phase shift  $\delta$ . The accuracy of the presented attenuation correction method is strongly related to the process of calculating  $K_{DP}$  as well as to the selection of the relationship parameters. The results obtained with this method are often close to the results based on the  $\Phi_{DP}$  constrained method.

### 3.5 Data merging methods for single-radar products

Attenuation correction algorithms and rainfall retrieval methods based on single radars do not take full advantage of the data redundancy provided by a network of radars. In the previous subsection, we showed that the performance of each attenuation correction method decreases with range as the radar beam size increases, and the energy pulse experiences cumulative attenuation effects. A single radar approach cannot handle total signal loss due to severe signal attenuation. To mitigate the total signal loss problem, networks of radars have been suggested [e.g., *Krajewski and Smith, 1995 and 2002*]. The multiple view of the domain of interest provided by a network offers a new way to address the attenuation correction problem. Generating a network-based product by merging single radar data during post processing can lead to increased spatio-temporal

characteristics of the product and can help eliminate gaps that result in the total signal loss.

Selecting an optimal way to merge radar data is significant and must consider a number of factors such as the size and shape of the domain of interest, number and location of the network's nodes, and the resolution and type of the desired rainfall product. Different merging techniques may perform differently depending on individual rainfall event characteristics or the geographic location of the network. In the current section, we use the polarimetric radar network simulator to evaluate a subset of possible radar data merging techniques. Our goal is to assess how different merging techniques can improve the overall quality of reflectivity and rainfall estimates over a given domain of interest. We start by proposing five different data merging strategies that will be used in the simulation.

### 3.5.1 Inverse-distance weighting [Method 1]

The first merging method is the inverse distance weighted interpolation method [Shepard, 1968], where a value at a given point is calculated as a weighted sum of inputs from individual radars. Based on distances separating radar nodes from each point within the domain of interest, weights are calculated using the following formula:

$$w_i = \frac{h_i^{-p}}{\sum_{i=1}^n h_i^{-p}} \quad (3.11)$$

where  $h_i$  is the distance from the radar and  $p$  characterizes the weighting function. To increase the weight of radars being closer to a point of interest, we use  $p=2$  as opposed to a simple linear weighting.

### 3.5.2 Minimum distance [Method 2]

Assuming that the closer the radar is to the area of interest the more precise are its estimates, we propose the “minimum distance” method as one viable data merging option. Any point from within the area of interest will be assigned the value observed by the radar that is the closest in distance to the location. The advantage of this method is its simplicity and how fast it can be implemented in an operational setting. Radar’s spatial resolution is the highest close to the radar and it decreases as we move away, but one needs to remember that most of the ground clutter and anomalous propagation can be observed at close ranges. Also, it is very likely that for a given rainfall event, even the closest radar may suffer a considerable amount of attenuation. Those contradicting factors make the method particularly worth examining in a simulation setup to see how it compares to other merging techniques.

### 3.5.3 Minimum PIA [Method 3]

As signal attenuation remains one of the most important factors affecting the quality of radar rainfall estimates at X-band frequencies, we include a method that for any point within the domain of interest will use observations made by the radar that has suffered the least amount of attenuation on its path to the location. The amount of attenuation can be calculated either by using the  $A_H - Z_H$  or the  $A_H - K_{DP}$  relationship. To illustrate how the minimum PIA method can improve the merging process, a single input rainfall field has been analyzed (refer to Figure 3.8, panel A) in the simulator and the contributions of individual radars from the minimum PIA method are shown in Figure 3.8, panel B. The results are compared to the minimum distance method presented in panel C. Four radar locations are denoted in the Figure as R1, R2, R3, and R4. Contributions of the individual radars to the rainfall product (limited to the HUC<sub>123</sub> watershed only) are color-coded. Heavy rainfall occurring in front of the radar denoted as R3 caused the minimum PIA method to eliminate its contribution to the final product.

The selected case serves only as an example, as the contributions of individual radars in the minimum PIA method will vary greatly for each rainfall input field.

#### 3.5.4 PIA-based weighting [Method 4]

Similarly to the inverse-distance weighting method, we implemented a weighting method based on the total path integrated attenuation (PIA) as experienced by individual radars. The attenuation estimates can be based on the  $A_H - Z_H$  or the  $A_H - K_{DP}$  relationship. Including contributions from all available radar nodes can potentially have an inverse effect on the quality of the product as we may be mixing “the good” with “the bad” in the process, and the overall performance of the method will be investigated using the simulator.

#### 3.5.5 Maximum value [Method 5]

The maximum value method, as the name suggests, compares input from all available radar nodes and selects the maximum reflectivity value as the final value for a given location. The argument behind the method is that when considering all radars, the one with the highest reflectivity value suffered the least attenuation and, hence, can provide the most valuable contribution. For radar reflectivity values corrected for attenuation, the method is expected to be biased and to lead to an overestimation of the results. For the purpose of this study, we will employ the method to reflectivity fields that were both corrected and uncorrected for attenuation.

The simulator served as a platform for testing data merging techniques. The presented set of merging methods can be expanded to include additional methods that are limited in their character only by the user’s initiative.

### 3.6 Results for network merging methods

Using the simulation setup presented in section 3.2, we consecutively applied all of the presented merging methods to the single radar reflectivity fields from all four

radars constituting the network. As previously described, we assessed the methods by evaluating their performance in reflectivity estimation as well as relative error in mean aerial precipitation. In Table 3.15, we present the mean difference and standard deviation of reflectivity as compared to the “true” reflectivity. The computed reflectivity values are restricted to those within the watershed  $HUC_{123}$  area only. The corresponding relative error (%) in mean aerial precipitation is presented in Table 3.16. Results for the individual watersheds ( $HUC_1$ ,  $HUC_2$ , and  $HUC_3$ ), together with observations for single locations  $P_1$ ,  $P_2$  and  $P_3$  for both reflectivity and mean aerial precipitation, are presented in Tables 3.17-3.28. To allow for efficient analysis of the presented results, we color-coded the best and the second best methods using the following color scheme:

-  - best result,
-  - second best.

In the tables, the attenuation correction methods are marked:  $Z_{Hm}$  – no attenuation correction applied,  $Z_{H1}$ ,  $Z_{H2}$ ,  $Z_{H3}$ ,  $Z_{H4}$ , and  $Z_{H5}$  – as described in section 3.3. The data merging methods are denoted:  $M_1$ ,  $M_2$ ,  $M_3$ ,  $M_4$ , and  $M_5$  (refer to section 3.5).

### 3.6.1 Performance analysis of the data merging methods

In an operational setting, time differences between radar products coming from individual network nodes are highly probable. Depending on the type of rainfall event and the network’s configuration, temporal differences could have a significant impact on the quality of the merged products and how individual merging methods perform. It is important to note that in the presented simulations we consider all radar observations to be synchronized between the nodes and instantaneous for the whole radar coverage.

The analysis of the results includes a qualitative comparison (selection of the best overall method) and a quantitative comparison between the merged products and the single radar approach.

Comparison of the results obtained for reflectivity values and results based on rainfall rates revealed the importance of the choice of the evaluation criterion. The difference in reflectivity expressed in  $dBZ$ , its mean, and standard deviation are often used in radar observations. The obvious disadvantage of this evaluation method is its non-linear relationship with rainfall rates. Across all simulated methods, the method providing the minimal mean difference was often not the method offering the smallest standard deviation range. This indicated that the selection of the merging method should be dictated by the immediate goal of the operation, which is to be either minimizing the mean differences or the standard deviation of the product. Based on the results obtained for the reflectivity estimates, we can conclude that the selection of the optimal merging method is strongly influenced by the previously applied attenuation correction strategy. When minimizing mean difference in reflectivity, no single method proved to be the best. Among the simulated methods, only the method based on weighted PIA consistently showed good performance. The distance weighting method (Method 1) consistently provided the best results for minimizing the standard deviation of reflectivity fields.

Supplementing the results based on reflectivity values with results based on rainfall rate showed that the non-linearity of the  $Z$ - $R$  relationship can affect the obtained results. For simulations focusing on mean aerial precipitation, the results showed a performance that is consistent with the methods based on PIA (minimum PIA and weighted PIA).

The size of the domain of interest (single point vs. watershed) was not a major factor affecting the results for rainfall rate based results.

Quantitative analysis shows that merging methods provided a significant decrease in the standard deviation of the obtained results when compared to single radar estimates. The methods based on minimum and weighted PIA also resulted in a significant decrease in the mean error value for both reflectivity- and rainfall rate-based results.

Overall, the merging process can significantly improve the quality of radar-based rainfall products. The presented results indicate that the weighting methods (both for reflectivity and rainfall rate products) and the minimum PIA method are the best among those tested.

In summary, the selection of the “optimal” merging technique should be based on a number of factors, including the physical configuration of the network, the desired rainfall product, and the applied attenuation correction methods. The polarimetric radar network simulator presented in this work provides a cost-effective means of testing different merging methods in a synthetic manner, but the accuracy of the obtained results must be validated by analyzing radar rainfall data coming from a network of radars.

### 3.7 Network based attenuation correction method

Previously, a number of single-radar attenuation correction methods have been evaluated using the simulator. In section 3.6, we examined how different data merging strategies can affect the quality of the network-based rainfall products. Among the analyzed, single radar attenuation correction methods, the “forward” method, also referred to as Method 1, showed promising performance in light rainfall and at ranges relatively close to the radar site. At longer ranges and in cases of moderate to heavy rainfall, the method can become instable and result in severe overestimation of reflectivity and, consequently, rainfall rate values. This instability in attenuation correction can be avoided if a total path attenuation value at far ranges ( $r_0$ ) from the radar can be obtained. In previous studies, different authors have applied the method in which the PIA value was approximated based on a point of known characteristics (building, terrain clutter, etc.) [e.g., *Delrieu et al.*, 1997, 1999; *Serrar et al.*, 2000]. The analytical solution for this approach has been proposed by *Marzoug and Amayenc* [1994] where the corrected reflectivity value is calculated based on intrinsic reflectivity  $Z_a$  and a known value of path integrated attenuation  $A(r_0)$ :

$$Z(r) = \frac{Z_a(r)}{\left[ A(r_0)^{1/\beta} + \frac{0.2 \ln(10)}{\beta} \int_r^{r_0} \left( \frac{Z_a(s)}{\alpha} \right)^{1/\beta} ds \right]^\beta} \quad (3.12)$$

The algorithm is also referred to as the “backward” method, and its main drawback is that a reliable estimation of the PIA value at a range  $r_0$  has been a limiting factor in a broader use of the method. In the case of a network of radars, estimates of PIA can be obtained using data from all radar networks rather than from a single point. Also, a network is capable of providing estimates for a range of locations within the domain of interest and, consequently, provides a PIA reference for any radar ray under consideration. In the following, we use the simulator to evaluate the “forward” method in a networked environment. The methodology for selecting the source of PIA information (one of the four radars in the discussed design) includes selecting a rectangular bounding box enclosing the domain of interest. For any given ray passing over the domain of interest, the location of the PIA is on the cross-section of the bounding box and the radar ray. PIA information is then selected from a network node closest to the cross-section. A schematic illustration of the process is presented in Figure 3.9.

### 3.7.1 Simulation results for the network based attenuation correction method

There are many possible strategies to obtain the PIA value for any given radar ray based on a network of radars. We have decided to use the previously obtained results as guidance in obtaining the most reliable PIA information. First, reflectivity values for each of the four radars were corrected using the expression in Equation 3.4 (the attenuation correction Method 2). Next, data from all four radars were merged using the weighted distance method (data merging Method 1). The above combination was selected from the set as the one providing the best results, both in terms of minimizing

mean and standard deviation for reflectivity based results. Finally, the “backward” attenuation correction method was applied to all four radars. The results for difference in reflectivity, based on data within the  $HUC_{123}$  domain of interest, are presented in Table 3.29. Corresponding results based on error in mean aerial precipitation are summarized in Table 3.30. The presented correction method has been denoted as  $Z_H 5$ . For comparison, the previously presented single radar attenuation correction methods are also presented in Tables 3.29 and 3.30.

After obtaining results for individual radars using the “backward” algorithm, data from all radars were merged using all previously discussed merging methods to create a set of final network products. Since, in theory, the merging process should improve the quality of the network product and provide better reflectivity values, the method has the potential to be applied in an iterative scheme, where the final product is used as the basis for PIA information when correcting individual radars using the method. To verify whether the results will improve with every iteration step, we employed the method in an iterative approach. Table 3.31 summarizes the reflectivity results for the watershed  $HUC_{123}$ , while Table 3.32 focuses on the mean aerial precipitation results for individual radars. Tables 3.21 and 3.22 present previously obtained results for simulated merging methods results for comparison. The merged product obtained in the first iteration step is denoted as  $Z_{H5}$ , and the results after two iterations are denoted with the symbol  $Z_{H5}'$ .

### 3.7.2 Performance analysis of the network based attenuation correction method

The “backward” method was applied to all four radars, with the PIA information based on the merged product, obtained by individually correcting all four radars for attenuation using the constrained method with a fixed parameter  $\alpha$ , and all available data later merged using the distance weighting method. By analyzing the results based on the differences in reflectivity values (Table 3.29), the method was shown to perform better

than the “forward” algorithm, but it was outperformed by the polarimetric methods based on a differential phase shift. On the other hand, when comparing the results presented in Table 3.30 and obtained for relative errors in mean aerial precipitation, the method is comparable to the polarimetric methods and in some cases proved to outperform both non-polarimetric and polarimetric, single radar methods.

The single radar product obtained in the simulation has been consecutively merged using all previously presented network merging techniques. The conclusion after applying the merging procedure is that when considering a network of radars, the polarimetric methods should be used to correct for attenuation of individual radars before the merging procedure is applied in order to improve the overall quality of network products. The “backward” method is very sensitive to errors in the PIA value. In the current simulator implementation, the PIA error is a consequence of the random fluctuations in the simulated reflectivity values and the quality of the attenuation correction method applied to single radar estimates. As presented in section 2.3.2, fluctuations in reflectivity are modeled to have the mean value equal to zero and a standard deviation  $\sigma=1$  dBZ. The standard deviation of reflectivity values directly translates to the accuracy of the PIA value used in the attenuation correction process and can lead to significant overestimation or underestimation of individual radar reflectivity profiles.

Applying the “backward” method in an iterative scheme, where the source of the PIA information was based on the merged product obtained in the first iteration of the procedure, did not improve the overall results. The merged product has a limited coverage of the spatial domain. Implementation of the “backward” algorithm requires high quality PIA information from locations outside of the domain of interest. With the limited spatial coverage of the merged product, the method could not be implemented successfully into an iterative scheme.

### 3.8 Summary of Chapter 3

In this chapter, we used the polarimetric radar simulator described in Chapter 2 to evaluate a number of attenuation correction strategies.

First, we simulated a set of single radar methods. Each of the methods was used to correct reflectivity values for four radars located within the spatial domain. To evaluate the methods, we compared the mean difference and standard deviation in reflectivity [dBZ] estimates between individual radars and the “true” reflectivity values. The results were supplemented with the mean and standard deviation of relative errors in mean aerial precipitation [mm/h] estimates. Based on the obtained results, we concluded that polarimetric attenuation correction methods based on a constrained differential phase shift outperform the non-polarimetric methods. In addition, the method described as the constrained method with optimal  $\alpha$  parameter did not perform as well as expected due to inherent problems with the removal of backscatter differential phase shift  $\delta$  from  $\Phi_{DP}$  profiles. It is also important to note that all single radar attenuation correction methods suffered from range dependent errors to a similar extent. The quality of products decreases as the distance from a radar increased. When analyzing how the size of the domain of interest affects the obtained results, we looked at simulation results obtained for single point locations and for watersheds of different sizes. At the single point level, the attenuation correction results were affected by the proximity to network nodes, whereas for watersheds, this effect was minimal.

Next, to test attenuation correction methods in a network environment, we used the simulator to evaluate a number of data merging strategies. The merging methods were based on a number of techniques ranging from taking a maximum available reflectivity value to more sophisticated methods like taking a combination of inputs from radars with weights based on path integrated attenuation (PIA) as experienced by individual radars. As for the single-radar methods, the results were presented for the differences in reflectivity estimates as well as for the relative error in mean aerial

precipitation. The main conclusions from the study showed that the selection of the optimal merging method depends on the assessment criterion (difference in reflectivity versus relative error in mean aerial precipitation). Reflectivity-based results indicated that to minimize mean differences in reflectivity, one needs to take into account which method has been used to correct reflectivity of individual radars before selecting the merging procedure. For mean aerial precipitation, methods based on PIA consistently outperformed other simulated methods. Quantitative analysis revealed that, when applied to single radar data, merging can significantly improve the quality of the network product both by minimizing the mean differences and the standard deviation of the simulated values. Merged products showed less sensitivity to the size of the domain of interest when compared to the single radar products.

Lastly, we proposed a network-based attenuation correction method. The method is based on the “backward” algorithm originally proposed by *Marzoug and Amayenc* [1994], and it relies on the accurate estimation of the path integrated attenuation (PIA) for every radar ray at distances considered to be “far ranges” (behind the storm). In reality, obtaining accurate PIA information for all radar rays is very difficult, if not impossible, due to the limited number of targets that could be used as a reference. For a network of radars, the PIA information can be obtained as a network product. The validity of this approach has been evaluated using the simulator. The method showed good performance when compared to single radar products, but the methods based on differential phase shift and merging using minimum and weighted PIA information proved to be a better choice. In an iterative scheme in which the final product becomes the source of PIA information, the method did not improve its performance mostly due to the limited coverage of the merged product.

The main conclusion from the presented set of simulation is that selection of the optimal attenuation scheme for a network of radars is significant. Many factors can contribute to the quality of the final rainfall product. The simulator is a cost-effective

way to test how a network's physical configuration (location of network's nodes, scanning strategy, radar technical specifications), selected attenuation correction algorithm, data merging scheme, rainfall retrieval methods, or the combination of the above interact in the process of generating a network rainfall product. To fully validate the results of the simulations, a set of experiments utilizing a network of polarimetric X-band radars accompanied by a range of ground validation instruments (rain gauges, disdrometers) must be performed. Only a long-term experiment that captures a variety of rainfall events can provide sufficient data to verify the findings obtained using the simulator. Information from such experiments could be used to eliminate some of the simulator's limitations and contribute to further development of the simulator.

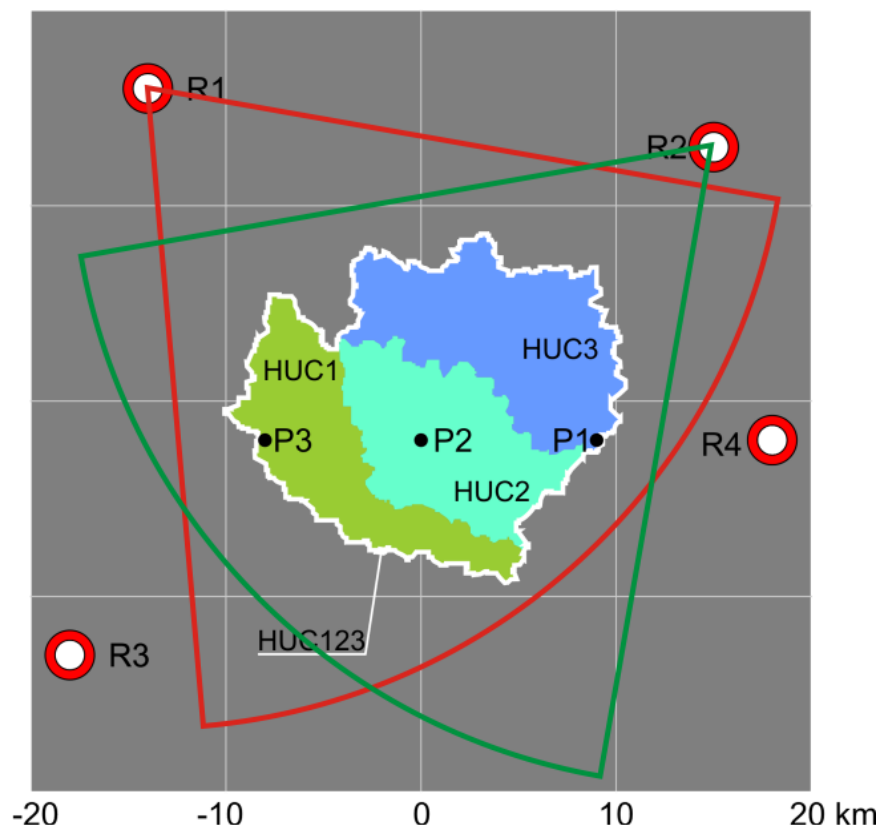


Figure 3.1: Network setup with indicated radars' locations, sample scan coverage and an outline of the watersheds of interest and the point locations of interest.

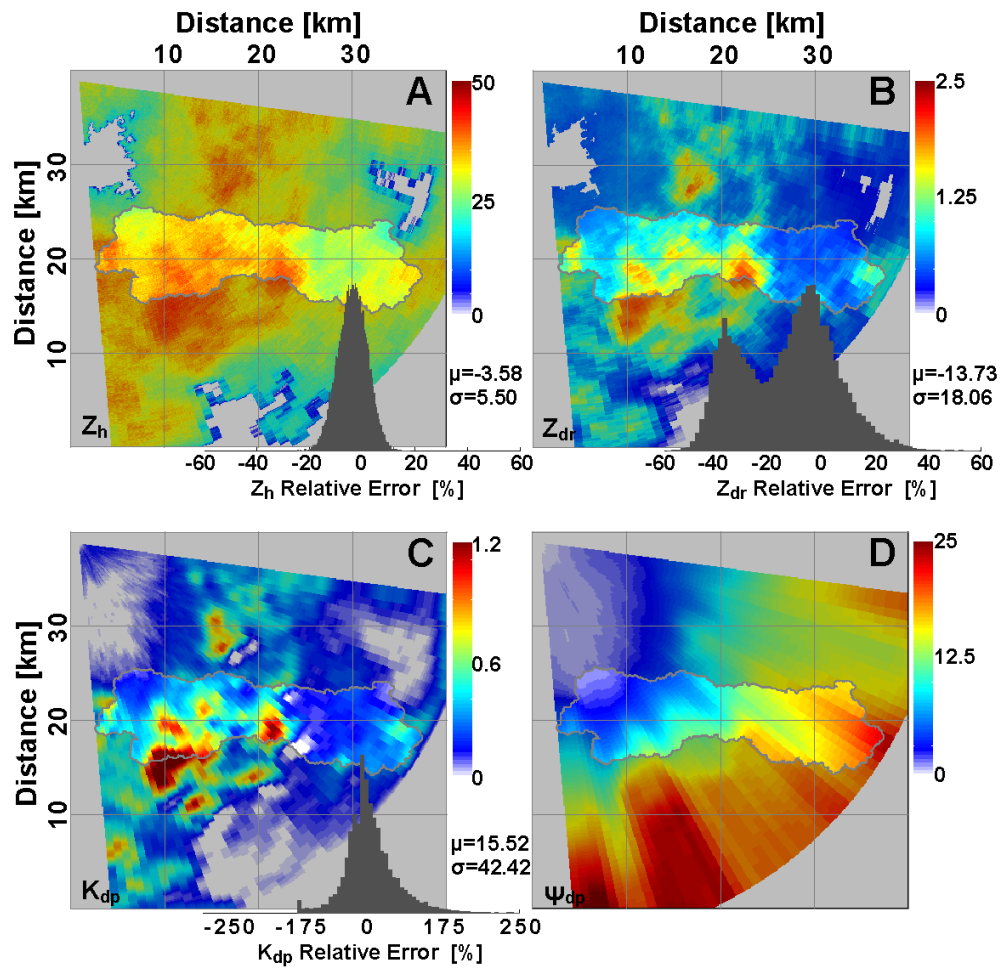


Figure 3.2: A set of polarimetric variables as simulated for a single radar.

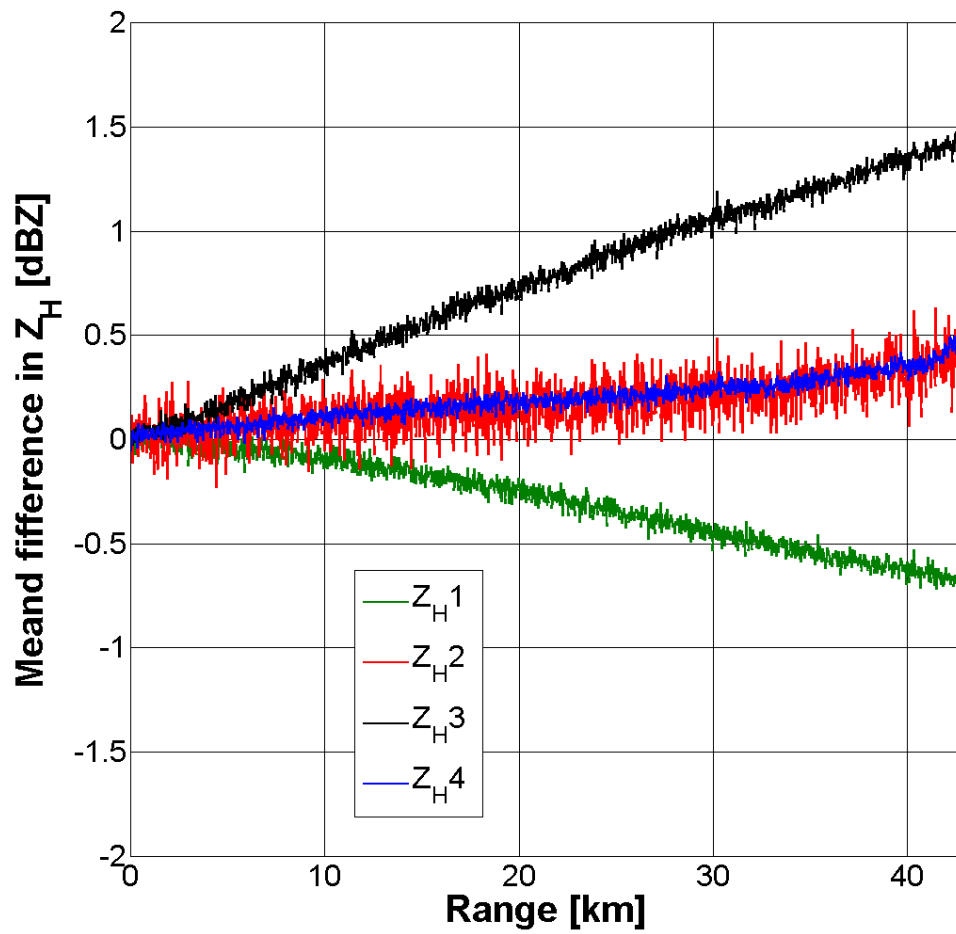


Figure 3.3: Range profiles of mean difference in reflectivity values for single-radar attenuation correction methods.

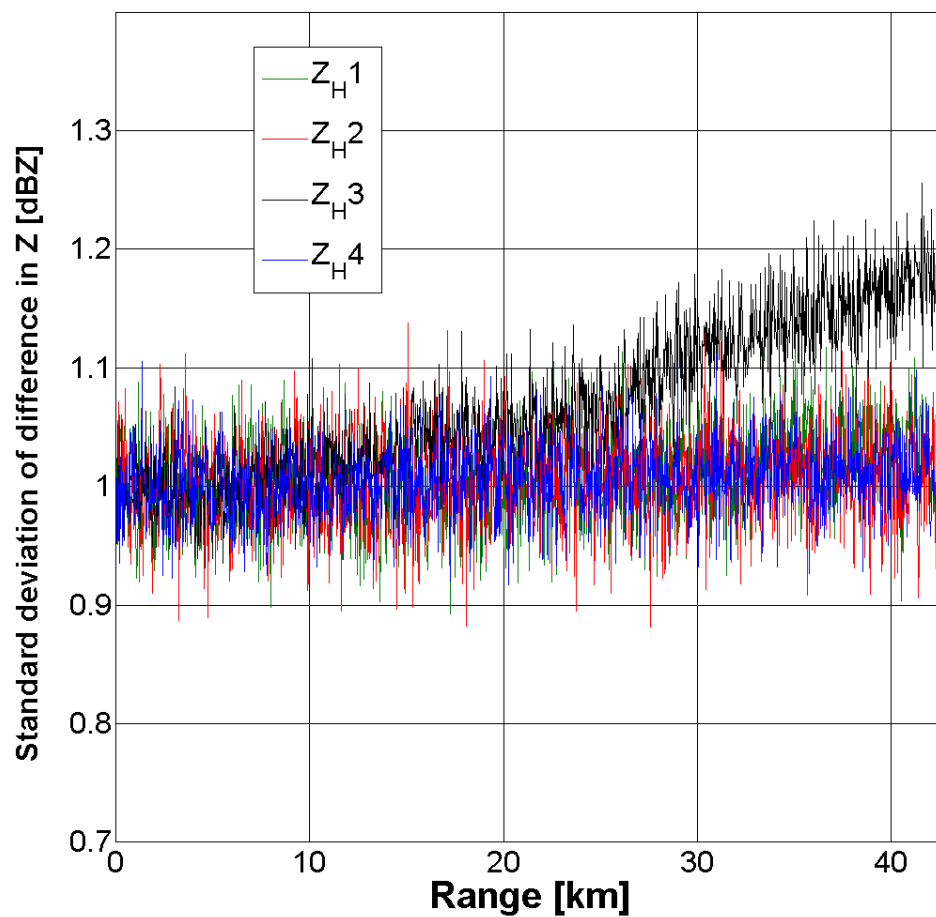


Figure 3.4: Standard deviation of the difference in reflectivity values for single-radar attenuation correction methods.

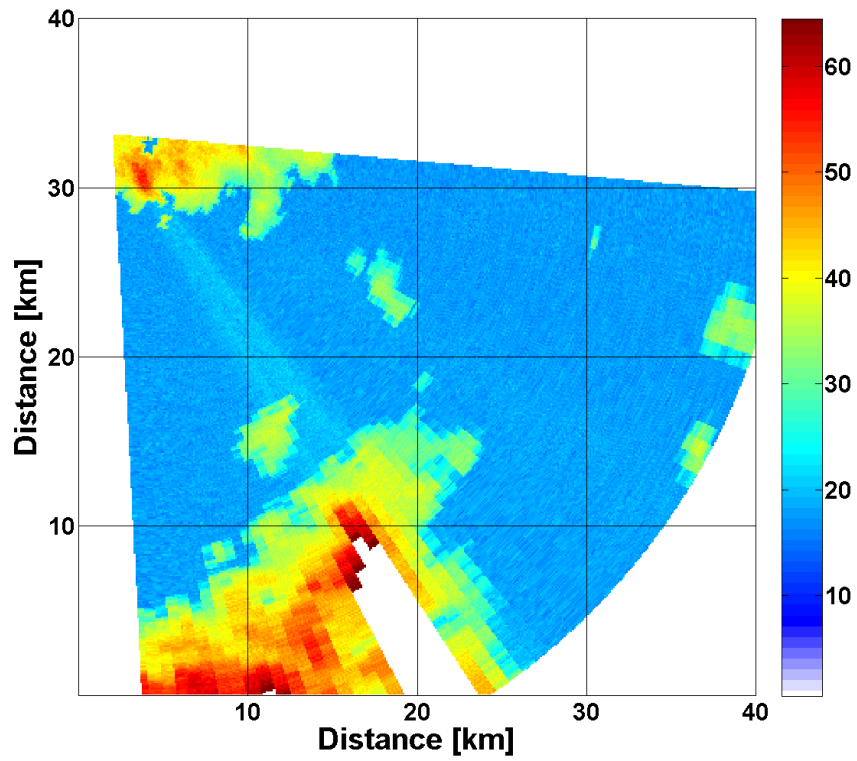


Figure 3.5: Reflectivity field corrected using the “forward” method. Instability of the method can be seen after radar beam passes high intensity region.

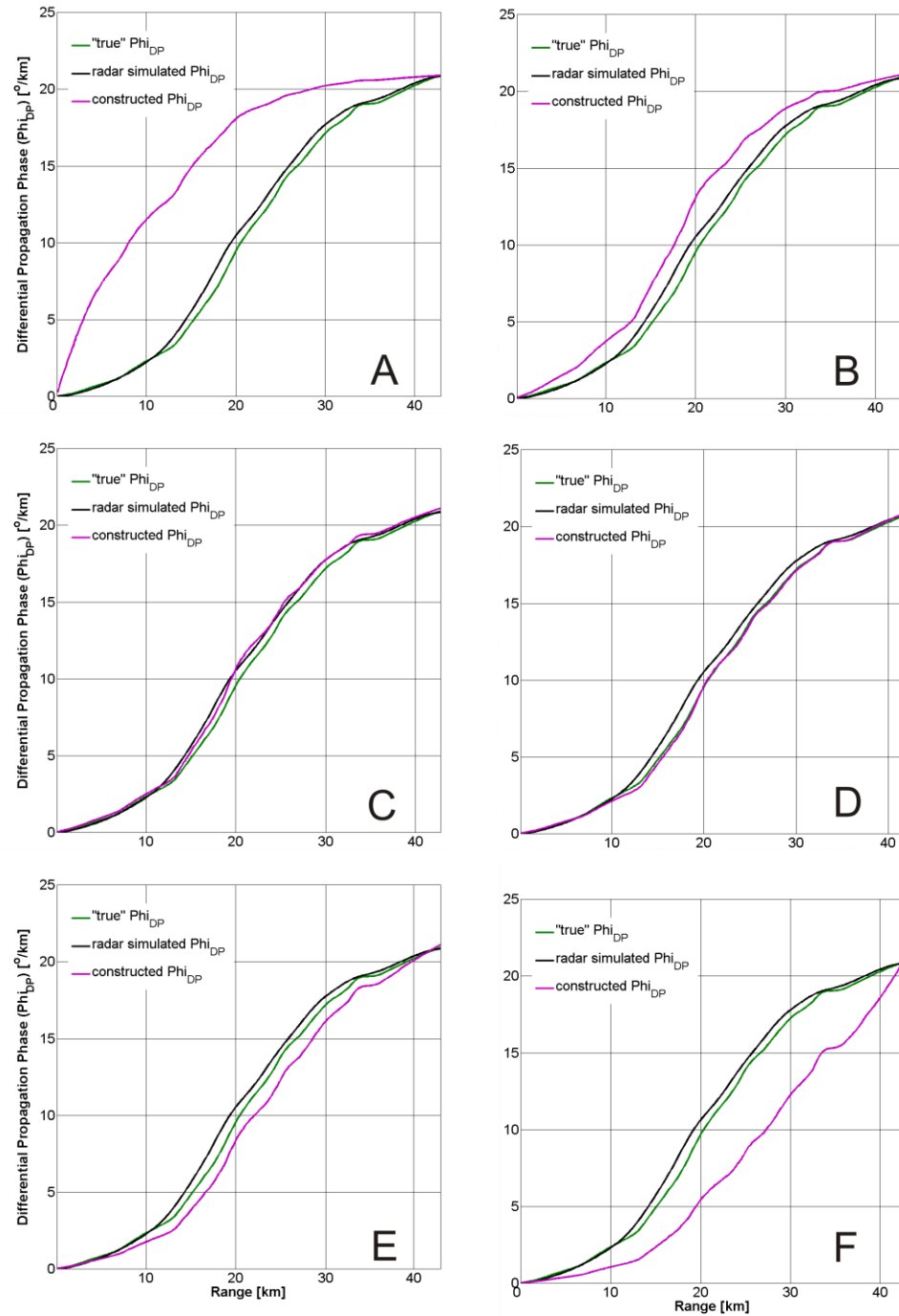


Figure 3.6: The process of estimating the "optimal"  $\alpha$  parameter. The "true" profile of differential phase shift (green line) is presented together with the profile obtained in simulations (black line) and the profile estimated using a given  $\alpha$  parameter (purple). A)  $\alpha=0.03$ , B)  $\alpha=0.2$ , C) "optimal"  $\alpha=0.27$ , D)  $\alpha=0.34$ , E)  $\alpha=0.39$ , F)  $\alpha=0.5$ .

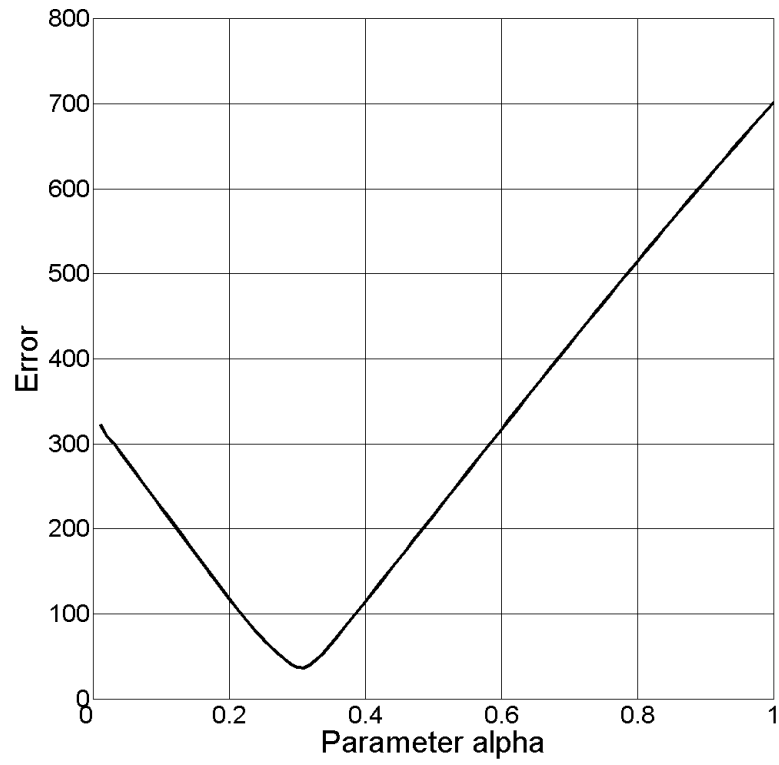


Figure 3.7: Error value calculated based on Equation 3.7 as a function of parameter  $\alpha$ .

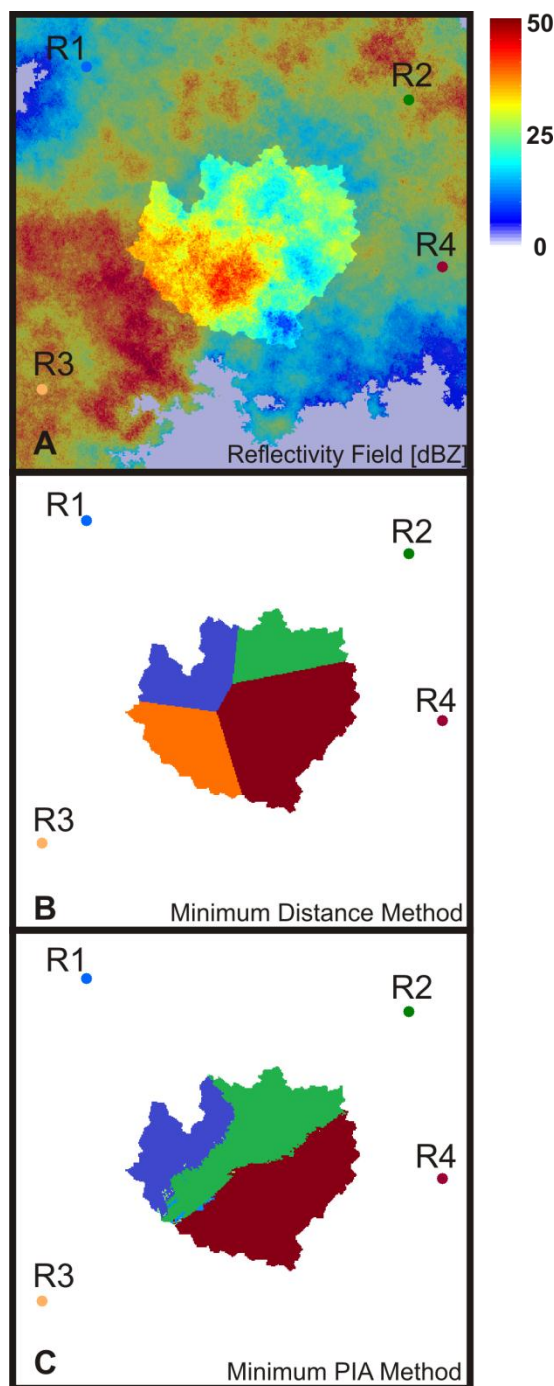


Figure 3.8: Comparison of network node contributions between the Minimum Distance method and the Minimum PIA method. A) Reflectivity field [dBZ], B) Minimum Distance method contributions, C) minimum PIA Method contributions

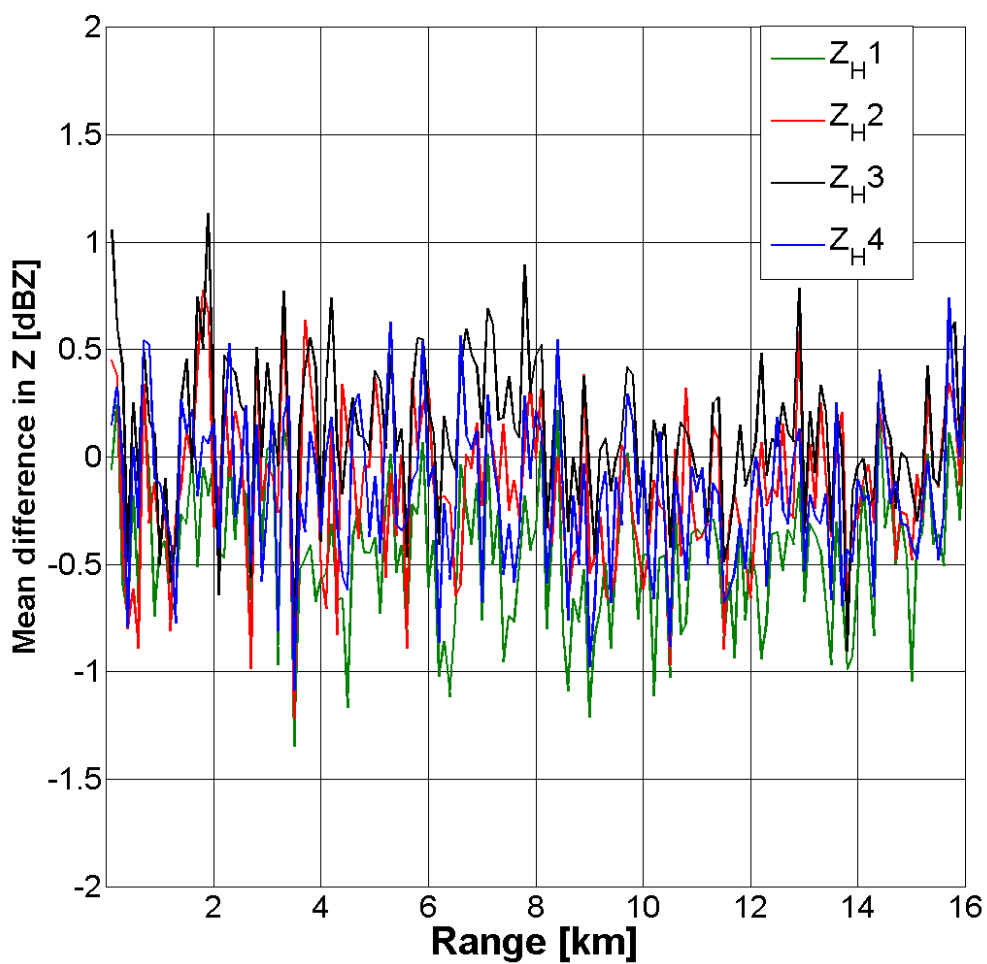


Figure 3.9: Range profiles of mean difference in reflectivity values for merged products.

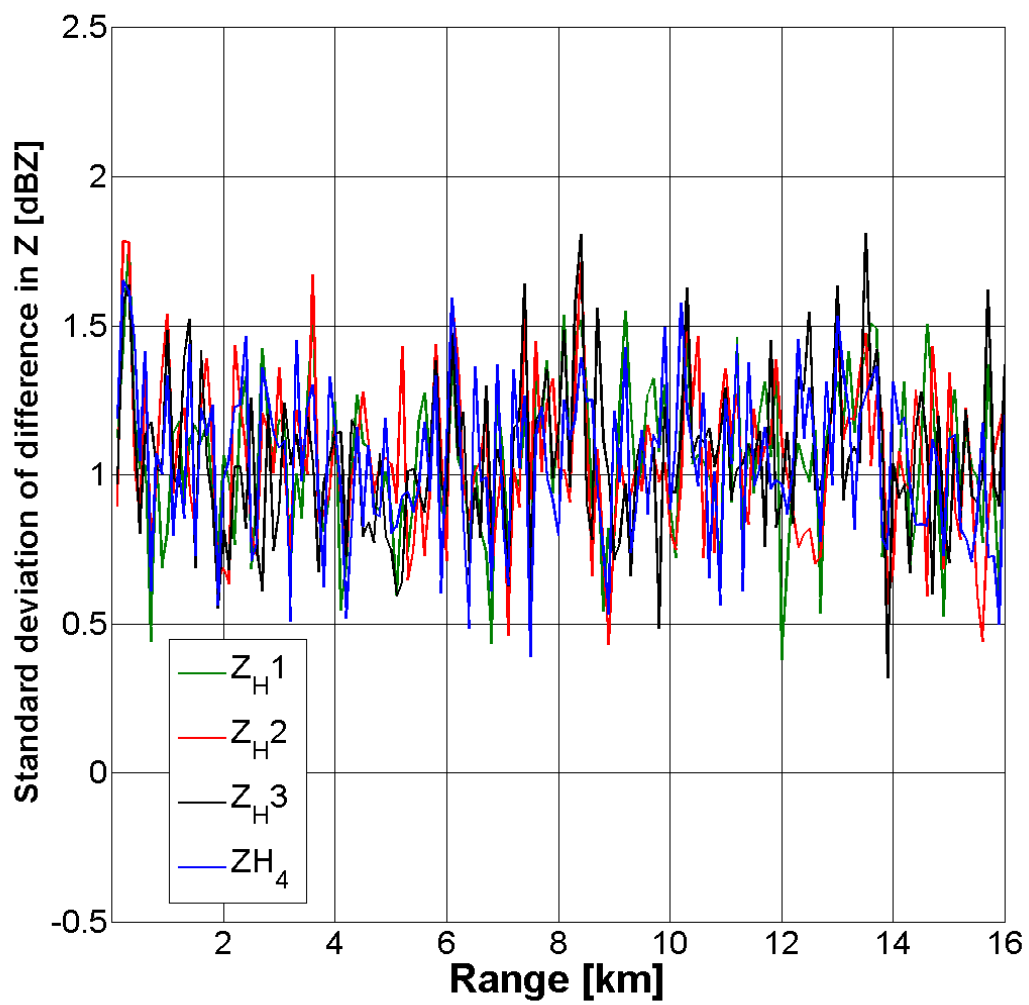


Figure 3.10: Standard deviation of the difference in reflectivity values for merged products.

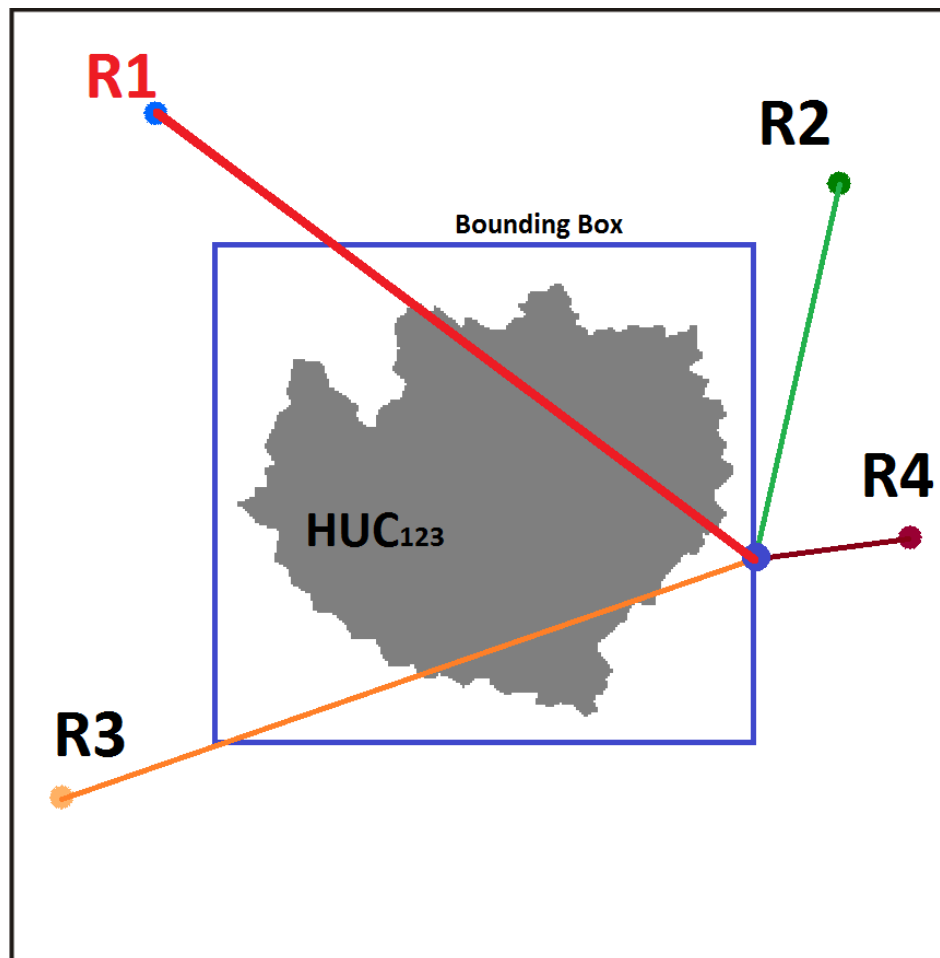


Figure 3.11: Schematic illustration of the "Backward" method, for network-based attenuation correction. R1, R2, R3, R4 are locations for network nodes. For each of the marked radar rays, the PIA value is estimated.

Table 3.1: Results summary based on single-radar correction methods for the area of interest (HUC123).

	MEAN REFLECTIVITY DIFFERENCE $\mu(\epsilon_Z)$ (dBZ)				
	$Z_{Hm}$	$Z_H 1$	$Z_H 2$	$Z_H 3$	$Z_H 4$
$R_1$	-1.09	0.37	-0.07	-0.42	-0.07
$R_2$	-0.97	0.37	-0.03	-0.32	-0.03
$R_3$	-1.26	0.28	-0.15	-0.52	-0.15
$R_4$	-0.85	0.30	-0.05	-0.32	-0.04
	STANDARD DEVIATION $\sigma(\epsilon_Z)$ (dBZ)				
	$Z_{Hm}$	$Z_H 1$	$Z_H 2$	$Z_H 3$	$Z_H 4$
$R_1$	1.88	1.48	1.45	1.58	1.46
$R_2$	1.77	1.43	1.35	1.51	1.37
$R_3$	1.89	1.46	1.39	1.57	1.41
$R_4$	1.71	1.38	1.39	1.50	1.40

Table 3.2: Results summary based on single-radar correction methods for the area of interest (HUC123).

	MEAN RELATIVE DIFFERENCE in <b>MAP</b> $\mu(\Delta R)$ [%]				
	$Z_{Hm}$	$Z_H 1$	$Z_H 2$	$Z_H 3$	$Z_H 4$
R <sub>1</sub>	-17.79	8.22	-2.37	-8.00	-1.62
R <sub>2</sub>	-15.41	9.80	-1.24	-6.12	-0.55
R <sub>3</sub>	-19.98	8.32	-3.76	-9.37	-3.18
R <sub>4</sub>	-12.95	5.12	-0.98	-5.37	0.02
	STANDARD DEVIATION $\sigma(\Delta R)$ [%]				
	$Z_{Hm}$	$Z_H 1$	$Z_H 2$	$Z_H 3$	$Z_H 4$
R1	15.10	25.93	7.47	10.27	8.72
R2	14.35	40.74	7.11	10.18	7.96
R3	16.16	40.74	8.36	11.44	9.84
R4	10.52	5.24	5.07	7.44	5.43

Table 3.3: Results summary based on single-radar correction methods for the area of interest (**HUC<sub>1</sub>**).

	MEAN REFLECTIVITY DIFFERENCE $\mu(\epsilon_Z)$ (dBZ)				
	$Z_{Hm}$	$Z_H 1$	$Z_H 2$	$Z_H 3$	$Z_H 4$
$R_1$	-1.06	0.38	-0.07	-0.41	-0.07
$R_2$	-1.13	0.47	0.00	-0.33	-0.01
$R_3$	-1.12	0.20	-0.17	-0.48	-0.17
$R_4$	-1.02	0.40	-0.04	-0.36	-0.03
	STANDARD DEVIATION $\sigma(\epsilon_Z)$ (dBZ)				
	$Z_{Hm}$	$Z_H 1$	$Z_H 2$	$Z_H 3$	$Z_H 4$
$R_1$	2.08	1.53	1.47	1.63	1.50
$R_2$	1.78	1.40	1.40	1.58	1.42
$R_3$	1.95	1.52	1.37	1.54	1.40
$R_4$	1.74	1.40	1.42	1.54	1.43

Table 3.4: Results summary based on single-radar correction methods for the area of interest (**HUC<sub>2</sub>**).

	MEAN REFLECTIVITY DIFFERENCE $\mu(\varepsilon_Z)$ (dBZ)				
	$Z_{Hm}$	$Z_H 1$	$Z_H 2$	$Z_H 3$	$Z_H 4$
R <sub>1</sub>	-1.06	0.45	-0.02	-0.38	-0.01
R <sub>2</sub>	-0.97	0.40	0.00	-0.32	-0.01
R <sub>3</sub>	-1.21	0.29	-0.13	-0.50	-0.14
R <sub>4</sub>	-0.81	0.30	-0.04	-0.30	-0.03
	STANDARD DEVIATION $\sigma(\varepsilon_Z)$ (dBZ)				
	$Z_{Hm}$	$Z_H 1$	$Z_H 2$	$Z_H 3$	$Z_H 4$
R <sub>1</sub>	1.78	1.43	1.42	1.55	1.43
R <sub>2</sub>	1.72	1.34	1.34	1.50	1.35
R <sub>3</sub>	1.90	1.40	1.38	1.56	1.40
R <sub>4</sub>	1.72	1.34	1.36	1.48	1.37

Table 3.5: Results summary based on single-radar correction methods for the area of interest (**HUC<sub>3</sub>**).

	MEAN REFLECTIVITY DIFFERENCE $\mu(\epsilon_Z)$ (dBZ)				
	$Z_{Hm}$	$Z_H 1$	$Z_H 2$	$Z_H 3$	$Z_H 4$
$R_1$	-1.14	0.30	-0.11	-0.47	-0.11
$R_2$	-0.85	0.27	-0.06	-0.31	-0.06
$R_3$	-1.42	0.34	-0.15	-0.56	-0.15
$R_4$	-0.76	0.23	-0.06	-0.31	-0.05
	STANDARD DEVIATION $\sigma(\epsilon_Z)$ (dBZ)				
	$Z_{Hm}$	$Z_H 1$	$Z_H 2$	$Z_H 3$	$Z_H 4$
$R_1$	1.82	1.47	1.44	1.57	1.45
$R_2$	1.80	1.52	1.33	1.46	1.34
$R_3$	1.83	1.46	1.42	1.60	1.43
$R_4$	1.68	1.38	1.39	1.49	1.40

Table 3.6: Results summary based on single-radar correction methods for the area of interest (**HUC<sub>1</sub>**).

	MEAN RELATIVE DIFFERENCE in <b>MAP</b> $\mu(\Delta R)$ [%]				
	$Z_{Hm}$	$Z_H 1$	$Z_H 2$	$Z_H 3$	$Z_H 4$
$R_1$	-15.47	6.76	-2.72	-6.93	-2.31
$R_2$	-19.14	8.19	-2.49	-7.99	-2.24
$R_3$	-17.56	6.21	-4.29	-9.02	-4.09
$R_4$	-16.11	5.32	-2.23	-7.37	-1.51
	STANDARD DEVIATION $\sigma(\Delta R)$ [%]				
	$Z_{Hm}$	$Z_H 1$	$Z_H 2$	$Z_H 3$	$Z_H 4$
$R_1$	15.78	27.15	9.56	11.36	10.73
$R_2$	15.83	19.75	9.57	12.68	10.49
$R_3$	16.80	42.80	8.77	11.59	10.20
$R_4$	13.16	8.01	7.70	10.73	7.96

Table 3.7: Results summary based on single-radar correction methods for the area of interest (**HUC<sub>2</sub>**).

	MEAN RELATIVE DIFFERENCE in <b>MAP</b> $\mu(\Delta R)$ [%]				
	$Z_{Hm}$	$Z_H 1$	$Z_H 2$	$Z_H 3$	$Z_H 4$
$R_1$	-16.54	6.01	-2.27	-7.12	-1.79
$R_2$	-15.72	6.24	-1.97	-6.70	-1.53
$R_3$	-19.23	4.66	-4.50	-9.36	-4.24
$R_4$	-12.08	3.83	-1.67	-5.20	-1.07
	STANDARD DEVIATION $\sigma(\Delta R)$ [%]				
	$Z_{Hm}$	$Z_H 1$	$Z_H 2$	$Z_H 3$	$Z_H 4$
$R_1$	15.00	10.31	9.13	11.15	9.87
$R_2$	15.02	14.79	8.88	11.38	9.40
$R_3$	17.35	17.98	10.67	12.94	11.56
$R_4$	12.24	8.67	7.66	9.41	8.04

Table 3.8: Results summary based on single-radar correction methods for the area of interest (**HUC<sub>3</sub>**).

	MEAN RELATIVE DIFFERENCE in <b>MAP</b> $\mu(\Delta R)$ [%]				
	$Z_{Hm}$	$Z_H 1$	$Z_H 2$	$Z_H 3$	$Z_H 4$
$R_1$	-17.69	4.86	-3.74	-8.47	-3.25
$R_2$	-12.99	7.50	-2.09	-5.77	-1.70
$R_3$	-22.57	7.68	-5.22	-10.94	-4.94
$R_4$	-11.16	2.81	-1.76	-5.09	-1.13
	STANDARD DEVIATION $\sigma(\Delta R)$ [%]				
	$Z_{Hm}$	$Z_H 1$	$Z_H 2$	$Z_H 3$	$Z_H 4$
$R_1$	15.07	15.91	9.50	10.78	10.00
$R_2$	14.85	46.64	7.96	10.18	8.52
$R_3$	16.49	58.24	10.81	13.19	12.04
$R_4$	10.68	6.95	6.58	7.94	6.87

Table 3.9: Results summary based on single-radar correction methods for single point location ( $\mathbf{P}_1$ ).

	MEAN REFLECTIVITY DIFFERENCE $\mu(\varepsilon_Z)$ (dBZ)				
	$Z_{Hm}$	$Z_H 1$	$Z_H 2$	$Z_H 3$	$Z_H 4$
$R_1$	-0.85	0.32	-0.09	-0.37	-0.02
$R_2$	-1.23	0.43	-0.09	-0.44	-0.09
$R_3$	-1.02	0.36	-0.13	-0.46	-0.15
$R_4$	-0.97	0.56	0.02	-0.39	0.03
	STANDARD DEVIATION $\sigma(\varepsilon_Z)$ (dBZ)				
	$Z_{Hm}$	$Z_H 1$	$Z_H 2$	$Z_H 3$	$Z_H 4$
$R_1$	2.39	1.35	1.60	1.59	1.63
$R_2$	2.06	1.81	1.80	1.88	1.83
$R_3$	1.93	1.37	1.32	1.36	1.31
$R_4$	1.60	1.27	1.38	1.46	1.22

Table 3.10: Results summary based on single-radar correction methods for single point location ( $\mathbf{P}_2$ ).

	MEAN REFLECTIVITY DIFFERENCE $\mu(\epsilon_Z)$ (dBZ)				
	$Z_{Hm}$	$Z_H 1$	$Z_H 2$	$Z_H 3$	$Z_H 4$
$R_1$	-0.99	0.55	-0.05	-0.69	-0.04
$R_2$	-1.09	0.41	-0.04	-0.41	-0.03
$R_3$	-1.19	0.32	-0.14	-0.36	-0.22
$R_4$	-0.94	0.46	-0.04	-0.29	0.07
	STANDARD DEVIATION $\sigma(\epsilon_Z)$ (dBZ)				
	ZHm	ZH 1	ZH 2	ZH 3	ZH 4
$R_1$	1.76	1.39	1.34	1.58	1.38
$R_2$	1.71	1.22	1.23	1.54	1.32
$R_3$	2.09	1.20	1.45	1.39	1.27
$R_4$	1.70	1.20	1.14	1.40	1.27

Table 3.11: Results summary based on single-radar correction methods for single point location ( $\mathbf{P}_3$ ).

	MEAN REFLECTIVITY DIFFERENCE $\mu(\epsilon_Z)$ (dBZ)				
	$Z_{Hm}$	$Z_H 1$	$Z_H 2$	$Z_H 3$	$Z_H 4$
$R_1$	-1.32	0.43	-0.15	-0.71	-0.11
$R_2$	-0.83	0.25	-0.14	-0.31	-0.12
$R_3$	-1.61	0.36	-0.36	-0.68	-0.06
$R_4$	-0.48	0.06	-0.19	-0.23	-0.02
	STANDARD DEVIATION $\sigma(\epsilon_Z)$ (dBZ)				
	ZHm	ZH 1	ZH 2	ZH 3	ZH 4
$R_1$	1.68	1.53	1.42	1.63	1.46
$R_2$	1.70	1.26	1.24	1.32	1.27
$R_3$	2.25	1.55	1.51	1.72	1.58
$R_4$	1.38	1.19	1.19	1.22	1.23

Table 3.12: Results summary based on single-radar correction methods for single point location ( $\mathbf{P}_1$ ).

	MEAN RELATIVE DIFFERENCE in $\mathbf{RR} \mu(\Delta R)$ [%]				
	$Z_{Hm}$	$Z_H 1$	$Z_H 2$	$Z_H 3$	$Z_H 4$
$R_1$	-7.85	7.97	1.89	-2.91	3.16
$R_2$	-13.62	11.98	2.93	-2.67	2.88
$R_3$	-11.81	8.99	0.00	-5.08	-0.19
$R_4$	-11.72	12.09	2.90	-3.39	2.43
	STANDARD DEVIATION $\sigma(\Delta R)$ [%]				
	$Z_{Hm}$	$Z_H 1$	$Z_H 2$	$Z_H 3$	$Z_H 4$
$R_1$	26.31	23.59	25.85	23.06	26.26
$R_2$	29.37	33.54	31.79	28.63	30.00
$R_3$	23.30	29.07	20.74	20.42	20.38
$R_4$	23.88	24.57	23.96	24.83	20.54

Table 3.13: Results summary based on single-radar correction methods for single point location ( $\mathbf{P}_2$ ).

	MEAN RELATIVE DIFFERENCE in $\mathbf{RR} \mu(\Delta R)$ [%]				
	$Z_{Hm}$	$Z_H 1$	$Z_H 2$	$Z_H 3$	$Z_H 4$
$R_1$	-11.87	12.16	1.55	-7.95	1.85
$R_2$	-13.27	9.14	1.34	-3.54	1.79
$R_3$	-14.05	7.39	0.30	-3.37	-1.60
$R_4$	-11.29	9.93	0.99	-2.19	3.44
	STANDARD DEVIATION $\sigma(\Delta R)$ [%]				
	$Z_{Hm}$	$Z_H 1$	$Z_H 2$	$Z_H 3$	$Z_H 4$
$R_1$	22.08	24.08	21.46	21.76	22.91
$R_2$	22.69	21.64	20.32	23.75	21.20
$R_3$	22.57	20.70	22.66	21.77	18.86
$R_4$	21.55	21.78	18.90	21.24	21.33

Table 3.14: Results summary based on single-radar correction methods for single point location ( $\mathbf{P}_3$ ).

	MEAN RELATIVE DIFFERENCE in $\mathbf{RR} \mu(\Delta R)$ [%]				
	$Z_{Hm}$	$Z_H 1$	$Z_H 2$	$Z_H 3$	$Z_H 4$
$R_1$	-16.58	10.66	0.13	-7.77	1.01
$R_2$	-9.48	6.49	-0.30	-2.72	0.13
$R_3$	-18.86	9.56	-2.88	-7.13	2.20
$R_4$	-5.23	3.07	-1.29	-1.72	1.69
	STANDARD DEVIATION $\sigma(\Delta R)$ [%]				
	$Z_{Hm}$	$Z_H 1$	$Z_H 2$	$Z_H 3$	$Z_H 4$
$R_1$	21.53	27.51	25.24	24.94	23.39
$R_2$	23.90	22.12	22.75	20.79	20.46
$R_3$	24.85	27.59	28.01	25.57	25.50
$R_4$	20.97	18.56	21.48	19.15	20.21

Table 3.15: Results for merging methods computed for the area of interest (**HUC<sub>123</sub>**).

	MEAN REFLECTIVITY DIFFERENCE $\mu(\varepsilon_Z)$ (dBZ)				
	$Z_{Hm}$	$Z_H 1$	$Z_H 2$	$Z_H 3$	$Z_H 4$
$M_1$	-0.77	0.41	0.04	-0.23	0.04
$M_2$	-0.84	0.24	-0.08	-0.33	-0.08
$M_3$	-0.34	0.23	0.07	-0.08	0.09
$M_4$	-0.42	0.34	0.12	-0.06	0.13
$M_5$	0.42	1.52	1.11	0.89	1.12
	STANDARD DEVIATION $\sigma(\varepsilon_Z)$ (dBZ)				
	$Z_{Hm}$	$Z_H 1$	$Z_H 2$	$Z_H 3$	$Z_H 4$
$M_1$	1.12	1.00	0.97	1.03	0.97
$M_2$	1.79	1.41	1.36	1.47	1.38
$M_3$	1.38	1.35	1.34	1.36	1.35
$M_4$	1.13	1.07	1.06	1.09	1.07
$M_5$	1.16	1.17	1.07	1.11	1.08

Table 3.16: Results for merging methods computed for the area of interest (**HUC<sub>123</sub>**).

	MEAN RELATIVE DIFFERENCE in <b>RR</b> $\mu(\Delta R)$ [%]				
	$Z_{Hm}$	$Z_H 1$	$Z_H 2$	$Z_H 3$	$Z_H 4$
$M_1$	-15.70	10.20	-1.88	-6.84	-1.12
$M_2$	-17.51	9.25	-3.38	-8.27	-2.81
$M_3$	-6.53	4.01	0.81	-2.06	2.13
$M_4$	-8.70	4.88	0.72	-2.82	1.88
$M_5$	5.86	37.56	19.28	14.64	20.57
	STANDARD DEVIATION $\sigma(\Delta R)$ [%]				
	$Z_{Hm}$	$Z_H 1$	$Z_H 2$	$Z_H 3$	$Z_H 4$
$M_1$	8.94	31.39	5.48	7.07	6.01
$M_2$	13.36	43.44	7.13	8.84	8.37
$M_3$	5.03	4.35	3.84	4.30	4.09
$M_4$	5.87	4.50	3.80	4.76	4.01
$M_5$	7.07	62.94	4.26	5.96	4.88

Table 3.17: Results for merging methods computed for the area of interest (**HUC<sub>1</sub>**).

	MEAN REFLECTIVITY DIFFERENCE $\mu(\varepsilon_Z)$ (dBZ)				
	$Z_{Hm}$	$Z_H 1$	$Z_H 2$	$Z_H 3$	$Z_H 4$
$M_1$	-0.84	0.44	0.03	-0.26	0.03
$M_2$	-0.98	0.22	-0.12	-0.41	-0.13
$M_3$	-0.37	0.24	0.06	-0.09	0.08
$M_4$	-0.45	0.35	0.12	-0.07	0.13
$M_5$	0.39	1.57	1.12	0.90	1.13
	STANDARD DEVIATION $\sigma(\varepsilon_Z)$ (dBZ)				
	$Z_{Hm}$	$Z_H 1$	$Z_H 2$	$Z_H 3$	$Z_H 4$
$M_1$	1.13	1.01	0.97	1.07	0.98
$M_2$	1.93	1.42	1.38	1.58	1.41
$M_3$	1.39	1.37	1.36	1.40	1.36
$M_4$	1.16	1.09	1.08	1.13	1.09
$M_5$	1.18	1.19	1.08	1.17	1.09

Table 3.18: Results for merging methods computed for the area of interest (**HUC<sub>2</sub>**).

	MEAN REFLECTIVITY DIFFERENCE $\mu(\varepsilon_Z)$ (dBZ)				
	$Z_{Hm}$	$Z_H 1$	$Z_H 2$	$Z_H 3$	$Z_H 4$
$M_1$	-0.77	0.45	0.06	-0.22	0.06
$M_2$	-0.83	0.28	-0.05	-0.32	-0.05
$M_3$	-0.32	0.28	0.10	-0.05	0.11
$M_4$	-0.41	0.38	0.15	-0.03	0.16
$M_5$	0.44	1.54	1.12	0.91	1.13
	STANDARD DEVIATION $\sigma(\varepsilon_Z)$ (dBZ)				
	$Z_{Hm}$	$Z_H 1$	$Z_H 2$	$Z_H 3$	$Z_H 4$
$M_1$	1.08	0.97	0.94	1.00	0.95
$M_2$	1.74	1.34	1.35	1.48	1.37
$M_3$	1.36	1.34	1.33	1.35	1.34
$M_4$	1.11	1.05	1.04	1.06	1.05
$M_5$	1.14	1.15	1.06	1.10	1.07

Table 3.19: Results for merging methods computed for the area of interest (**HUC<sub>3</sub>**).

	MEAN REFLECTIVITY DIFFERENCE $\mu(\varepsilon_Z)$ (dBZ)				
	$Z_{Hm}$	$Z_H 1$	$Z_H 2$	$Z_H 3$	$Z_H 4$
$M_1$	-0.72	0.36	0.02	-0.23	0.03
$M_2$	-0.75	0.21	-0.07	-0.29	-0.07
$M_3$	-0.33	0.20	0.05	-0.09	0.07
$M_4$	-0.41	0.30	0.10	-0.08	0.11
$M_5$	0.42	1.48	1.08	0.87	1.09
	STANDARD DEVIATION $\sigma(\varepsilon_Z)$ (dBZ)				
	$Z_{Hm}$	$Z_H 1$	$Z_H 2$	$Z_H 3$	$Z_H 4$
$M_1$	1.14	1.02	0.98	1.04	0.99
$M_2$	1.72	1.44	1.35	1.44	1.37
$M_3$	1.38	1.34	1.34	1.35	1.34
$M_4$	1.14	1.07	1.07	1.09	1.07
$M_5$	1.16	1.17	1.07	1.11	1.08

Table 3.20: Results for merging methods computed for the area of interest (**HUC<sub>1</sub>**).

	MEAN RELATIVE DIFFERENCE in <b>RR</b> $\mu(\Delta R)$ [%]				
	$Z_{Hm}$	$Z_H 1$	$Z_H 2$	$Z_H 3$	$Z_H 4$
$M_1$	-16.23	7.77	-2.73	-7.49	-2.32
$M_2$	-17.85	5.14	-4.18	-9.02	-4.03
$M_3$	-6.93	2.89	-0.20	-2.69	0.69
$M_4$	-8.91	3.81	-0.21	-3.28	0.54
$M_5$	5.43	34.92	18.51	14.18	19.23
	STANDARD DEVIATION $\sigma(\Delta R)$ [%]				
	$Z_{Hm}$	$Z_H 1$	$Z_H 2$	$Z_H 3$	$Z_H 4$
$M_1$	9.60	22.55	7.05	8.29	7.62
$M_2$	14.32	22.37	8.02	10.28	9.36
$M_3$	6.64	7.07	6.32	6.39	6.75
$M_4$	7.30	7.35	6.31	6.62	6.72
$M_5$	8.10	52.49	5.99	7.33	6.84

Table 3.21: Results for merging methods computed for the area of interest (**HUC<sub>2</sub>**).

	MEAN RELATIVE DIFFERENCE in <b>RR</b> $\mu(\Delta R)$ [%]				
	$Z_{Hm}$	$Z_H 1$	$Z_H 2$	$Z_H 3$	$Z_H 4$
$M_1$	-14.85	5.78	-2.13	-6.43	-1.64
$M_2$	-14.90	3.94	-2.89	-6.86	-2.37
$M_3$	-6.25	3.00	0.11	-2.20	0.86
$M_4$	-8.13	3.81	0.08	-2.77	0.83
$M_5$	6.43	29.80	18.53	14.73	19.38
	STANDARD DEVIATION $\sigma(\Delta R)$ [%]				
	$Z_{Hm}$	$Z_H 1$	$Z_H 2$	$Z_H 3$	$Z_H 4$
$M_1$	9.49	9.29	7.78	8.21	7.99
$M_2$	13.48	8.89	8.62	9.79	9.03
$M_3$	7.05	7.86	7.31	7.37	7.70
$M_4$	7.22	7.89	6.96	6.87	7.05
$M_5$	8.22	19.56	7.61	7.78	8.02

Table 3.22: Results for merging methods computed for the area of interest (**HUC<sub>3</sub>**).

	MEAN RELATIVE DIFFERENCE in <b>RR</b> $\mu(\Delta R)$ [%]				
	$Z_{Hm}$	$Z_H 1$	$Z_H 2$	$Z_H 3$	$Z_H 4$
$M_1$	-13.82	7.79	-2.35	-6.21	-1.89
$M_2$	-14.79	7.52	-3.31	-6.72	-3.05
$M_3$	-6.27	2.43	-0.18	-2.57	0.77
$M_4$	-8.14	3.03	-0.37	-3.25	0.47
$M_5$	6.27	35.09	17.93	14.07	18.75
	STANDARD DEVIATION $\sigma(\Delta R)$ [%]				
	$Z_{Hm}$	$Z_H 1$	$Z_H 2$	$Z_H 3$	$Z_H 4$
$M_1$	9.84	32.57	7.08	7.78	7.37
$M_2$	15.22	45.07	9.12	9.55	9.95
$M_3$	6.49	6.24	5.87	5.90	5.86
$M_4$	7.15	6.71	6.02	6.31	6.03
$M_5$	7.92	74.60	6.15	6.97	6.58

Table 3.23: Results for merging methods computed for single point location ( $\mathbf{P}_1$ ).

	MEAN REFLECTIVITY DIFFERENCE $\mu(\varepsilon_Z)$ (dBZ)				
	$Z_{Hm}$	$Z_H 1$	$Z_H 2$	$Z_H 3$	$Z_H 4$
$M_1$	-0.74	0.49	0.03	-0.28	0.05
$M_2$	-1.02	0.36	-0.13	-0.46	-0.15
$M_3$	-0.09	0.44	0.04	-0.07	0.18
$M_4$	-0.25	0.48	0.12	-0.05	0.21
$M_5$	0.60	1.64	1.19	0.90	1.17
	STANDARD DEVIATION $\sigma(\varepsilon_Z)$ (dBZ)				
	$Z_{Hm}$	$Z_H 1$	$Z_H 2$	$Z_H 3$	$Z_H 4$
$M_1$	1.04	1.03	1.00	0.97	0.97
$M_2$	1.93	1.37	1.32	1.36	1.31
$M_3$	1.30	1.33	1.26	1.22	1.39
$M_4$	1.02	1.04	0.97	0.98	1.08
$M_5$	1.08	1.17	1.22	1.12	1.13

Table 3.24: Results for merging methods computed for single point location ( $\mathbf{P}_2$ ).

	MEAN REFLECTIVITY DIFFERENCE $\mu(\varepsilon_Z)$ (dBZ)				
	$Z_{Hm}$	$Z_H 1$	$Z_H 2$	$Z_H 3$	$Z_H 4$
$M_1$	-0.84	0.53	0.03	-0.27	0.06
$M_2$	-0.94	0.46	-0.04	-0.29	0.07
$M_3$	-0.34	0.33	0.11	-0.17	0.22
$M_4$	-0.45	0.49	0.15	-0.07	0.22
$M_5$	0.31	1.55	1.05	0.85	1.07
	STANDARD DEVIATION $\sigma(\varepsilon_Z)$ (dBZ)				
	$Z_{Hm}$	$Z_H 1$	$Z_H 2$	$Z_H 3$	$Z_H 4$
$M_1$	1.01	0.81	0.84	0.93	0.87
$M_2$	1.70	1.20	1.14	1.40	1.27
$M_3$	1.28	1.25	1.33	1.40	1.25
$M_4$	1.03	0.91	0.97	0.98	0.96
$M_5$	1.09	0.94	1.00	1.05	1.04

Table 3.25: Results for merging methods computed for single point location ( $\mathbf{P}_3$ ).

	MEAN REFLECTIVITY DIFFERENCE $\mu(\varepsilon_Z)$ (dBZ)				
	$Z_{Hm}$	$Z_H 1$	$Z_H 2$	$Z_H 3$	$Z_H 4$
$M_1$	-0.55	0.22	-0.12	-0.22	0.02
$M_2$	-0.48	0.06	-0.19	-0.23	-0.02
$M_3$	-0.20	0.14	-0.10	-0.12	0.07
$M_4$	-0.32	0.23	-0.02	-0.09	0.12
$M_5$	0.47	1.47	0.93	0.83	1.09
	STANDARD DEVIATION $\sigma(\varepsilon_Z)$ (dBZ)				
	$Z_{Hm}$	$Z_H 1$	$Z_H 2$	$Z_H 3$	$Z_H 4$
$M_1$	1.11	0.93	0.93	0.97	1.01
$M_2$	1.38	1.19	1.19	1.22	1.23
$M_3$	1.37	1.32	1.23	1.28	1.20
$M_4$	1.14	1.07	0.97	1.01	1.00
$M_5$	1.13	1.06	0.97	1.03	1.08

Table 3.26: Results for merging methods computed for single point location ( $\mathbf{P}_1$ ).

	MEAN RELATIVE DIFFERENCE in $\mathbf{RR}$ $\mu(\Delta R)$ [%]				
	$Z_{Hm}$	$Z_H 1$	$Z_H 2$	$Z_H 3$	$Z_H 4$
$M_1$	-10.08	10.13	1.88	-3.30	2.07
$M_2$	-11.81	8.99	0.00	-5.08	-0.19
$M_3$	0.86	10.18	2.82	0.86	5.83
$M_4$	-2.66	9.83	3.33	0.52	5.26
$M_5$	12.26	33.51	24.10	17.97	23.44
	STANDARD DEVIATION $\sigma(\Delta R)$ [%]				
	$Z_{Hm}$	$Z_H 1$	$Z_H 2$	$Z_H 3$	$Z_H 4$
$M_1$	15.95	21.09	17.12	15.67	16.15
$M_2$	23.30	29.07	20.74	20.42	20.38
$M_3$	23.32	26.80	21.18	20.63	26.06
$M_4$	17.31	20.21	17.06	16.64	19.47
$M_5$	22.24	29.73	26.64	22.89	24.55

Table 3.27: Results for merging methods computed for single point location ( $\mathbf{P}_2$ ).

	MEAN RELATIVE DIFFERENCE in $\mathbf{RR} \mu(\Delta R)$ [%]				
	$Z_{Hm}$	$Z_H 1$	$Z_H 2$	$Z_H 3$	$Z_H 4$
$M_1$	-11.81	10.10	1.51	-3.32	2.03
$M_2$	-11.29	9.93	0.99	-2.19	3.44
$M_3$	-3.40	7.58	4.23	-0.38	5.74
$M_4$	-5.89	9.54	3.73	0.00	4.88
$M_5$	6.89	30.65	20.46	16.73	20.89
	STANDARD DEVIATION $\sigma(\Delta R)$ [%]				
	$Z_{Hm}$	$Z_H 1$	$Z_H 2$	$Z_H 3$	$Z_H 4$
$M_1$	13.77	14.27	13.70	14.20	13.82
$M_2$	21.55	21.78	18.90	21.24	21.33
$M_3$	19.18	20.10	21.94	20.12	21.55
$M_4$	15.16	15.55	16.12	15.10	16.06
$M_5$	18.56	20.28	20.03	20.39	20.67

Table 3.28: Results for merging methods computed for single point location ( $\mathbf{P}_3$ ).

	MEAN RELATIVE DIFFERENCE in $\mathbf{RR} \mu(\Delta R)$ [%]				
	$Z_{Hm}$	$Z_H 1$	$Z_H 2$	$Z_H 3$	$Z_H 4$
$M_1$	-7.21	4.85	-0.72	-2.29	1.69
$M_2$	-5.23	2.82	-1.29	-1.72	1.69
$M_3$	-0.71	4.74	0.42	0.14	3.12
$M_4$	-3.47	5.39	0.89	-0.25	3.42
$M_5$	9.96	29.30	18.04	16.22	21.54
	STANDARD DEVIATION $\sigma(\Delta R)$ [%]				
	$Z_{Hm}$	$Z_H 1$	$Z_H 2$	$Z_H 3$	$Z_H 4$
$M_1$	16.41	15.29	15.25	15.33	16.41
$M_2$	20.97	18.56	19.30	19.15	20.21
$M_3$	22.66	23.43	20.45	20.53	19.84
$M_4$	18.18	18.36	16.10	16.33	16.86
$M_5$	20.61	24.23	19.05	20.62	21.56

Table 3.29: Results summary based on single-radar correction methods for the area of interest (**HUC<sub>123</sub>**) - network-based approach.

	MEAN REFLECTIVITY DIFFERENCE $\mu(\varepsilon_Z)$ (dBZ)					
	$Z_{Hm}$	$Z_H 1$	$Z_H 2$	$Z_H 3$	$Z_H 4$	<b><math>Z_H 5</math></b>
$R_1$	-1.09	0.37	-0.07	-0.42	-0.07	-0.18
$R_2$	-0.97	0.37	-0.03	-0.32	-0.03	-0.21
$R_3$	-1.26	0.28	-0.15	-0.52	-0.15	-0.14
$R_4$	-0.85	0.30	-0.05	-0.32	-0.04	-0.32
	STANDARD DEVIATION $\sigma(\varepsilon_Z)$ (dBZ)					
	$Z_{Hm}$	$Z_H 1$	$Z_H 2$	$Z_H 3$	$Z_H 4$	<b><math>Z_H 5</math></b>
$R_1$	1.88	1.48	1.45	1.58	1.46	1.96
$R_2$	1.77	1.43	1.35	1.51	1.37	1.83
$R_3$	1.89	1.46	1.39	1.57	1.41	1.92
$R_4$	1.71	1.38	1.39	1.50	1.40	2.57

Table 3.30: Results summary based on single-radar correction methods for the area of interest (**HUC<sub>123</sub>**) - network-based approach.

	MEAN RELATIVE DIFFERENCE in <b>MAP</b> $\mu(\Delta R)$ [%]					
	$Z_{Hm}$	$Z_H 1$	$Z_H 2$	$Z_H 3$	$Z_H 4$	<b><math>Z_H 5</math></b>
R <sub>1</sub>	-17.79	8.22	-2.37	-8.00	-1.62	-1.16
R <sub>2</sub>	-15.41	9.80	-1.24	-6.12	-0.55	-1.86
R <sub>3</sub>	-19.98	8.32	-3.76	-9.37	-3.18	-1.14
R <sub>4</sub>	-12.95	5.12	-0.98	-5.37	0.02	-2.88
	STANDARD DEVIATION $\sigma(\Delta R)$ [%]					
	$Z_{Hm}$	$Z_H 1$	$Z_H 2$	$Z_H 3$	$Z_H 4$	<b><math>Z_H 5</math></b>
R1	15.10	25.93	7.47	10.27	8.72	8.08
R2	14.35	40.74	7.11	10.18	7.96	7.54
R3	16.16	40.74	8.36	11.44	9.84	8.58
R4	10.52	5.24	5.07	7.44	5.43	7.32

Table 3.31: Results for merging methods computed for the area of interest (HUC<sub>123</sub>) - network-based approach.

	MEAN REFLECTIVITY DIFFERENCE $\mu(\varepsilon_Z)$ (dBZ)						
	$Z_{Hm}$	$Z_H 1$	$Z_H 2$	$Z_H 3$	$Z_H 4$	$Z_H 5$	$Z_H 5'$
$M_1$	-0.77	0.41	0.04	-0.23	0.04	0.01	-0.52
$M_2$	-0.84	0.24	-0.08	-0.33	-0.08	-0.36	-0.99
$M_3$	-0.34	0.23	0.07	-0.08	0.09	-0.62	-1.82
$M_4$	-0.42	0.34	0.12	-0.06	0.13	-0.29	-1.21
$M_5$	0.42	1.52	1.11	0.89	1.12	1.55	1.30
	STANDARD DEVIATION $\sigma(\varepsilon_Z)$ (dBZ)						
	$Z_{Hm}$	$Z_H 1$	$Z_H 2$	$Z_H 3$	$Z_H 4$	$Z_H 5$	$Z_H 5'$
$M_1$	1.12	1.00	0.97	1.03	0.97	1.20	1.39
$M_2$	1.79	1.41	1.36	1.47	1.38	2.53	2.86
$M_3$	1.38	1.35	1.34	1.36	1.35	2.45	2.98
$M_4$	1.13	1.07	1.06	1.09	1.07	1.64	2.01
$M_5$	1.16	1.17	1.07	1.11	1.08	1.41	1.59

Table 3.32: Results for merging methods computed for the area of interest (**HUC<sub>123</sub>**) - network-based approach.

	MEAN RELATIVE DIFFERENCE in <b>RR</b> $\mu(\Delta R)$ [%]						
	$Z_{Hm}$	$Z_H 1$	$Z_H 2$	$Z_H 3$	$Z_H 4$	<b><math>Z_H 5</math></b>	<b><math>Z_H 5'</math></b>
$M_1$	-15.70	10.20	-1.88	-6.84	-1.12	-0.74	-7.67
$M_2$	-17.51	9.25	-3.38	-8.27	-2.81	-2.58	-9.46
$M_3$	-6.53	4.01	0.81	-2.06	2.13	-8.56	-21.36
$M_4$	-8.70	4.88	0.72	-2.82	1.88	-5.52	-16.53
$M_5$	5.86	37.56	19.28	14.64	20.57	30.10	26.67
	STANDARD DEVIATION $\sigma(\Delta R)$ [%]						
	$Z_{Hm}$	$Z_H 1$	$Z_H 2$	$Z_H 3$	$Z_H 4$	<b><math>Z_H 5</math></b>	<b><math>Z_H 5'</math></b>
$M_1$	8.94	31.39	5.48	7.07	6.01	5.08	4.93
$M_2$	13.36	43.44	7.13	8.84	8.37	5.52	5.94
$M_3$	5.03	4.35	3.84	4.30	4.09	7.52	8.84
$M_4$	5.87	4.50	3.80	4.76	4.01	7.03	7.47
$M_5$	7.07	62.94	4.26	5.96	4.88	6.57	8.16

CHAPTER 4  
DEVELOPMENT OF UTILITIES IN SUPPORT OF DATA  
PROCESSING, ANALYSIS, AND DISPLAY

4.1 Introduction

The University of Iowa Polarimetric Radar Network was developed to serve as a US hydrologic community resource. Operated as a single instrument, the network's goal is to provide high spatial and temporal resolution rainfall data for spatial domains, such as cities, watersheds, or ground networks for satellite product validation, that are typical for hydrologic research interests. The University of Iowa serves as a home base for the network and is its main testing and development site. The network consists of four mobile (trailer mounted), polarimetric, X-band radars. All radars are identical in their design and were manufactured by ProSensing, Inc. Figure 4.1 shows one of the network's nodes during its operational deployment in Iowa City, IA.

Each radar in the network can be individually configured to support a specific operation mode for a given research scenario. This includes specifying the antenna scanning strategy as well as the radar's transmission and data collection mode. A suite of utilities supports flexibility in operating the network. The specific goals of those utilities include but are not limited to: securing an acceptable balance between the radar's vertical and horizontal channels, calculating polarimetric variables based on recorded radar signal, applying quality control procedures, computing metadata, and displaying collected variables.

In this section, we provide a detailed description of the utilities that have been developed and provide a set of examples that show how the utilities can be used to support the network's data collection and analysis. We start by listing the network's technical specifications and then provide an overview of the data acquisition system. We also present the network's operating modes.

#### 4.2 The network's technical specifications

The University of Iowa Polarimetric Radar Network is a four-node network designed to sample backscatter from precipitation using the pulse-Doppler design [Morris and Harkness, 1996]. Each radar employs a 25kW peak power, 9.41 GHz magnetron transmitter. To avoid interference between the nodes, each magnetron has its center frequency adjusted by approximately 10 MHz increments, which allows the radars to observe essentially the same resolution volume without causing interference during operational deployment. The 6' dual-polarized (H/V) parabolic antennae are mounted on pedestals supporting full 360° antenna rotation in azimuth and a -2° to 182° elevation span, both with 0.03° precision. The maximum rotation speed of 20 °/s can be set, but the speed should not exceed 10 °/s in order to allow for reliable and continuous operations in a high wind situation.

The power output from the magnetron is directed to the antenna by a rotary joint that allows azimuthal rotation and a set of flexible waveguides that permit the antenna's motion in elevation during the data collection process. The parabolic dish antenna with a weather-sealed radome can produce a 3 dB beamwidth 1.4° wide.

The network operator can select the pulse length from the 100, 200, 500, or 1000 nanoseconds range that corresponds to a range resolution of 15, 30, 75, and 150 meters, respectively. The system has been designed as Coherent-on-Receive [Junyent, 2007], which means that the transmitted power and the corresponding signal phase are continuously sampled to preserve the signal's phase and to allow for estimation of the Doppler shift when the reflected signal is collected by the digital receiver. This is a typical design for radars that have a magnetron as a source of electromagnetic energy since magnetrons generate electromagnetic pulses with a random phase value for each pulse.

The radar's design allows for measurement of the following radar observables: radar equivalent reflectivity factor at  $H$  and  $V$  polarization ( $Z_H$ ,  $Z_V$ ), differential

reflectivity ( $Z_{DR}$ ), specific differential phase shift ( $K_{DP}$ ), mean Doppler velocity, and spectrum width.

### 4.3 Data acquisition system

Data acquisition is controlled by specifying a number of parameters and options in a display GUI program that was developed by ProSensing, Inc. In the process, the control parameters define the radar's operation through the Radar Control Board (RCB). The digital receiver is controlled by specifying the digital IF frequency, receiver filter bandwidth, and decimation steps. Additional parameters include the data processing algorithm (Pulse Pair or FFT) and the data recording type (raw  $I/Q$  pairs or processed data). The flow chart in Figure 4.2 illustrates how the process of data acquisition is controlled. The core elements of the data processing loop are described below.

#### 4.3.1 Radar Control Board (RCB) parameters

The Radar Control Board serves as the master timing device for a number of switches and trigger-enabled components in the radar. By specifying parameters in the GUI program, the operator sends a configuration block to the RBC, which determines timing sequences and, consequently, the radar's pulse length, pulse pattern, and spacing between consecutive pulses, as well as the start of the digital receiver range profile samples.

Five different pulsing modes can be selected in the GUI. The Pulse Pair (PP) mode is a standard mode where two pulses are transmitted per group. The DPP mode is similar to PP but with three pulses per group being transmitted. Two Fast Fourier Transform (FFT and FFT2) pulsing schemes [Rabiner and Gold, 1975] result in three different processing methods: FFT with a constant Pulse Repetition Interval (PRI), and FFT2 where a dual PRI can be programmed to allow for better clutter filtering and an extended unambiguous velocity measurement [Cho, 2005]. The FFT2I is the interleaved version of the FFT2 and has been programmed to allow for a more reliable unfolding of

the Doppler velocity during post-processing. Figure 4.3 and Figure 4.4 give a graphical representation of the available pulsing modes, where additional characteristics have also been presented.

#### 4.3.2 Digital receiver control parameters

A radar's digital receiver is a sampling system in which the continuous (analog) signal is measured at discrete intervals defined by the sampling frequency of the system ( $f_s$ ). In the case of the network in consideration, the sampling frequency is fixed at 80 MHz, but the resulting sampling frequency can be modified in a number of decimation steps that result in a lower  $f_s$  value.

In general, Pulsed-Doppler radars are configured to measure two components of the received signal [Bringi and Chandrasekar, 2001], the in-phase ( $I$ ) and quadrature-phase ( $Q$ ) components of the signal where the  $Q$  component is a 90°-phase-shifted version of the  $I$  component. The  $I/Q$  complex sample pair stores information on the magnitude and phase of the received signal. The first step in the data acquisition loop is to read a block of raw  $I/Q$  samples from the digital receiver. The size of the raw data block needs to be determined based on the parameters (*indicated in italic font below*) as it depends on the pulsing mode (PP or FFT), the number of range gates ( $nrg$ ), the number of pulses per group ( $nps$ ) (PP or DPP) in the pulse-pair mode, or the length of the FFT block ( $fftlen$ ) multiplied by the number of FFT blocks ( $fftblocks$ ) per group in the case of the FFT pulsing mode, plus the number of averaged groups ( $nave$ ) in the processing. Among other parameters that need to be selected by the operator and that are related to the digital receiver block are the digital LO frequency ( $f_{LO}$ ), the digital receiver bandwidth, and the digital decimation level.

### 4.3.3 Data Processing Algorithm

A full understanding of the data processing algorithm is required in order to write custom utilities that support radar data analysis. In this subsection, we define variables and transformations that are fundamental to the data processing algorithm.

A range gate sample ( $S$ ) as recorded by a radar is a complex ( $I/Q$ ) data point:

$$S_{H,V}(g, p, rg) = I + jQ \quad (4.1)$$

where the subscript  $V$  or  $H$  indicates the receiver channel, the  $g$  index is the group number between 0 and  $nave-1$  (see Figure 4.3 and Figure 4.4 for definition), the  $p$  index is the pulse number within the group (0 to  $nps-1$ ), and  $rg$  is the range gate count between 0 and  $nrg-1$ . The notation can characterize any given range sample in a unique way.

For the Pulse-Pair operating mode, the cross-correlation ( $C$ ) at a range gate  $rg$  between the  $p$  and  $p+1$  pulse samples is defined as:

$$C(rg) = \sum_{i=0}^{nave-1} S(g, p, rg) \cdot S^*(g, p+1, rg) \quad (4.2)$$

where  $S^*$  is the complex conjugate of  $S$ . Cross correlation is a complex variable and can be expressed in terms of  $I$  and  $Q$  samples as:

$$\begin{aligned} C(rg) &= \text{Re}[C(rg)] + j \text{Im}[C(rg)] \\ \text{Re}[C(rg)] &= \sum_{g=0}^{nave-1} [I(g, p, rg) \cdot I(g, p+1, rg) + Q(g, p, rg) \cdot Q(g, p+1, rg)] \\ \text{Im}[C(rg)] &= \sum_{g=0}^{nave-1} [Q(g, p, rg) \cdot I(g, p+1, rg) - I(g, p, rg) \cdot Q(g, p+1, rg)] \end{aligned} \quad (4.3)$$

In the FFT modes, blocks of  $I/Q$  samples are Fast Fourier Transformed ( $FFT$ ) [Rabiner and Gold, 1975]:

$$\vec{F}(i, rg) = F(g, 0 : L-1, rg) = FFT[S(g, 0 : L-1, rg)] \quad (4.4)$$

where, again,  $g$  is the group index,  $rg$  is the range gate index, and  $FFT$  processing is implemented on an  $FFT$  block containing  $L$  pulses from pulse 0 to  $L-1$  (see Figure 4.4).

Once a range sample profile is recorded by the digital receiver, its phase information must be corrected because the radars are Coherent-on-Receive in design, as explained in section 4.2. The correction of the phase is based on information stored during pulse transmission in a sample for each transmitted pulse.

$$\bar{S}_{H,V}(g, p, rg) = \frac{S_{H,V}(g, p, rg) \cdot S_{H,V}^*(g, p, TX\_gate)}{|S_V(g, p, TX\_gate)|} \quad (4.5)$$

It is important to note that the  $V$  channel transmitted pulse is used to correct both  $V$  and  $H$  sample profiles.

Clutter filtering of the collected samples is optional for the pulse-pair processing mode and can be selected by the operator in the GUI program. If the selection is made, a mean value ( $DC$ ) is first calculated separately for  $V$  and  $H$  channels based on all the data samples in the clutter filtering interval  $cave$ .

$$DC_{H,V}(pa, rg) = \frac{1}{cave \cdot nps} \sum_{g=pa}^{pa+cave-1} \sum_{p=0}^{nps-1} S_{H,V}(g, p, rg) \quad (4.6)$$

where  $pa$  is the post averaging index (between 0 and  $pave-1$ ). The resulting complex value is then subtracted from all the samples in the corresponding clutter averaging interval:

$$\bar{S}_{H,V}(g, p, rg) = S_{H,V}(g, p, rg) - DC_{H,V}(pa, rg) \quad (4.7)$$

Depending on the data processing mode, the set of calculated parameters and their definitions will vary. We now define computed radar parameters with respect to the data processing mode. A graphical representation for each of the pulsing modes is presented in Figure 4.3 (PPD and DPP) and Figure 4.4 (FFT, FFT2 and FFT2I).

#### 4.3.3.1 Pulse-Pair Mode (PP)

In the PP mode, as in all available modes, the Coherent-on-Receive algorithm is implemented first to correct the phase information. Depending on the operator's choice,

the clutter filtering procedure may follow. Next, the following radar parameters are calculated by averaging data through the entire *nave* interval:

Power:

$P_{H0}$ ,  $P_{H1}$  and  $P_{V0}$ ,  $P_{V1}$  are mean power values [in watts  $\cdot 10^{-3}$ ] for a given range gate and are calculated by averaging the first and second pulses for all the groups separately,

$$\begin{aligned} P_{H,V0}(rg) &= \sum_{g=0}^{nave-1} |S_{H,V}(g,0,rg)|^2 \\ P_{H,V1}(rg) &= \sum_{g=0}^{nave-1} |S_{H,V}(g,1,rg)|^2 \end{aligned} \quad (4.8)$$

Often, storing power returns for both channels separately is not desired (e.g., to decrease the size of collected data). The operator has a choice to sum the powers in the processing, which results in an alternative formula being used,

$$P_{H,V}(rg) = \sum_{g=0}^{nave-1} \sum_{np=0}^1 |S_{H,V}(g,np,rg)|^2 \quad (4.9)$$

Doppler Pulse Pair:

In the PP mode, the estimation of velocity is based on the “time domain” processing. The basis for velocity calculation is the phase shift between two successive pulses. At the data processing stage, the mean autocovariance (referred to as a Doppler Pulse Pair  $PP_{H,V}$ ) between two successive pulses for the  $H$  and  $V$  channels is calculated separately.

$$PP_{H,V}(rg) = \sum_{g=0}^{nave-1} S_{H,V}(g,0,rg) S_{H,V}^*(g,1,rg) \quad (4.10)$$

The Doppler Pulse Pair can later be used to estimate the phase shift between pulses and, consequently, to obtain the radial velocity of targets.

V-H Cross-Correlation

Similarly to the radial velocity in the PP mode, the differential propagation phase  $\Phi_{DP}$  estimation is also based on the “time domain” processing. During the data acquisition stage, the V-H Cross-Correlation is calculated and stored in a raw data file:

$$C_{HV}(rg) = \sum_{g=0}^{nave-1} \sum_{np=0}^1 S_V(g, np, rg) S_H^*(g, np, rg) \quad (4.11)$$

In the post-processing stage, the H/V cross-correlation is used to estimate the differential propagation phase  $\Phi_{DP}$ .

#### 4.3.3.2 DPP Mode

In the DPP Mode, the radar transmission pulse sequence is made up of groups of three pulses ( $nps=3$ ) (see Figure 4.3 for a graphical representation of the method). The values recorded in the data acquisition stage are similar to the ones from the PP mode:

Power:

$$\begin{aligned} P_{H,V0}(rg) &= \sum_{g=0}^{nave-1} |S_{H,V}(g,0,rg)|^2 \\ P_{H,V1}(rg) &= \sum_{g=0}^{nave-1} |S_{H,V}(g,1,rg)|^2 \\ P_{H,V2}(rg) &= \sum_{g=0}^{nave-1} |S_{H,V}(g,2,rg)|^2 \end{aligned} \quad (4.12)$$

If the summation of powers is selected by the operator, the calculation is as follows:

$$P_{H,V}(rg) = \sum_{g=0}^{nave-1} \sum_{np=0}^2 |S_{H,V}(g,np,rg)|^2 \quad (4.13)$$

Doppler Pulse Pair:

In the case of the three-pulse sequence, the autocovariance of the signal is calculated for the time lag between the first and the second pulse as well as for the time lag between the second and the third pulse.

$$\begin{aligned}
PP_{H,V0}(rg) &= \sum_{g=0}^{nave-1} S_{H,V}(g,0,rg) S_{H,V}^*(g,1,rg) \\
PP_{H,V1}(rg) &= \sum_{g=0}^{nave-1} S_{H,V}(g,1,rg) S_{H,V}^*(g,2,rg)
\end{aligned} \tag{4.14}$$

The calculations are carried out for  $H$  and  $V$  channels separately, so the resulting set of variables includes  $PP_{H0}$ ,  $PP_{H1}$ ,  $PP_{V0}$ , and  $PP_{V1}$ .

#### V-H Cross-Correlation

$$C_{HV}(rg) = \sum_{g=0}^{nave-1} \sum_{np=0}^2 S_V(g,np,rg) S_H^*(g,np,rg) \tag{4.15}$$

#### 4.3.3.3 The FFT Mode

In the FFT mode (FFT, FFT2 and FFT2I), the clutter filtering is not optional and is performed based on the *cave* number of FFT blocks after the Coherent-on-Receive procedure is implemented to correct the phase information for a given range profile.

After the phase correction and clutter filtering procedures, each FFT block consisting of *fftlen* number of pulses is transformed to the frequency domain in the FFT processor:

$$\vec{F}_{H,V}(g,rg) = F_{H,V}(g,0:fftlen-1,rg) = FFT[S_{H,V}(g,0:fftlen-1,rg)] \tag{4.16}$$

The following power and cross spectra are calculated based on the FFT transformed signals:

$$\begin{aligned}
PS_V(rg) &= \sum_{g=0}^{nave-1} \left| \vec{F}_V(g,rg) \right|^2 \\
PS_H(rg) &= \sum_{g=0}^{nave-1} \left| \vec{F}_H(g,rg) \right|^2 \\
CS_{HV}(rg) &= \sum_{g=0}^{nave-1} \vec{F}_V(g,rg) \vec{F}_H^*(g,rg)
\end{aligned} \tag{4.17}$$

#### 4.3.3.4. FFT2 Mode

In the FFT2 mode, the radar TX pulse sequence shown in Figure 4.4 is made up of alternating PRI FFT blocks.

$$\vec{F}_{H,V}(g,b,rg) = F_{H,V}(g,b,0:ffilen-1,rg) = FFT[S_{H,V}(g,b,0:ffilen-1,rg)] \quad (4.18)$$

where  $b$  is the FFT block index (0 or 1).

The following power spectra ( $PS$ ) and cross-spectra ( $CS$ ) products are computed:

$$\begin{aligned} PS_{H0,V0}(rg) &= \sum_{g=0}^{nave-1} \left| \vec{F}_{H,V}(g,0,rg) \right|^2 \\ PS_{H1,V1}(rg) &= \sum_{g=0}^{nave-1} \left| \vec{F}_{H,V}(g,1,rg) \right|^2 \\ CS_{HV0}(rg) &= \sum_{g=0}^{nave-1} \vec{F}_V(g,0,rg) \vec{F}_H^*(g,0,rg) \\ CS_{HV1}(rg) &= \sum_{g=0}^{nave-1} \vec{F}_V(g,1,rg) \vec{F}_H^*(g,1,rg) \end{aligned} \quad (4.19)$$

#### 4.3.3.5 FFT2I Mode

In the FFT2I Mode, the radar TX pulse sequence shown in Figure 4.4 is made up of interleaved alternating PRI FFT blocks. Compared to the FFT method, the blocks are much larger, each block contains  $cave$  number of sub-blocks, and each sub-block contains  $ffilen$  number of pulses.

$$\vec{F}_{H,V}(g,b,sb,rg) = F_{H,V}(g,b,sb,0:ffilen-1,rg) = FFT[S_{H,V}(g,b,sb,0:ffilen-1,rg)] \quad (4.20)$$

where  $sb$  is the sub-block index between 0 and  $cave-1$ .

The following power spectra ( $PS$ ) and cross-spectra ( $CS$ ) products are computed:

$$\begin{aligned} PS_{H0,V0}(rg) &= \sum_{g=0}^{pave-1} \sum_{sb=0}^{cave-1} \left| \vec{F}_{H,V}(g,0,sb,rg) \right|^2 \\ PS_{H1,V1}(rg) &= \sum_{g=0}^{pave-1} \sum_{sb=0}^{cave-1} \left| \vec{F}_{H,V}(g,1,sb,rg) \right|^2 \\ CS_{HV0}(rg) &= \sum_{g=0}^{pave-1} \sum_{sb=0}^{cave-1} \vec{F}_V(g,0,sb,rg) \vec{F}_H^*(g,0,sb,rg) \\ CS_{HV1}(rg) &= \sum_{g=0}^{pave-1} \sum_{sb=0}^{cave-1} \vec{F}_V(g,1,sb,rg) \vec{F}_H^*(g,1,sb,rg) \end{aligned} \quad (4.21)$$

For all the data processing modes (PP, DPP, FFT, FFT2, FFT2I), the radar's operator has the option to record a "raw"  $I/Q$  complex sample pair instead of the products presented above. Recording "raw"  $I/Q$  pairs significantly increases the resulting data volume but provides us with the most fundamental radar signal information and allows us to build custom utilities to explore a radar's signal characteristics.

#### 4.4 Custom Data Processing Utilities

Depending on the data processing mode and a number of control parameters, the actual recorded data type and format will vary. To allow for efficient data handling, we developed a set of functions that automate the recognition of the recorded data format and perform a number of tasks fundamental to data collection and the analysis process.

##### 4.4.1 Radar data format

As seen in Figure 4.2, radar-recorded files have an organized structure. Each file starts with a file header where basic information about radar status and collected data format is stored. In addition, the complete record of all parameters selected by the operator can be found in the file header.

Following the file header is a set of interleaved profile headers and data blocks. Profile headers store information that is relevant to a given data block, such as azimuth and elevation of a recorded profile data, corresponding timestamp, GPS location coordinates, etc. Additional information, such as the temperature readings from a number of sensors located strategically within radar's hardware and position information from two inclinometers that indicate any deviation from the pedestal's vertical orientation, is also stored in the profile headers.

Data blocks store radar observables in a format selected by the operator (raw  $I/Q$  pairs or processed data). Depending on the radar pulsing mode, range gate size, maximum range, and the data processing format, the size of the data block can vary

significantly and must be estimated before radar observables can be read and converted to polarimetric variables.

The radar acquisition system records data in a binary format and saves files in a local storage area. Based on the operator's choice, individual files can correspond to single radar profiles (rays) or sector scans (including volume scan), can be defined to have a specific size (in MB), or can span a predefined time window (in minutes). The initial step in developing custom computer programs was to implement a logical module that recognized data type, size, and format based on the file header information. This module has been implemented as a static library written in C code and is being attached to all programs developed hereafter.

#### 4.4.2 Estimation of the radar calibration constant

The dynamic nature of radar measurement means that the received signal can fluctuate over many orders of magnitude. Losses in the antenna and waveguides, together with the level of noise inherent to radar's design, affect a radar's performance and must be accounted for before recorded values can be converted to polarimetric variables such as the reflectivity of differential phase shift.

Prior to its commissioning, each network node underwent a set of tests designed to estimate a number of parameters such as: the receiver's gain [dB] and noise figure for both  $H$  and  $V$  channels [dB], the isolation level between the channels [dB], the transmitter's peak power [dBm], and the antenna waveguide losses. All of the parameters must be incorporated separately into the radar equation in the form of a constant that is specific to each radar and each radar's polarimetric channel [*Doviak and Zrnica, 1993*].

One of the utilities written into the support network's operations is a program calculating the value of the constant based on the information from the transceiver's test.

Below, we present how the method has been implemented. We start by following the derivation of the radar equation and defining the radar constant.

The transmitted power density  $S_t$  [W/m<sup>2</sup>] of a radar can be expressed as:

$$S_t = \frac{P_t G}{4\pi r^2} \quad (4.22)$$

where  $P_t$  is the transmitted power [W],  $G$  is the antenna gain, and  $r$  is the distance to the target [m]. We start this derivation with a point target. The power density captured by the target and re-radiated towards the radar is:

$$S_r = \frac{S_t \sigma}{4\pi r^2 l_t} = \frac{P_t G \sigma}{(4\pi)^2 r^4} \quad (4.23)$$

where  $\sigma$  is target's effective area or back-scattering cross section [m<sup>2</sup>].

The received power at the antenna feed is the product of the antenna's effective aperture  $A_{eff}$  and the incident power density of the scattered field:

$$P_r = A_{eff} S_r = A_{eff} \frac{P_t G \sigma}{(4\pi)^2 r^4} \quad (4.24)$$

Since  $A_{eff} = G\lambda^2/4\pi$ , the received power can be written in the form of a radar equation for a single target:

$$P_r = \frac{P_t G^2 \lambda^2 \sigma}{(4\pi)^3 r^4} \quad (4.25)$$

The measured power by the radar data system at the receiver is the received power at the antenna feed  $P_r$  amplified by the receiver gain  $G_{rec}$ :

$$P_{rm} = \frac{P_t G^2 G_{rec} \lambda^2 \sigma}{(4\pi)^3 r^4} \quad (4.26)$$

Equation 4.26 can be extended to a volume target by replacing  $\sigma$  with the product of volume reflectivity  $\eta$  [m<sup>2</sup>m<sup>-3</sup>] and the volume of a given radar cell  $V$  [m<sup>3</sup>]. The range cell volume of a pulsed radar with an approximately Gaussian shape antenna pattern can be calculated as:

$$V = r^2 \frac{c\tau}{2} \int_0^{\pi} \int_0^{2\pi} f^2(\theta, \phi) \sin(\theta) d\theta d\phi = r^2 \frac{c\tau}{2} \pi \theta_{3dB}^2 / 8 \ln(2) \quad (4.27)$$

where  $r$  is the range to the center of the volume [m],

$$f = \exp\left(-\frac{4 \ln(2) \theta^2}{\theta_{3dB}^2}\right) \exp\left(-\frac{4 \ln(2) \phi^2}{\phi_{3dB}^2}\right) \quad (4.28)$$

$c$  is the speed of light [m/s],  $\tau$  is the transmit pulse length expressed in seconds, and for a parabolic dish antenna, the 3dB beam width [radians] in horizontal and vertical direction can be considered equal to  $\phi_{3dB} = \theta_{3dB}$ .

The resulting expression for the measured power from a volume target is [Doviak and Zrnic, 1993]:

$$P_{Vm} = \frac{P_t G^2 G_{rec} \lambda^2}{(4\pi)^3} \frac{c \tau \pi \theta_{3dB}^2 \eta}{r^2 16 \ln(2)} \quad (4.29)$$

Solving the above equation for  $\eta$  can be used to estimate the volume reflectivity at a range  $r$ :

$$\eta = P_{Vm} r^2 \frac{1024 \pi^2 \ln(2)}{P_t G^2 G_{rec} \lambda^2 c \tau \theta_{3dB}^2} \quad (4.30)$$

The more common measure of volume reflectivity is the radar reflectivity factor  $Z$  [ $\text{mm}^6 \text{m}^{-3}$ ], and it is related to  $\eta$  as:

$$Z = \eta \frac{\lambda^4 10^{18}}{\pi^5 |K|^2} \quad (4.31)$$

where  $K$  is the dielectric factor, and at X-band radars operating at 9.41GHz,  $|K|^2 \approx 0.94$ . Substituting  $Z$  in place of  $\eta$  in Equation 4.30, we get:

$$Z = P_{Vm} r^2 \frac{1024 \lambda^2 \ln(2)}{P_t G^2 G_{rec} \pi^3 c \tau \theta_{3dB}^2 |K|^2} 10^{18} \quad (4.32)$$

By combining all the radar-specific values in the above equation to a single constant, we get:

$$C = \frac{512\lambda^2 \ln(2)}{P_t G^2 G_{rec} \pi^3 \Delta r \theta_{3dB}^2 |K|^2} 10^{24} \quad (4.33)$$

where we use substitution for the range resolution  $\Delta r = c\tau/2$  [m].

Finally, the constant can be applied to the equation estimating volume reflectivity  $Z$  [dBZ]:

$$Z = 10\log 10(P_{vm}) + 20\log(r) - 10\log(\Delta r) + 10\log(C) \quad (4.34)$$

The goal of this subsection was to present the methodology for calculating a radar calibration constant  $C$  and to demonstrate how it is used to estimate radar reflectivity values. Based on the calibration tests performed on the transceiver, parameters such as the transmitted power and receiver gain are adjusted to include losses experienced in the digital receiver and waveguides.

It is important to note that the calibration constant  $C$  is an approximation, as it assumes a perfect balance between  $H$  and  $V$  channels and an ideal rectangular transmitted pulse. An alternative way to estimate the calibration constant is to analyze radar returns from a well-defined reflector [Atlas, 2002]. Since a corner reflector test has not been performed, the above procedure is a good first approximation, and its results are currently implemented in the data processing system. In Table 4.1, we summarize the values of the calibration constants calculated for The University of Iowa Polarimetric Radar Network nodes.

#### 4.4.3 Calculation of polarimetric variables

In its current implementation, the radar data acquisition system does not include a module where collected observables are converted to polarimetric variables. A custom set of functions needed to be programmed to allow for the conversion of radar observables into a set of polarimetric variables such as the radar reflectivity factor for horizontal,  $Z_H$ , and vertical,  $Z_V$ , polarizations, differential reflectivity,  $Z_{DR}$ , differential phase shift,  $\Phi_{DP}$ , and radial velocity information,  $v$ . Polarimetric variables are estimated

based on a pulse-pair processing algorithm (autocovariance processing as opposed to spectral processing).

Based on the “raw” radar files, custom programs calculating polarimetric variables generate separate files for each of the variables. In addition, all the header information is extracted to separate files, which allows for efficient analysis of the header-type data. In the current subsection, a brief summary of the implemented methodology for variable calculation is presented.

#### 4.4.3.1 Radar reflectivity factor:

Reflectivity  $Z$  [dBZ] in both horizontal and vertical polarization is estimated using Equation 4.34. The radar constant  $C$  is calculated separately for each channel based on the transceiver test report and the method presented in subsection 4.4.2.

Differential reflectivity  $Z_{DR}$  (dB) is estimated based on horizontal and vertical reflectivity as:

$$Z_{DR} = Z_H - Z_V \quad (4.35)$$

where horizontal and vertical reflectivity factors are in units of dBZ.

#### 4.4.3.2 Differential phase shift

As suggested by *Mueller* [1984], for autocovariance based processing, the estimator for a two-way differential propagation phase shift [radians] is:

$$\phi_{DP} = \arg(C_{VH}) = a \tan\left(\frac{\text{Im}[C_{VH}]}{\text{Re}[C_{VH}]}\right) \quad (4.36)$$

where  $C_{HV}$  is the cross-correlation between channels  $H$  and  $V$ , as defined in Equations 4.11 and 4.15. The presented form of the differential phase shift calculation is applicable to pulse-pair processing modes (PP and DPP).

The phase shift for a single channel  $\phi_{H,V}$  [radians] can be calculated using the same expression as in 4.36, but we employ the Doppler pulse pair estimates (Equations 4.10 and 4.14) instead of the cross-correlation:

$$\phi_{H,V} = \arg(PP_{H,V}) = a \tan\left(\frac{\text{Im}[PP_{V,H}]}{\text{Re}[PP_{V,H}]}\right) \quad (4.37)$$

#### 4.4.3.3 Radial velocity

In a pulsed radar, the Doppler velocity estimates are based on phase shift estimates (Equation 4.37) rather than directly on frequency change. This is because for carrier frequencies close to 10 GHz, the actual Doppler frequency shift caused by hydrometeors is relatively small and hard to measure with an acceptable level of accuracy [Abeyssekera, 1998]. Instead, the phase shift between two consecutive pulses is used and the radial velocity can be estimated as:

$$v(r) = \frac{-\lambda}{4\pi T_s} \arg(PP_{H,V}) = \frac{-\lambda}{4\pi T_s} a \tan\left(\frac{\text{Im}[PP_{V,H}]}{\text{Re}[PP_{V,H}]}\right) = \frac{-\lambda}{4\pi T_s} \phi_{H,V} \quad (4.38)$$

where  $T_s$  is the time lag between two consecutive pulses.

The resulting velocity is negative for air motion towards the radar, while positive velocities represent air motion away from the radar.

#### 4.4.3.4 Spectral analysis

For the FFT processing mode (FFT, FFT2 and FFT2I), three spectral moments are estimated based on the power spectrum recorded by the radar. The power spectrum often referred to as the Doppler spectrum is a power-weighted distribution of the radial velocities of the hydrometeors within a resolution volume. Following Cadzow [1982], we implemented estimators for the spectral moments.

The signal power, or the zero moment of the Doppler spectrum, can be related to liquid water content or precipitation rate in a resolution volume.

$$\overline{P_r} = \sum_{-v_{\max}}^{v_{\max}} PS_{H,V} \quad (4.39)$$

where  $\pm v_{\max} = \lambda/4T_s$  defines the Nyquist interval for the summation [Freeman, 2004].

Mean Doppler velocity or the first Doppler moment of the spectrum essentially represents the air motion towards or away from the radar.

$$\overline{v} = \frac{\sum_{-v_{\max}}^{v_{\max}} v_i PS_{H,V}}{\sum_{-v_{\max}}^{v_{\max}} PS_{H,V}} \quad (4.39)$$

Spectral width  $\sigma_v$  is computed as a square root of the second moment about the first moment and is a measure of the velocity dispersion within the resolution volume.

$$\overline{\sigma_v^2} = \frac{\sum_{-v_{\max}}^{v_{\max}} (v_i - \overline{v})^2 PS_{H,V}}{\sum_{-v_{\max}}^{v_{\max}} PS_{H,V}} \quad (4.39)$$

#### 4.4.3.5 Raw I/Q Pairs

Although it requires no additional processing, the set of utilities designed to compute radar variables includes the option to store raw *I/Q* pairs if the radar operator chooses to do so.

#### 4.4.4 Custom data visualization tools

In the process of scientific research and discovery, visual inspection and analysis of data play important roles. This is especially true for the field of weather radar application. Having the ability to visually inspect collected data was the motivation to develop a set of tools capable of producing simple maps of radar-generated variables.

First, the “raw” radar data is converted to polarimetric variables and parsed into separate files, each representing a variable of one type. Based on information stored in

data block headers, information about azimuth, elevation, and time stamp is extracted for any given radar profile.

In the case of volume type data, the files are further separated into individual single-elevation scans (full 360° or a sector scan). If data were collected during the vertically-pointing-radar mode (antenna elevation = 90°), the data are presented as a time series of profiles rather than as a radar-centric, polar map. Figures 4.5 and 4.6 present sample maps with radar variables generated using the utilities introduced in the current section.

#### 4.4.5 Metadata computation

During operational deployment, a network consisting of four radars and overlooking a domain of interest can generate a considerable amount of data over a short period of time. For example, in the case of The University of Iowa Polarimetric Radar Network, when each radar scans with a maximum range ~30km and range gate spacing of 75m, the Pulse-Pair (sum powers) mode will result in a ~180 MB per hour data rate per radar (the actual number may vary based on the type of data post averaging). If raw I/Q pairs are recorded for an FFT mode with 16 pulses per block, this rate can go up to ~96 GB per hour (the actual number may vary based on the type of data post averaging). Vast amounts of recorded data make the process of data analysis difficult. Often, rainfall events represent only a small fraction of the collected datasets, and finding and selecting those events with respect to their intensity can take a considerable amount of time when no additional information is available.

To assist in efficient maintenance and analysis of data collected by The University of Iowa Polarimetric Radar Network, an automatic data acquisition and storage system has been developed. Metadata computation is an integral part of the system, and in the current subsection we provide a brief description of it.

The central data acquisition and storage system periodically checks each network node to determine whether any new data files have been created. If new data files are available in the system, data are compressed and transferred to the central data archive where files are decompressed and quality-controlled. Next, two sets of metadata are calculated.

The first set of metadata focuses on extracting descriptive information. Table 4.2 presents the list of members of the set. Corresponding values are stored in database tables and can serve as a basis for future data search criteria.

The second set of metadata is based on recorded variables. This set is designed to support the process of finding rainfall events that meet specific user-defined criteria. Since the “raw” radar data files do not include polarimetric variables, the metadata module includes procedures that compute the radar variables that are defined in section 4.4.3. Unlike operational networks, The University of Iowa Polarimetric Radar Network does not have a well-defined scanning strategy. Rather, it can be configured to cover a number of scanning patterns. Such flexibility in radar operating modes poses a difficulty in specifying metadata that can provide useful information using the same criteria for a range of operating conditions. Our focus was on information that would help discriminate between rain/no-rain periods and that would also to help distinguish light precipitation events from severe ones. To account for variable maximum radar range and range gate spacing, each metadata is discretized to represent five individual range bins. For any given radar file, the radar range profile is scaled to five equally-spaced range sectors. Data within each sector is processed to represent the maximum, mean, median, and minimum values of a given polarimetric variable. The averaging and/or integration of polarimetric variables occur both in space and time. A 10-minute time-averaging interval has been selected. In Table 4.3, we present a set of metadata that is computed in the data acquisition process. Stored in a relational database, computed metadata can be used to assist in the search for rainfall events that meet user-defined criteria.

#### 4.5 Summary of Chapter 4

In Chapter 4, we introduce The University of Iowa Polarimetric Radar Network by providing its technical specifications and basic design structure. Next, we provide a description of the data acquisition system by illustrating how data files are created and explaining what elements control the process of data acquisition. We also provide the list of parameters that can be controlled by the network's operator to achieve different data processing modes. A description of the structure of radar-generated data files and basic data types creates the basis for custom programs and functions that can be written to support efficient data generation display and storage. We also provide a description of a set of custom utilities that have been programmed to perform a number of tasks, including computation of the radar calibration constant, estimation of polarimetric variables, customization of visualization tools, and metadata computation. Finally, we provide examples of how the programs can be used to support efficient data analysis, display, and storage.



Figure 4.1: X-band polarimetric radar network node at Iowa City landfill.

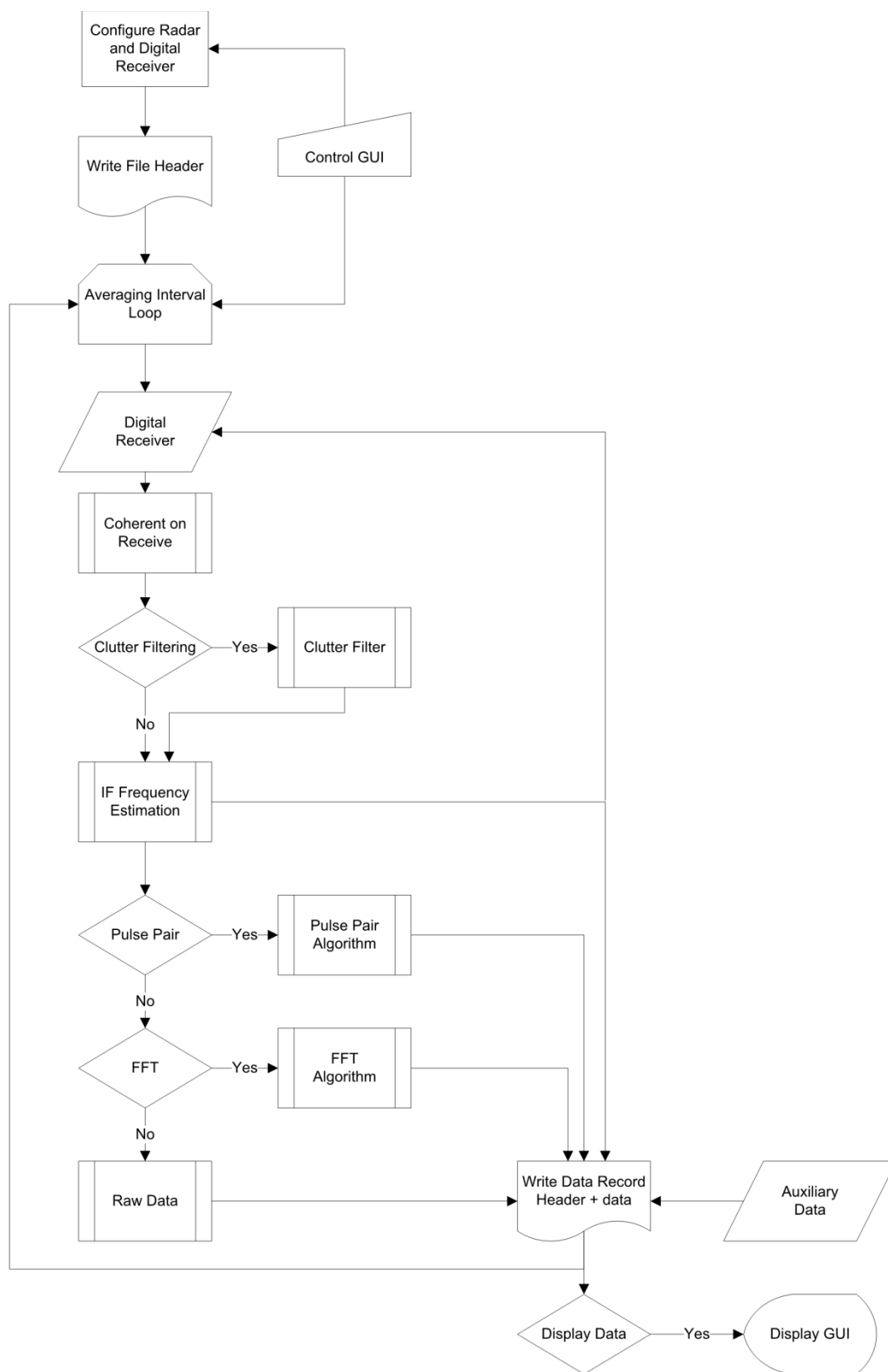


Figure 4.2: Data acquisition algorithm flow chart.

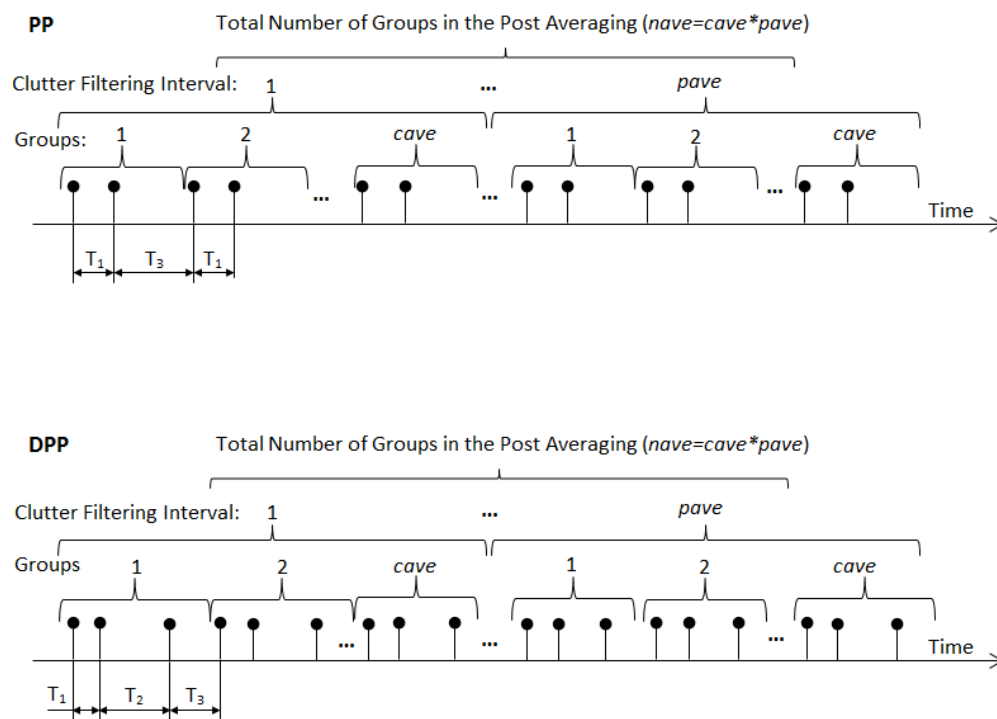


Figure 4.3: Pulse-Pair and Double Pulse-Pair Mode pulsing sequences.

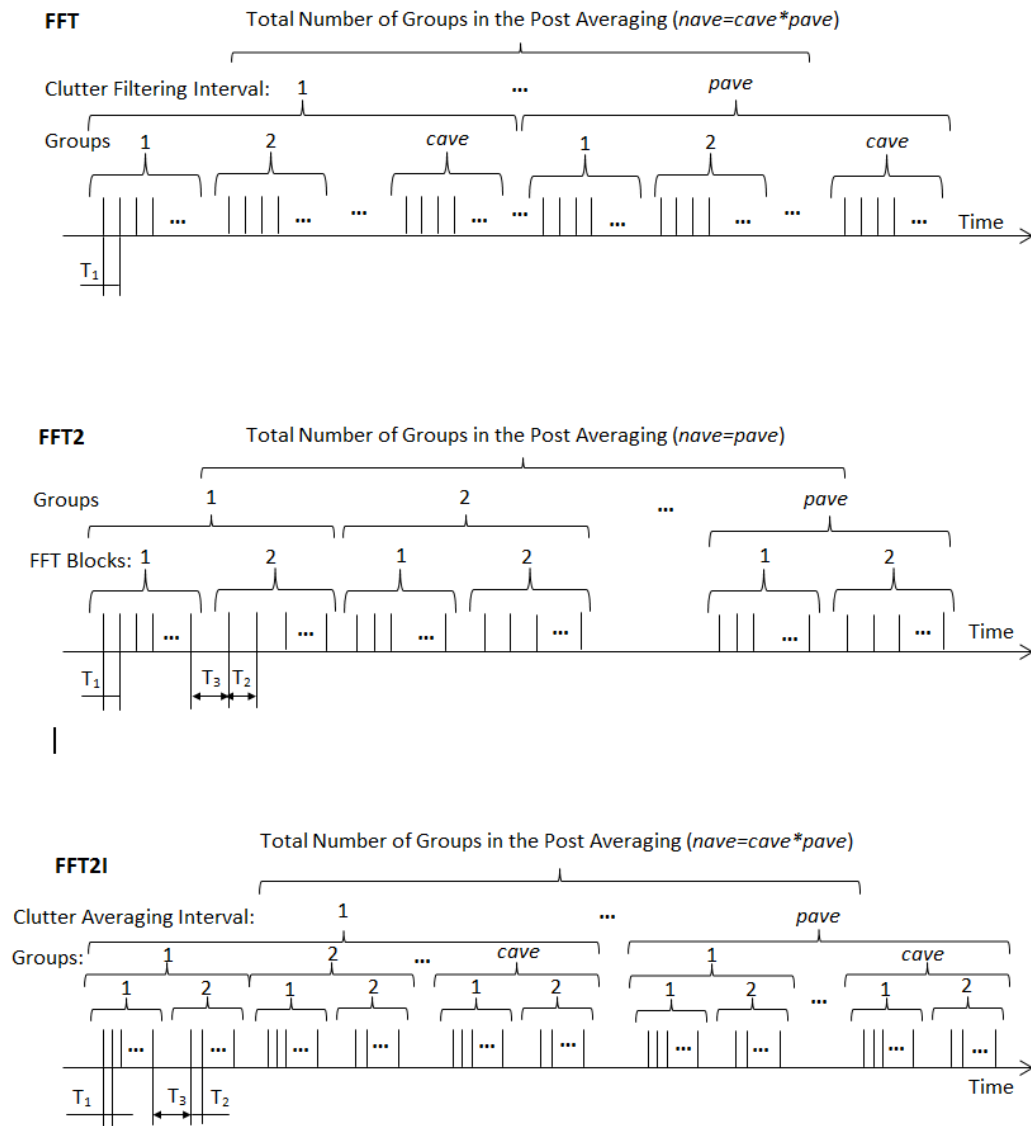


Figure 4.4: FFT Mode pulsing sequences.

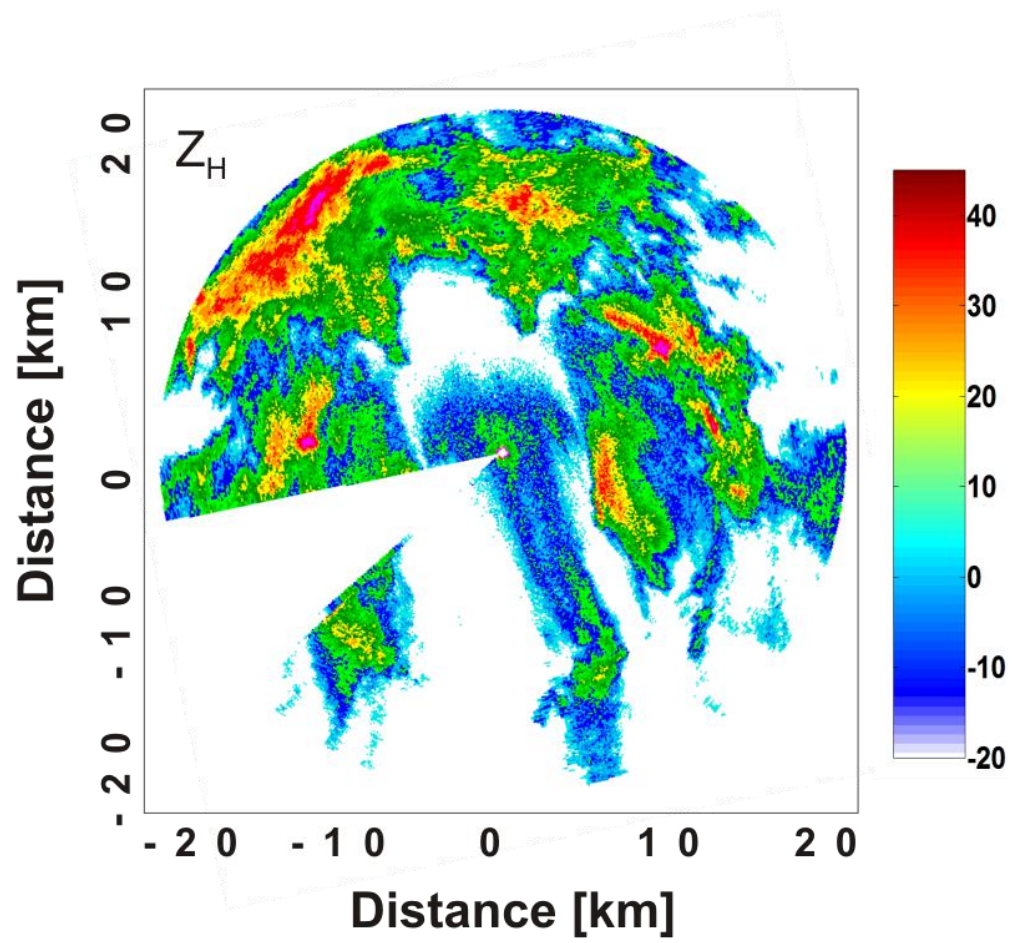


Figure 4.5: Sample data visualization product. Horizontal reflectivity,  $Z_H$  polar plot.

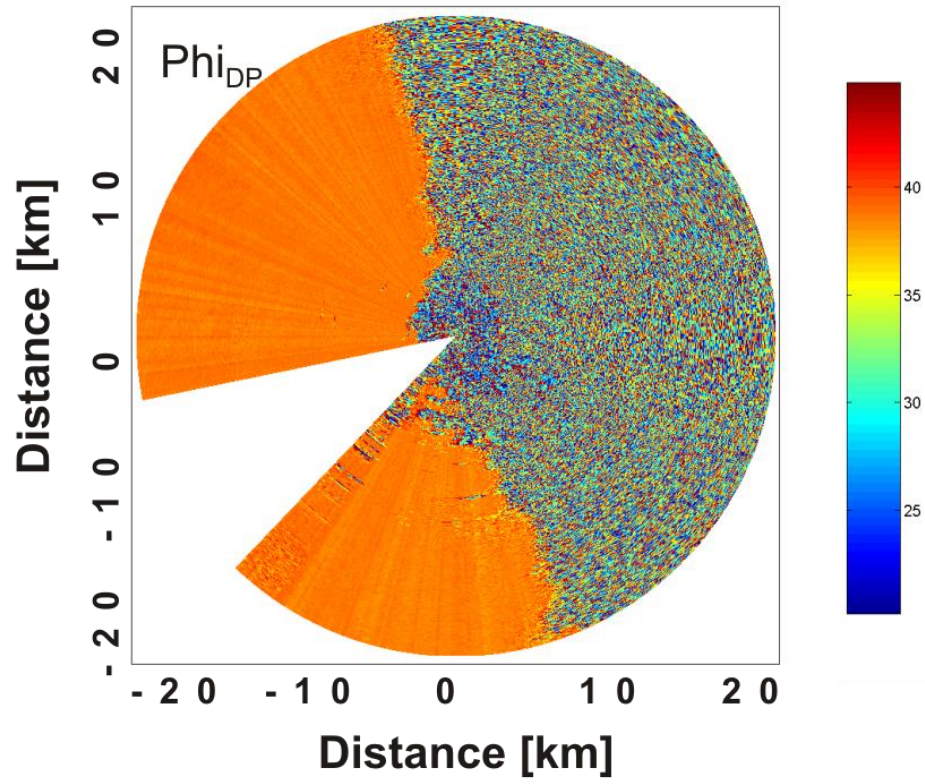


Figure 4.6: Sample data visualization product. Differential phase shift  $\Phi_{DP}$ .

Table 4.1: Values of radar constant  $C$  for individual radars.

<b>Radar</b>	<b>XPOL-2</b>		<b>XPOL-3</b>		<b>XPOL-4</b>		<b>XPOL-5</b>	
<b>Channel</b>	H	V	H	V	H	V	H	V
<b>Radar Constant</b>	66.50	65.05	64.90	64.90	65.54	64.14	66.58	65.30

Table 4.2: Members of descriptive metadata table.

<b>Name</b>	<b>Value example</b>	<b>Description</b>
File_name	XPOL-20110417-230554	Name of file
UTC_time	20110418 04:05:28	UTC time of the first record in file
Radar_id	XPOL-5	Radar name
Site_info	Cedar Rapids airport	User defined information
Lat	39.451	Radar latitude [decimal degrees]
Lon	-91.654	Radar longitude [decimal degrees]
Emperiment	Wet Radome Test	User defined experiment info
Azimuth_offset	25	Radar orientation with respect to North [degrees]
Max_range	22.5	Maximum sampled range [km]
No_gates	300	Number of range gates
Gate_size	75	Size of range gate [m]
Server_mode	PP	Pulse sequence [PP,DPP, FFT, FFT2. FFT2I]
Sum_powers	0	Sum powers in PP mode? [0=No,1=Yes]
Rec_raw	0	Record I/Q pairs? [0=No,1=Yes]
Dig_rec_filter	5	Bandwidth of receiver filter [20,10,5,2,1][MHz]
Clutter_filter	1	Clutter Filter (on/off)
No_rays	7000	Number of rays in file
Data_rate	10	Number of rays per second
Antenna_mode	5	Scanning mode [1=Point, 2=PPI, 3=RHI, 4=azimuth raster, 5=elevation raster, 6=volume]

Table 4.3: Members of hydrologic metadata. Rays are subdivided into 5 sectors; only first sector (bin1) is presented in the table. Every member with name ending with “avg” is based on 10-minute average. Members are calculated for PP and DPP modes.

<b>Name</b>	<b>Value example</b>	<b>Description</b>
Max_ZH_bin1	67.23	Maximum reflectivity observed in the first sector [dBZ]. Range is divided in 5 sectors
Max_ZH_bin1_avg	40.13	Same as Max_ZH_bin1 but averaged over 10 minutes.
Mean_ZH_bin1_avg	23.24	Mean reflectivity [dBZ]
Min_ZH_bin1	-37.00	Minimum reflectivity [dBZ]
Min_ZH_bin1_avg	-10.74	Same as Min_ZH_bin1 but averaged over 10 minutes.
Std_ZH_bin1_avg	20.04	Standard deviation of reflectivity in sector 1 [dBZ]
Max_ZDR_bin1	3.42	Maximum differential reflectivity observed in the first sector [dB].
Max_ZDR_bin1_avg	1.18	Same as Max_ZH_bin1 but averaged over 10 minutes.
Mean_ZDR_bin1_avg	0.24	Mean differential reflectivity [dB]
Min_ZDR_bin1	-3.22	Minimum differential reflectivity [dB]
Min_ZDR_bin1_avg	-0.92	Same as Min_ZDR_bin1 but averaged over 10 minutes.
Std_ZDR_bin1_avg	3.05	Standard deviation of differential reflectivity in sector 1 [dB]

## CHAPTER 5

### CALIBRATION OF THE UNIVERSITY OF IOWA POLARIMETRIC RADAR NETWORK

#### 5.1 Introduction

Establishing a network of four polarimetric, mobile, X-band radars requires a multi-phase effort. Before field deployment, network radars must undergo rigorous testing and calibration processes. Testing should be performed under a variety of climatological conditions to evaluate the effect of the environment on the network's performance, and calibration should be conducted periodically to track any changes occurring over time. Depending on the deployment strategy, network nodes should be positioned to provide optimal coverage of the domain of interest and to maximize the network's functionality. Each radar site must meet specific criteria: high elevation, an unobstructed view of the domain of interest, ease of access, public safety from microwave radiation, proximity to electrical power, and internet access. Understanding the signal processing steps and the data collection process, the available operation modes, and the capabilities and limitations of the radars are all necessary for proper network operation.

A number of calibration tests were performed to prepare The University of Iowa Polarimetric Radar Network for operational deployment. First, the network's manufacturer, ProSensing, Inc, completed the transceiver and antenna tests. Upon arrival in Iowa City, the network's mechanical functionality was assessed through a number of tests including different antenna scanning strategies and sample data collection tests. To further examine the network's performance, inter- and cross-calibration tests were conducted at the Iowa City landfill, which serves as one of the deployment sites for the network.

The goal of the inter-calibration procedure is to determine whether there is a systematic imbalance between the  $H$  and  $V$  channels of the individual network nodes. Any imbalance in alternatively polarized channels can lead to an erroneous estimation of polarimetric variables and can, consequently, adversely affect the quality of the network's performance. Because the most promising rainfall estimation and attenuation correction methods are based on polarimetric observables [e.g., *Carey et al.*, 2000; *Brandes et al.*, 2001; *Gorgucci et al.*, 2001; *Matrosov et al.*, 2002], any channel imbalance would directly affect the performance of the methods and should be eliminated prior to operational deployment.

Even though all the network's nodes are identical in their design and have been built to perform identically in all conditions, it has been shown that significant differences in the calibration and performance of weather radars can be observed over time [*Seo et al.*, 2011].

The cross-calibration test aims to evaluate the level of agreement (or disagreement) between individual network nodes when radars are collocated and make simultaneous observations of precipitation, targeting essentially the same resolution volume.

The following section describes the inter-calibration and cross-calibration experiments. First, we give an overview of the experiment's design and follow with a presentation of the obtained results. In the summary, we discuss the experiment's results.

## 5.2 Experiment design

The change in raindrop oblates with increasing equivolumetric drop diameter is the fundamental phenomenon behind radar polarimetry [*Bringi and Chandrasekar*, 2002]. From a radar's perspective, this effect becomes less pronounced as the radar antenna elevation changes from horizontal to vertical due to the fact that the horizontal cross-section of falling drops is approximately circular regardless of drop diameter,

unless significant canting of drops occurs due to the advection of the precipitation system and/or strong air turbulence.

The effect of advection or strong winds and, therefore, the raindrop mean canting angle can be minimized if the radar's antenna rotates in the azimuthal direction while pointing vertically at a 90° elevation. Thanks to the mechanical design that includes a rotary joint and flexible waveguides, The University of Iowa Polarimetric Network radars can maintain azimuthal antenna rotation regardless of the antenna's elevation angle value. This allowed us to test the assumption that power received by horizontal and vertical channels should be approximately equal for a vertically-pointing radar maintaining azimuthal antenna rotation. Any systematic imbalance between the horizontal and vertical channels can become a source of error in polarimetric variable estimation and should be eliminated before operational deployment.

To test the above assumption, we positioned three network nodes at the Iowa City landfill, a deployment site located just outside of Iowa City. During the experiment, radars were pointing vertically at a 90° elevation with an antenna angular rotation speed equal to 5°/s. The experimental setup with three network nodes located at the Iowa City landfill is shown in Figure 5.1. In the following, we present data collected during the experiment and continue with our analysis and interpretation of the obtained results.

### 5.3 H/V channel imbalance analysis (inter-calibration)

During the early springs of 2010 and 2011, three of the network nodes collocated at the Iowa City landfill observed a number of precipitation events ranging in severity from light stratiform precipitation to strong convective cells. Although the radars are identical in design, for reference, we will refer to the individual nodes as XPOL-2, XPOL-3, and XPOL-5 because those are the “working” code-names of each of the nodes within The University of Iowa hydrometeorology group. During the events, radars sampled the atmosphere with a 30 meter range resolution and the maximum range up to

10 km using the Pulse-Pair processing mode (see Chapter 4 for definition). Collected “raw” data were converted to polarimetric variables, namely horizontal ( $Z_H$ ) and vertical ( $Z_V$ ) radar reflectivity factors that are expressed in units of dBZ.

Polarimetric variables were plotted and visually inspected to distinguish between rain and no-rain periods. Visual inspection of the collected data unveiled a number of features present in the data that needed to be addressed first. In Figure 5.2, we demonstrate what a typical dataset collected for the purpose of this study looks like. Figure 5.2 shows a history of horizontal reflectivity profiles corresponding to approximately one hour of radar data. Besides the clearly visible rain/no-rain periods, other interesting features visible in the figure include the bright band, snow, and ice regions and noise bands visible up to about the 2 km range. In addition, we have discovered that when multiple, collocated radars operate simultaneously, bands of interference can occur. By visually inspecting the collected data, we were able to familiarize ourselves with possible error sources and better design the calibration experiment.

We analyzed a number of precipitation events to test the level of channel balance (or imbalance) for individual network nodes. Below, we present a short description of the selected events and discuss our obtained results.

### 5.3.1 Analysis of the XPOL-2 node

To estimate the  $H/V$  channel imbalance for the network node referred to as XPOL-2, we selected three rainfall events occurring on three separate days and ranging in severity from light stratiform to strong convective. The first analyzed event started on the 20<sup>th</sup> of May 2011 at approximately 21:30 UTC and lasted about 4.5 hours or until 02:00 UTC on the 21<sup>st</sup> of May 2011. The XPOL-2 radar was set to record 288 range bins for every profile with a 30 meters spatial resolution and resulted in a total observable range of 8.64 km. The effective data recording rate was equal to 8 reflectivity profiles

per second. The pulse length was set to 60 m. The antenna rotation speed for all of the discussed cases was 5°/s. Figure 5.3 shows a time series of radar profiles corresponding to approximately one hour of recording. The event can be characterized as moderate with periods of stronger, convective precipitation followed by a steady, uniform rainfall. It can be seen that stronger reflectivity values corresponding to the melting layer of the system are visible at approximately 3.5 km above the ground. We compared the reflectivity values recorded by the horizontal channel to the values recorded by the vertical channel for the rainy periods where reflectivity in both channels was greater than 15 dBZ and less than 45 dBZ. This allowed us to eliminate data corresponding to non-rainy conditions as well as data that could possibly be contaminated with hail or non-meteorological targets (birds, insects, planes, etc.). We selected approximately 40,000 values for every range gate from ranges mostly below the bright band zone, which translates to ~1 hour and 25 minutes of equivalent radar data.

Figure 5.4 presents the mean horizontal and vertical radar reflectivity factor values [dBZ] as a function of range [km]. Figure 5.5 illustrates the average difference between the channels and is represented as a mean differential reflectivity factor  $Z_{DR}$  [dB]. It is important to note that the vertical axis corresponding to height [km] for Figures 5.4 and 5.5 shows a range in elevation from 300 m to 6 km. Below 300 m, the radar experiences a “blind zone” (a distance approximately equal in size to the pulse length when the radar is in a transmission mode) [Sauvageot, 1992]. In addition, for a radar operated at 9.41 GHz and utilizing a 1.8 meter parabolic antenna dish, it takes approximately 250 m for the energy beam to fully form and follow the “far-range” conditions [Doviak and Zrnic, 1993].

When analyzing Figure 5.5, we can observe that, depending on the distance from the radar, the mean  $Z_{DR}$  value oscillates around -0.2 dB. To allow for accurate polarimetric estimates, such a difference should not be greater than 0.1 dB [Matrosov, 2002], which means that a correction factor must be applied to the radar’s reflectivity

estimates for the given event. Since no reference observations were available, the correction factor was arbitrarily selected to equally affect both channels. For XPOL-2, the correction factor for channel  $H$  was set at 0.1 dBZ, and for the channel  $V$  it was set to -0.1 dBZ. To verify the presented results, we analyzed two additional rainfall events that were recorded by the XPOL-2 node.

On April 21<sup>st</sup>, 2011, XPOL-2 operated for almost four hours in a vertically pointing mode from approximately 19:30 UTC to 23:30 UTC. The rainy period within the recorded window lasted only ~30 minutes and consisted of a moderate event with a melting layer at approximately 2.7 km altitude. The radar was set to record 192 range bins for every profile, with a 30 meter spatial resolution resulting in a total observable range of 5.76 km. The effective data recording rate was equal to 8 reflectivity profiles per second. The pulse length was set to 60 m. We converted the recorded data to horizontal and vertical radar reflectivity factor values and calculated the mean profile of differential reflectivity using only those bins where both channels' recorded values were greater than 15 dBZ but lower than 45 dBZ. With close to 8000 data points per range gate, mostly associated with ranges above the melting layer, the collected dataset corresponds to ~17 minutes of equivalent rainfall. In Figure 5.6, we compare the results for the individual channels. The highly varying character of reflectivity profiles up to 1.5 km in range can be explained by a very limited data sample for ranges close to the radar. On the other hand, the observed system provided a substantial amount of data for ranges above the melting layer and is primarily associated with randomly-oriented ice particles and snow.

The third analyzed event was recorded the following day on April 22<sup>nd</sup>, 2011 from 12:45 UTC to 15 UTC with the rainy period lasting approximately 90 minutes. The event was similar in nature to the previous one, with the melting layer at ~2.7 km. The radar was set to record 256 range bins for every profile, with a 30 meter spatial resolution resulting in the total observable range of 7.76 km. The effective data recording rate was

equal to 8 reflectivity profiles per second. The pulse length was set to 60 m. The recorded data was converted to horizontal and vertical radar reflectivity factor values, and the mean profile of differential reflectivity was calculated using only those bins where both channels' recorded values were greater than 15 dBZ but lower than 45 dBZ. We selected close to 20,000 values per range gate or ~40 min of equivalent rainfall, mostly corresponding to ice and snow regions, for analysis. Figure 5.7 presents the obtained profiles for reflectivity. The mean differential reflectivity profiles for all three analyzed cases are presented in Figure 5.8. Based on the obtained results, the XPOL-2 radar can be characterized by a channel imbalance that varies between -0.9 dBZ and -0.1 dBZ.

### 5.3.2 Analysis of the XPOL-3 node

To analyze the channel imbalance for the network node referred to as XPOL-3, we selected four separate events that were recorded during the month of April 2011. The first analyzed event was recorded on the 18<sup>th</sup> of April 2011 starting at approximately 04:00 UTC and lasting about 3.5 hours or until about 07:30 UTC on the same day. In Figure 5.9, a time series of radar profiles corresponding to approximately one hour of recording is shown. The event was a steady stratiform system. The melting layer was observed at approximately 1.8km, which is consistent with a typical mid-latitude stratiform precipitation system [Martin, 2006]. The XPOL-3 radar was set to record 288 range bins for every profile with a 30 meter spatial resolution, resulting in a total observable range of 8.64 km. The effective data recording rate was equal to 11 reflectivity profiles per second. The increased number of profiles recorded per second was a result of a lower number of pulses averaged in the clutter filtering process (6 pulse pairs for cases analyzed with XPOL-2 and 5 pulse pairs for XPOL-3; see section 4.3.3 for the definition of the clutter filtering procedure). The pulse length was set to 60 m.

We compared the reflectivity values that were recorded by the horizontal channel to the values recorded by the vertical channel for the rainy periods where reflectivity in

both channels was greater than 15 dBZ and less than 45 dBZ. Applying the selection criterion resulted in over 80,000 data points per range gate, or 2 hours equivalent of data corresponding to ranges below the melting layer. The mean horizontal and vertical reflectivity values [dBZ] as a function of range [km] are presented in Figure 5.10. Figure 5.11 illustrates the mean differential reflectivity. Depending on the distance from the radar, the mean value oscillates around -0.4 dB, which means that a correction factor must be applied to the radar's reflectivity estimates. It is important to note that the vertical axis in both Figure 5.10 and Figure 5.11 starts at an altitude of 300 m and does not include the radar's blind zone or the ranges where the radar's beam is not fully formed. Similarly to the XPOL-2 case, the correction factor was estimated to equally affect both channels. For XPOL-3, the correction factor for the channel  $H$  was 0.2 dBZ, and for the  $V$  channel it was -0.2dBZ.

To verify the obtained results, we studied three additional cases, and their results are provided below.

On the 15<sup>th</sup> of April, a moderate stratiform rainfall event was recorded by XPOL-3, which was set to collect data for 288 bins with 30 meter range resolution and a data rate of 9.25 rays per second. The melting layer was visible at ~2.4 km altitude. We selected the equivalent of just over one hour of data per range gate from both below and above the melting layer regions. The mean reflectivity values for the  $H$  and  $V$  channels are presented in Figure 5.12.

Two additional recordings obtained on the 21<sup>st</sup> and the 22<sup>nd</sup> of April 2011 used the matching settings with 256 range bins, each corresponding to a 30 meter range resolution and a data rate of 8 rays per second. The selected equivalent rainy periods were 20 min for the event on the 21<sup>st</sup> of April and 40 minutes for the 22<sup>nd</sup> of April and correspond to the area above the bright band regions for both cases. The resulting mean reflectivity profiles for the  $H$  and  $V$  channels are plotted in Figures 5.13 and 5.14.

The mean differential reflectivity profiles for all four analyzed cases are grouped in Figure 5.15 and allow for a direct comparison of the results. As can be observed in the figure, the channel imbalance is present in all of the cases and oscillates between -0.25 and -0.35 dB. The XPOL-3 node showed a rather consistent behavior over many different rainfall regimes, and the measured imbalance can be, to a certain degree, eliminated by introducing a correction factor into both channels.

### 5.3.3 Analysis for the XPOL-5 node

To analyze the channel's imbalance for the network node referred to as XPOL-5, we selected three rainfall events observed in early 2010, which was during the initial network deployment at the Iowa City landfill. The first analyzed event was recorded on the 2<sup>nd</sup> of April 2010 at approximately 18:30 UTC and lasted about 5 hours, or until about 23:30 UTC on the same day. Figure 5.16 shows a time series of radar profiles corresponding to approximately one hour observations. The event can be characterized as a moderate to strong steady rainfall event. The melting layer is visible at approximately 2.3 km. The XPOL-5 radar was set to record 352 range bins for every profile, with a 30 meter spatial resolution resulting in the total observable range of 10.56 km. The effective data recording rate was equal to 16 reflectivity profiles per second. The increased number of profiles recorded per second is a result of a lower number of pulses averaged in the clutter filtering process (3 pulse pairs per group). The pulse length was set to 150 m.

We compared the reflectivity values recorded by the horizontal channel to the values recorded by the vertical channel for the rainy periods where reflectivity in both channels was greater than 15 dBZ and less than 45 dBZ. The range gate bins meeting the selection criterion were associated with ranges below the melting layer. On average, close to 30,000 data points per range gate were selected, which corresponds to ~30 minutes of continuous rainfall. The mean horizontal and vertical reflectivity values

[dBZ] as a function of range [km] are presented in Figure 5.17. Figure 5.18 illustrates the mean difference between the channels. Depending on the distance from the radar, the mean value oscillates around -0.04 dB, which can be considered a well-balanced  $H/V$  pair, and no correction factor was needed for the XPOL-5 node. In Figure 5.17 and Figure 5.18, the vertical axis corresponding to the altitude starts at 300 m elevation. To verify the obtained results, we selected two additional cases for analysis.

On the 24<sup>th</sup> of March 2010, the XPOL-5 node was recording data using 192 range bins and 30 m range resolution based on a 150 m pulse length. The data rate was set to 20 rays per second. With an average of 13,000 data points per range gate, we analyzed ~11 minutes of data coming from ranges below the bright band. The corresponding reflectivity profiles for channels  $H$  and  $V$  are presented in Figure 5.19.

On the 5<sup>th</sup> of April 2010, the same network node was recording data with a range resolution increased to 15 m per gate and a maximum range of 7.68 km. The pulse length was set to 150 meters, and the data rate was set to 20 rays per second. The collected data set provided over 80,000 data points per range gate from regions both below and above the bright band. This resulted in over one hour of equivalent data. We provide the mean reflectivity profiles for both channels in Figure 5.20.

The obtained mean differential reflectivity profiles for all three analyzed cases are grouped in Figure 5.21, which allows for a direct comparison of the results. As it can be observed in the figure, the XPOL-5 node shows only a minimal imbalance, and no correction factor needed to be implemented into the corresponding data.

#### 5.3.4 H/V channel imbalance analysis summary

Three network nodes were collocated at the Iowa City landfill to allow for inter-calibration of individual radar channels for each of the nodes. Data was collected in a vertically pointing mode during rainfall events ranging from stratiform to moderate. Following the assumption that the mean differential reflectivity is expected to be zero for

a vertically pointing radar maintaining a steady azimuthal antenna rotation, we estimated that for two of the nodes, the channels were not balanced and a correction factor needed to be applied. Specifically, the XPOL-2 results varied significantly between the analyzed cases. The XPOL-3 node showed a consistent level of imbalance from case to case, and the XPOL-5 node was the only one where the observed imbalance was minimal and required no correction factor. There is a number of possible reasons for the channels to be out of balance. One explanation is that, over time, separate channels can experience an increase in the internal losses to a different degree. Another possible explanation is the uncertainty in transceiver calibration tests. Based on the analysis presented in section 4.2.2, we can conclude that any error in the transceiver calibration will propagate to the radar constant estimation procedure and can, in turn, cause a systematic difference in the channels' balance. This could explain the systematic differences observed for the XPOL-3 node.

Another important observation is related to how the estimated imbalance changes with range. For all the analyzed cases, large differences between the  $V$  and  $H$  channels were observed up to a distance of approximately 1 km from the radar. A possible explanation for the close-range large differences can be: ground clutter contamination, noise associated with the radar's mechanics, high air turbulence, energy associated with the side lobes interfering with the main lobe, or the process of beam formation. Also, we found that, when available, regions above the melting layer associated with randomly distributed ice and snow particles can provide an excellent target for the calibration of the  $H/V$  channels' balance. The area above the melting layer is usually at least 2 km away from the radar, which allows for minimal ground clutter contamination and a fully formed beam. Also, often with no precipitation on the ground, scanning above the cloud condensation level can provide a significant amount of reflectivity for a calibration test.

For polarimetric radars, the balancing of individual channels is a factor that needs to be assessed in preparation for the operational deployment of a network. The presented

procedure can be used periodically to test whether the correction factors need to be adjusted over time. One very important advantage of the presented procedure is the fact that the method does not require additional instrumentation during the test. Polarimetric variables, when estimated using a balanced radar, are not sensitive to relative transceiver calibration.

It is important to note that for all three network nodes, the difference between channels showed little range dependence except in the initial kilometer.

We now move to the cross-calibration experiment in order to study and compare how individual radars agree with each other when they observe essentially the same resolution volume. To evaluate the level of agreement between individual radars and allow for cross-calibration of the network's nodes, we used rainfall events recorded during the early spring of 2011, when three of the network's nodes were collocated at the Iowa City Landfill. Below, we present the results of our analysis.

#### 5.4 Network cross-calibration experiment

Correcting for channel imbalance in individual network radars is an important step that improves polarimetric radar estimates for each of the network's nodes separately.

For a network of radars operated as a single instrument, it is also important to estimate how individual radars compare during a simultaneous observation of essentially the same resolution volume. In the weather radar community, radars whose observations are consistently higher than those made with independent, well-calibrated instruments are referred to as "hot," and they are termed "cold" if they systematically underestimate observations. The application of network-based algorithms for attenuation correction, rainfall estimation, and data merging relies on the assumption that all radars are equally calibrated and balanced with respect to one another. In a situation where one (or more)

of the radars is considerably “hotter” or “colder” than the rest, the network algorithms for attenuation correction and rainfall estimation will be directly affected.

To assess the level of agreement between individual radars, we used data collected during the spring of 2011 by the network nodes collocated at the Iowa City landfill. All three nodes were located within 30 meters of each other, as depicted in Figure 5.1. Clustering of the network nodes was dictated by the assumption that operating radars at such close proximity would, in fact, mean that the radars are essentially sampling the same resolution volume. This assumption is valid in an average sense for steady rainfall events that are observed for extended periods of time [e.g., *Habib et al.*, 2001; *Ciach and Krajewski*, 2006].

Due to technical difficulties experienced during the data collection process, no three network nodes were operational at the same time during the experiment. At most, two radars were collecting data during the same rainfall event. We were able to record a number of events when pairs of vertically pointing radars were collecting data; hence, the study is based on a pair-wise comparison. First, we will compare the XPOL-2 and XPOL-3 nodes and will later analyze XPOL-3 and XPOL-5. The pair-wise comparison should allow for indirect cross-calibration off all three radars participating in the experiment.

#### 5.4.1 The XPOL-2 and XPOL-3 pair

The cross-calibration between the XPOL-2 and XPOL-3 nodes was based on two rainfall events. The first event was recorded on the 21<sup>st</sup> of April, and the second event occurred the following day on the 22<sup>nd</sup> of April 2011. Little precipitation occurred on the ground for both events; hence, the analysis is based on data corresponding to the ranges above the cloud condensation levels. Both radars were set to operate in a matching mode. Specifically, the range resolution was set to 30 meters, the maximum sampled range was 5.76 km, the pulse length was 60 m, and the antenna rotation speed was 5°/s.

Visual inspection of the collected data allowed us to identify regions where radar interference was occurring. The interference regions were subsequently eliminated from the analysis. Following the same strategy as for the inter-calibration tests, we selected only those range gates where the reflectivity for both channels was greater than 15 dBZ and less than 45 dBZ. Before making a direct radar comparison, we corrected the *H/V* channel imbalance in both radars by taking the arithmetic mean of their estimates. An approximately 20 min data equivalent was selected from the event occurring on the 21<sup>st</sup> of April, and the obtained results are presented in Figure 5.22, where mean reflectivity profiles as calculated for individual radars are shown. Figure 5.23 shows the mean reflectivity profile based on data collected during the April 22<sup>nd</sup> event. As in the previous case, reflectivity profiles are calculated as a mean value from the *H* and *V* channels. The difference between the XPOL-2 and XPOL-3 nodes in reflectivity estimation for both cases is presented in Figure 5.24. The large difference for regions below 3km in range is the result of little precipitation occurring on the ground and data from those regions being dominated by noise. When analyzing the results, we can observe that for both the 21<sup>st</sup> and 22<sup>nd</sup> of April cases, for regions above the bright band, the radars show a consistent difference in reflectivity estimation oscillating around 0.2 dBZ, with the XPOL-3 radar being “hotter” than the XPOL-2 node.

#### 5.4.2 The XPOL-3 and XPOL-5 pair

The cross-calibration analysis of the XPOL-3 and XPOL-5 pair is based on two events occurring on the 12<sup>th</sup> and 13<sup>th</sup> of November, 2010. The radars were collocated at the Iowa City landfill, and the scanning strategy for both radars was as follows. The radars operated in a vertically pointing mode with antennas rotating at 5°/s angular velocity. The pulse length for both radars was set to 150 meters, with a range gate resolution of 75 m and a 12 km maximum sampled range. Implementing the Pulse-Pair mode resulted in a 9.25 ray per second data rate. Since both events occurred when radars

were continuously collecting data, we chose to analyze them together as a single rainfall case. During the visual inspection process, we removed the reflectivity profiles associated with radar interference. Application of the same selection criterion for reflectivity values greater than 15 dBZ and less than 45 dBZ resulted in an average of 75,000 data points per range gate, which is equivalent to two hours of rainfall data associated with ranges from the radar to the melting layer zone.

For both radars, the estimates of horizontal and vertical reflectivity profiles were first averaged to eliminate any channel imbalance. Figure 5.25 shows the averaged reflectivity profiles for both radars. The difference between the calculated profiles oscillates around the 0.5 dBZ value, as shown in Figure 5.26.

### 5.5 Summary of Chapter 5

During the initial deployment of The University of Iowa Polarimetric Radar Network, three of the network's nodes were collocated at a test site located at the Iowa City landfill. The radars were positioned within 30 meters of each other and operated in a vertically-pointing mode. This experimental design was intended to allow for the network's inter- and cross-calibration tests. The inter-calibration focused on the estimation and, subsequently, the elimination of any systematic imbalance between the radars' horizontally and vertically polarized channels. The cross-calibration procedure was intended to assess the extent to which the estimates of the radar reflectivity factor vary from radar to radar when each of the nodes is sampling essentially the same resolution volume.

Both procedures are important quality control steps and should be performed periodically to assure the accurate application of rainfall estimation methods, hydrometeor classification algorithms, or attenuation correction procedures, as all are directly linked to the inter- and cross-calibration results.

Based on the analyzed events, we estimated the imbalance between horizontally and vertically polarized channels for the XPOL-2, XPOL-3, and XPOL-5 network nodes. In addition, we conducted a pair-wise analysis of reflectivity profiles for the XPOL-2, XPOL-3, and XPOL-5 pairs.

The analysis points out that although identical in their design, the radars show discrepancies in reflectivity estimation that needs to be addressed before their operational deployment. The findings for the inter-calibration tests revealed the XPOL-5 radar to be the only one that could be considered balanced. While the XPOL-3 radar showed a systematic imbalance with moderate oscillations that could be modified by implementing a correction factor, the XPOL-2 radar showed behavior that is difficult to correct due to the imbalance between the V and H channels that fluctuated considerably between the analyzed rainfall events. The cross-calibration experiment further amplified the need for periodic calibration tests, with individual radars showing differences in reflectivity estimation that should be corrected before their operational deployment.

In the course of the experiment, we employed a number of previously-developed custom tools for data processing, display, and analysis.



Figure 5.1: Radars of the University of Iowa Polarimetric Radar Network at the Iowa City landfill during the calibration experiment (April 2011).

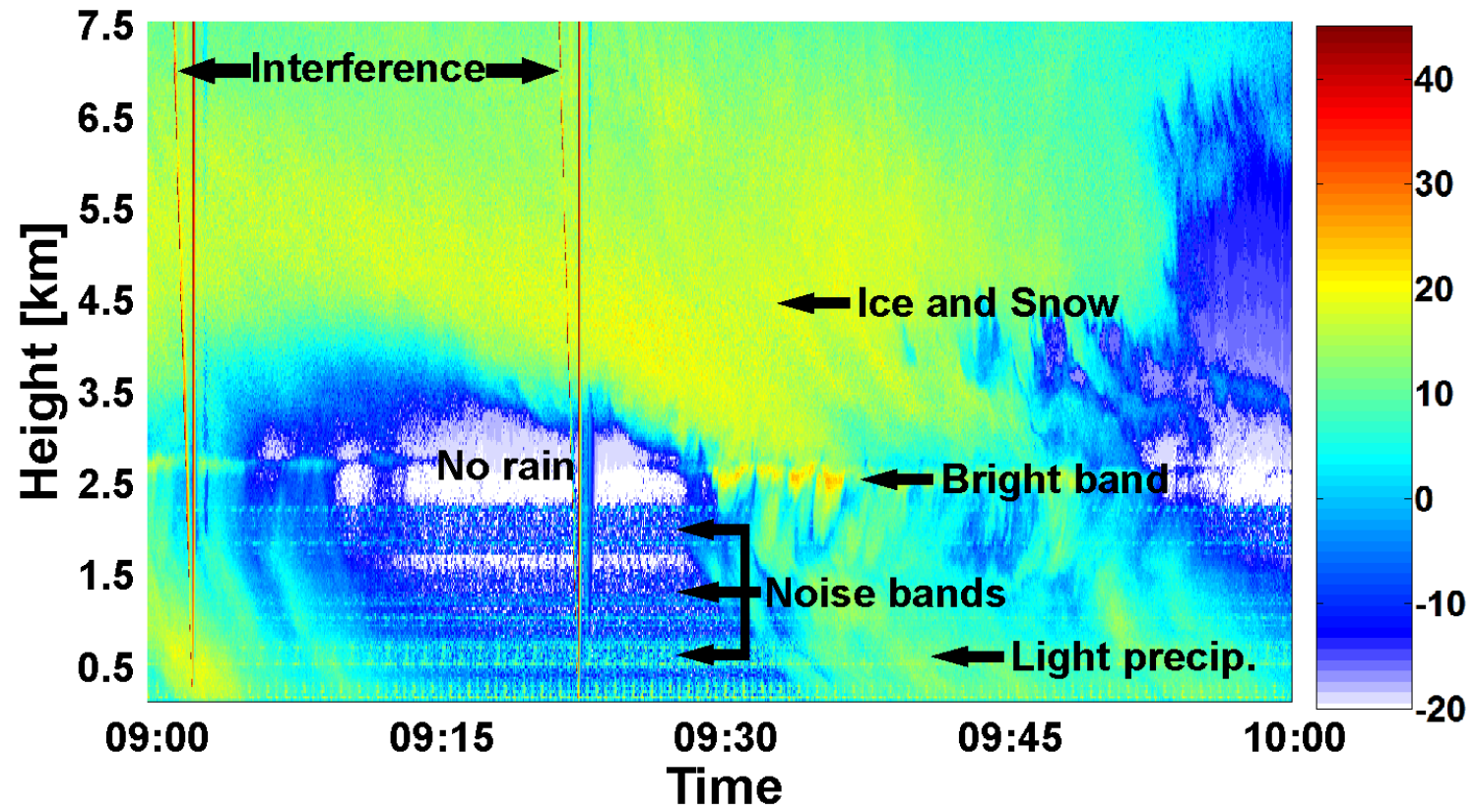


Figure 5.2: Example of a time series of reflectivity profiles collected during the calibration experiment.

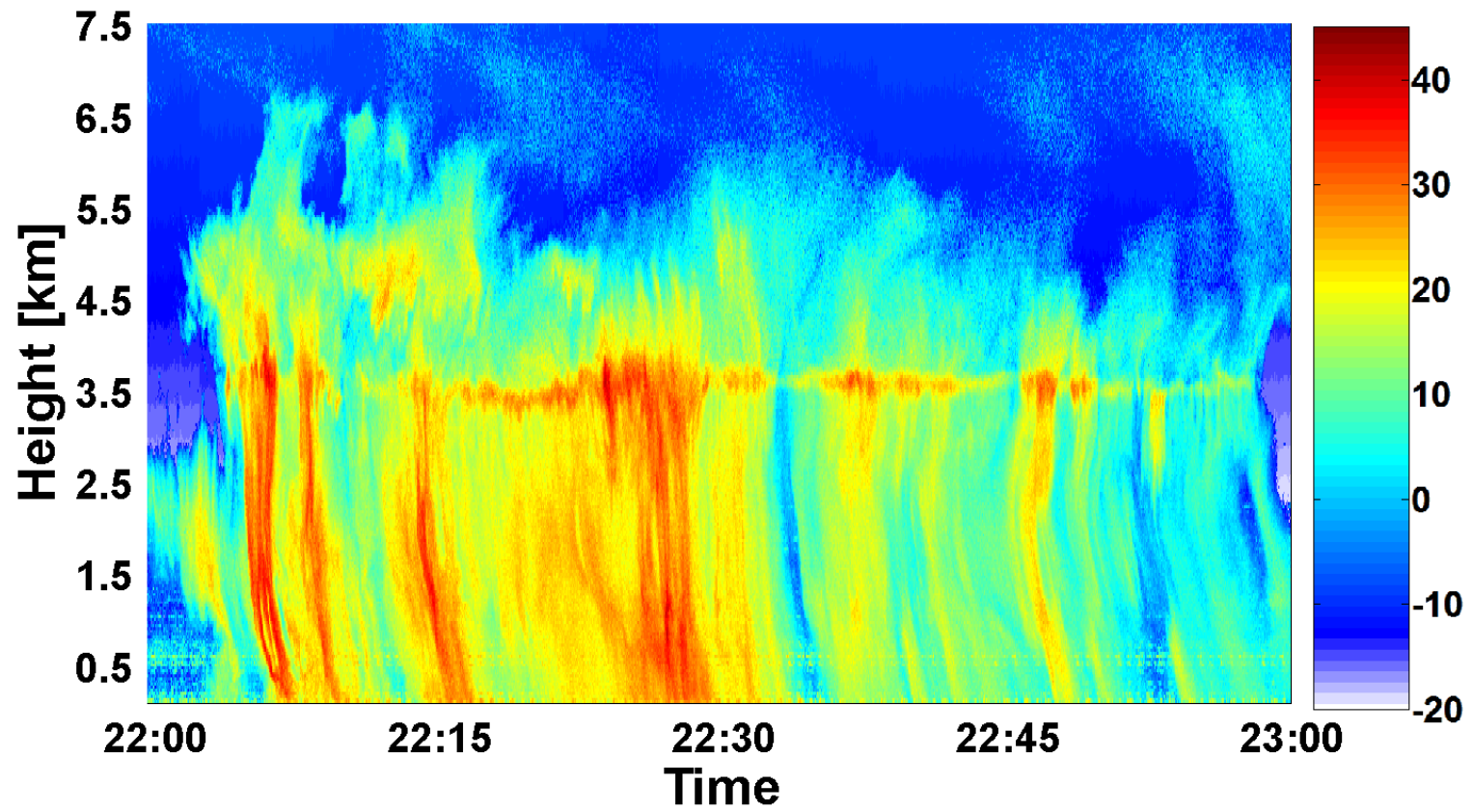


Figure 5.3: Time series of reflectivity profiles recorded by the XPOL-3 node on 05/20/2011 at the Iowa City landfill.



Figure 5.4: Mean reflectivity profiles for horizontal  $Z_H$  and vertical  $Z_V$  reflectivity recorded on 05/20/2011 by the XPOL-2 radar.

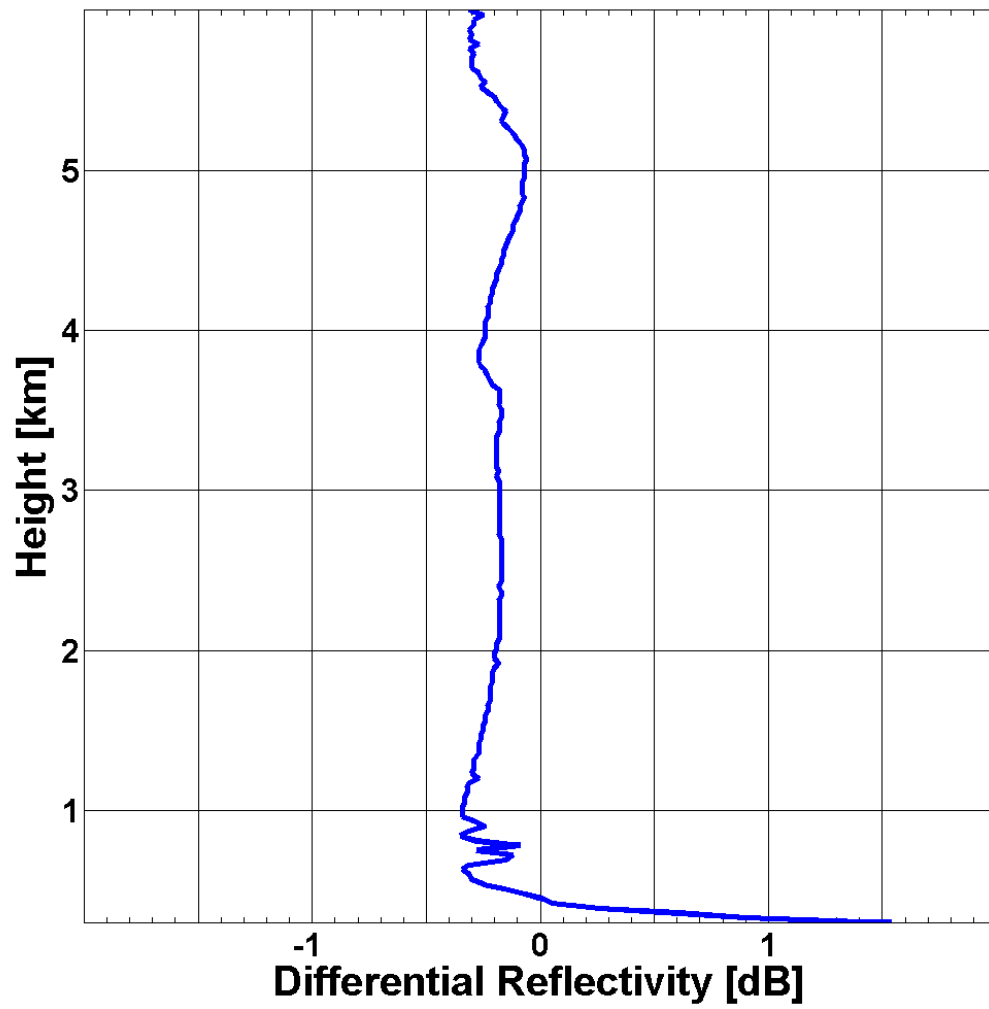


Figure 5.5: Mean differential reflectivity  $Z_{DR}$  profiles recorded on 05/20/2011 by the XPOL-2 radar.

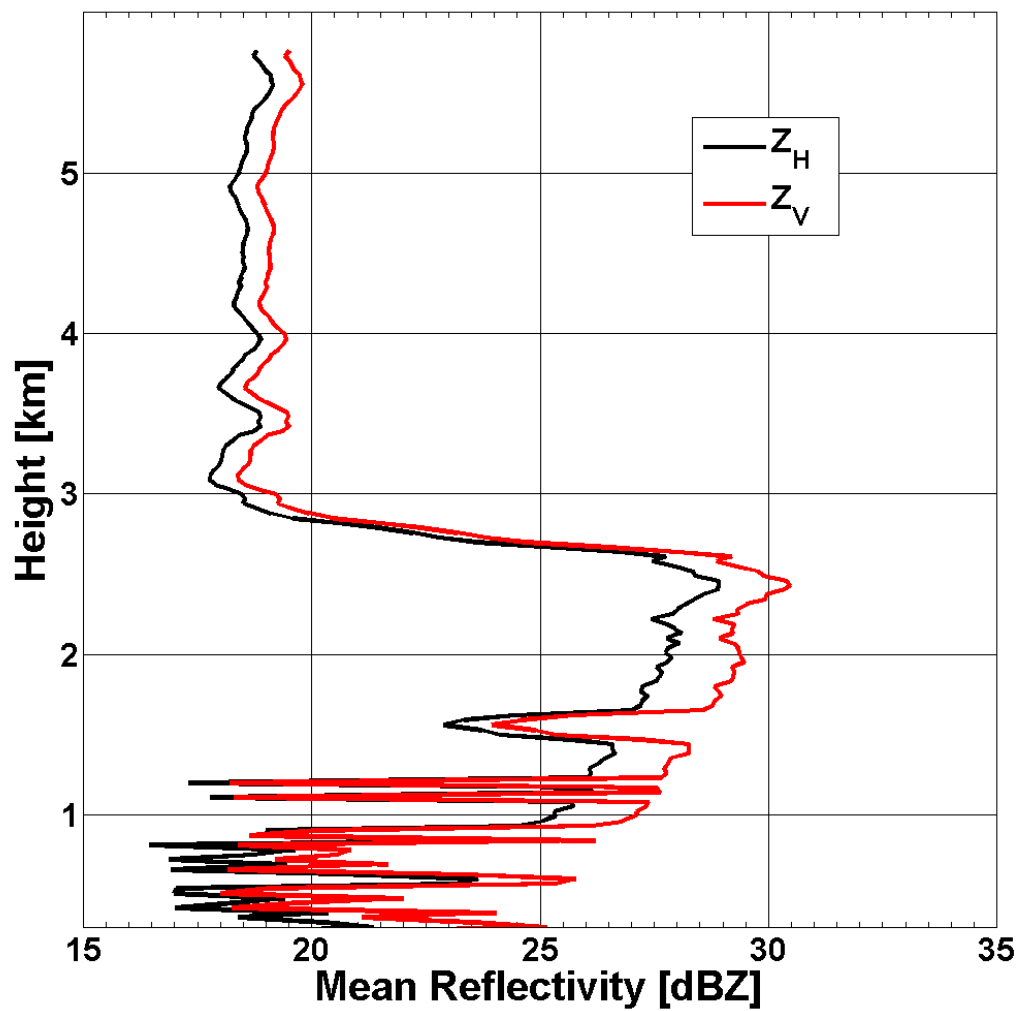


Figure 5.6: Mean reflectivity profiles for horizontal  $Z_H$  and vertical  $Z_V$  reflectivity recorded on 04/21/2011 by the XPOL-2 radar.

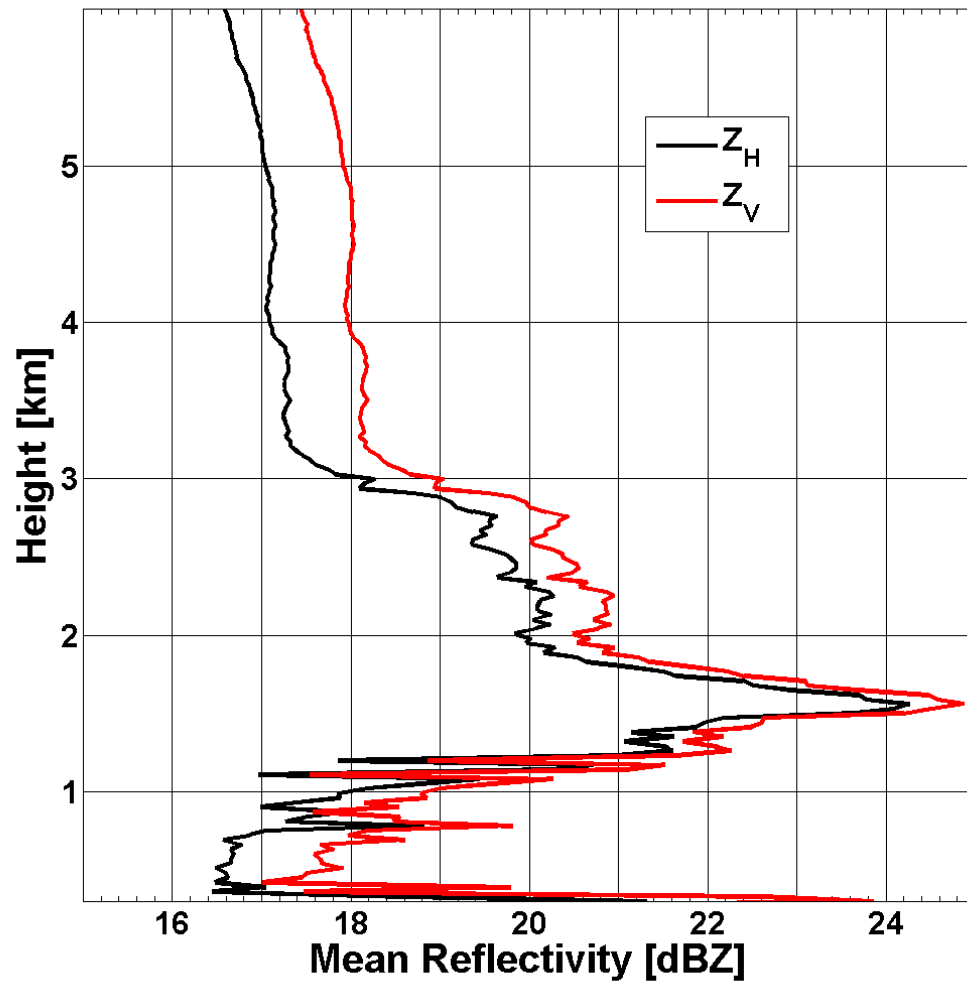


Figure 5.7: Mean reflectivity profiles for horizontal  $Z_H$  and vertical  $Z_V$  reflectivity recorded on 04/22/2011 by the XPOL-2 radar.

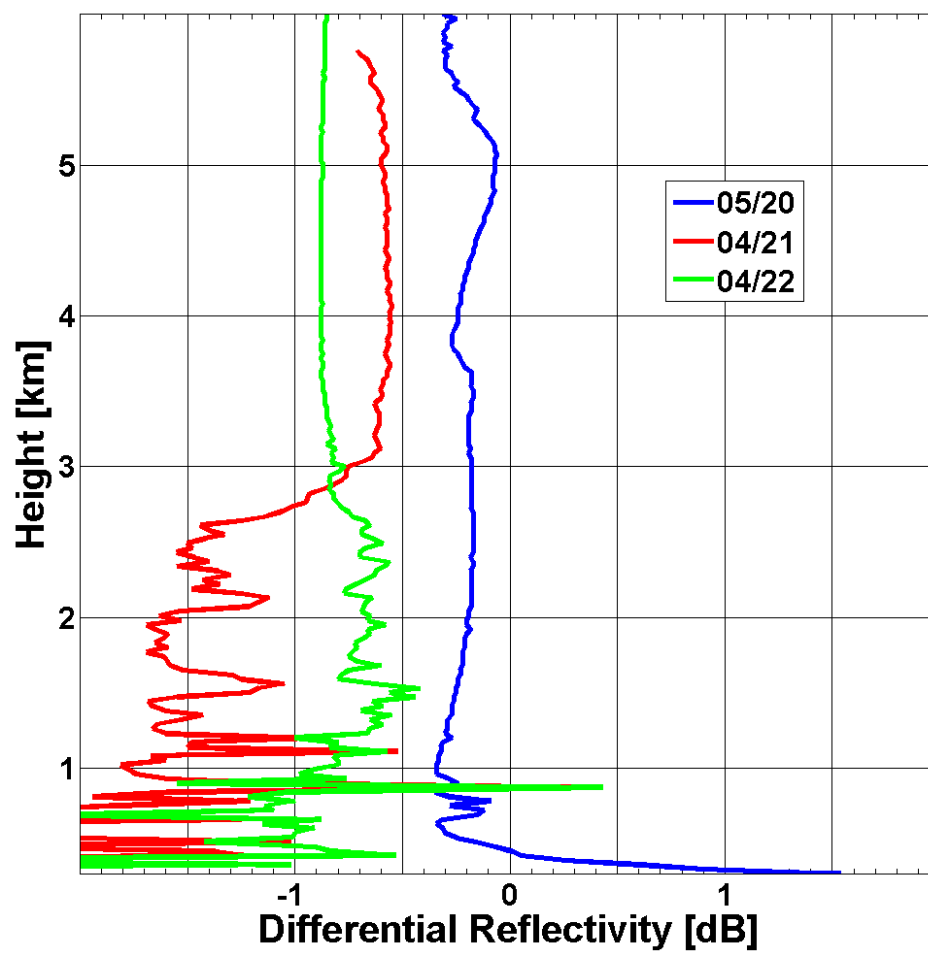


Figure 5.8: Mean differential reflectivity profiles for the three analyzed cases recorded by the XPOL-2 radar.

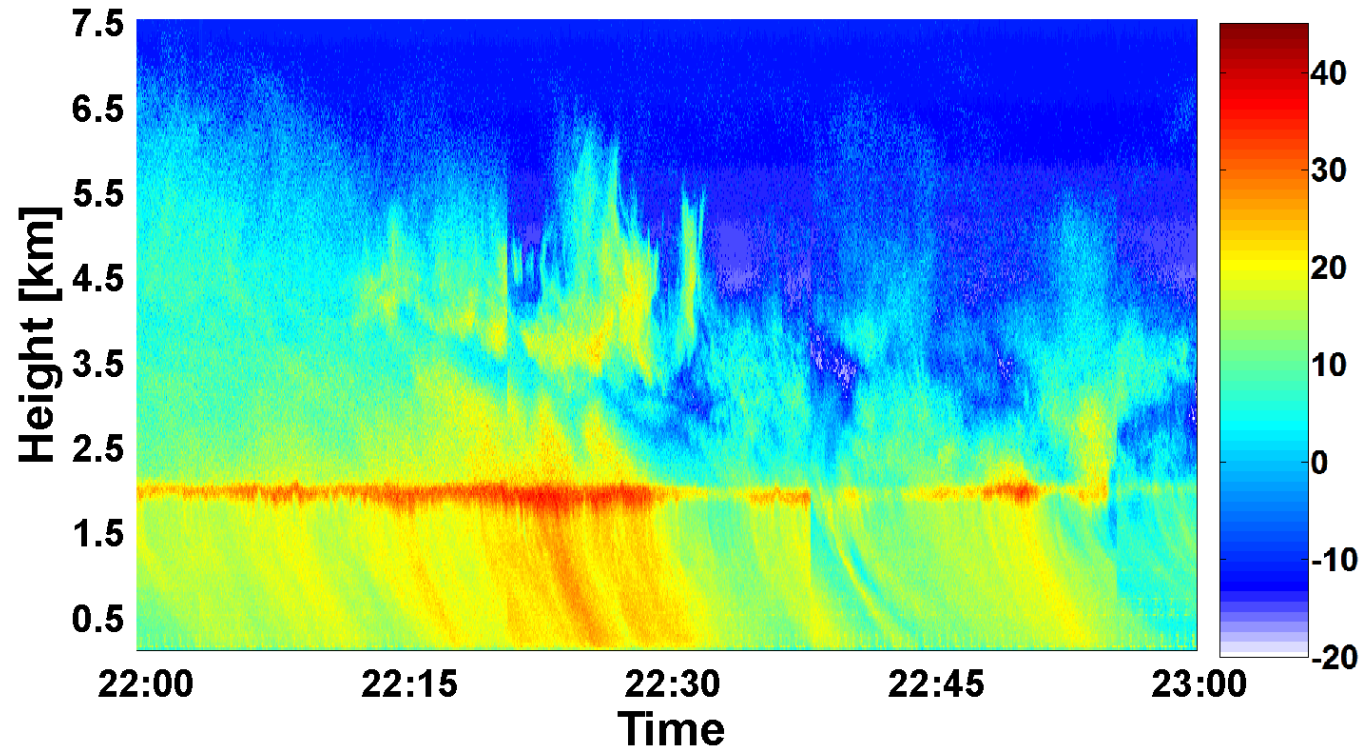


Figure 5.9: Time series of reflectivity profiles recorded by the XPOL-3 node on 04/18/2011 at the Iowa City landfill.

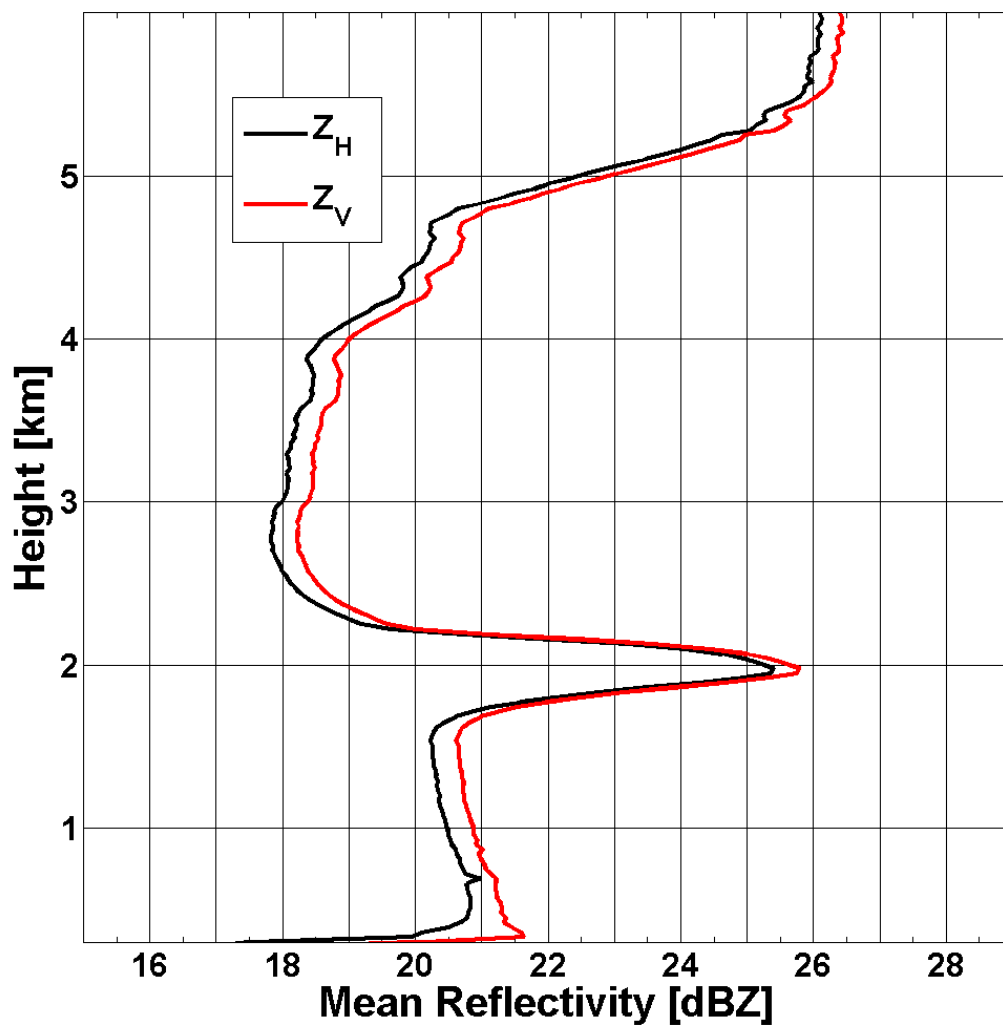


Figure 5.10: Mean reflectivity profiles for horizontal  $Z_H$  and vertical  $Z_V$  reflectivity recorded on 04/18/2011 by the XPOL-3 radar.

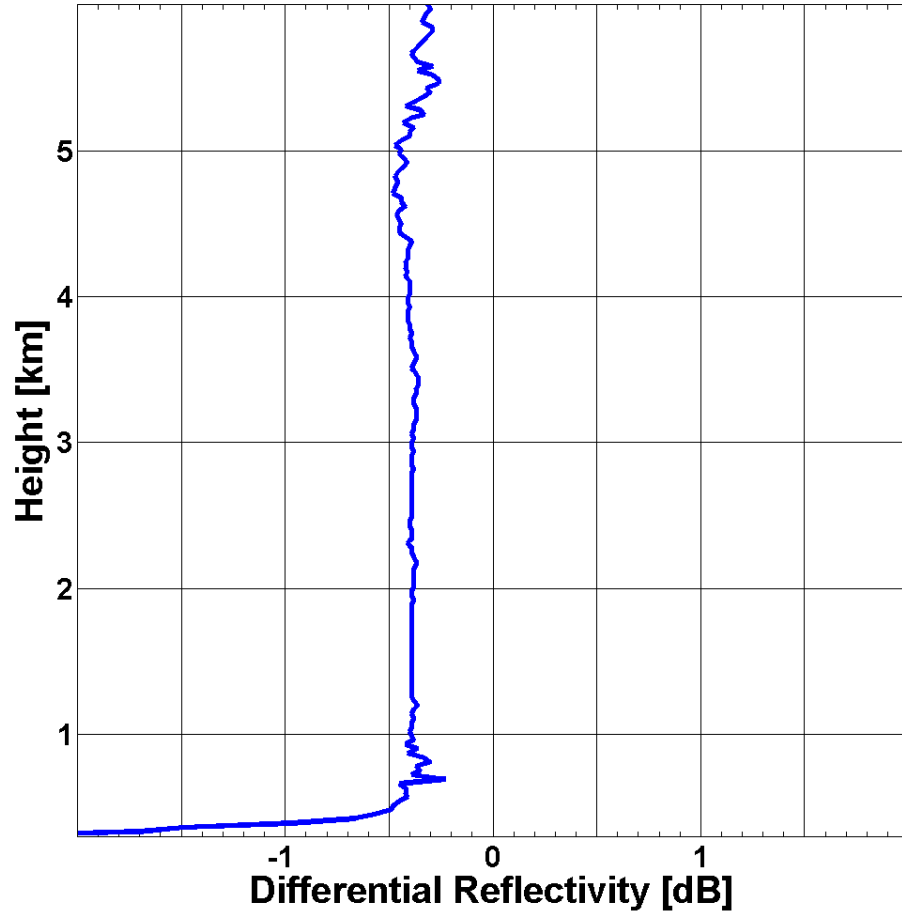


Figure 5.11: Mean differential reflectivity  $Z_{DR}$  profiles recorded on 04/18/2011 by the XPOL-3 radar.

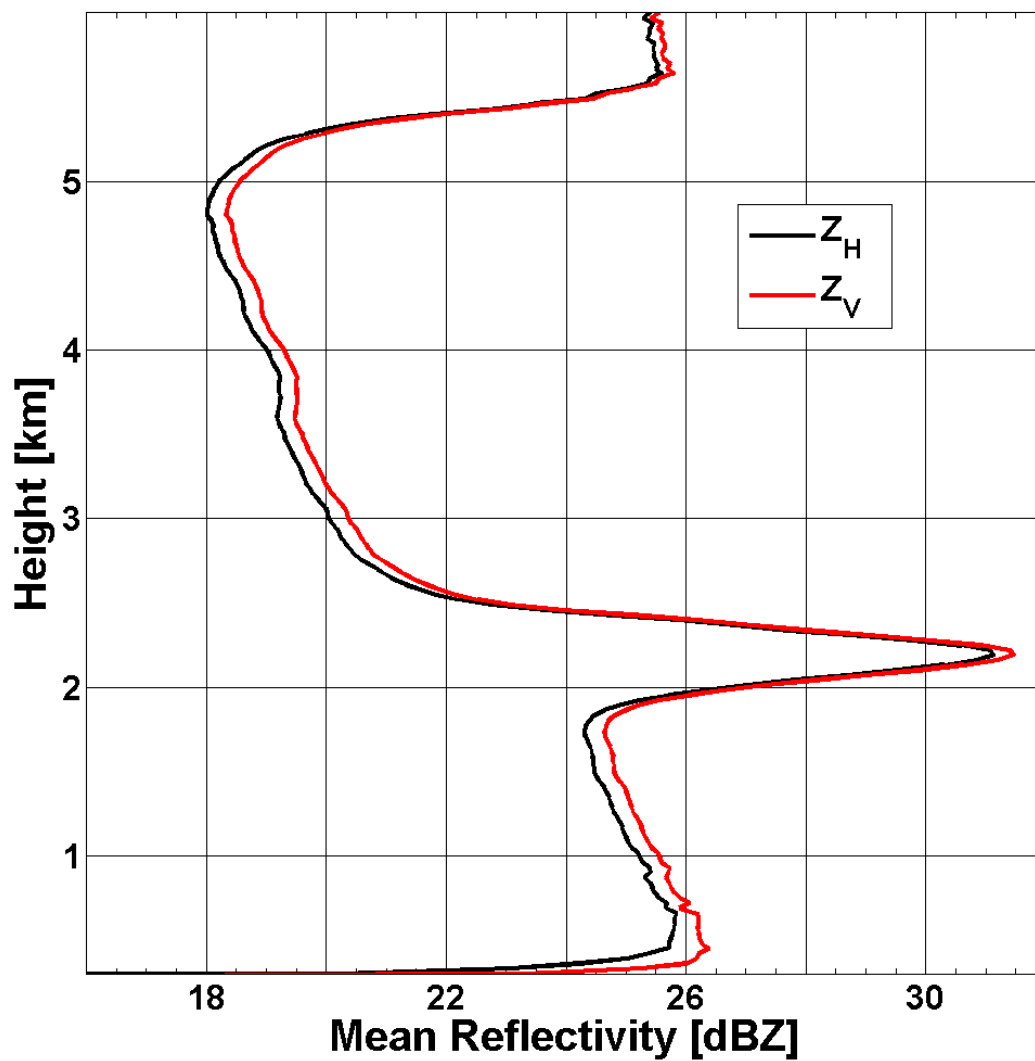


Figure 5.12: Mean reflectivity profiles for horizontal  $Z_H$  and vertical  $Z_V$  reflectivity recorded on 04/15/2011 by the XPOL-3 radar.

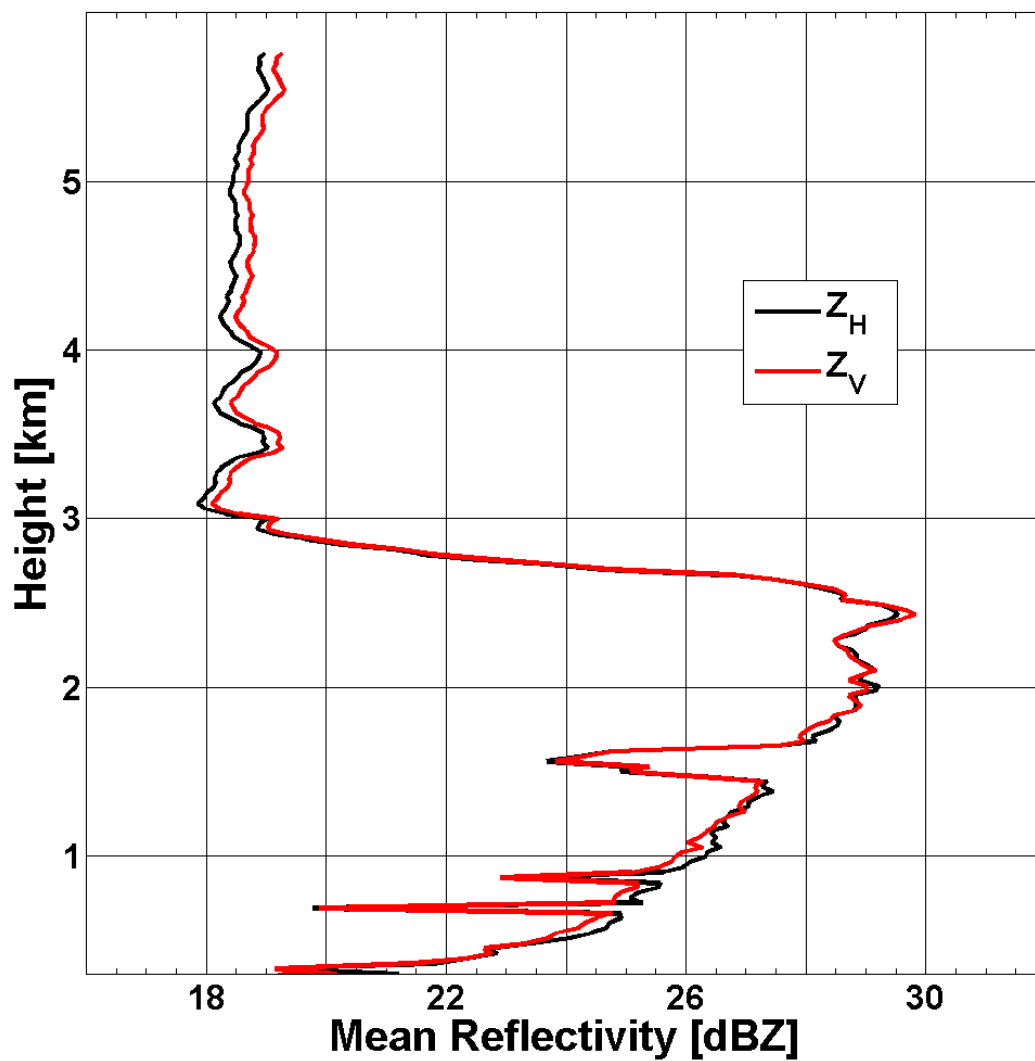


Figure 5.13: Mean reflectivity profiles for horizontal  $Z_H$  and vertical  $Z_V$  reflectivity recorded on 04/21/2011 by the XPOL-3 radar.

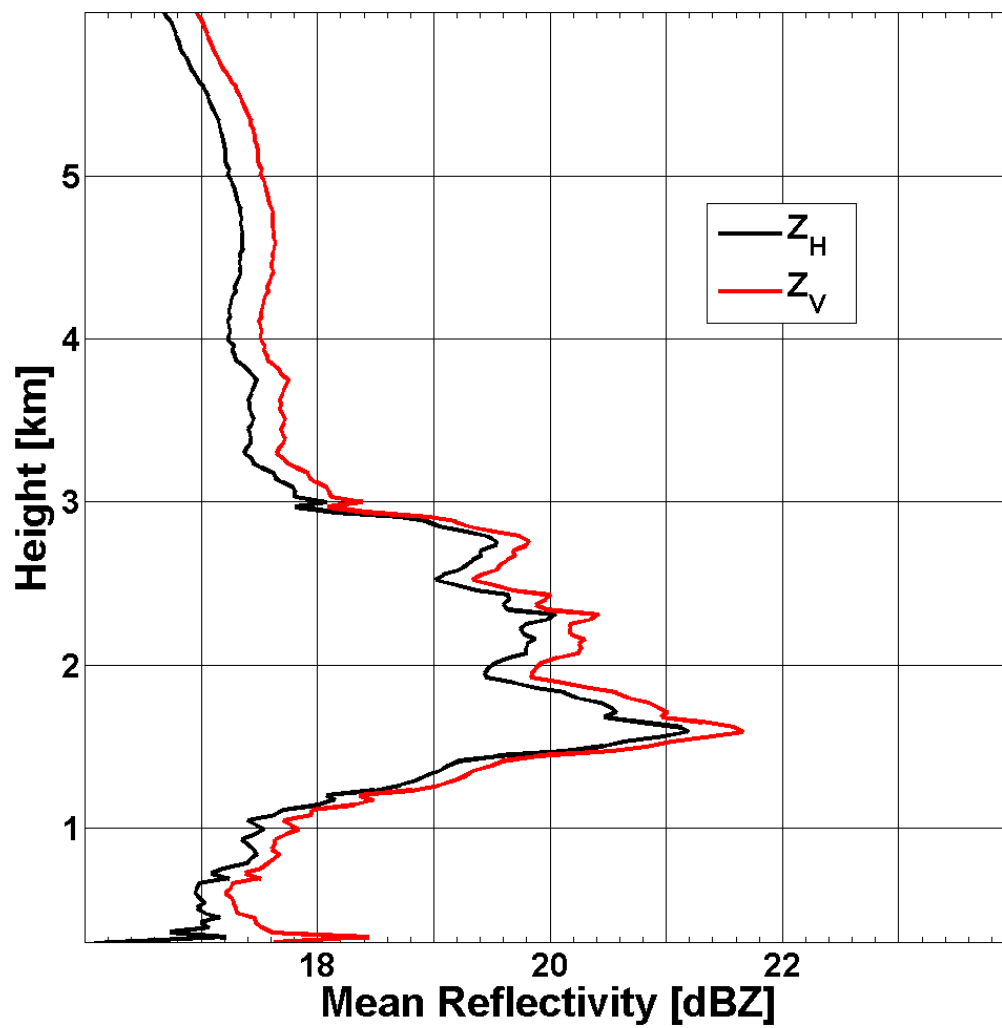


Figure 5.14: Mean reflectivity profiles for horizontal  $Z_H$  and vertical  $Z_V$  reflectivity recorded on 04/22/2011 by the XPOL-3 radar.

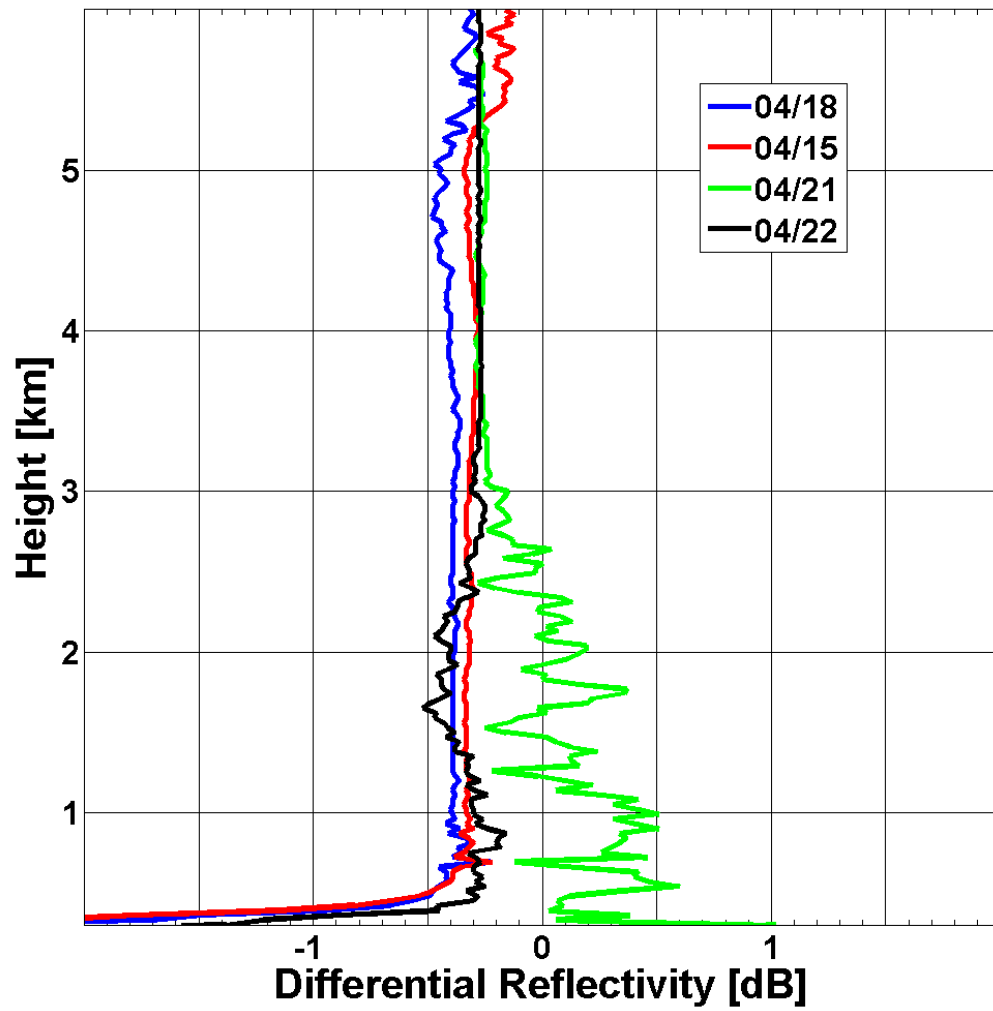


Figure 5.15 Mean differential reflectivity profiles for the four analyzed cases recorded by the XPOL-3 radar.

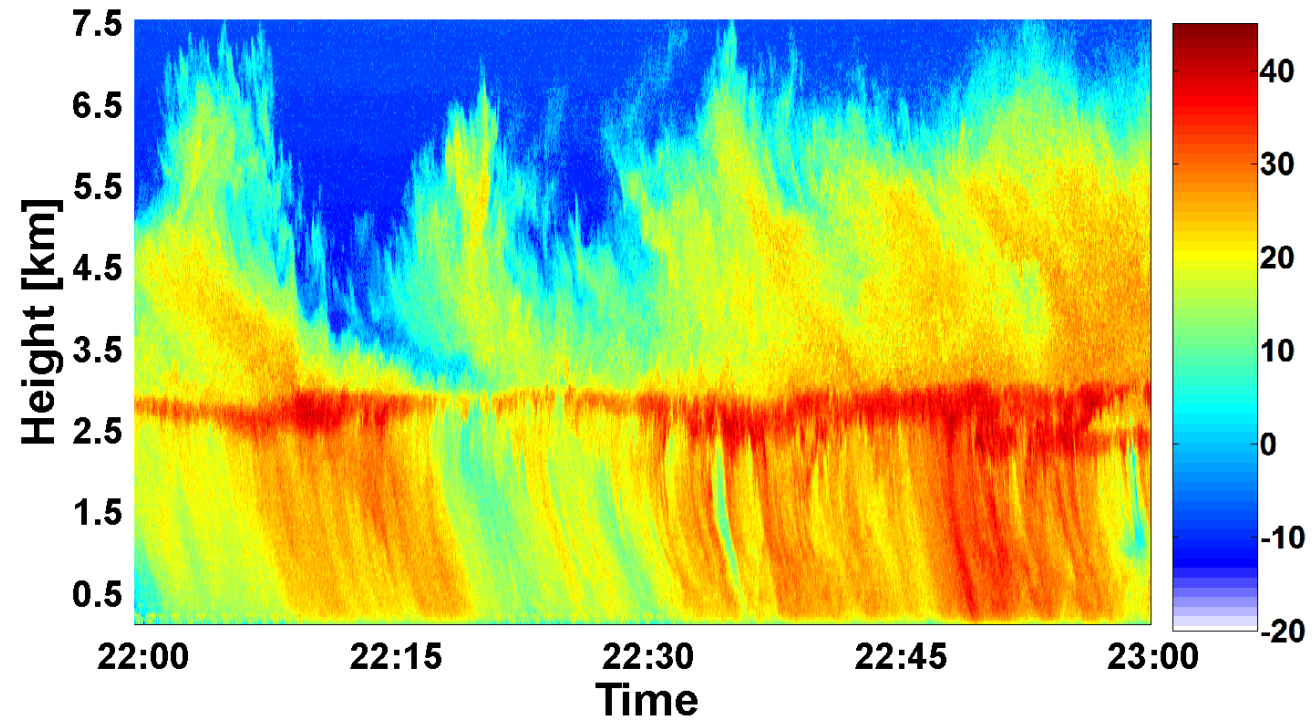


Figure 5.16: Time series of reflectivity profiles recorded by the XPOL-5 node on 04/02/2011 at the Iowa City landfill.

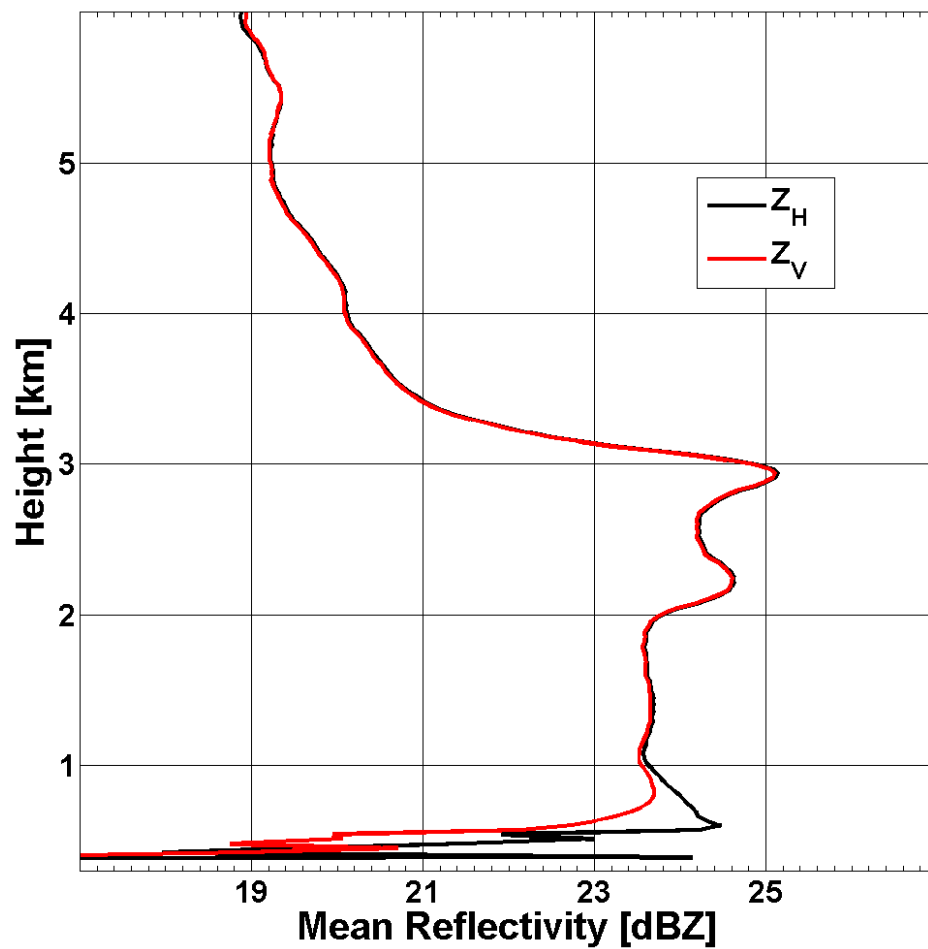


Figure 5.17: Mean reflectivity profiles for horizontal  $Z_H$  and vertical  $Z_V$  reflectivity recorded on 04/02/2011 by the XPOL-5 radar.

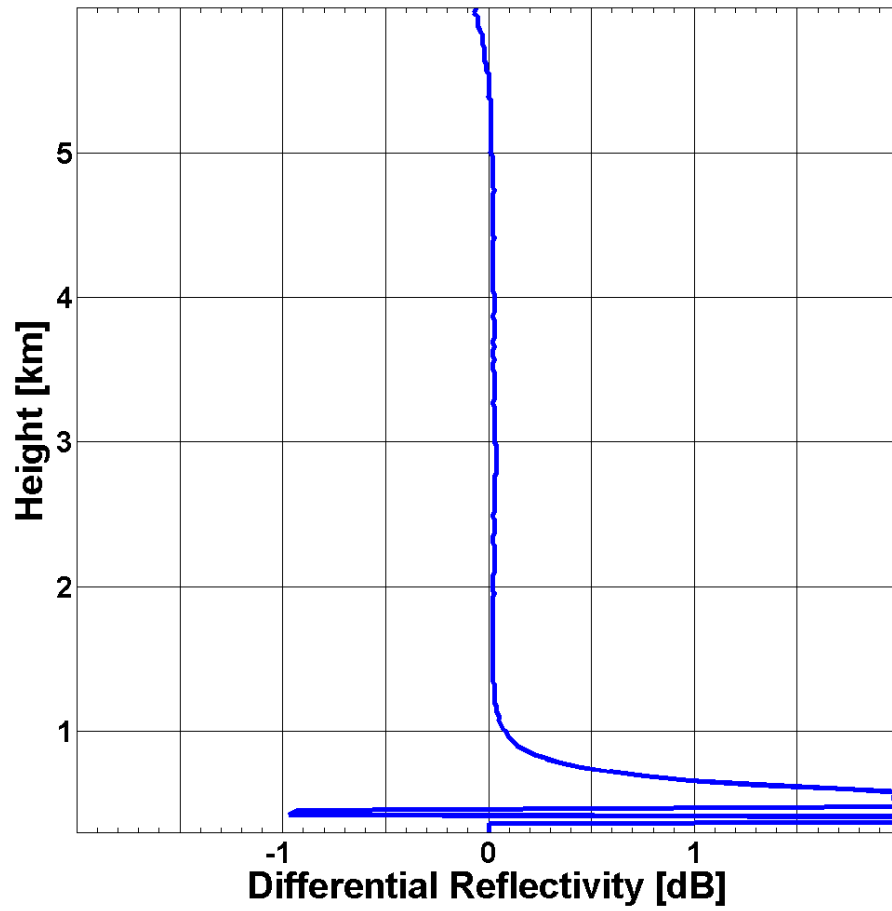


Figure 5.18: Mean differential reflectivity  $Z_{DR}$  profiles recorded on 04/02/2011 by the XPOL-5 radar.

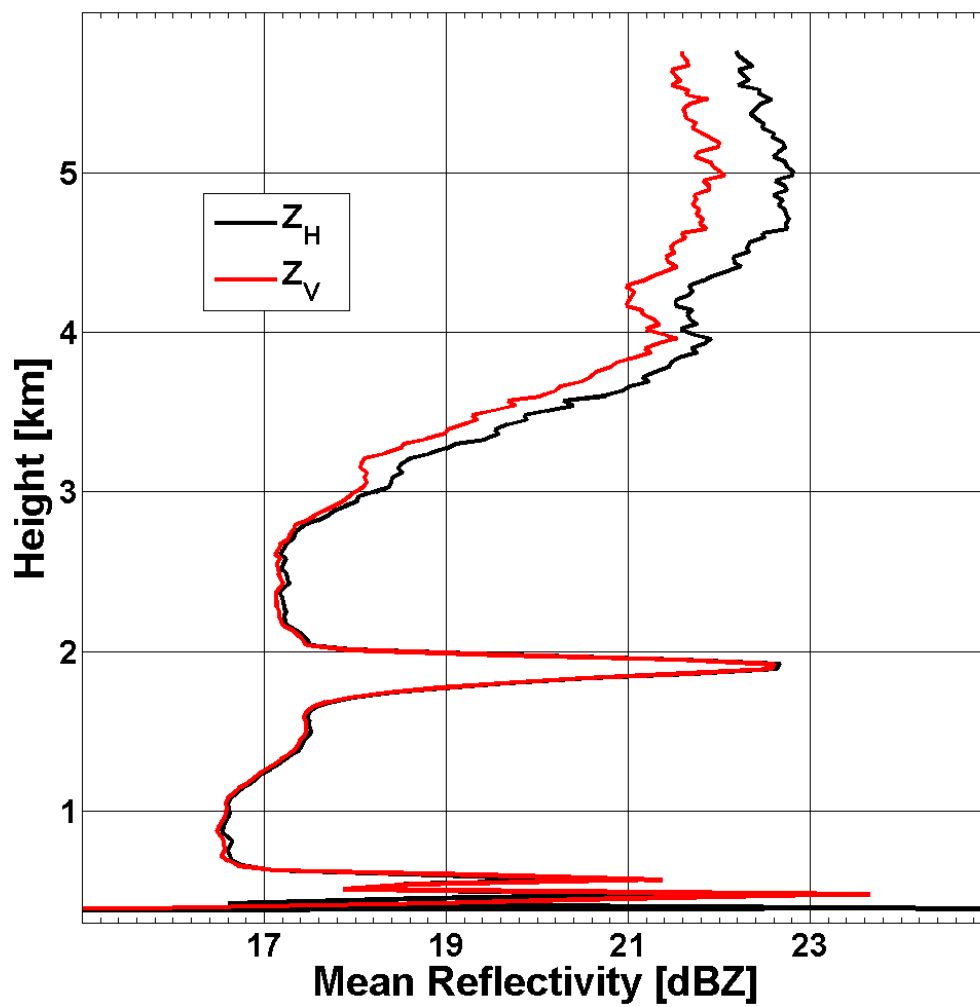


Figure 5.19: Mean reflectivity profiles for horizontal  $Z_H$  and vertical  $Z_V$  reflectivity recorded on 03/24/2011 by the XPOL-5 radar.

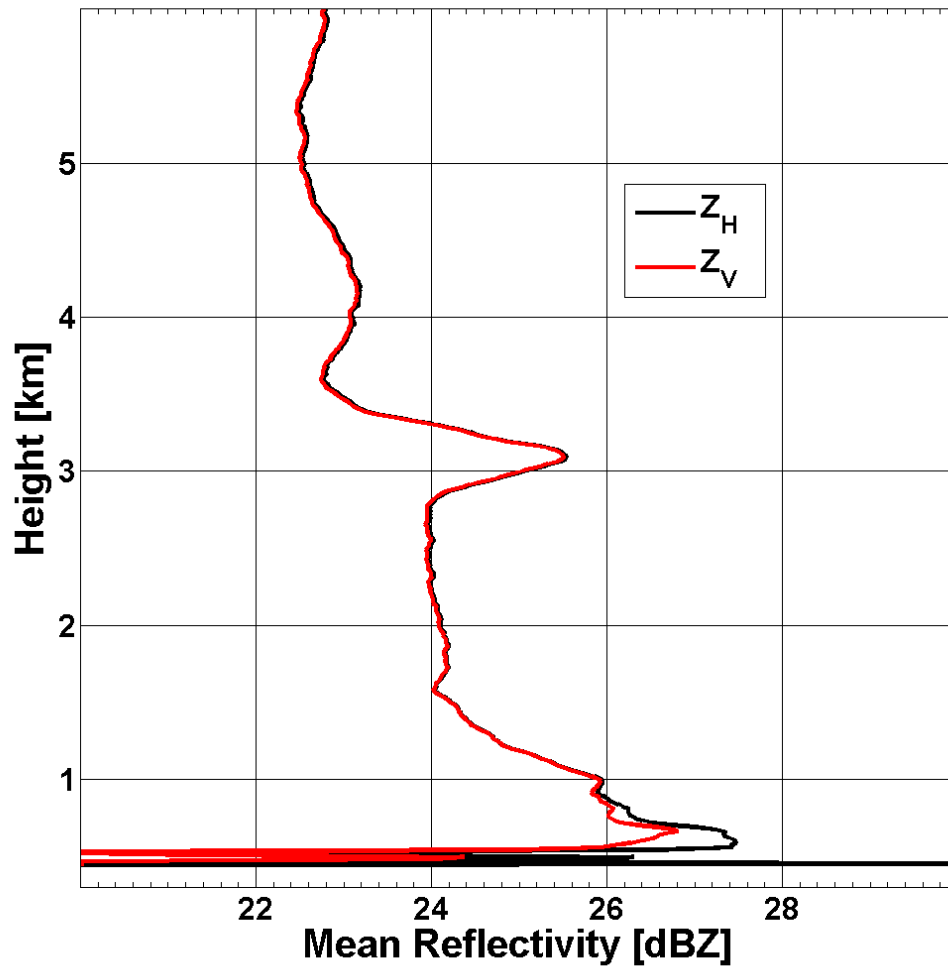


Figure 5.20: Mean reflectivity profiles for horizontal  $Z_H$  and vertical  $Z_V$  reflectivity recorded on 04/05/2011 by the XPOL-5 radar.

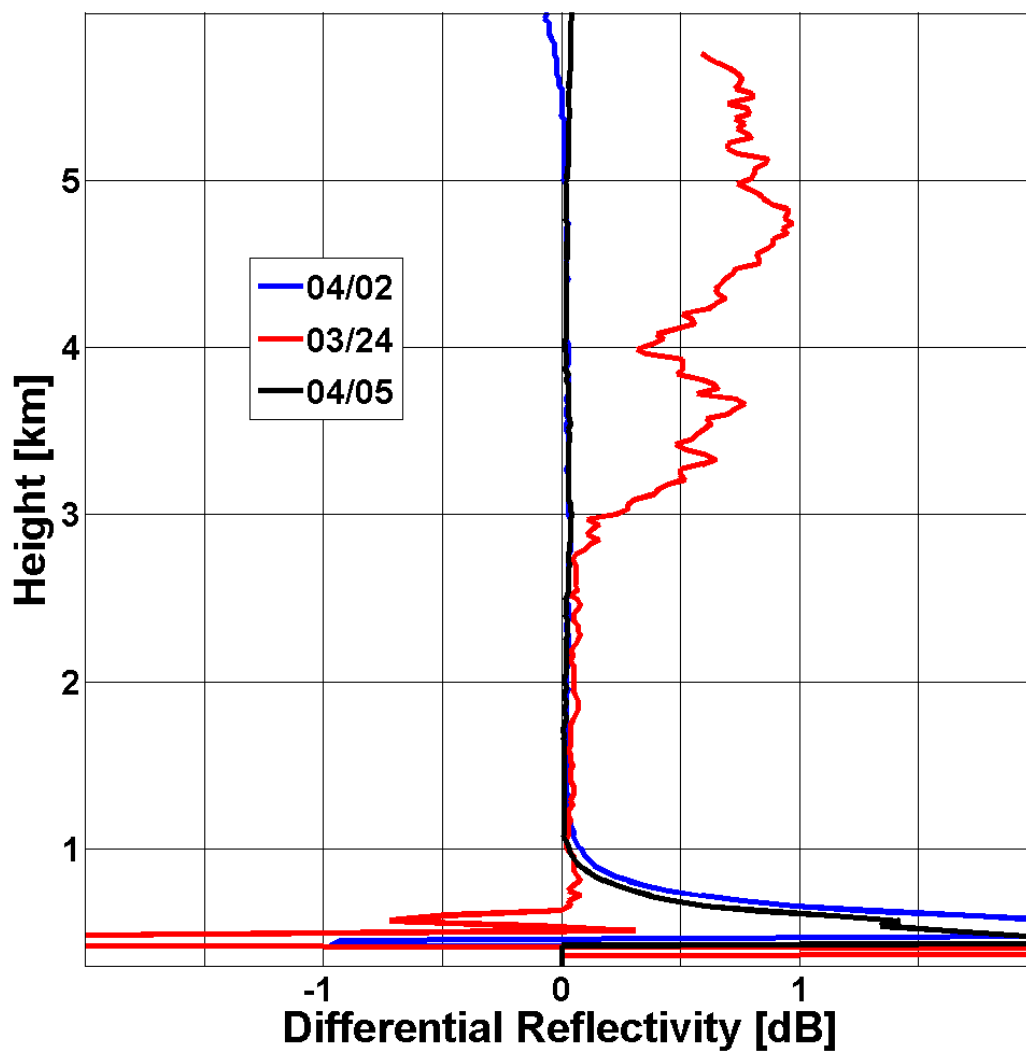


Figure 5.21: Mean differential reflectivity profiles for the three analyzed cases recorded by the XPOL-5 radar.

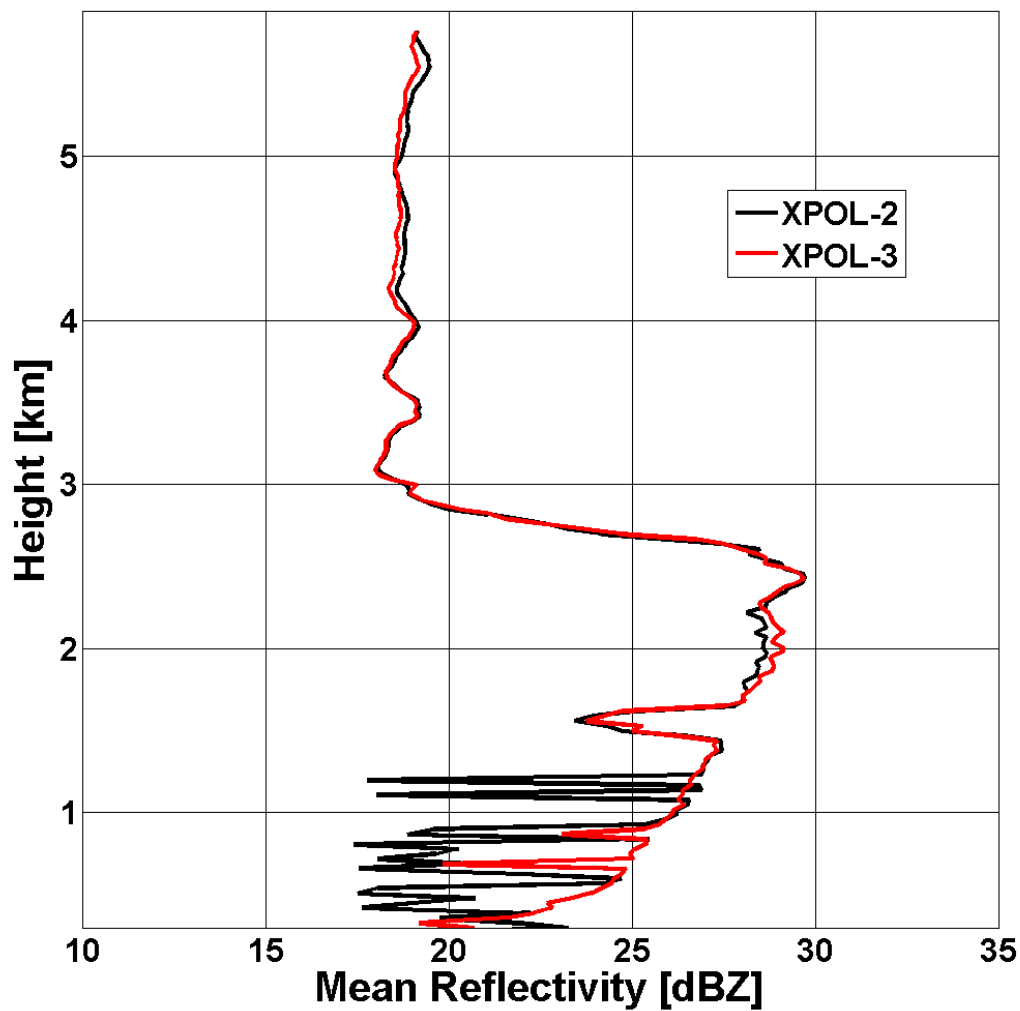


Figure 5.22: Mean reflectivity profiles as simultaneously recorded by the XPOL-2 and XPOL-3 network nodes on 04/21/2011.

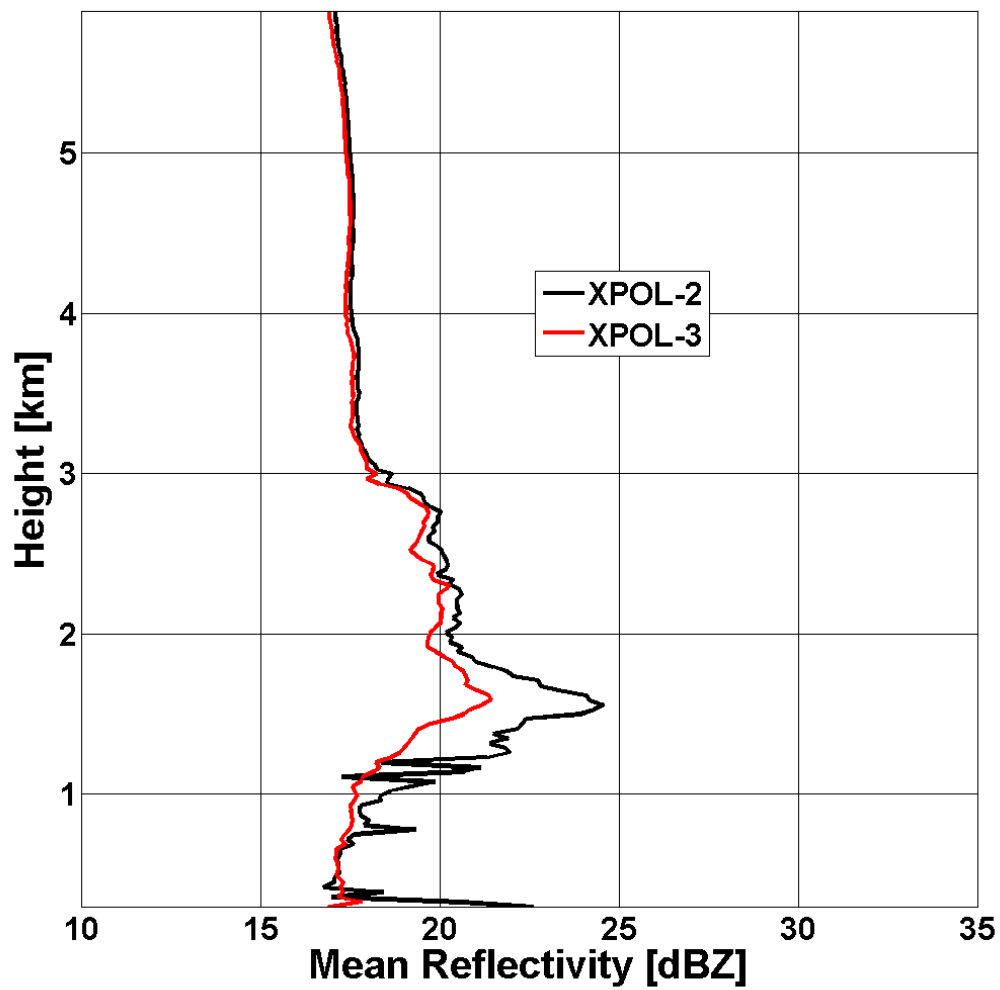


Figure 5.23: Mean reflectivity profiles as simultaneously recorded by the XPOL-2 and XPOL-3 network nodes on 04/22/2011.

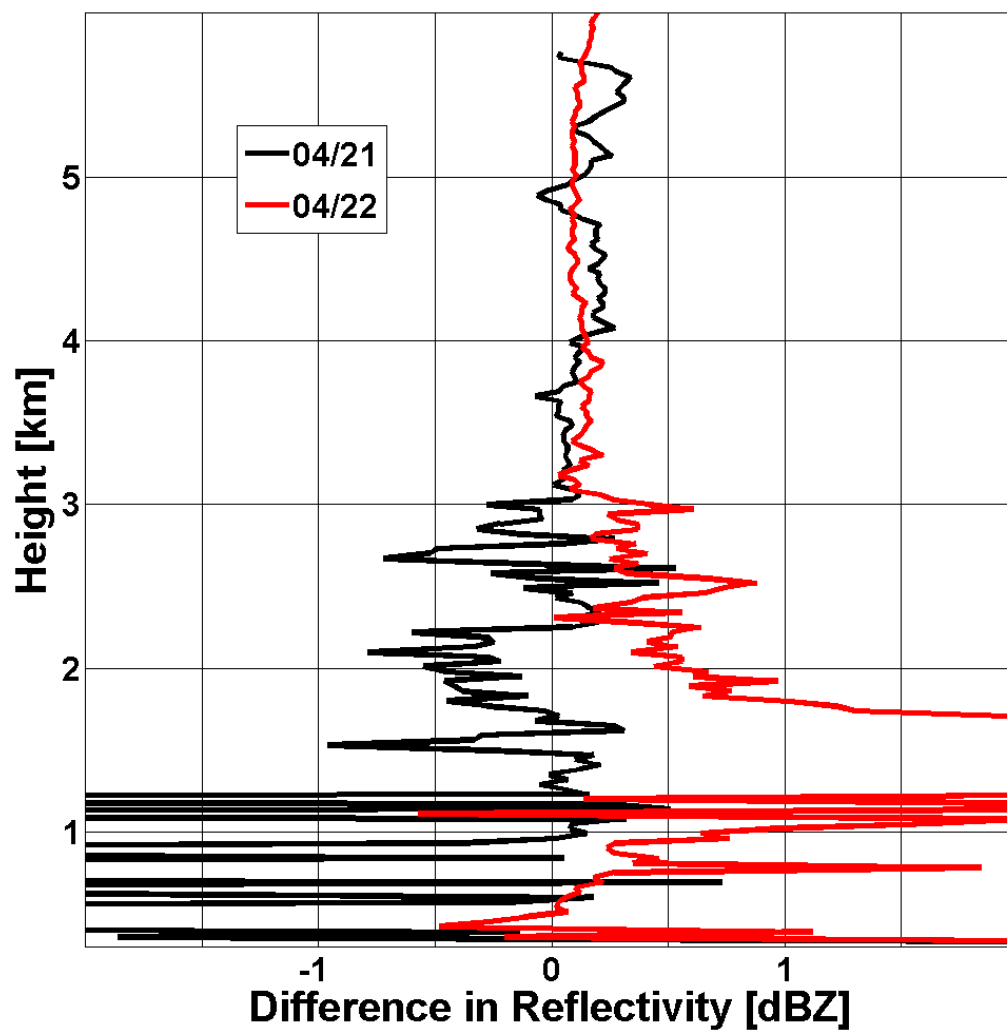


Figure 5.24: Mean difference between reflectivity profiles estimated by XPOL-2 and XPOL-3 radar for two separate rainfall events.

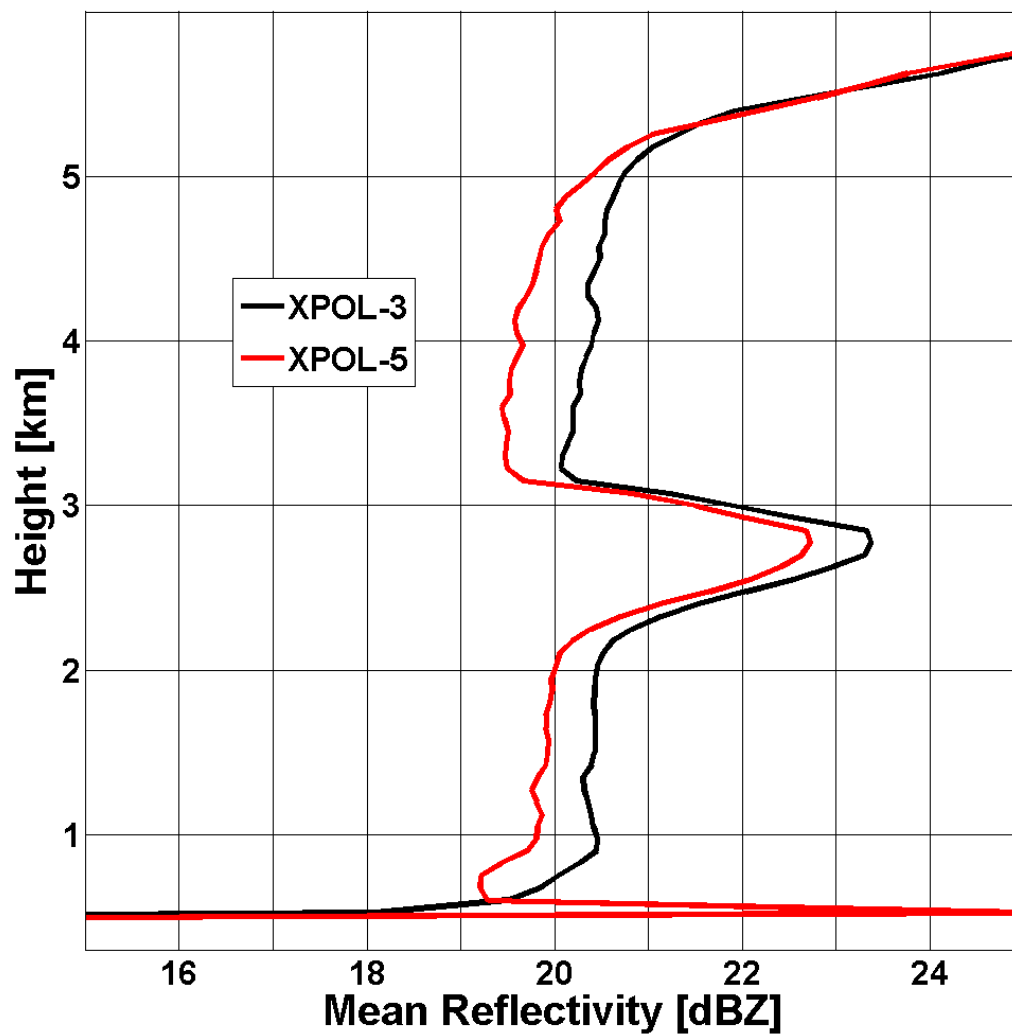


Figure 5.25: Mean reflectivity profiles as simultaneously recorded by the XPOL-3 and XPOL-4 network nodes on 12-13/11/2010.



CHAPTER 6  
THE IMPLEMENTATION OF ATTENUATION CORRECTION  
ALGORITHMS TO DATA COLLECTED BY THE UNIVERSITY OF  
IOWA POLARIMETRIC RADAR NETWORK

6.1 Introduction

In Chapter 3, we discussed a number of attenuation correction and data merging techniques, both in a single-radar and a network arrangement. Our assumption was that the polarimetric radar network simulator defined in Chapter 2 can, to a certain degree, simulate key processes and characteristics of an actual radar network. In an attempt to validate the simulator's results and confirm its use as a valid and valuable research tool, we implemented the attenuation correction methods tested in the simulator to the data collected by The University of Iowa Polarimetric Radar Network.

The high spatio-temporal variability of rainfall and the great complexity of a radar system's design render the process of radar rainfall measurement challenging, and the obtained measurements are often associated with a considerable level of error. The polarimetric radar network simulator described in Chapter 2 cannot fully represent the complexity of the radar rainfall measurement process. Consequently, a comparison of simulator findings to the conclusions from the analysis of a real network data is difficult. In this chapter, we implement a number of single-radar and network-based attenuation correction algorithms to the data collected by The University of Iowa Polarimetric Radar Network in an attempt to confirm the finding of the analysis presented in Chapter 3. We discuss the challenges that are inherent in the operational implementation of single-radar and network-based attenuation correction methods. Due to the technical complications associated with the network's deployment, our analysis is limited to data recorded by the network that consists of two radars.

## 6.2 Network configuration

The initial deployment of the network involved positioning two of the network's nodes near Iowa City, IA. As our domain of interest, we selected the Clear Creek watershed (HUC 07080209) – a heavily instrumented basin in which a number of instruments supporting hydrologic research are installed. Figure 6.1 provides a sketch of the network's conceptual configuration, with its four anticipated radar locations and additional hydrologic instruments.

The XPOL-5 radar was positioned at the Iowa City landfill (41.644, -91.623) on a man-made hill, which provided an unobstructed view of the domain of interest, and the XPOL-3 radar was installed within the premises of the Eastern Iowa Airport (CID) (41.887, -91.734). Both locations offer a fence-secured access with minimal exposure to the public. To allow for uninterrupted operations and a remote control of the network, both radars were provided with internet connectivity and a power supply. The straight-line distance between the radars was estimated at 28.52 km. We configured both radars to sample the atmosphere using a raster scan with four elevations (0°, 3°, 6°, and 9°) and an azimuthal range spanning 330° (285°-225°). We set the maximum sampled range at 21km for each radar.

Four dual, tipping-bucket type rain gauges were located within the domain of interest [Ciach, 2003]. The rain gauges provided single-point rainfall rate estimates with 5-min temporal resolution for the duration of the experiment. In Table 6.1, we provide detailed information about the relative (with respect to the radars) positioning of the rain gauges. Figure 6.2 provides a graphical representation of the actual network configuration.

## 6.3 Collected data sample

The analysis presented in this chapter is based on two rainfall events that were recorded by the network. The first rainfall event was observed on the 3<sup>rd</sup> and 4<sup>th</sup> of

December 2011 starting at 12/03/1012 22:00 UTC. The observed rainfall lasted approximately 15 hours and can be described as a combination of a stratiform event with several stronger, individual rainfall cells. The second event occurred on the 14<sup>th</sup> and the 15<sup>th</sup> of December 2011, with the rainy period lasting ~20 hours. Both radars were recording in a Pulse-Pair mode, with the pulse length equal to 150m and the range gate size set to 30m. With the azimuthal antenna rotation speed set to 6 °/s and the data rate equal to 8 profiles per second, it took each radar 55 seconds to complete a 330° elevation scan for each of the four elevations, resulting in a ~4-minute update time. The recorded radar data was consecutively converted to a polarimetric variable, namely the horizontal and the vertical reflectivity, the differential reflectivity, and the differential phase shift. To visually inspect the data, we employed the previously developed utilities to generate a series of images of radar-centric, polarimetric variables. Based on our visual inspection, we observed that the 0°-elevation data for both radars suffered from intense beam blockage due to obstructions in the radars' line of sight. Further analysis revealed that the data collected at elevations 6° and 9° were often contaminated by bright band reflection, making the 3° elevation data most suitable for analysis. Figure 6.3 offers an example of beam blockage experienced at 0° elevation.

#### 6.4 Radar-rain gauge comparison

We start the analysis of the collected data by comparing the radar-based total rainfall accumulation for the observed events with the rain gauge measurements. The precise estimation of the exact radar range gate that corresponds to the location of each of the rain gauges is difficult. In addition, rainfall advection, along with beam height above the ground, can contribute to the spatial misalignment of the observed rainfall with respect to the rain gauge on the ground [*Krajewski and Smith, 2002*]. In order to minimize the misalignment error, we chose to consider as a radar-based observation a spatial window with dimensions of ~200m x 200m rather than a single radar range gate.

The quality control of the radar data was limited to the removal of reflectivity values greater than 50 dBZ and less than 10 dBZ. All reflectivity values from range gates with centers within the spatial window were averaged to a single value of reflectivity (averaging occurred in units of  $\text{mm}^6 \text{m}^{-3}$ ). We selected only values from the second elevation scan ( $3^\circ$ ) and converted the obtained reflectivity to the rainfall rate using the  $Z=300R^{1.4}$  relationship [Marshall and Palmer, 1948]. Finally, we accumulated the rainfall rate values to the rainfall total accumulation [mm] for the whole rainfall period for the radar- and rain gauge-based measurements. In Table 6.2, we summarize the obtained results for the two rainfall events separately.

The analysis revealed large discrepancies between the radar-based total rainfall accumulations and the rain gauge estimates. In addition, there was a considerable level of disagreement between the XPOL-3 and the XPOL-5 radar-based accumulation, with the XPOL-5 radar generally estimating higher rainfall amounts as compared to the XPOL-3 radar. In order to better understand the sources of such large differences between the individual radars and the radars and rain gauges, we visually inspected the dataset with respect to the sectors corresponding to the rain gauge locations. As presented in Figure 6.4, our investigation revealed that the XPOL-3 data that was collected with the antenna elevation angle equal  $3^\circ$  was still contaminated with a considerable amount of ground clutter, especially in the direction towards the area of interest. It is possible that the ground clutter obstructing the radar's beam path resulted in partial beam blockage and, as a consequence, yielded a strong underestimation of the observed reflectivity values. To further examine the underlying differences, in Figure 6.5 we plotted the time series of rain gauge rainfall rate estimates (Figure 6.5 panel A) and compared them to the radar-derived rainfall rates (Figure 6.5 panel B). Besides considerable underestimation of the radar-based rainfall rates by both radars, compared to rain gauge we can see that the XPOL-5 radar shows a tendency to record reflectivity values that are much greater than the values recorded by the XPOL-3 radar for the

corresponding time stamp. This has been further exploited in Figures 6.6 and 6.7, when we present the results in a form of a scatter plot. The reason for systematic underestimation of the rainfall rate values could be attributed to the “wet radome attenuation” problem. In addition, the 4-minute radar data update time, together with the character of the rainfall event (stratiform precipitation mixed with fast moving, isolated cells) can result in the underestimation of radar-based estimates. This problem can be mitigated in the future by implementing a higher update time and/or an advection correction algorithm [Shapiro *et al.*, 2010; Krajewski *et al.*, 2011]. Other possible sources or error include, but are not limited to, the errors in the  $Z$ - $R$  conversion, non-uniform beam filling, super-refraction and calibration errors. It is difficult to clearly identify the reason for sporadic discrepancies between the XPOL-5 and XPOL-3 radar without investigating a larger data sample which will be a subject of a future study.

#### 6.5. Basin-centric rainfall accumulation estimation

From the analysis of the rain gauge total rainfall estimates in the previous subsection, we observed that all four rain gauges included in the study recorded total rainfall accumulations close to 17 mm for the first event and 10 mm for the second event (refer to Table 6.2 for specific values). Based on this observation, we assumed that the analyzed rainfall events delivered uniformly distributed rainfall amounts over the whole domain of interest, corresponding to the radar overlap section. To verify this assumption, we estimated the mean aerial precipitation [mm/h] for the area marked in Figure 6.8, which was covered by both network nodes. The mean aerial precipitation values were calculated for each radar scan, resulting in a ~4 minute update time. For the purpose of this study, we only used data from the 3° antenna elevation scans. This selection was motivated by our visual inspection, which revealed a considerable amount of ground clutter in the data from 0° elevation scans and frequent bright band contamination for the higher elevation data. We subsequently converted the mean aerial precipitation estimates

for each of the radars to the rainfall total accumulations. For the first event, the accumulation values for the XPOL-3 and XPOL-5 radars were calculated to be 2.83 mm and 20.94 mm, respectively, and the XPOL-3 and XPOL-5 values were 3.33 mm and 21.43 mm, respectively, for the second event. To better understand the obtained results and the observed discrepancies, we generated maps of total rainfall accumulation for both of the radars and presented them in Figure 6.9. The figure shows rainfall accumulation maps for the 3° elevation data. As demonstrated in the accumulation maps, the data from the XPOL-3 radar, which is located at the Cedar Rapids airport, is strongly affected by the presence of ground clutter. The clutter is especially strong towards the location of the four rain gauges considered in the study. Such strong ground clutter obstruction could have led to partial beam blockage and, consequently, to the strong underestimation of the reflectivity values. The XPOL-5 3° elevation shows no significant clutter contamination. For both radars, the 6° elevation data was affected by the bright band effect, in which the radar beam intersects the melting layer and is typically associated with strong reflection (Figure 6.10). Analyzing the results of the total rainfall accumulation with respect to the presented accumulation maps helped us better understand the source of significant differences between the measurements provided by the XPOL-3 and the XPOL-5 radars.

The analysis of accumulation maps demonstrates additional benefits that result from operating a network of radars. In the case of The University of Iowa Polarimetric Radar Network, the XPOL-3 radar suffered from severe beam blockage that limited the radars' rainfall observing capabilities. Our alternative positioning of the XPOL-5 radar provided us with rainfall observation capability for the whole domain of interest.

## 6.6 Implementation of single-radar attenuation correction

### methods

In the current subsection, we discuss the challenges associated with the implementation of the single-radar attenuation correction methods to radar data. Our

goal is to identify essential aspects of the polarimetric data collected by The University of Iowa Polarimetric Radar Network that must be recognized, understood, and accounted for before an attenuation correction method can be implemented operationally. Any systematic behavior (noise, clutter, etc.) observed in the data can also be used to improve upon the polarimetric radar network simulator described in Chapter 2 by better representing the accuracy of the polarimetric, X-band radar rainfall measurement process. After discussing the challenges, we apply a number of attenuation correction algorithms to the collected data sample and then discuss the obtained results.

The goal of an attenuation correction algorithm is to remove the effect of signal attenuation that occurs as a consequence of the radar signal passing through regions of intense precipitation. The successful implementation of attenuation correction methods that rely on reflectivity measurements depends upon the quality of the reflectivity signal itself. The radar reflectivity factor in both horizontal and vertical polarization is often contaminated with ground clutter, bright band returns, anomalous propagation [e.g. *Moszkowicz et al.*, 1994; *Greco and Krajewski*, 2000; *Steiner and Smith*, 2002], or non-meteorological targets (birds, planes, trees, insects, dust, etc.). Different techniques have been suggested to address the problem of data contamination, but the operational implementation of those techniques requires a long-term analysis of radar data for any radar installation under many meteorological conditions. The differential phase shift  $\Phi_{DP}$  measurements and the derivative specific differential phase shift  $K_{DP}$  are not subject to partial beam blockage and calibration errors; at the X-band frequency, the relationship between the signal attenuation and specific differential phase is almost linear [*Jameson*, 1992]. This led to an increased interest in attenuation correction and rainfall retrieval algorithms based on the differential phase shift, often in combination with reflectivity and differential reflectivity measurements [e.g. *Zrnić and Ryzhkov*, 1996; *Bringi et al.*, 2001; *Park et al.*, 2005].

The operational implementation of attenuation correction algorithms is challenging because of the complexity of radar system designs and the inherent errors associated with radar data. The systematic errors can be addressed by calibration and averaging techniques, but random errors pose a much greater challenge. Both systematic and random errors must be recognized and accounted for before any attenuation correction algorithm can be operationally implemented.

The available radar network dataset allowed us to identify some of the characteristics that are associated with the collected radar data for reflectivity and differential phase shift measurements. The reflectivity measurement characteristics are presented in subsection 6.5. Below, we focus on the characteristics of differential phase shift measurements. In Figure 6.11, panel A, we present a sample profile of the differential phase shift  $\Phi_{DP}$  collected by one of the network's radars, and we provide the corresponding reflectivity profile in panel B. In the figure, we superimposed the raw  $\Phi_{DP}$  profile onto the smoothed one (please refer to section 2.3.3 for a description of the smoothing technique). At low rainfall rates, the differential phase shift signal changes are dominated by noise and the backscatter differential phase shift. The smoothing procedure can successfully eliminate the random fluctuations but, as we can observe in the figure, applying the smoothing procedure to the whole range profile is not desirable. For regions with no precipitation, the differential phase shift signal shows random behavior and, when included in the smoothing procedure, can weight the results for regions with ongoing precipitation. The random behavior of the differential phase shift in the no-precipitation regions has not been adequately represented in the polarimetric radar network simulator presented in Chapter 2. The problem of random  $\Phi_{DP}$  fluctuations must be addressed before we can successfully implement the attenuation correction methods that are based on the differential phase shift measurements. To eliminate the non-rainy sections of the  $\Phi_{DP}$  profiles conditioning on reflectivity values can be used. It is also important to note that at low rainfall rates  $<5\text{mm/h}$ , changes in the differential phase shift

are small compared to the associated noise and greatly limit the usability of this measurement for attenuation correction and rainfall estimation efforts.

In the process of implementing the single radar attenuation correction methods, we followed the procedures described in section 3.3 and implemented the following methods: a) the “forward” algorithm of *Hitschfeld and Bordan* [1954] that is described in section 3.3.1, b) the  $\Phi_{DP}$  constrained method (also in 3.3.2), c) the self-consistent method with constraints (also in 3.3.3), and d) the  $K_{DP}$ -based method (in 3.3.4). The results for each of the methods for single point total rainfall accumulations, as well as the total rainfall accumulation for the domain of interest overlooked by both radars, are presented in Table 6.3.

It is important to note that the analyzed rainfall case, due to mostly light to moderate rainfall intensities, did not cause considerable signal attenuation. With little attenuation, the correction methods cannot be fully tested. In addition, the high level of noise in the differential phase shift variable and a considerable amount of ground clutter in the reflectivity profiles contributed to the difficulty in implementing and assessing the attenuation correction methods. Based on the obtained results, we could see that for light to moderate precipitation, the *Hitschfeld and Bordan* [1954] method was the easiest one to implement and was more stable than the algorithms that are based on the differential phase shift. The general conclusion from this exercise confirms the difficulties in the operational implementation of attenuation correction methods and the necessity for data quality control before performing the attenuation correction procedure. Nevertheless, the exercise had a great educational impact, and the findings will contribute to the further development of the polarimetric radar network simulator.

### 6.7 Network data merging

As discussed throughout this document, the full benefit of operating a network of radars is achieved when data collected by individual network nodes is shared in the post-

processing stage in order to improve the quality of network rainfall products. Motivated by the simulation results presented in Chapter 3, we applied a set of data merging techniques to the data sample collected by The University of Iowa Polarimetric Radar Network. Our goal was to improve the capabilities of the network by allowing the data merging process and to compare the results of the merging process with the simulation results presented in Chapter 3. The implemented merging methods included: a) the distance weighted average [Method 1], b) the maximum reflectivity value method [Method 2], c) the minimum PIA method [Method 3], and d) the PIA weighted method [Method 4]. The definitions of the methods are identical to those presented in Section 3.5. All methods were applied to the data collected by the XPOL-3 and XPOL-5 network nodes for the previously described rainfall event observed during the 12/03/2011-12/04/2011 period. After the merging process, we converted the reflectivity values into rainfall rate estimates using the  $Z=300R^{1.4}$  relationship and calculated total rainfall accumulation values for both the point location (corresponding to individual rain gauges) and the area of interest overlooked by both radars. The results of the merging procedure for each of the methods are summarized in Tables 6.4 – 6.8.

Our analysis of the obtained results further strengthened the conclusions presented in Chapter 3, which indicated that while the data merging process can improve the quality of a network rainfall product, the merging method must be selected with caution. Among the tested methods, all but the maximum value method outperformed the single radar methods. In a situation where one of the radars is strongly affected by the presence of ground clutter and corresponding beam blockage, a merging technique can greatly improve the overall result. For the weighting methods, this can lead to the degradation of the results due to the inclusion of contaminated radar data. Similarly to the results obtained in the simulator and presented in Chapter 3, the merging methods were also affected by the attenuation correction methods applied before the merging occurred. Among the main differences between the results obtained in the merging process for The

University of Iowa Polarimetric network and the network simulated in the simulator is the presence of bright band and ground clutter contamination. The removal of ground clutter remains one of the most significant challenges in the process of implementation attenuation correction methods and data merging techniques.

### 6.8 Summary of Chapter 6

In Chapter 6, we discuss the challenges associated with the operational implementation of the attenuation correction methods to X-band radar data. We analyze the process of implementing single radar attenuation correction methods and data merging techniques based on a data sample collected by The University of Iowa Polarimetric Radar Network. In the process, we identified ground clutter contamination, partial beam blockage, and bright band reflections as the most significant features that degrade reflectivity measurements. The necessary quality control step for radar reflectivity data should include the removal of data contaminants to improve the performance of attenuation correction methods. To successfully implement attenuation correction methods based on the differential phase shift estimates, it is necessary to first address the problem of the backscatter differential phase shift and the discrimination between rainy and dry sections of the profiles. Based on the obtained results, we see limited usability of the differential phase shift signal in the process of attenuation correction and rainfall estimation at light to moderate rainfall conditions due to the low sensitivity of the signal, as compared to the observed noise levels.

After discussing some of the challenges of radar data attenuation correction, we implemented a number of single radar methods as well as data merging techniques in order to verify the findings of the polarimetric radar network simulator that is presented in Chapter 3. Based on the rain gauge data collected for the duration of the analyzed rainfall event, we hypothesized that the rainfall amount was uniformly distributed over the domain of interest. To assess the performance of the attenuation correction and data

merging methods, we compared rain gauge-based rainfall accumulations with the rainfall total accumulation results that are based on radar data. To simplify the analysis, we do not discuss the errors associated with the rain gauge measurement process and assume that the  $Z$ - $R$  relationship accurately converts radar reflectivity to rainfall rate amounts. Although a comprehensive evaluation of the simulator could not be achieved in the study due to a limited radar data set, the exercise presented in this chapter complements the educational aspect of the simulation studies completed in Chapter 3. The data collected by The University of Iowa Polarimetric Radar Network can be used to further enhance the accuracy of the simulator.

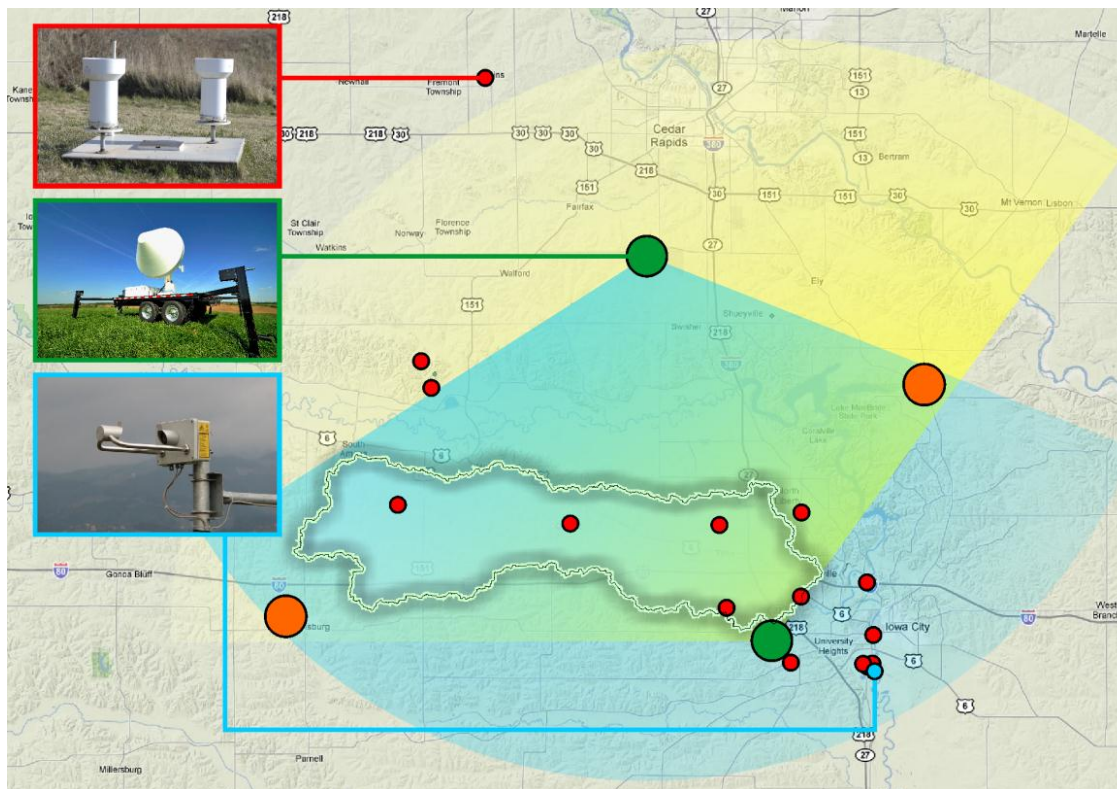


Figure 6.1: Configuration of The University of Iowa Polarimetric Radar Network.

The green dots reflect the location of deployed units and the orange dots are the anticipated locations for additional nodes. Red dots show locations of a rain gauge and disdrometer network.

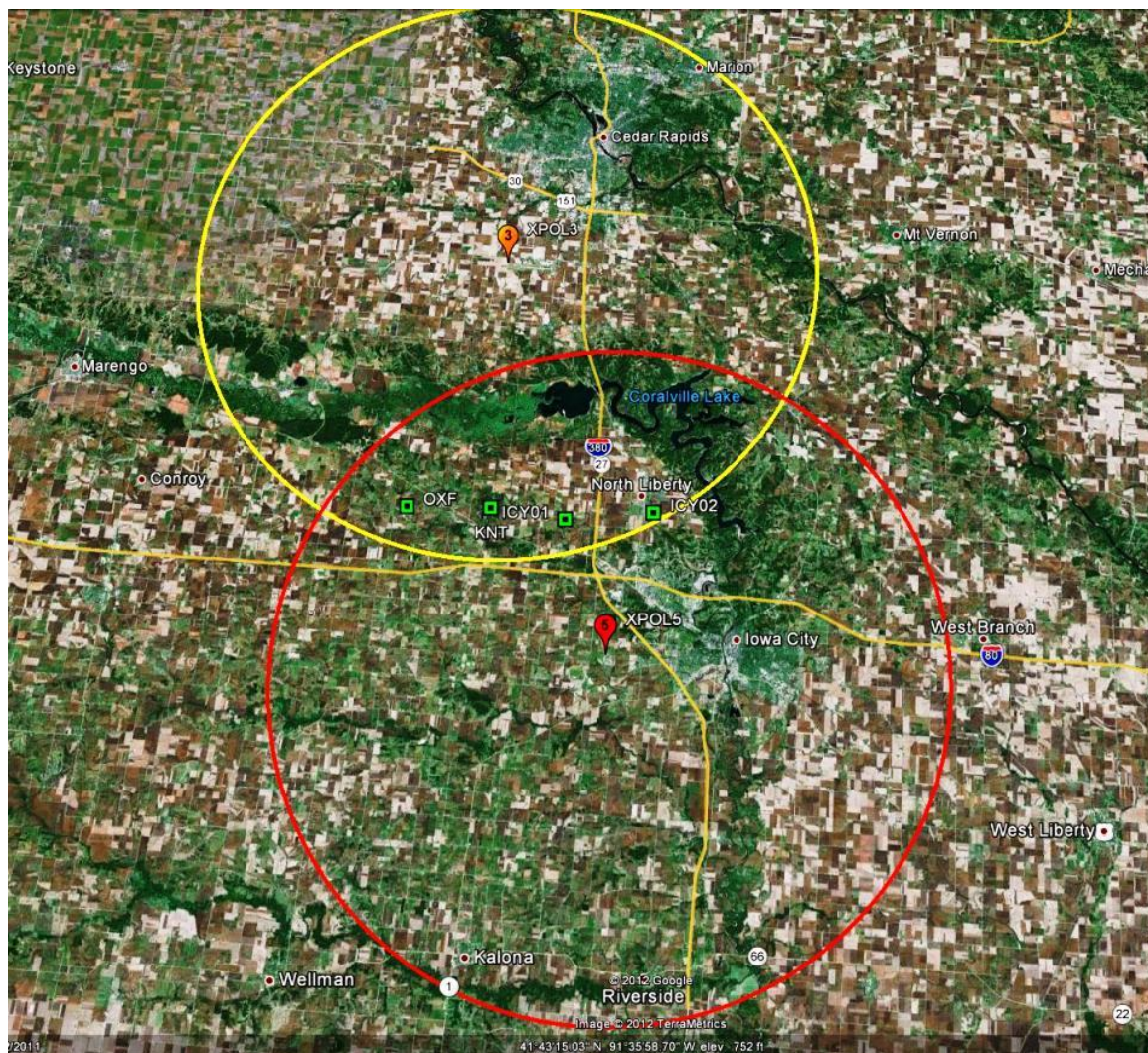


Figure 6.2: Geographic distribution of the network's elements. The red (yellow) ring shows the coverage of the XPOL-5 (XPOL-3) radar. Rain gauges are showed with green markers.

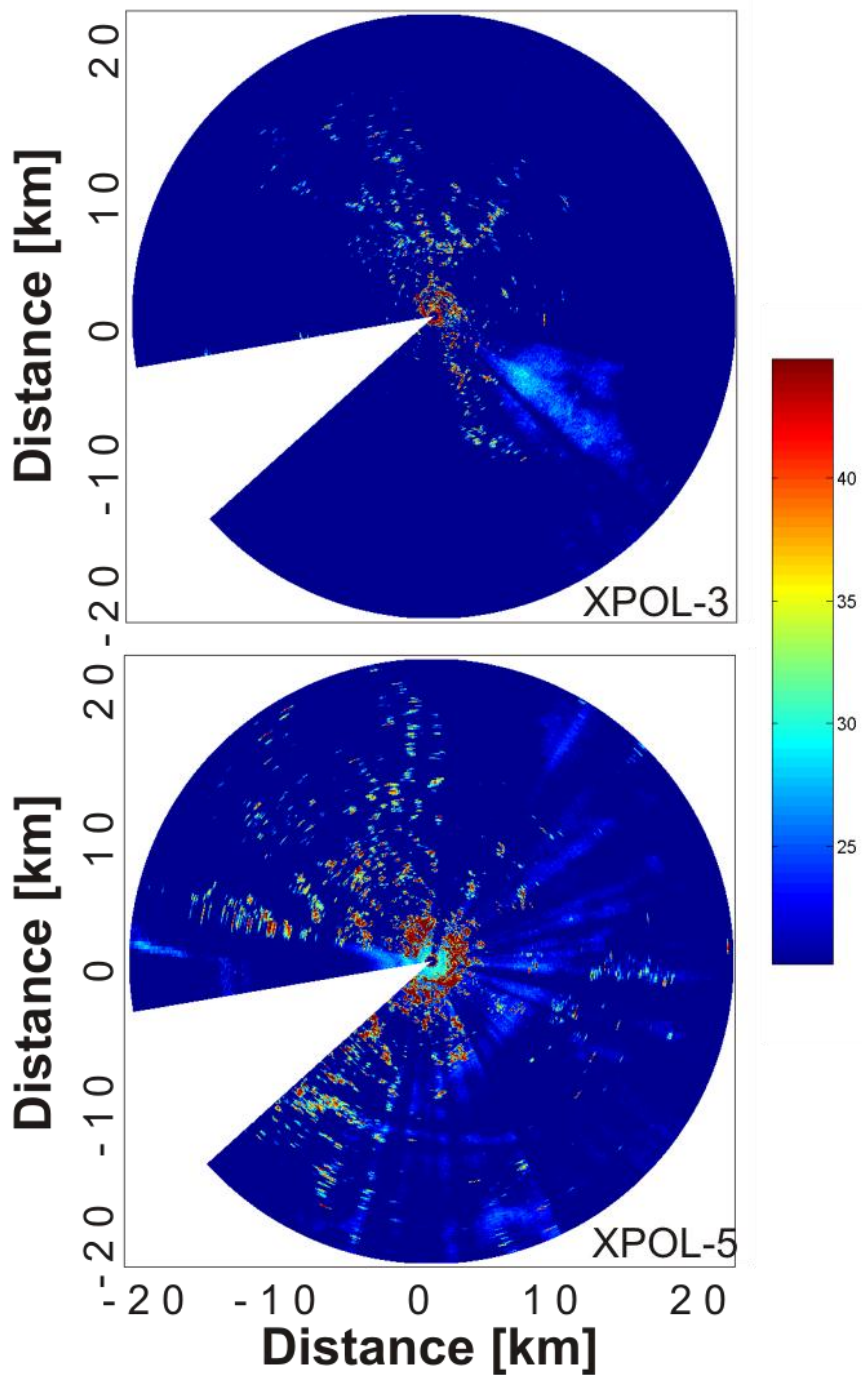


Figure 6.3: Beam blockage by ground clutter as experienced by XPOL-3 and XPOL-5 radars at  $0^\circ$  elevation. Only narrow bands of reflectivity are visible due to the blockage.



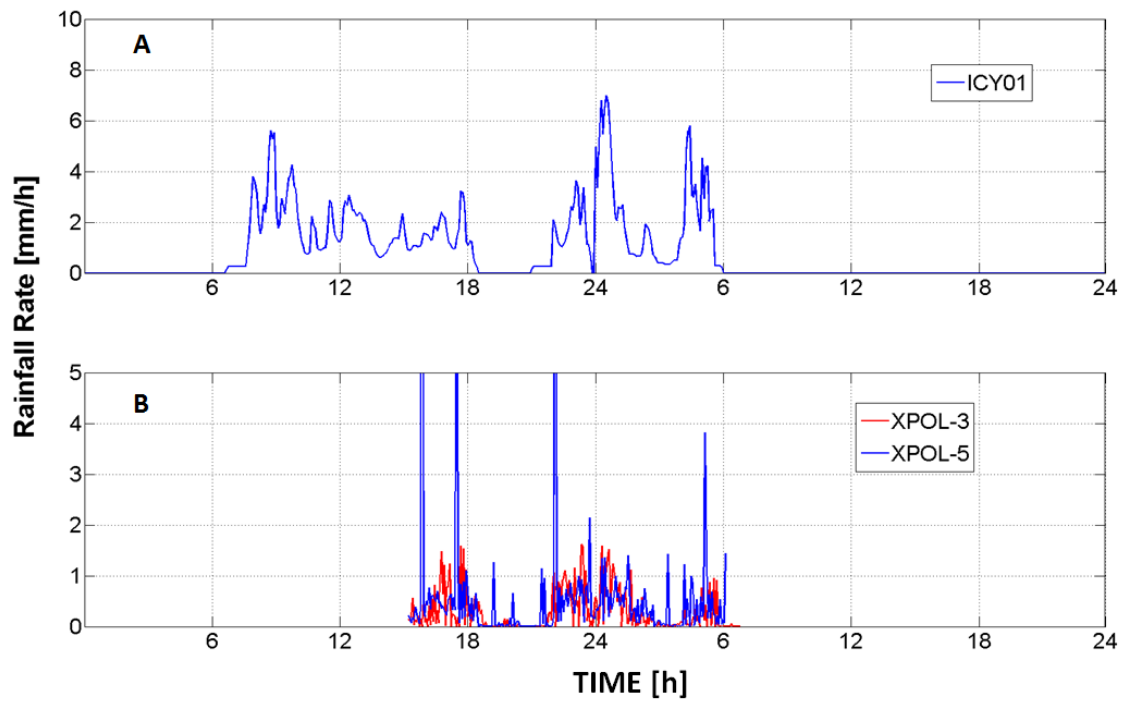


Figure 6.5: Rainfall rate time series. A) Rainfall rate recorded by the ICY01 rain gauge.  
B) Rainfall rates derived based on radar observations.

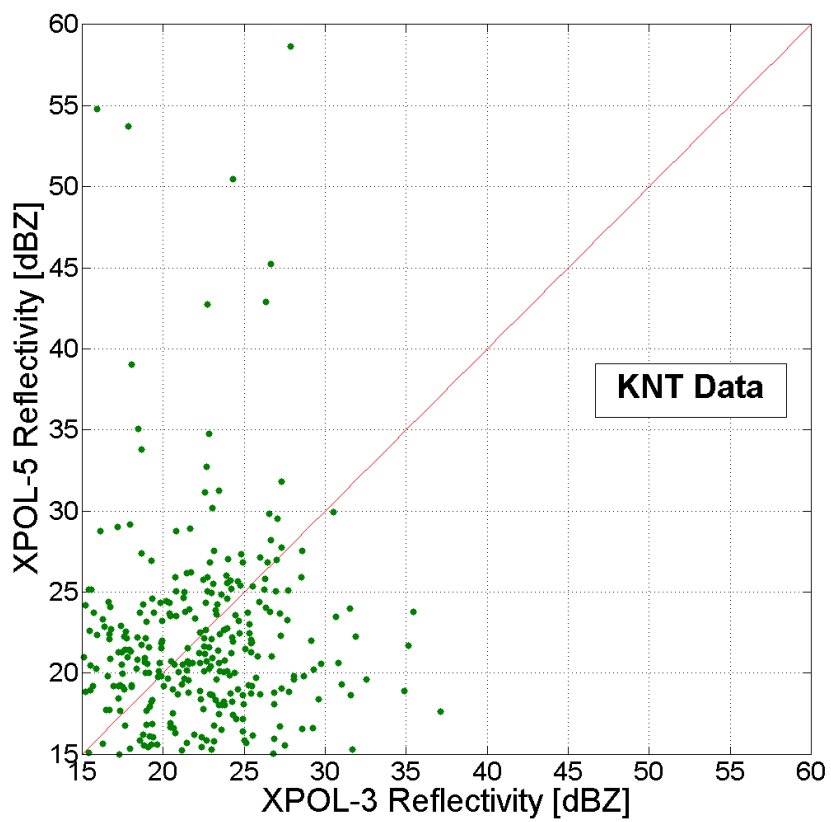


Figure 6.6: Comparison of radar derived rainfall rates for XPOL-3 and XPOL-5 nodes. Selected data points correspond to the location of the KNT rain gauge.

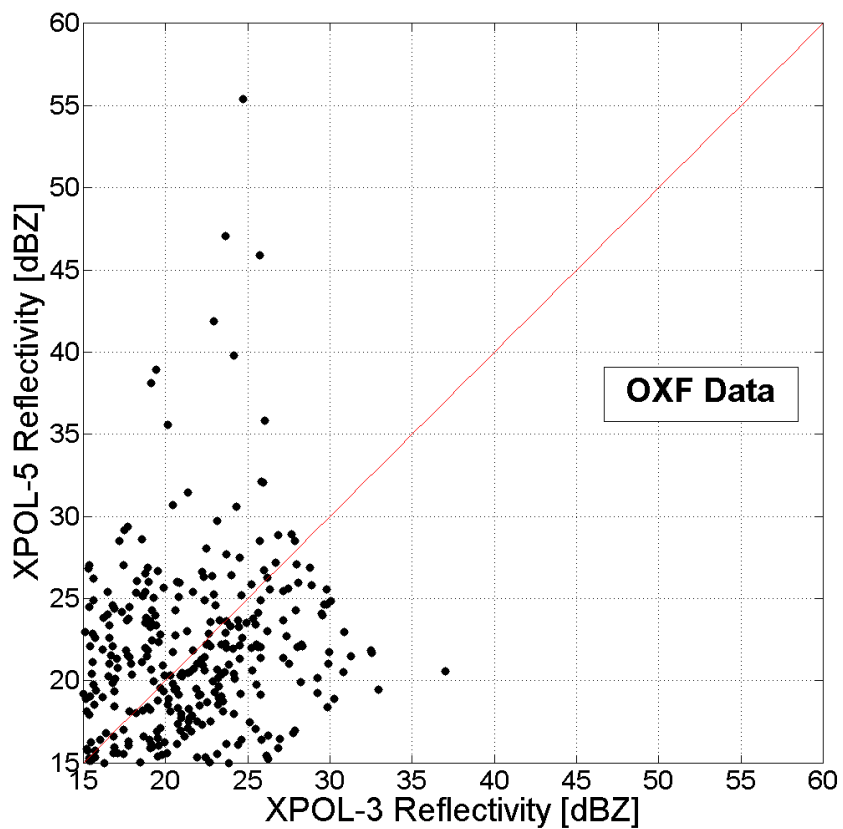


Figure 6.7: Comparison of radar derived rainfall rates for XPOL-3 and XPOL-5 nodes. Selected data points correspond to the location of the OXF rain gauge.

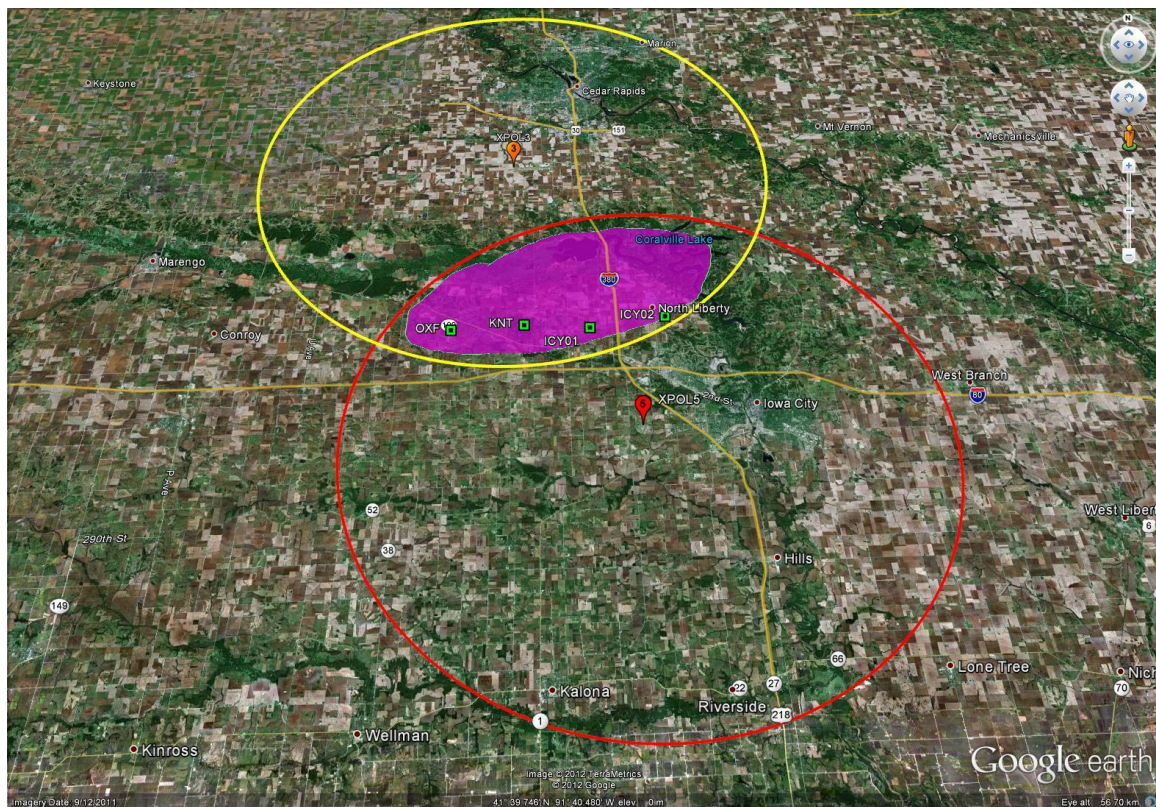


Figure 6.8: Overlap area for the XPOL-2 and XPOL-5 radars used as the area of interest for calculation of the total rainfall accumulation.

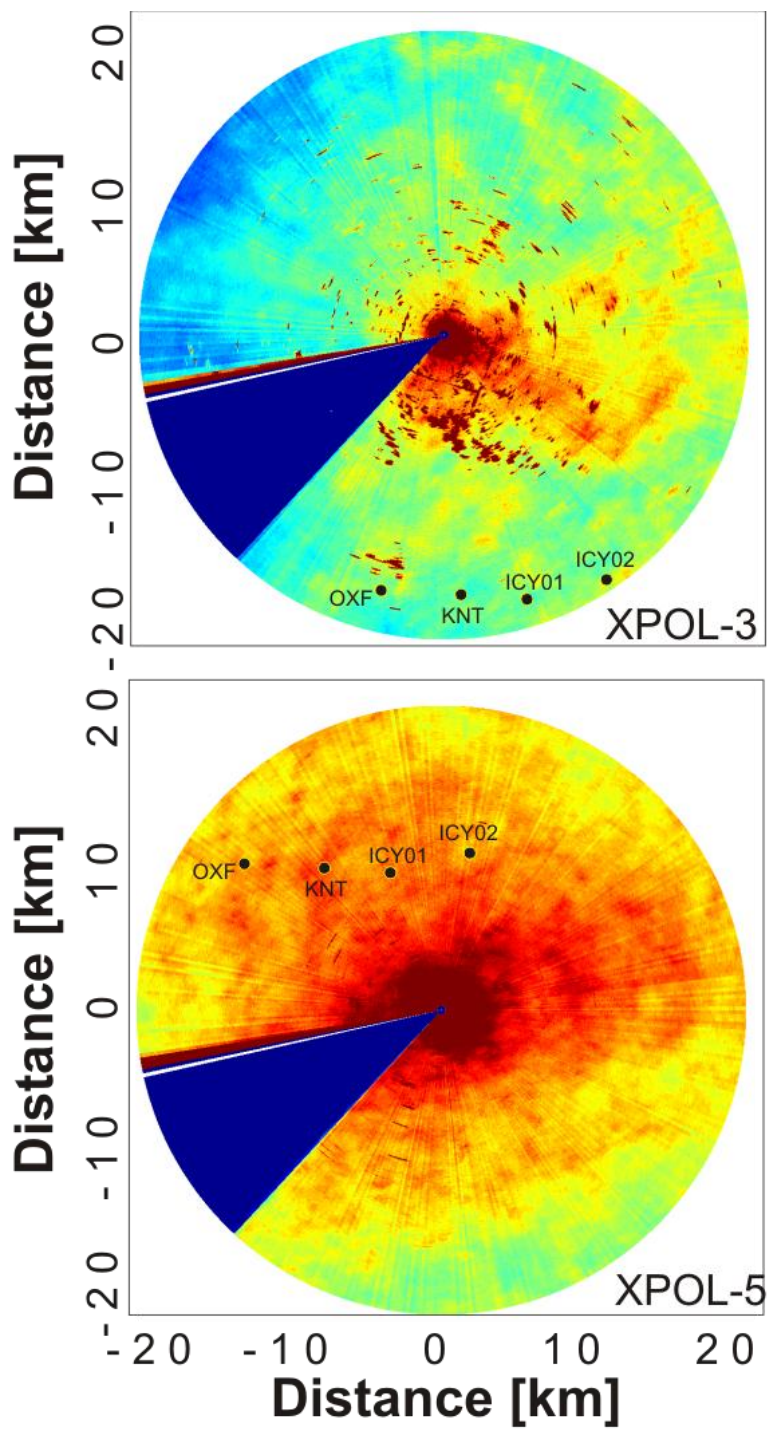


Figure 6.9: Total rainfall accumulation maps for the 12/03/2012-12/04/2012 event. Data based on 3° elevation scans.

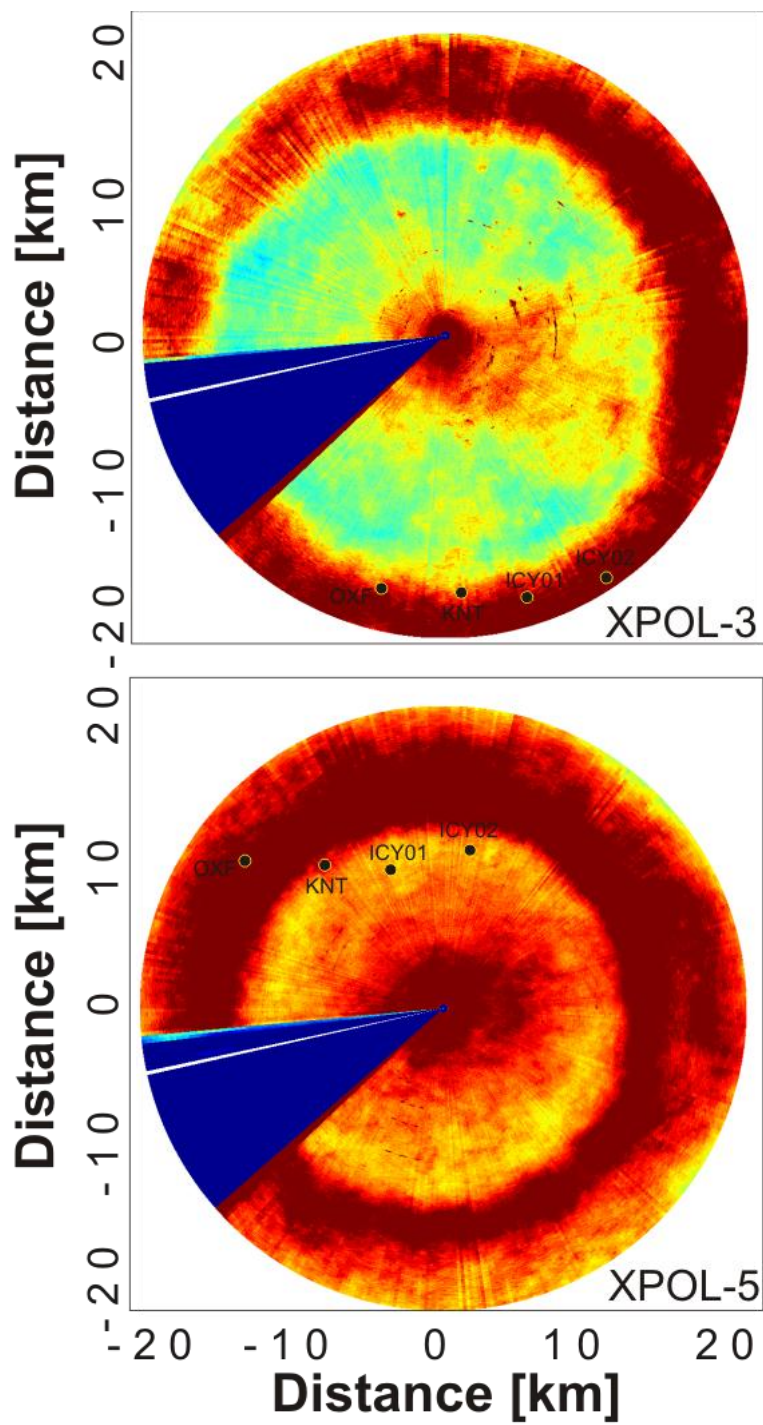


Figure 6.10: Bright band contamination. Total rainfall accumulation maps for the 12/03/2012-12/04/2012 event. Data based on 6° elevation scans.

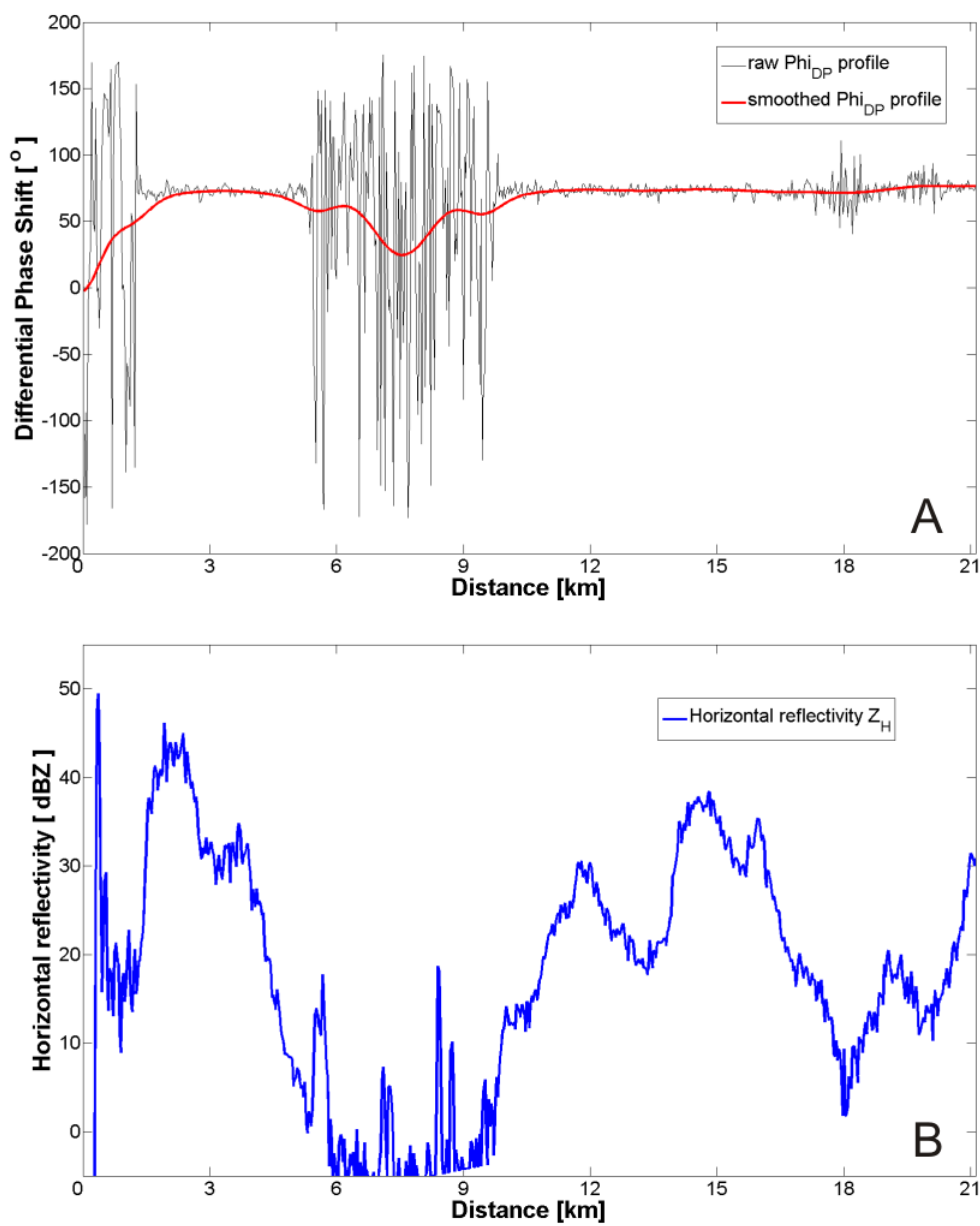


Figure 6.11: A) Example of a  $\Phi_{DP}$  profile (black line) and its smoothed version (red line),  
B) Corresponding reflectivity profile.

Table 6.1: Rain gauge network configuration. The table lists latitude and longitude location of each rain gauge used in the study together with their distance and azimuth orientation from the XPOL-3 and XPOL-5 radars/

<b>R-G</b>	<b>ICY01</b>		<b>ICY02</b>		<b>OXF</b>		<b>KNT</b>	
<b>Location</b>	<b>lat</b>	<b>lon</b>	<b>lat</b>	<b>lon</b>	<b>lat</b>	<b>lon</b>	<b>lat</b>	<b>lon</b>
	41.724	-91.666	41.731	-91.598	41.725	-91.788	41.727	-91.724
<b>To radar</b>	<b>distance</b>	<b>azimuth</b>	<b>distance</b>	<b>azimuth</b>	<b>distance</b>	<b>azimuth</b>	<b>distance</b>	<b>azimuth</b>
<b>XPOL-3</b>	19.0km	162.6 °	20.6km	177.0 °	18.6km	193.3 °	18.2km	177.3°
<b>XPOL-5</b>	9.5km	338.2 °	9.9km	11.9 °	16.4km	303.3 °	12.2km	316.6 °

Table 6.2: Rainfall accumulations [mm] for two events as estimated by XPOL-2 and XPOL-5 radars, for locations corresponding to rain gauges, together with rain gauge-based rainfall accumulations.

<b>EVENT 1 (12/03/2012-12/04/2012) rainfall total accumulation [mm]</b>				
	<b>ICY01</b>	<b>ICY02</b>	<b>OXF</b>	<b>KNT</b>
<b>XPOL-3</b>	4.44	3.62	4.79	6.52
<b>XPOL-5</b>	8.92	7.14	44.67	43.86
<b>Rain gauge</b>	16.82	17.20	17.18	16.95
<b>EVENT 2 (12/14/2012) rainfall total accumulation [mm]</b>				
	<b>ICY01</b>	<b>ICY02</b>	<b>OXF</b>	<b>KNT</b>
<b>XPOL-3</b>	3.36	1.90	4.57	14.48
<b>XPOL-5</b>	21.32	4.21	60.44	39.39
<b>Rain gauge</b>	10.85	8.87	10.51	10.76

Table 6.3 Single-radar attenuation correction methods. Rainfall accumulations [mm] for the 12/03/2012 event as estimated by XPOL-2 and XPOL-5 radars, for locations corresponding to rain gauges and the overlap area.

	$Z_{Hm}$	$Z_H 1$	$Z_H 2$	$Z_H 3$	$Z_H 4$
<b>ICY01 LOCATION</b>					
<b>XPOL-3</b>	4.44	8.32	6.09	4.62	5.99
<b>XPOL-5</b>	8.92	15.15	14.11	9.9	13.01
<b>ICY02 LOCATION</b>					
<b>XPOL-3</b>	3.62	9.12	5.55	4.22	4.77
<b>XPOL-5</b>	7.14	16.16	14.74	10.98	14.18
<b>OXF LOCATION</b>					
<b>XPOL-3</b>	4.79	10.11	6.16	5.30	6.01
<b>XPOL-5</b>	44.67	52.12	45.03	44.32	46.19
<b>KNT LOCATION</b>					
<b>XPOL-3</b>	6.52	12.07	8.03	7.50	6.67
<b>XPOL-5</b>	43.86	50.81	46.22	47.39	44.42
<b>RADAR OVERLAP AREA</b>					
<b>XPOL-3</b>	5.10	9.07	7.71	7.00	5.44
<b>XPOL-5</b>	20.94	28.28	22.84	23.87	23.43

Table 6.4 Network data merging. Rainfall accumulation [mm] results for the 12/03/2012 event and the rain gauge **ICY01** location. Rain gauge recorded accumulation was 16.82 mm.

	<b>Z<sub>Hm</sub></b>	<b>Z<sub>H 1</sub></b>	<b>Z<sub>H 2</sub></b>	<b>Z<sub>H 3</sub></b>	<b>Z<sub>H 4</sub></b>
<b>M1</b>	8.03	13.79	12.51	8.84	11.61
<b>M2</b>	9.01	17.03	16.00	9.9	13.60
<b>M3</b>	7.22	13.22	12.90	6.23	10.21
<b>M4</b>	8.02	14.99	14.01	7.89	12.21

Table 6.5 Network data merging. Rainfall accumulation [mm] results for the 12/03/2012 event and the rain gauge **ICY02** location. Rain gauge recorded accumulation was 17.2 mm.

	<b>Z<sub>Hm</sub></b>	<b>Z<sub>H 1</sub></b>	<b>Z<sub>H 2</sub></b>	<b>Z<sub>H 3</sub></b>	<b>Z<sub>H 4</sub></b>
<b>M1</b>	6.48	14.84	13.08	9.71	12.42
<b>M2</b>	7.22	16.19	16.20	11.11	14.19
<b>M3</b>	5.25	14.14	14.00	9.03	12.76
<b>M4</b>	5.85	12.77	8.36	7.75	10.99

Table 6.6 Network data merging. Rainfall accumulation [mm] results for the 12/03/2012 event and the rain gauge **OXF** location. Rain gauge recorded accumulation was 17.18 mm.

	$Z_{Hm}$	$Z_H 1$	$Z_H 2$	$Z_H 3$	$Z_H 4$
<b>M1</b>	27.24	33.76	23.54	19.39	25.25
<b>M2</b>	44.80	53.01	45.11	45.21	44.82
<b>M3</b>	29.98	42.07	32.82	27.61	31.30
<b>M4</b>	37.95	47.37	40.81	34.54	40.03

Table 6.7 Network data merging. Rainfall accumulation [mm] results for the 12/03/2012 event and the rain gauge **KNT** location. Rain gauge recorded accumulation was 16.95 mm.

	<b>Z<sub>Hm</sub></b>	<b>Z<sub>H 1</sub></b>	<b>Z<sub>H 2</sub></b>	<b>Z<sub>H 3</sub></b>	<b>Z<sub>H 4</sub></b>
<b>M1</b>	32.34	38.86	30.29	29.55	31.39
<b>M2</b>	44.12	51.00	48.05	47.83	46.42
<b>M3</b>	38.38	41.87	31.67	30.19	39.53
<b>M4</b>	36.67	40.22	34.34	41.11	35.44

Table 6.8 Network data merging. Rainfall accumulation [mm] results for the 12/03/2012 event and the radar **overlap area**.

	$Z_{Hm}$	$Z_H 1$	$Z_H 2$	$Z_H 3$	$Z_H 4$
<b>M1</b>	13.02	18.66	15.26	15.43	14.43
<b>M2</b>	34.93	42.21	45.19	37.23	33.60
<b>M3</b>	17.31	20.83	21.43	16.32	16.91
<b>M4</b>	17.22	20.25	23.87	18.22	22.83

## CHAPTER 7

### SUMMARY AND CONCLUSIONS

#### 7.1 Introduction

This chapter reviews the objectives introduced in Chapter 1 and summarizes the obtained results. Furthermore, we discuss technical aspects of the network data collection as well as the limitations of the computer simulation approach. Finally, we indicate future directions of the project presented in this work.

#### 7.2 Revisiting the original objective

As presented in Chapter 1, the broad objective of this study is to contribute to better rainfall estimation through the use of polarimetric weather radar networks. The specific goals were formulated to support the development, operations, and evaluation of The University of Iowa Polarimetric Radar Network. The problem of signal attenuation and how it should be addressed in a networked environment remains the leading focus throughout this work.

Recent advancements in radar polarimetry have resulted in a significant increase in the accuracy of radar rainfall estimates. Attenuation correction methods utilizing polarimetric information show much better stability when compared to non-polarimetric methods and can be credited for the recent increased interest and more widespread use of small, often mobile, X-band radar applications.

To address the problem of attenuation correction in a network of radars, we used computer simulations and analyzed data collected by The University of Iowa Polarimetric Radar Network. We developed a set of utilities in support of data collection and analysis and applied them to conduct a series of inter- and cross-calibration experiments. The calibration experiments were dictated by the need to secure an acceptable level of imbalance in sensitivity between the individual radars as well as radars' H- and V-

polarized channels. In the following we discuss the objectives of this work and provide a brief summary of the obtained results.

### 7.3 Summary of the obtained results

In Chapter 2, we presented a detailed description of a polarimetric radar network simulator. The simulator has been developed to imitate, to a certain degree, the data collection mechanisms of a network of polarimetric, X-band radars and provide a cost-effective way to evaluate a number of rainfall retrieval, attenuation correction, and data merging methods. To demonstrate the basic functionality of the simulator, we conduct a number of simulation scenarios.

In Chapter 3, the developed polarimetric radar simulator is used to evaluate a number of attenuation correction strategies. First, we simulated a set of single radar methods. Each of the analyzed methods is used to correct reflectivity values for four radars located within the spatial domain. To evaluate the methods, we compared the mean difference and standard deviation in reflectivity [dBZ] estimates between individual radars and the “true” reflectivity values. The results were supplemented with the mean and standard deviation of relative errors in mean aerial precipitation [mm/h] estimates. Based on the obtained results, we concluded that polarimetric attenuation correction methods based on a constrained differential phase shift outperform the non-polarimetric methods. In addition, the method described as the constrained method with optimal  $\alpha$  parameter did not perform as well as expected due to inherent problems with the removal of backscatter differential phase shift  $\delta$  from  $\Phi_{DP}$  profiles. It is also important to note that all single radar attenuation correction methods suffered from range dependent errors. Next, to test attenuation correction methods in a network environment, we used the simulator to evaluate a number of data merging strategies. The merging methods were based on a number of techniques ranging from taking a maximum available reflectivity value to more sophisticated methods like taking a combination of inputs from radars with

weights based on path integrated attenuation (PIA) as experienced by individual radars. One of the conclusions from the study presented in Chapter 3 is that the selection of the optimal merging method depends on the assessment criterion (difference in reflectivity versus relative error in mean aerial precipitation). Reflectivity-based results indicated that to minimize mean differences in reflectivity, one needs to take into account which method has been used to correct reflectivity of individual radars before selecting the merging procedure. For mean aerial precipitation, methods based on PIA consistently outperformed other simulated methods. Quantitative analysis revealed that, when applied to single radar data, merging can significantly improve the quality of the network product both by minimizing the mean differences and the standard deviation of the simulated values. Merged products showed less sensitivity to the size of the domain of interest when compared to the single radar products. Lastly, we proposed a network-based attenuation correction method. The method relies on the accurate estimation of the path integrated attenuation (PIA) for every radar ray at distances considered to be “far ranges” (behind the storm). The validity of this approach has been evaluated using the simulator. The method showed good performance when compared to single radar products, but the methods based on differential phase shift and merging using minimum and weighted PIA information proved to be a better choice. In an iterative scheme in which the final product becomes the source of PIA information, the method did not improve its performance mostly due to the limited coverage of the merged product.

The simulator is a cost-effective way to test how a network’s physical configuration (location of network’s nodes, scanning strategy, radar technical specifications), selected attenuation correction algorithm, data merging scheme, rainfall retrieval methods, or the combination of the above interact in the process of generating a network rainfall product.

In Chapter 4, we describe The University of Iowa Polarimetric Radar Network by providing its technical specifications and basic design structure. We also provide a

description of the data acquisition system by illustrating how data files are created and explaining what elements control the process of data acquisition. Finally, we demonstrate a set of custom utilities that have been programmed to perform a number of tasks, including computation of the radar calibration constant, estimation of polarimetric variables, customization of visualization tools, and metadata computation.

Chapter 5 describes the inter- and cross-calibration procedure. During the initial deployment of The University of Iowa Polarimetric Radar Network, three of the network's nodes were collocated at a test site located at the Iowa City landfill. The radars were positioned within 30 meters of each other and operated in a vertically-pointing mode. The inter-calibration focused on the estimation and, subsequently, the elimination of any systematic imbalance between the radars' horizontally and vertically polarized channels. The cross-calibration procedure was intended to assess the extent to which the estimates of the radar reflectivity factor vary from radar to radar when each of the nodes is sampling essentially the same resolution volume. Both procedures are important quality control steps and should be performed periodically to assure the accurate application of rainfall estimation methods, hydrometeor classification algorithms, or attenuation correction procedures, as all are directly linked to the inter- and cross-calibration results. Based on the analyzed events, we estimated the imbalance between horizontally and vertically polarized channels for the XPOL-2, XPOL-3, and XPOL-5 network nodes. In addition, we conducted a pair-wise analysis of reflectivity profiles for the XPOL-2, XPOL-3, and XPOL-5 pairs.

The analysis points out that although identical in their design, the radars show discrepancies in reflectivity estimation that needs to be addressed before their operational deployment. The findings for the inter-calibration tests revealed the XPOL-5 radar to be the only one that could be considered balanced. While the XPOL-3 radar showed a systematic imbalance with moderate oscillations that could be modified by implementing a correction factor, the XPOL-2 radar showed behavior that is difficult to correct due to

the imbalance between the V and H channels that fluctuated considerably between the analyzed rainfall events. The cross-calibration experiment further amplified the need for periodic calibration tests, with individual radars showing differences in reflectivity estimation that should be corrected before their operational deployment.

In Chapter 6, we discussed the challenges associated with the operational implementation of the attenuation correction methods to X-band radar data. We analyzed the process of implementing single radar attenuation correction methods and data merging techniques based on a data sample collected by The University of Iowa Polarimetric Radar Network. In the process, we identified ground clutter contamination, partial beam blockage, and bright band reflections as the most significant features that degrade reflectivity measurements. Based on the obtained results, we see limited usability of the differential phase shift signal in the process of attenuation correction and rainfall estimation at light to moderate rainfall conditions due to the low sensitivity of the signal, as compared to the observed noise levels. Next, we implemented a number of single radar methods as well as data merging techniques in order to verify the findings of the polarimetric radar network simulator that is presented in Chapter 3. Based on the rain gauge data collected for the duration of the analyzed rainfall event, we hypothesized that the rainfall amount was uniformly distributed over the domain of interest. To assess the performance of the attenuation correction and data merging methods, we compared rain gauge-based rainfall accumulations with the rainfall total accumulation results that are based on radar data. To simplify the analysis, we do not discuss the errors associated with the rain gauge measurement process and assume that the  $Z-R$  relationship accurately converts radar reflectivity to rainfall rate amounts. Although a comprehensive evaluation of the simulator could not be achieved in the study due to a limited radar data set, the exercise presented in this chapter complements the educational aspect of the simulation studies completed in Chapter 3. The data collected by The University of Iowa Polarimetric Radar Network can be used to further enhance the accuracy of the simulator.

#### 7.4 Note on the technical aspects of network data collection

In the presented study, in Chapters 4, 5 and 6 we used radar data collected by The University of Iowa Polarimetric Radar Network. In this subsection we address the technical difficulties experienced in the process of developing the network and during early data collection.

As presented in Chapter 4, the network consists of four, identical in their design polarimetric, X-band radars. The radars were designed and manufactured by ProSensing, Inc. The custom design of the radars allows for operational flexibility, but also poses some challenges due to the uniqueness of the design and the prototype character of the project. Since the commissioning of the radars in 2010 a number of design flaws have been discovered. One of the issues that affected the data collection process was the lack of efficient air-conditioning system. The A/C system in its original form did not allow for proper work of the radars during warm weather and substantially limited radar time to mostly nocturnal and/or winter collection periods. To address the problem, a new air-conditioning system has been installed and is being tested by the group. Additional difficulties experienced when operating the radars included pedestal malfunction due to moisture build-up, software errors and electronics failures.

The mentioned above problems in the initial operation period considerably limited our ability to collect rainfall data and resulted in the presented analysis being limited to only a few rainfall cases. Continued effort by the group to eliminate any experienced and potential network problem is underway to secure continuous and uninterrupted operation of the network.

#### 7.5 Conclusions and future directions

An accurate estimation of rainfall at high spatial and temporal scales is a challenging endeavor. Polarimetric, X-band radars became a focus of many research studies due to their rainfall measuring capabilities and a low (relative to conventional

radar systems) purchase cost. The attenuation of radar signal by intervening rainfall remains a major limiting factor for radars operated at X-band frequencies. The polarimetric expansion in radar systems offers new ways to address the problem of attenuation correction, but proposes little help in the case of the total signal extinction due to beam blockage or heavy rainfall events.

In this work we investigate how operating a network of radars can help develop a better attenuation correction strategy and lead to improved rainfall estimation techniques. The analysis starts with computer simulations as a cost-effective way to evaluate a number of simulation scenarios in a controlled, computer-designed environment. The findings from the simulator are later used as guidance in operating The University of Iowa Polarimetric Radar Network. To fully validate the results of the simulations, a set of experiments utilizing a network of polarimetric X-band radars accompanied by a range of ground validation instruments (rain gauges, disdrometers) must be performed. Only a long-term experiment that captures a variety of rainfall events can provide sufficient data to verify the findings obtained using the simulator. Information from such experiments could be used to eliminate some of the simulator's limitations and contribute to further development of the simulator.

Due to the technical difficulties in the early stage of network development (please see section 7.4 for details) the analysis involving the data collected by The University of Iowa Polarimetric Radar Network is limited to only a few rainfall events. Together with the results obtained in the simulation process the presented work offers a first look at challenges associated with operating a network of radars as well as guidance to optimal operation of a network. Based on the obtained results the work will continue to maximize the rainfall observing potential of The University of Iowa Polarimetric Radar Network.

## REFERENCES

- Abeyssekera, S. S. (1998), Performance of pulse-pair method of Doppler estimation, *IEEE Transactions on Aerospace and Electronic Systems*, 34(2), 520-531.
- Anagnostou, E.N. and W.F. Krajewski (1997), Simulation of radar reflectivity fields: Algorithm formulation and evaluation, *Water Resources Research*, 33(6), 1419-1429.
- Anagnostou, E.N., W.F. Krajewski and J.A. Smith (1999), Uncertainty quantification of mean-areal radar rainfall estimates, *Journal of Atmospheric and Oceanic Technology*, 16(2), 206-215.
- Anagnostou, E. N., M. N. Anagnostou, W. F. Krajewski, A. Kruger, and J. M. Benjamin (2004), High-resolution rainfall estimation from X-band polarimetric radar measurements. *Journal of Hydrometeorology*, 5, 110–128.
- Anagnostou, Emmanouil N., Mircea Grecu, Marios N. Anagnostou (2006), X-band Polarimetric Radar Rainfall Measurements in Keys Area Microphysics Project, *Journal of Atmospheric Sciences*, 63, 187–203, doi: 10.1175/JAS3592.1.
- Andsager, Karen, Kenneth V. Beard, Neil F. Laird (1999), Laboratory Measurements of Axis Ratios for Large Raindrops, *Journal of Atmospheric Sciences*, 56, 2673–2683.
- Arjen Y. Hoekstra and Mesfin M. Mekonnen (2012), The water footprint of humanity PNAS 2012 109: 3232-3237.
- Arnold, C. P., Jr., and C. H. Dey (1986), Observing-systems simulation experiments: Past, present, and future, *Bulletin of the American Meteorological Society*, 67(6), 687–695.
- Atlas, D. and Banks, H. (1951), The interpretation of microwave reflections from rainfall, *Journal of Meteorology*, 8, 271–282.
- Atlas, D. (2002), Radar calibration: Some simple approaches, *Bulletin of the American Meteorological Society*, 83, 1313–1316.
- Austin, P.M. (1987), Relation between measured radar reflectivity and surface rainfall, *Monthly Weather Review*, 115, 1053–1069.
- Beard, K.V., and C. Chuang (1987), A new model for the equilibrium shape of raindrops, *Journal of Atmospheric Sciences*, 44, 1509–1524.
- Berne, A., G. Delrieu, H. Andrieu (2005), Estimating the Vertical Structure of Intense Mediterranean Precipitation Using Two X-Band Weather Radar Systems. *Journal of Oceanic and Atmospheric Technology*, 22, 1656–1675.
- Berne A., and R. Uijlenhoet (2005), A stochastic model of range profiles of raindrop size distributions: Application to radar attenuation correction, *Geophysical Research Letters*, 32(10), L10803.
- Blackman, T. M., and A. J. Illingworth (1997), Examining the lower limit of  $K_{DP}$  rain-rate estimation including a case study at S-band. Preprints, 28th Int. Conf. on Radar Meteorology, Austin, TX, Amer. Meteor. Soc., 117–118.

- Brandes, E. A., A. V. Ryzhkov, and D. S. Zrnić (2001), An evaluation of radar rainfall estimates from specific differential phase. *Journal of Atmospheric and Oceanic Technology*, 18:363–374.
- Bringi, V.N., J.W.F. Goddard and S.M. Cherry (1982), Comparison of dual polarization radar measurements of rain with ground based disdrometer measurements, *Journal of Applied Meteorology*, 21, 252–264.
- Bringi, V. N. ; Chandrasekar, V. ; Balakrishnan, N. ; Zrnic, D. S. (1990) An examination of propagation effects in rainfall on radar measurements at microwave frequencies, *Journal of Atmospheric and Oceanic Technology*, 7 (6). pp. 829-840. ISSN 0739-0572.
- Bringi, V., and A. Hendry (1990), Technology of polarization diversity radars for meteorology, *Radar Meteorology*, David Atlas, Ed., Amer. Meteor. Soc., 153-190.
- Bringi, V. N., T. D. Keenan, and V. Chandrasekar (2001), Correcting C-band radar reflectivity and differential reflectivity data for rain attenuation: A self-consistent method with constraints, *IEEE Transactions on Geosciences and Remote Sensing*, 39, 1906–1915.
- Bringi, V., and V. Chandrasekar (2001), *Polarimetric Doppler Weather Radar: Principles and Applications*. Cambridge University Press, 636 pp.
- Bringi, V.N., G.Huang, V.Chandrasekar and T.D. Keenan (2002), An Areal Rainfall Estimator Using Differential Phase, *Journa of Atmospheric and Oceanic Technology*, Vol. 19, No. 5, pp. 633-645.
- Brock, F. V., K. C. Crawford, R. L. Elliott, G. W. Cuperus, S. J. Stadler, H. L. Johnson, and M. D. Eilts (1995), The Oklahoma mesonet: A technical overview, *Journal of Atmospheric and Oceanic Technology*, 12, 5–19.
- Carey, L. D., S. A. Rutledge, D. A. Ahijevich, and T. D. Keenan (2000), Correcting propagation effects in C-band polarimetric radar observations of tropical convection using differential propagation phase, *Journal of Applied Meteorology*, 39:1405–1433.
- Caumont O, V. Ducrocq, G. Delrieu, M. Gosset, J.-P. Pinty, J. Parent du Châtelet, H. Andrieu, Y. Lemaître, and G. Scialom (2006), A radar Simulator for High-Resolution Non-hydrostatic Models, *Journal of Atmospheric and Oceanic Technology*, Vol. 23, 1049–1067.
- Cheong, B. L., R. D. Palmer, and M. Xue (2008), A time series weather radar simulator based on high-resolution atmospheric models, *Journal of Atmospheric and Oceanic Technology*, 25, 230–243.
- Cho, J. Y. N. (2005), Multi-PRI signal processing for the terminal Doppler weather radar. Part II: Range–velocity ambiguity mitigation, *Journal of Atmospheric and Oceanic Technology*, 22, 1507–1519.
- Ciach, G. J. (2003), Local Random Errors in Tipping-Bucket Rain Gauge Measurements, *Journal of Atmospheric and Oceanic Technology*, 20, 752–759.

- Ciach, G.J. and W.F. Krajewski (2006), Analysis and modeling of spatial correlation structure of small-scale rainfall in Central Oklahoma, *Advances in Water Resources*, 29, 1450–1463.
- Collett, E. (2005), Field guide to polarization, *SPIE Field Guides*, vol. FG05, SPIE.
- Collier, C.G. (2009), On the propagation of uncertainty in weather radar estimates of rainfall through hydrological models, *Meteorological Applications*, 16(1), 35–40.
- Crum, Timothy D., Alberty, Ron L. (1993), The WSR-88D and the WSR-88D operational support facility, *Bulletin of the American Meteorological Society*, 74.9.
- Delrieu, G., S. Caoudal, J.D. Creutin (1997), Feasibility of using mountain return for the correction of ground-based X-band weather radar data *Journal of Atmospheric and Oceanic Technology*, 14:3, 368–385.
- Delrieu, G., L. Huc, and J-D. Creutin (1999), Attenuation in rain for X-band and C-band weather radar systems: Sensitivity with respect to the drop size distribution, *Journal of Applied Meteorology*, 38:57–68.
- Doviak, R.J. and D.S. Zrnić, (1993), *Doppler Radar and Weather Observations*, Academic Press.
- Freeman R. L. (2004), Telecommunication System Engineering, John Wiley & Sons. pp.399. ISBN 0-471-45133-9.
- Fujita, M. (1983), An algorithm for estimating rain rate by dual-frequency radar, *Radio Science*, 18, 697–708.
- Germann, U., Berenguer, M., Sempere-Torres, D., Zappa, M. (2009), REAL - ensemble radar precipitation estimation for hydrology in a mountainous region, *Quarterly Journal of the Royal Meteorological Society*, 135( 639), 445–456 ISSN 0035-9009.
- Gorgucci, E. (2001), Rainfall estimation from polarimetric radar measurements: Composite algorithms immune to variability in raindrop shape–size relation, *Journal of Atmospheric and Oceanic Technology*, 18:1773–1786.
- Gorgucci, E., G. Scarchilli, V. Chandrasekar and G. Scarchilli (2002), Estimation of raindrop size distribution parameters from polarimetric radar variables, *Journal of Atmospheric Sciences*, 59, 2373–2384.
- Gorgucci, Eugenio, V. Chandrasekar, Luca Baldini (2006), Correction of X-Band radar observation for propagation effects based on the self-consistency principle, *Journal of Atmospheric and Oceanic Technology*, 23, 1668–1681.
- Gosset, M., and I. Zawadzki (2001), Effect of nonuniform beam filling on the propagation of the radar signal at X-band frequencies. Part I: Changes in the  $k(Z)$  relationship, *Journal of Atmospheric and Oceanic Technology*, 18, 1113–1126.
- Gosset, M. (2004), Effect of nonuniform beam filling on the propagation of radar signals at X-band frequencies. Part II: Examination of differential phase shift, *Journal of Atmospheric and Oceanic Technology*, 21, 358–367.

- Greco, M. and W.F. Krajewski (2000), A large-sample investigation of statistical procedures for radar-based short-term, quantitative precipitation forecasting, *Journal of Hydrology*, 239(1-4), 69-84.
- Green, A.W. (1975), An approximation for the shape of large raindrops, *Journal of Applied Meteorology*, 14, 1578-1583.
- Habib, E., W.F. Krajewski and G.J. Ciach (2001), Estimation of rainfall inter-station correlation, *Journal of Hydrometeorology*, 2(6), 621-629.
- Habib, E., Aduvala, A., and Meselhe, E. A. (2008), Analysis of radar-rainfall error characteristics and implications for streamflow simulations uncertainty, *Journal of Hydrologic Sciences*, 53(3), 568-587.
- Cadzow, J. W. (1982), Spectral estimation: An over-determined rational model equation approach, Proceedings IEEE special issue on spectral estimation, 70(9), 907-939.
- Hitschfeld W., and J. Bordan (1954), Errors inherent in the radar measurements of rainfall at attenuating wavelengths, *Journal of Applied Meteorology*, 11, 58-67.
- Hildebrand, P. H. (1978), Iterative correction for attenuation of 5 cm radar in rain, *Journal of Applied Meteorology*, 17, 508-514.
- Iguchi, T. and Meneghini, R. (1994), Intercomparison of single-frequency methods for retrieving a vertical rain profile from airborne or spaceborne radar data, *Journal of Atmospheric and Oceanic Technology*, 11, 1507-1516.
- Jameson, A. (1989), The interpretation and meteorological application of radar backscatter amplitude ratios at linear polarizations, *Journal of Atmospheric and Oceanic Technology*, 6, 908-919.
- Jameson, A. (1992), The effect of temperature on attenuation-correction schemes in rain using polarization propagation differential phase shift, *Journal of Applied Meteorology*, 31, 1106-1118.
- Johnson, B., and E. A. Brandes (1987), Attenuation of a 5-cm wavelength radar signal in the Lahoma-Oriente storms, *Journal of Atmospheric and Oceanic Technology*, 4, 512-517.
- Joss, J., and A. Waldvogel (1990), Precipitation measurement and hydrology, *Radar in meteorology* (A90-39376 17-47), Boston, MA, American Meteorological Society, p. 577-606.
- Junyent F. (2007), Networked weather radar system using coherent on receive technology, *Electronic Doctoral Dissertations for UMass Amherst*. Paper AAI3282734.
- Junyent, F., V. Chandrasekar, D. McLaughlin, E. Insanic, and N. Bharadwaj (2010), The CASA integrated project 1 networked radar system, *Journal of Atmospheric and Oceanic Technology*, 27, 61-78.
- Kabèche, Ahmed, Jacques Testud (1995), Stereoradar Meteorology: A new unified approach to process data from airborne or ground-based meteorological radars, *Journal of Atmospheric and Oceanic Technology*, 12, 783-799.

- Keenan, T.D., et al. (1998), The BMRC/NCAR C-Band polarimetric (C-POL) radar system, *Journal of Atmospheric and Oceanic Technology*, 15, pp. 871–886.
- Kozu, T., and K. Nakamura (1991), Rainfall parameter estimation from dual-radar measurements combining reflectivity profile and path integrated attenuation, *Journal of Atmospheric and Oceanic Technology*, 8, 259–270.
- Kozu, T., and T. Iguchi (1996), A preliminary study of non-uniform beam filling correction for spaceborne radar rainfall measurement, *IEICE transactions on communications*, E79–B, 763–769.
- Krajewski, W.F. and K.P. Georgakakos (1985), Synthesis of radar-rainfall data, *Water Resources Research*, 21(5), 764-768.
- Krajewski, W.F., R. Raghavan and V. Chandrasekar (1993), Physically-based simulation of space-time radar rainfall measurements, *Journal of Applied Meteorology*, 32(2), 268-283.
- Krajewski, W.F. and J.A. Smith (1995), Uncertainty analysis in radar-rainfall estimation, In "New Concepts of Uncertainty in Hydrology and Water Resources" (Kundzewicz, ed.), *Cambridge University Press*, 181-189.
- Krajewski, W.F. and J.A. Smith (2002), Radar hydrology: Rainfall estimation, *Advances in Water Resources*, 25, 1387–1394.
- Krajewski, W.F., A. Kruger, J.A. Smith, R. Lawrence, C. Gonyon, R. Goska, B.-C. Seo, P. Domaszczyński, M.L. Baek, M.K. Ramamurthy, J. Weber, A.A. Bradley, S.A. DelGreco, and M. Steiner (2011), Towards better utilization of NEXRAD data in hydrology: An overview of Hydro-NEXRAD, *Journal of Hydroinformatics*, 13.2, 255-266.
- Le Bouar, E., J. Testud, and T. D. Keenan (2001), Validation of the rain profiling algorithm ZPHI from the C-band polarimetric weather radar in Darwin, *Journal of Atmospheric and Oceanic Technology*, 18, 1819–1837.
- Maki, M., T. Maesaka, A. Kato, S. Shimizu, D.-S. Kim, K. Iwanami, S. Tsuchiya, T. Kato, Y. Kikomuri and K. Kieda (2010), X-band Polarimetric Radar Networks in Urban Areas, *Proc. Sixth European Conf. on Radar in Meteorology and Hydrology*.
- Marshall, J., and W.M. Palmer (1948), The distribution of raindrops with size, *J. Atmos. Sci.*, 5, 165–166.
- Martin, J. E. (2006), *Mid-Latitude Atmospheric Dynamics: A First Course*. Wiley, 324 pp.
- Martin, W.J., and M. Xue (2006), Sensitivity analysis of convection of the 24 May 2002 IHOP case using very large ensembles, *Mon. Wea. Rev.*, 134, 192–207.
- Marzano, F. S., D. Scaranari, M. Celano, P. P. Alberoni, G. Vulpiani, M. Montopoli (2006), Hydrometeor classification from dual-polarized weather radar: extending fuzzy logic from S-band to C-band data, *Advances in Geosciences* 7, 109-114.

- Marzoug, M. and P. Amayenc (1994), A class of single- and dual-frequency algorithms for rain-rate profiling from a spaceborne radar. Part I: Principle and tests from numerical simulations, *J. Atmos. Oceanic Technol.*, 11, 1480–1506.
- Matrosov, S.Y., K.A. Clark, B.E. Martner, and A. Tokay (2002), X-band polarimetric radar measurements of rainfall, *J. Appl. Meteor.*, 41, 941–952.
- Matrosov, Sergey Y., David E. Kingsmill, Brooks E. Martner, F. Martin Ralph (2005), The Utility of X-Band Polarimetric Radar for Quantitative Estimates of Rainfall Parameters, *Journal of Hydrometeorology*, 6, 248–262.
- Masutani, M., et al. (2006), Observing system simulation experiments at NCEP, NCEP Off. Note 451, Environ. Model. Cent., Natl. Cent. for Environ. Predict., Natl. Weather Serv., NOAA, U.S. Dep. of Commer., Camp Springs, Md.
- Melnikov V. M. and D. S. Zrnić (2004), Simultaneous transmission mode for the polarimetric WSR-88D. Statistical biases and standard deviations of polarimetric variables. Cooperative Institute for Mesoscale Meteorological Studies, University of Oklahoma. 1313 Haley Circle, Norman, OK, 73069
- Meneghini, R., J. Eckerman, and D. Atlas (1983), Determination of rain rate from a spaceborne radar using measurements of total attenuation, *IEEE Transactions on Geosciences and Remote Sensing*, 21, 34–43.
- Mishchenko, M.I., L.D. Travis, and D.W. Mackowski (1996), T-matrix computations of light scattering by nonspherical particles: A review, *J. Quant. Spectrosc. Radiat. Transfer*, 55, 535–575.
- Morris, G.V. Harkness, L. (1996), Airborne Pulsed Doppler Radar, Artech House.
- Moszkowicz, S., G.J. Ciach and W.F. Krajewski (1994), Statistical detection of anomalous propagation in radar reflectivity patterns, *Journal of Atmospheric and Oceanic Technology*, 11(4), 1026–1034.
- Mueller, E.A. (1984), Calculation procedure for differential propagation phase shift. Preprints, 22<sup>nd</sup> Conference on Radar Meteorology, Zurich, Amer. Meteor. Soc., 397–398.
- Muste, M., D. Kim, N. Arnold, T. Whiteaker, C. Just and A. Kruger (2009), Digital watershed inception using community project components, Special Issue on Cyberinfrastructure for Hydrology and Environmental Engineering, Proceedings of Institution of Civil Engineers Water Management, Thomas Telford Journal, London, UK.
- Oguchi, T.: Electromagnetic wave propagation and scattering in rain and other hydrometeors, *IEEE Proceedings*, 71, 1029–1078, 1983.
- Otto T. and H. W. J. Russchenberg (2010), Estimation of the raindrop-size distribution at X-band using specific differential phase and differential backscatter phase, ERAD 2010 - The 6th European Conference on Radar in Meteorology and Hydrology.

- Park, S-G., V.N. Bringi, V. Chandrasekar, M. Maki, and K. Iwanami (2005a), Correction of radar reflectivity and differential reflectivity for rain attenuation at X-band. Part I: Theoretical and empirical basis, *Journal of Atmospheric and Oceanic Technology*, 22:1621–1632.
- Park, S-G., M. Maki, and K. Iwanami V.N. Bringi, V. Chandrasekar (2005b), Correction of radar reflectivity and differential reflectivity for rain attenuation at X-band. Part II: Evaluation and application, *Journal of Atmospheric and Oceanic Technology*, 22:1633–1655.
- Paul J., Steve Lapczak (2002), Evolution of the Canadian operational radar network, *Proceedings. 2nd European Conference on Radar in Meteorology and Hydrology (ERAD)*. Delft, The Netherlands, 370–382.
- Postel SL, Daily GC, Ehrlich PR (1996), Human appropriation of renewable fresh water, *Science*, 271:785–788.
- Postel SL (2000), Entering an era of water scarcity: The challenges ahead, *Ecological Applications*, 10:941–948.
- Pruppacher, H.R., and A.K.V. Beard (1970), A wind tunnel investigation of the internal circulation and shape of water drops falling at terminal velocity in air, *Quarterly Journal of the Royal Meteorological Society*, 96, 408, 247-256, 1477-870.
- Rabiner, L. R. and Gold, B. (1975), *Theory and Application of Digital Signal Processing*, Prentice-Hall, Englewood Cliffs.
- Ryde, J. W. (1946), The attenuation and radar echoes produced at centimeter wavelengths by various meteorological phenomena, *Meteorological Factors in Radio Wave Propagation*, Physical Society, London, 169-188.
- Ryzhkov, A., and D. S. Zrnich (1995), Precipitation and attenuation measurements at a 10-cm wavelength, *Journal of Applied Meteorology*, 34, 2121–2134.
- Ryzhkov, A.V., S.E. Giangrande, V.M. Melnikov, T.J. Schuur (2005), Calibration issues of dual-polarization radar measurements, *Journal of Atmospheric and Oceanic Technology*, 22:8, 1138-1155.
- Sachidananda, M., and D. Zrnich (1986), Differential propagation phase shift and rainfall rate estimation, *Radio Sci.*, 21(2), 235-247.
- Sauvageot, H. 1992. *Radar Meteorology*, Norwood, Mass.: Artech House.
- Sauvageot, H. (1996), Polarimetric radar at attenuated frequencies as a hydrological sensor, *Journal of Atmospheric and Oceanic Technology*, 13, 630–637.
- Sauvageot, H., F. Mesnard, A. J. Illingworth, and J. W. F. Goddard (1998), Rainfall rate measurement with a polarimetric radar at an attenuated wavelength, *Geophysical Research Letters*, 25(15), 2841–2844.
- Schleiss, M., A. Berne and R. Uijlenhoet (2009), Geostatistical simulation of 2D fields of raindrop size distributions at the meso-gamma scale, *Water Resources Research*, 45, W07415.

- Schleiss, M., J. Jaffrain, and A. Berne (2011), Statistical analysis of rainfall intermittency at small spatial and temporal scales, *Geophysical Research Letters*, 38, L18403.
- Seo, B.-C. W.F. Krajewski and J.A. Smith (2011), Four-dimensional reflectivity data comparison between two ground-based radars: Methodology and statistical analysis, submitted to *Hydrological Sciences Journal*.
- Serrar, S., G. Delrieu, J-D. Creutin, and R. Uijlenhoet (2000), Mountain reference technique: Use of mountain returns to calibrate weather radars operating at attenuating wavelengths, *Journal of Geophysical Research*, 105:2281–2290.
- Shapiro, Alan, Katherine M. Willingham, Corey K. Potvin (2010), Spatially Variable Advection Correction of Radar Data. Part I: Theoretical Considerations, *Journal of the Atmospheric Sciences*, 67, 3445–3456.
- Shepard D. (1968), A two-dimensional interpolation function for irregular-spaced data, *Proceedings 23rd National conference of Association for Computing Machinery (ACM)*, 517-524.
- Smyth T.J., and A.J. Illingworth (1998), Correction for attenuation of radar reflectivity using polarization data, *Q. J. R. Meteorol. Soc.*, 124, pp.2393-2415.
- Steiner, Matthias, James A. Smith (2002), Use of Three-Dimensional Reflectivity Structure for Automated Detection and Removal of Nonprecipitating Echoes in Radar Data, *Journal of Atmospheric and Oceanic Technology*, 19, 673–686.
- Testud, J., E. Le Bouar, E. Obligis, and M. Ali-Mehenni (2000), The rain profiling algorithm applied to polarimetric weather radar, *J. Atmos. Oceanic Technol.*, 17, 332–356.
- Testud, J., S. Oury, R.A. Black, P. Amayenc, and X. Dou (2001), The concept of “normalized” distribution to describe raindrop spectra: A tool for cloud physics and cloud remote sensing, *J. Appl. Meteor.*, 40, 1118–1140.
- Uijlenhoet, R. and A. Berne (2008), Stochastic simulation experiment to assess radar rainfall retrieval uncertainties associated with attenuation and its correction, *Hydrology and Earth System Sciences*, 12, 587-601.
- Villarini, G., F. Serinaldi, J.A. Smith and W.F. Krajewski (2009), On the stationarity of annual flood peaks in the Continental United States during the 20th Century, *Water Resources Research*, 45, W088417.
- Villarini G., W.F. Krajewski, A.A. Ntelekos, K.P. Georgakakos and J.A. Smith (2010), Probabilistic forecasting of flash floods: Combined effects of uncertainties in radar-rainfall estimates and flash flood guidance, *Journal of Hydrology*, 394(1-2), 275-284.
- Vivekanandan, J., W.M. Adams and V.N. Bringi (1991), Rigorous approach to polarimetric radar modeling of hydrometeor distribution orientations, *Journal of Applied Meteorology*, vol.3, pp. 1053-1063.
- Vivekanandan, J., Zrnić, D. S., Ellis, S. M., Oye, R., Ryzhkov, A. V., and Straka, J. (1999), Cloud microphysics retrieval using S-band dualpolarization radar measurements, *Bulletin of the American Meteorological Society*, 80, 3, 381–388.

- Waterman, P.C. (1971), Symmetry, unitarity, and geometry in electromagnetic scattering, *Phys. Rev. D*, 3, 825–839.
- Xiao, Q., and J. Sun (2007), Multiple radar data assimilation and short-range quantitative precipitation forecasting of a squall line observed during IHOP 2002, *Monthly Weather Review*, 135, 3381–3404.
- Zahiri, E.P., M. Gosset, J.P. Lafore, and V. Gouget (2008), Use of a radar simulator on the output fields from a numerical mesoscale model to analyze X-band rain estimators, *J. Atmos. Oceanic Technol.*, 25, 341–367.
- Zawadzki, I. (1984), Factors affecting the precision of radar measurements of rain, *22d Conf. on Radar Meteorology*, Zurich, Switzerland, Amer. Meteor. Soc., 251–256.
- Zhang, Guifu, Juanzhen Sun, Edward A. Brandes, 2006: Improving Parameterization of Rain Microphysics with Disdrometer and Radar Observations. *Journal of Atmospheric Sciences*, 63, 1273–1290.
- Zrnić, D.S., and A.V. Ryzhkov (1999), Polarimetry for weather surveillance radars, *Bull. Am. Meteorol. Soc.* 80, 389–406.